

TECHNISCHE UNIVERSITÄT MÜNCHEN

Fakultät für Medizin

# Quantification of Cerebral Oxygenation and Perfusion by Multi-Parametric Magnetic Resonance Imaging in Carotid Artery Stenosis

Stephan Simon Kaczmarz

Vollständiger Abdruck der von der Fakultät für Medizin der Technischen Universität München zur Erlangung des akademischen Grades eines

Doktors der Naturwissenschaften (Dr. rer. nat.)

genehmigten Dissertation.

Vorsitzender: Prof. Dr. Wolfgang Weber  
Prüfer der Dissertation: 1. Priv.-Doz. Dr. Christine Preibisch  
2. Prof. Dr. Axel Haase  
3. apl. Prof. Dr. Sibylle Ziegler

Die Dissertation wurde am 17.11.2020 bei der Technischen Universität München eingereicht und durch die Fakultät für Medizin am 13.07.2021 angenommen.



# Abstract

Cerebrovascular diseases (CVD) are a major cause of death in developed countries. Being just one CVD among many others, internal carotid artery stenosis (ICAS) accounts for 10-20% of all strokes. In ICAS, brain feeding arteries are narrowed by a plaque, which is known to cause severe cerebral hemodynamic perturbations. However, current diagnostics do not consider those effects on the brain tissue. At the same time, possible severe complications aggravate treatment decisions. Thus, ICAS may greatly benefit from novel multi-parametric quantitative hemodynamic methods based on magnetic resonance imaging (MRI).

MRI allows non-invasive imaging with excellent soft tissue contrast and is of pivotal interest for brain imaging. The great flexibility of pulse sequences allows to assess a large variety of hemodynamic processes. Several parameters of the complex blood supply can be locally mapped within the whole brain by MR-based perfusion and oxygenation imaging techniques. Quantitative imaging furthermore allows to number specific tissue properties. However, especially clinically applicable methods are lacking and characterization in clinical studies is clearly demanded, which additionally requires a multi-parametric data evaluation framework.

Aiming for this gap, the present cumulative thesis comprises four journal publications. The main purpose was to test the hypothesis that clinically applicable MRI-based quantitative perfusion and oxygenation imaging is sensitive to hemodynamic perturbations in ICAS. Furthermore, multi-parametric MRI was hypothesized to enable new insights to the pathophysiology and offer perspectives to improve clinical diagnostics.

In the first journal publication, a novel method was introduced to delineate individual watershed areas (iWSA), which are especially vulnerable for perfusion deficits. The necessity for individual segmentations was demonstrated by increased spatial iWSA variability in ICAS.

In the second journal publication, fiber orientation effects within white matter (WM) of oxygenation sensitive imaging were characterized. The results showed comparably low average anisotropy driven variations and thus point to careful applicability in WM, which may increase the sensitivity compared to previous evaluations, restricted to grey matter (GM) only.

In the third journal publication, six quantitative hemodynamic MRI parameters were evaluated in ICAS patients and age-matched healthy controls within iWSAs. The results demonstrated complementary information by the multi-parametric approach as well as high sensitivity and specificity of the proposed methods in GM and even WM. Application of iWSAs furthermore significantly improved the sensitivity to hemodynamic impairments in ICAS and provided new insights to pathophysiologic mechanisms in ICAS at the same time.

Finally, methodological improvements to the oxygenation sensitive technique were introduced in the fourth journal publication. The results showed significantly decreased values of previously overestimated relative oxygen extraction fraction (rOEF) towards physiologically meaningful values. Furthermore, increased sensitivity to ICAS impairments was shown by unveiling formerly undetected focal rOEF increases, which supports widespread future applications.

In conclusion, quantitative multi-parametric oxygenation and perfusion MRI is of highest clinical relevance with great potential to improve diagnostics, treatment decisions and longitudinal treatment efficacy monitoring in ICAS and several other pathologies. Furthermore, quantitative hemodynamic imaging offers fascinating perspectives in neuroscience.





# Contents

<b>Abstract</b>	<b>1</b>
<b>List of Included Journal Publications</b>	<b>5</b>
<b>List of Related Publications</b>	<b>7</b>
<b>1 Introduction</b>	<b>15</b>
1.1 Clinical Relevance . . . . .	16
1.2 Thesis Purpose . . . . .	17
1.3 Thesis Structure . . . . .	17
<b>2 Principles of Magnetic Resonance Imaging</b>	<b>19</b>
2.1 Physical principles of the NMR signal . . . . .	19
2.2 Magnetic Resonance Imaging . . . . .	24
2.3 Imaging Techniques . . . . .	25
2.4 MR Hardware . . . . .	29
<b>3 Quantification of Cerebral Perfusion, Oxygenation and Diffusion</b>	<b>31</b>
3.1 Neuro-Vascular System . . . . .	31
3.2 Perfusion Imaging . . . . .	35
3.3 Oxygenation Imaging . . . . .	43
3.4 Structural Imaging . . . . .	44
<b>4 Clinical Background of Internal Carotid Artery Stenosis</b>	<b>47</b>
4.1 Anatomy of Major Neck Arteries . . . . .	48
4.2 Cerebral Vascular Territories . . . . .	49
4.3 Internal Carotid Artery Stenosis . . . . .	50
4.4 Diagnosis and Treatment Options . . . . .	51
<b>5 Database for Hemodynamic MRI Evaluation</b>	<b>53</b>
5.1 Processing Pipeline . . . . .	53
5.2 Applications in Journal Publications . . . . .	55
<b>6 Compliance with Ethical Standards</b>	<b>57</b>
<b>7 Journal Publications</b>	<b>59</b>
7.1 Journal Publication I . . . . .	59
7.2 Journal Publication II . . . . .	74
7.3 Journal Publication III . . . . .	91
7.4 Journal Publication IV . . . . .	110
<b>8 Discussion</b>	<b>121</b>
8.1 Review of Existing Literature . . . . .	121

## Contents

---

8.2 Present Work . . . . .	125
8.3 Perspectives . . . . .	128
<b>Bibliography</b>	<b>131</b>
<b>List of Symbols and Abbreviations</b>	<b>157</b>
<b>List of Figures</b>	<b>163</b>
<b>List of Tables</b>	<b>167</b>
<b>Acknowledgments</b>	<b>169</b>

# List of Included Journal Publications

The present dissertation is based on the following four journal publications:

- JP-I **S. Kaczmarz**, V. Griese, C. Preibisch, M. Kallmayer, M. Helle, I. Wustrow, E. T. Petersen, H.-H. Eckstein, C. Zimmer, C. Sorg, and J. Goettler, “*Increased variability of watershed areas in patients with high-grade carotid stenosis*“, *Neuroradiology*, Vol. 60, No. 3, pp. 311-323, Mar. 2018. DOI: 10.1007/s00234-017-1970-4
- JP-II **S. Kaczmarz**, J. Goettler, C. Zimmer, F. Hyder and C. Preibisch, “*Characterizing white matter fiber orientation effects on multi-parametric quantitative BOLD assessment of oxygen extraction fraction*“, *Journal of Cerebral Blood Flow and Metabolism*, Vol. 40, No. 4, pp. 760-774, Apr. 2020. DOI: 10.1177/0271678X19839502
- JP-III **S. Kaczmarz**, J. Goettler, J. Petr, M.B. Hansen, K. Mouridsen, C. Zimmer, F. Hyder, C. Preibisch, “*Hemodynamic impairments within individual watershed areas in asymptomatic carotid artery stenosis by multimodal MRI*“, *Journal of Cerebral Blood Flow and Metabolism*, Epub ahead of print: 271678X20912364, Apr. 2020. DOI: 10.1177/0271678X20912364
- JP-IV **S. Kaczmarz**, F. Hyder, C. Preibisch, “*Oxygen extraction fraction mapping with multi-parametric quantitative BOLD MRI: reduced transverse relaxation bias using 3D-GraSE imaging*“, *NeuroImage*, Vol. 220, p. 117095, Oct. 2020. DOI: 10.1016/j.neuroimage.2020.117095

The above four journal publications are referred to as JP-I, JP-II, JP-III and JP-IV, respectively. Summaries and full texts of the publications are presented in Chapter 7.



# List of Related Publications

The author contributed also to the following subject-related journal publications:

## Senior-authored Journal Publications

- J1 N. Sollmann, H. Liebl, C. Preibisch, C. Zimmer, M. Obara, J.S. Kirschke, **S. Kaczmarz**. *"Super-selective ASL and 4D ASL-based MR angiography in a patient with Moyamoya disease"*, Clinical Neuroradiology, Epub ahead of print, August 2020, DOI: 10.1007/s00062-020-00961-8.
- J2 S.V. Frolov, S. Sindeev, J.S. Kirschke, P. Arnold, S. Prothmann, D. Liepsch, A. Balasso, A. Potlov, I. Larrabide, **S. Kaczmarz**. *"CFD and MRI studies of hemodynamic changes after flow diverter implantation in a patient-specific model of the cerebral artery"*, Experiments in Fluids, Vol. 59, No. 11, Article number 176, 2018.

## Co-authored Journal Publications

- J3 J. Goettler, **S. Kaczmarz**, R. Nuttall, V. Griese, N. Napiorkowski, M. Kallmayer, I. Wustrow, H.-H. Eckstein, C. Zimmer, C. Preibisch, K. Finke, C. Sorg. *"The stronger one-sided relative hypoperfusion, the more pronounced ipsilateral spatial attentional bias in patients with asymptomatic carotid stenosis"*, JCBFM, Vol. 40, No. 2, pp. 314-327, Feb. 2020.
- J4 J. Goettler, **S. Kaczmarz**, M. Kallmayer, I. Wustrow, H.-H. Eckstein, C. Zimmer, C. Sorg, C. Preibisch, F. Hyder. *"Flow-metabolism uncoupling in patients with asymptomatic unilateral carotid artery stenosis assessed by multi-modal magnetic resonance imaging"*, JCBFM, Vol. 39, No. 11, pp. 2132-2143, Nov. 2019.
- J5 J. Goettler, C. Preibisch, I. Riederer, L. Pasquini, P. Alexopoulos, K.P. Bohn, I. Yakushev, E. Beller, **S. Kaczmarz**, C. Zimmer, T. Grimmer, A. Drzezga, C. Sorg. *"Reduced blood oxygenation level dependent connectivity is related to hypoperfusion in Alzheimer's disease"*, JCBFM, Vol. 39, No. 7, pp. 1314-1325, Jul. 2019.
- J6 S. Sindeev, P.G. Arnold, S. Frolov, S. Prothmann, D. Liepsch, A. Balasso, P. Berg, **S. Kaczmarz**, J.S. Kirschke. *"Phase-contrast MRI versus numerical simulation to quantify hemodynamical changes in cerebral aneurysms after flow diverter treatment"*, PLoS One, Vol. 13, No. 1, e0190696, eCollection 2018.
- J7 J. Goettler, M. Lukas, A. Kluge, **S. Kaczmarz**, J. Gempt, F. Ringel, M. Mustafa, B. Meyer, C. Zimmer, M. Schwaiger, S. Foerster, C. Preibisch, T. Pyka. *"Intra-lesional spatial correlation of static and dynamic FET-PET parameters with MRI-based cerebral blood volume in patients with untreated glioma"*, European Journal of Nuclear Medicine and Molecular Imaging, Vol. 44, No. 3, pp. 392-397, Mar. 2017.

The author contributed also to the following conference abstracts:

## First-authored Conference Abstracts

- C1 **S. Kaczmarz**, J. Goettler, J. Petr, N. Sollmann, A. Hock, M. B. Hansen, K. Mouridsen, C. Zimmer, F. Hyder, C. Preibisch. *"Evaluation of treatment efficacy in asymptomatic carotid artery stenosis patients by clinically applicable hemodynamic MRI and cognitive testing"* (**Early Career Fellowship**). Proc of 37th ESMRMB Meeting, Program number (PN) S07.07, Virtual Meeting, September 30 - October 2, 2020 (oral presentation)
- C2 **S. Kaczmarz**, J. Goettler, J. Petr, N. Sollmann, L. Schmitzer, A. Hock, M. B. Hansen, K. Mouridsen, C. Zimmer, F. Hyder, C. Preibisch. *"Treatment efficacy of asymptomatic carotid artery stenosis patients evaluated by clinically applicable hemodynamic MRI and cognitive testing"* (**Summa Cum Laude Merit Award**). Proc of 28th Scientific Meeting of ISMRM, PN 1059, Virtual Meeting, August 8-13, 2020 (oral presentation)
- C3 **S. Kaczmarz**, J. Kufer, L. Schmitzer, J. Goettler, M.E. Archila Melendez, A. Hock, C. Sorg, C. Zimmer, F. Hyder, C. Preibisch. *"Comparison of calibrated fMRI with calibration factor M determined by hypercapnia vs. gas-free R2"*. Proc of 28th Scientific Meeting of ISMRM, PN 1113, Virtual Meeting, August 8-13, 2020 (oral presentation)
- C4 **S. Kaczmarz**, J. Goettler, A. Hock, C. Zimmer, F. Hyder, C. Preibisch. *"Similar mechanisms and locations of white matter lesions in elderly healthy controls and asymptomatic carotid artery stenosis patients"*. Proc of 28th Scientific Meeting of ISMRM, PN 1449, Virtual Meeting, August 8-13, 2020 (digital poster)
- C5 **S. Kaczmarz**, J. Petr, N. Sollmann, A. Hock, C. Zimmer, F. Hyder, C. Preibisch, J. Goettler. *"Recovery of cerebrovascular reactivity after treatment of asymptomatic carotid artery stenosis is assessable by non-invasive breath-hold fMRI within global watershed areas"*. Proc of 54th DGNR Meeting in Clinical Neuroradiology, Frankfurt, Germany, October 9-12, 2019 (oral presentation)
- C6 **S. Kaczmarz**, J. Petr, M. B. Hansen, A. Hock, J. Kufer, K. Mouridsen, C. Zimmer, F. Hyder, C. Preibisch, J. Goettler. *"Hemodynamic impairments in asymptomatic unilateral carotid artery stenosis are most pronounced within individual watershed areas"*. Proc of 54th DGNR Meeting in Clinical Neuroradiology, Frankfurt, Germany, October 9-12, 2019 (oral presentation)
- C7 **S. Kaczmarz**, J. Goettler, J. Petr, M. B. Hansen, J. Kufer, C. Zimmer, K. Mouridsen, F. Hyder, C. Preibisch. *"Multi-modal evaluation of haemodynamic impairments within individual watershed areas reveals increased sensitivity in unilateral carotid artery stenosis"* (**Student Support Programme Fellow**). Proc of 36th ESMRMB Meeting, PN S24.08, Rotterdam, The Netherlands, October 3-5, 2019 (oral presentation)
- C8 **S. Kaczmarz**, J. Goettler, J. Petr, M. B. Hansen, J. Kufer, A. Hock, K. Mouridsen, C. Zimmer, F. Hyder, C. Preibisch. *"Haemodynamic impairments in asymptomatic unilateral carotid artery stenosis are most pronounced within individual watershed areas"*. Proc of 29th ISCBFM Meeting, PN BS08-5, Yokohama, Japan, May 11-16, 2019 (oral presentation)

- C9 **S. Kaczmarz**, J. Goettler, A. Hock, C. Zimmer, F. Hyder, C. Preibisch. "*White matter fiber orientation effects of mq-BOLD derived oxygen extraction fraction*" (**Early Career Investigator Award**). Proc of 29th ISCBFM Meeting, PN PA00-A26, Yokohama, Japan, May 11-16, 2019 (poster)
- C10 **S. Kaczmarz**, J. Goettler, N. Sollmann, A. Hock, C. Sorg, C. Zimmer, K. Mouridsen, F. Hyder, C. Preibisch, J. Petr. "*Recovery of cerebrovascular reactivity after treatment of asymptomatic carotid artery stenosis is assessable by non-invasive breath-hold fMRI within global watershed areas*". Proc of 29th ISCBFM Meeting, PN PB01-J09, Yokohama, Japan, May 11-16, 2019 (poster)
- C11 **S. Kaczmarz**, J. Goettler, N. Sollmann, J. Kufer, M. B. Hansen, A. Hock, C. Sorg, C. Zimmer, K. Mouridsen, F. Hyder, C. Preibisch, J. Petr. "*Recovery of cerebrovascular reactivity after asymptomatic carotid artery stenosis treatment is assessable by Breathhold-fMRI within global watershed areas*" (**Magna Cum Laude Merit Award**). Proc of 27th Scientific Meeting of ISMRM, PN 739, Montréal, Canada, May 11-16, 2019 (oral presentation)
- C12 **S. Kaczmarz**, J. Goettler, A. Hock, C. Zimmer, F. Hyder, C. Preibisch. "*Impact of unilateral carotid artery stenosis on white matter fiber orientation effects of mq-BOLD derived oxygen extraction fraction*" (**Educational Stipend Fellow**). Proc of 27th Scientific Meeting of ISMRM, PN 154, Montréal, Canada, May 11-16, 2019 (power pitch)
- C13 **S. Kaczmarz**, J. Goettler, J. Petr, M. B. Hansen, J. Kufer, A. Hock, C. Sorg, C. Zimmer, K. Mouridsen, F. Hyder, C. Preibisch. "*Hemodynamic impairments in asymptomatic unilateral carotid artery stenosis are increased within individual watershed areas*" (**Magna Cum Laude Merit Award**). Proc of 27th Scientific Meeting of ISMRM, PN 3246, Montréal, Canada, May 11-16, 2019 (electronic poster)
- C14 **S. Kaczmarz**, J. Goettler, A. Hock, D. Karampinos, C. Zimmer, F. Hyder, C. Preibisch. "*Assessment of white matter anisotropy effects in mq-BOLD based mapping of relative Oxygen Extraction Fraction*" (**Magna Cum Laude Merit Award**). Proc of 26th Scientific Meeting of ISMRM, PN 502, Paris, France, June 16-21, 2018 (oral presentation)
- C15 **S. Kaczmarz**, J. Goettler, A. Hock, D. Karampinos, C. Zimmer, F. Hyder, C. Preibisch. "*Reducing T2-related bias in mq-BOLD derived maps of Oxygen Extraction Fraction by 3D acquisition*". Proc of 26th Scientific Meeting of ISMRM, PN 5023, Paris, France, June 16-21, 2018 (electronic poster)
- C16 **S. Kaczmarz**, K. van de Ven, M. Helle, H. Hooijman, C. Zimmer, J. Goettler, C. Preibisch. "*Charakterisierung der Grenzzonen-Physiologie bei Patienten mit hochgradigen Carotis-Stenosen mittels multi-parametrischer MRT*". Proc of 52nd DGMR Meeting in Clinical Neuroradiology, PN 79, Cologne, Germany October 11-14, 2017 (poster)
- C17 **S. Kaczmarz**, J. Goettler, V. Griese, J. Petr, K. van de Ven, M. Helle, H. Kooijman, A. Kluge, D. Karampinos, C. Zimmer, C. Sorg, C. Preibisch. "*Evaluation of hemodynamic impairments in healthy elderly participants and patients with high-grade unilateral carotid artery stenosis*". Proc of 25th Scientific Meeting of ISMRM, PN 4562, Honolulu, Hawaii (USA), April 22-27, 2017 (electronic poster)

- C18 **S. Kaczmarz**, J. Goettler, V. Griese, J. Petr, C. Zimmer, C. Sorg, C. Preibisch. "Evaluation of hemodynamic impairments in unilateral high-grade carotid artery stenosis patients and healthy age-matched participants". Proc of 28th ISCBFM Meeting, PN PS06-091, Berlin, Germany, April 1-4, 2017 (poster)
- C19 **S. Kaczmarz**, J. Goettler, H. Kooijman, K. Van De Ven, D. Karampinos, C. Zimmer, C. Preibisch. "Evaluation of pCASL sequences for CBF measures in healthy subjects and patients with high-grade carotid artery stenosis" (**Student Support Programme Fellow**). Proc of 33rd ESMRMB Meeting, PN 67, Vienna, Austria, September 29 - October 1, 2016 (oral presentation)
- C20 **S. Kaczmarz**, J. Goettler, A. Kluge, D. Karampinos, C. Zimmer, C. Preibisch. "Evaluation of perfusion and hypoxia parameters in healthy subjects and patients with high-grade carotid artery stenosis" (**Educational Stipend Fellow**). Proc of 24th Scientific Meeting of ISMRM, PN 4383, Singapore, Singapore, May 7-13, 2016 (electronic poster)

## Senior-authored Conference Abstracts

- C21 G. Hoffmann, J. Kufer, L. Schmitzer, C. Zimmer, C. Preibisch, **S. Kaczmarz**. "Perfusion imaging under hypercapnia: Single echo pCASL vs. dual echo pCASL". Proc of 37th ESMRMB Meeting, PN L01.120, Virtual Meeting, September 30 - October 2, 2020 (lightning talk)
- C22 J. Kufer, J. Goettler, S. Epp, M. B. Hansen, C. Zimmer, K. Mouridsen, F. Hyder, C. Preibisch, **S. Kaczmarz**. "Effective oxygen diffusivity mapping with multiparametric quantitative BOLD and pCASL: Comparison between healthy young and elderly subjects" (**Summa Cum Laude Merit Award**). Proc of 28th Scientific Meeting of ISMRM, PN 1108, Virtual Meeting, August 8-13, 2020 (oral presentation)
- C23 J. Kufer, J. Goettler, C. Zimmer, F. Hyder, C. Preibisch, **S. Kaczmarz**. "MRI-based assessment of impaired oxygen diffusivity in asymptomatic internal carotid artery stenosis". Proc of 54th DGNR Meeting in Clinical Neuroradiology, Frankfurt, Germany, October 9-12, 2019 (oral presentation)
- C24 J. Kufer, J. Goettler, C. Zimmer, F. Hyder, C. Preibisch, **S. Kaczmarz**. "Effective oxygen diffusivity is ipsilaterally decreased in asymptomatic unilateral internal carotid artery stenosis". Proc of 36th ESMRMB Meeting, PN S24.09, Rotterdam, The Netherlands, October 3-5, 2019 (oral presentation)
- C25 J. Kufer, J. Goettler, M. B. Hansen, A. Hock, C. Zimmer, K. Mouridsen, F. Hyder, C. Preibisch, **S. Kaczmarz**. "Relating lateralized mq-BOLD-based relative oxygen extraction fraction to areas of elevated DSC-based oxygen extraction capacity in asymptomatic unilateral carotid artery stenosis". Proc of 29th ISCBFM Meeting, PN PB01-J08, Yokohama, Japan, May 11-16, 2019 (poster)
- C26 J. Kufer, J. Goettler, C. Zimmer, F. Hyder, C. Preibisch, **S. Kaczmarz**. "Effective oxygen diffusivity is lateralized within the anterior circulation territory in asymptomatic unilateral carotid artery stenosis". Proc of 29th ISCBFM Meeting, PN PL03-W11, Yokohama, Japan, May 11-16, 2019 (poster)



## Co-authored Conference Abstracts

- C27 L. Schmitzer, **S. Kaczmarz**, N. Sollmann, C. Zimmer, C. Preibisch, J. Goettler. *"Stable fractional anisotropy and mean diffusivity after treatment in patients with asymptomatic high grade internal carotid artery stenosis"*. Proc of 28th Scientific Meeting of ISMRM, PN 1054, Virtual Meeting, August 8-13, 2020 (oral presentation)
- C28 R. Berg, T. Leutritz, **S. Kaczmarz**, C. Zimmer, N. Weiskopf, C. Preibisch. *"Evaluating Compressed SENSE acceleration for multi-parametric quantitative mapping of  $R1$ ,  $R2^*$ ,  $PD$ , and  $MTsat$  with the hMRI toolbox"*. Proc of 28th Scientific Meeting of ISMRM, PN 3776, Virtual Meeting, August 8-13, 2020 (electronic poster)
- C29 C. Preibisch, M. Archila-Melendez, **S. Kaczmarz**, C. Sorg. *"Studying the impact of impaired perfusion and oxygen metabolism on resting-state fMRI-based functional connectivity by simulating blood oxygenation fluctuations"*. Proc of 28th Scientific Meeting of ISMRM, PN 3975, Virtual Meeting, August 8-13, 2020 (electronic poster)
- C30 R. Berg, **S. Kaczmarz**, T. Leutritz, N. Weiskopf, C. Zimmer, C. Preibisch. *"Evaluating Compressed SENSE acceleration for quantitative mapping of longitudinal relaxation rate  $R1$ "*. Proc of 54th DGNR Meeting in Clinical Neuroradiology, Frankfurt, Germany, October 9-12, 2019 (poster)
- C31 C. Preibisch, S. Koutsouli, **S. Kaczmarz**, S. Epp, V. Riedl. *"Quantitative functional MRI of human visual cortex activation using multi-parametric quantitative BOLD"*. Proc of 54th DGNR Meeting in Clinical Neuroradiology, Frankfurt, Germany, October 9-12, 2019 (poster)
- C32 L. Schmitzer, **S. Kaczmarz**, N. Sollmann, C. Zimmer, C. Preibisch, J. Goettler. *"Stable localization of watershed areas after revascularization therapy in patients with asymptomatic internal carotid artery stenosis"*. Proc of 54th DGNR Meeting in Clinical Neuroradiology, Frankfurt, Germany, October 9-12, 2019 (poster)
- C33 L. Schmitzer, **S. Kaczmarz**, Nico Sollmann, Claus Zimmer, Christine Preibisch, Jens Goettler. *"Watershed Areas in Patients with asymptomatic high grade Internal Carotid Artery Stenosis"*. Proc of 36th ESMRMB Meeting, PN S04.05, Rotterdam, The Netherlands, October 3-5, 2019 (oral presentation)
- C34 R. Berg, **S. Kaczmarz**, T. Leutritz, N. Weiskopf, C. Zimmer, C. Preibisch. *"Evaluating Compressed SENSE acceleration for quantitative mapping of longitudinal relaxation rate  $R1$ "*. Proc of 36th ESMRMB Meeting, PN L06.23, Rotterdam, The Netherlands, October 3-5, 2019 (poster)
- C35 K. Katarzyna, S. Epp, S. Koutsouli, **S. Kaczmarz**, C. Preibisch, V. Riedl. *"Multi-parametric quantitative fMRI imaging in humans during fixation and visual stimulation"*. Proc of 25th Scientific Meeting of OHBM, PN Th534, Rome, Italy, June 9-13, 2019 (electronic poster)
- C36 J. Goettler, **S. Kaczmarz**, C. Zimmer, C. Sorg, C. Preibisch, F. Hyder. *"Uncoupling of cerebral blood flow and oxidative metabolism in patients with asymptomatic high-grade carotid artery stenosis assessed by multi-modal MRI"*. Proc of 29th ISCBFM Meeting, PN BS08-6, Yokohama, Japan, May 11-16, 2019 (oral presentation)

- C37 L. Schmitzer, **S. Kaczmarz**, N. Sollmann, C. Zimmer, C. Preibisch, J. Goettler. *"Watershed areas in patients with asymptomatic unilateral internal carotid-artery stenosis: stable spatial extent after revascularization therapy"*. Proc of 29th ISCBFM Meeting, PN BS14-4, Yokohama, Japan, May 11-16, 2019 (oral presentation)
- C38 J. Goettler, **S. Kaczmarz**, N. Sollmann, L. Schmitzer, C. Zimmer, C. Preibisch. *"Assessment of territory-specific perfusion delay and its recovery after revascularization treatment in asymptomatic carotid stenosis patients"*. Proc of 29th ISCBFM Meeting, PN PA00-A31, Yokohama, Japan, May 11-16, 2019 (poster)
- C39 C. Preibisch, S. Koutsouli, **S. Kaczmarz**, S. Epp, V. Riedl. *"Quantitative functional imaging of visual cortex activity in humans using multi-parametric blood oxygenation level dependent MRI"*. Proc of 27th Scientific Meeting of ISMRM, PN 3736, Montréal, Canada, May 11-16, 2019 (electronic poster)
- C40 J. Goettler, **S. Kaczmarz**, C. Zimmer, C. Sorg, F. Hyder, C. Preibisch. *"Uncoupling of cerebral blood flow and oxidative metabolism in patients with asymptomatic high-grade carotid artery stenosis assessed by multi-modal MRI"*. Proc of 53rd DGNR Meeting in Clinical Neuroradiology, PN 174, Frankfurt, Germany, October 3-6, 2018 (poster)
- C41 C. Preibisch, **S. Kaczmarz**, J. Goettler, C. Zimmer. *"Reducing systematic bias in MR-based oxygen extraction fraction derived from multi-parametric quantitative assessment of blood oxygenation level dependent signal"*. Proc of 53rd DGNR Meeting in Clinical Neuroradiology, PN 143, Frankfurt, Germany, October 3-6, 2018 (poster)
- C42 J. Goettler, **S. Kaczmarz**, C. Zimmer, C. Sorg, C. Preibisch, F. Hyder. *"Reduced cerebral blood flow and oxygen consumption in asymptomatic unilateral carotid stenosis patients assessed by arterial spin labeling and multi-parametric quantitative BOLD imaging"*. Proc of 26th Scientific Meeting of ISMRM, PN 4798, Paris, France, June 16-21, 2018 (electronic poster)
- C43 M. Wolf, **S. Kaczmarz**, J. Goettler, C. Zimmer, S. Schwarzbauer, C. Preibisch. *"Correlation-based temporal similarity mapping of DSC-MRI data in patients with asymptomatic unilateral high-grade carotid stenosis"*. Proc of 26th Scientific Meeting of ISMRM, PN 1894, Paris, France, June 16-21, 2018 (poster)
- C44 I. Tsiachristos, **S. Kaczmarz**, J. Goettler, C. Preibisch. *"Comparison of PVE correction methods for ASL perfusion MRI on a cohort of healthy subjects"*. Proc of 34th ESMRMB Meeting, PN 394, Barcelona, Spain, October 19-21, 2017 (poster)
- C45 P. Arnold, S. Sindeev, **S. Kaczmarz**, S. Prothmann, C. Zimmer, J. Kirschke. *"Comparisons of Hemodynamic before/after flow-diverter placement with MRI measurements and CFD simulations"*. Proc of 23rd Congress of European Society of Biomechanics, July 2 - 5, 2017, Sevilla, Spain (poster)
- C46 V. Griese, **S. Kaczmarz**, A. Kluge, K. van de Ven, M. Helle, H. Kooijman, C. Zimmer, C. Sorg, J. Goettler, C. Preibisch. *"Analysis of cerebrovascular watershed areas in patients with high-grade carotid artery stenosis using DSC-based time-to-peak maps"* (**Magna Cum Laude Merit Award**), Proc of 25th Scientific Meeting of ISMRM, PN 147, Honolulu, Hawaii (USA), April 22-27, 2017 (oral presentation)

- C47 J. Goettler, **S. Kaczmarz**, R. Nuttall, V. Griese, H. Kooijman, M. Helle, K. van de Ven, C. Zimmer, K. Finke, C. Sorg, C. Preibisch. *"One-sided hypoperfusion is associated with contralateral attention deficits in asymptomatic high-grade carotid stenosis patients"*. Proc of 25th Scientific Meeting of ISMRM, PN 149, Honolulu, Hawaii (USA), April 22-27, 2017 (oral presentation)
- C48 J. Goettler, I. Riederer, L. Pasquini, **S. Kaczmarz**, C. Zimmer, C. Preibisch, C. Sorg. *"Reduced BOLD connectivity is related to hypoperfusion in Alzheimers disease"*. Proc of 25th Scientific Meeting of ISMRM, PN 4120, Honolulu, Hawaii (USA), April 22-27, 2017 (electronic poster)
- C49 C. Ulas, **S. Kaczmarz**, C. Preibisch, J. I. Sperl, M. I. Menzel, A. Haase, B. Menze. *"A spatio-temporal denoising approach based on total variation regularization for Arterial Spin Labeling"*. Proc of 25th Scientific Meeting of ISMRM, PN 3634, Honolulu, Hawaii (USA), April 22-27, 2017 (electronic poster)
- C50 J. Goettler, **S. Kaczmarz**, R. Nuttall, V. Griese, C. Zimmer, C. Sorg, C. Preibisch. *"One-sided hypoperfusion is associated with contralateral attention deficits in asymptomatic high-grade carotid-stenosis patients"*. Proc of 28th ISCBFM Meeting, PN PS06-093, Berlin, Germany, April 1-4, 2017 (poster)
- C51 J. Goettler, M. Lukas, A. Kluge, **S. Kaczmarz**, J. Gempt, F. Ringel, M. Mustafa, C. Zimmer, M. Schwaiger, S. Foerster, C. Preibisch, T. Pyka. *"Inter- und intra-individuelle Korrelation von 18F-Fluorethylthiopyridin-PET und Perfusion-MR Parametern bei unbehandelten Gliomen"*. Proc of 51st DGNR Meeting in Clinical Neuroradiology, PN 97, Cologne, Germany October 5-8, 2016 (oral presentation)
- C52 J. Goettler, **S. Kaczmarz**, R. Nuttall, C. Zimmer, K. Finke, C. Sorg, C. Preibisch. *"Kognitive Auswirkungen von zerebraler Hypoperfusion bei Patienten mit asymptomatischer hochgradiger Carotis-Stenose"*. Proc of 51st DGNR Meeting in Clinical Neuroradiology, PN 313, Cologne, Germany October 5-8, 2016 (oral presentation)
- C53 J. Goettler, A. Kluge, M. Lukas, **S. Kaczmarz**, J. Gempt, F. Ringel, M. Mustafa, M. Schwaiger, C. Zimmer, S. Foerster, C. Preibisch, T. Pyka. *"Intra- and inter-individual association of FET-PET- and MR-perfusion-parameters in untreated glioma"*. Proc of 24th Scientific Meeting of ISMRM, PN 1387, Singapore, Singapore, May 7-13, 2016 (poster)



# 1 Introduction

Tomographic imaging techniques allow unique insights to the human brain and are widely applied for medical and research applications. They allow localized measurements of structural, functional and metabolic information. Among many techniques, magnetic resonance imaging (MRI) became an invaluable tool in clinical diagnostics [1]. MR images are extremely rich in information and offer manifold different contrasts. And as MRI is a non-invasive technique, it is highly appealing for widespread applications in medicine and neuroscience. Supported by an active MR research community in physics, medicine and neuroscience, a vast number of novel imaging methods have been developed [2].

Besides MRI, other established tomographic imaging techniques are available for hemodynamic brain imaging. Specifically, computed tomography (CT) relies on attenuation of externally applied X-rays through the patients brain. It offers fast imaging at comparably low costs and can derive anatomical and functional information [3]. However, it does not give metabolic information. And even with latest phase-contrast or spectral X-ray imaging, the available contrasts remained limited [4, 5]. Another method is positron emission tomography (PET), which is applied in nuclear medicine. Radioactively labeled tracers are intravenously injected to the patient and accumulate at the tissue of interest. Positrons resulting from radioactive  $\beta^+$  decay and electrons annihilate and the gamma quants are used for imaging. PET offers perfusion and metabolic information, e.g., by radioactively labeled water and glucose [6]. Even though CT and PET are important for clinical imaging, reachable contrasts remain restricted and ionizing radiation as well as radioactive tracers constitute limitations.

In contrast, MRI is a non-invasive technique. Since it became clinically available in the 1980's, it opened fascinating novel possibilities in diagnostics and research. MRI is an extremely powerful imaging modality, due to its high flexibility and sensitivity to various tissue properties [7]. In MRI, signals in clinical imaging mostly arise from  $^1H$  nuclei and allow structural, functional and metabolic imaging of tissues [2]. It is sensitive to different metrics with high biological significance [2], such as magnetic properties, perfusion, diffusion and many more [8]. And by combining imaging sequences with different contrasts in multi-parametric MRI, even highly complementary information can be achieved within one scan session.

With its excellent soft tissue contrast, MRI is of pivotal interest for imaging of the brain. Compared to any other organs, the brain has the highest oxygen metabolic rate and receives 15% of the whole cardiac output [9]. As the brain has no energy storage capacities, permanent supply is crucial. Its main source of energy is the oxidative glucose metabolism and the required oxygen and glucose are both supplied via the blood stream. Hemodynamic imaging is thus of highest interest and allows to better understand brain function as well as impairments in numerous cerebral diseases. Specifically, the combination of perfusion and oxygenation imaging can measure several parameters related to the delivery of blood from the arteries to the capillary bed as well as the oxygen extraction from the blood vessels to the brain tissue. While MRI-based perfusion mapping with contrast agent is already clinically applied, recently reported accumulations of the applied Gadolinium [10] warrant stricter indications [11, 12] and non-invasive alternatives are increasingly gaining interest. Furthermore, novel methods like MRI-based oxygenation mapping appear highly promising for future applications.

As MRI signals are arbitrarily scaled during the acquisition process, conventional MRI techniques are mainly used qualitatively for clinical applications. In contrast, quantitative imaging aims to measure parameter values independent of hardware or experimental conditions. Resulting parameters shall be only sensitive to specific physical or physiological tissue properties. Quantitative imaging often requires MR sequence modifications, acquisition of differently weighted data and its evaluation according to biophysical models. Therefore, acquisition is more costly but in turn allows easier data interpretation. In addition, it is fundamental to assess biological changes in diseases, improved monitoring of treatment effects and longitudinal comparisons [8]. Moreover, quantitative functional imaging is highly important to quantify neuronal activity in terms of energy consumption [13]. Especially combinations of quantitative techniques are highly promising to improve the understanding of disease related effects [8].

Taken together, multi-parametric quantitative hemodynamic MRI of the brain is highly promising, but methodological improvements and extensive clinical trials are clearly demanded.

### 1.1 Clinical Relevance

A major cause of death in developed countries worldwide are cerebrovascular diseases (CVD) [9]. Within one year, more than 6 million new cases of CVD were diagnosed just within the European Union (EU) with increasing prevalence and over 426 000 people died [14]. The economic costs within the EU alone amount to 45 billion euros per year [14] and are responsible for 18% of the healthcare expenditure [15]. While CVDs often relate to an increased risk of stroke, it is promising that the majority of strokes might be preventable by early detection of cerebrovascular risk factors [9]. This highlights the importance of better diagnostic imaging to improve the quality of life and increase the life expectancy for millions of people. Due to its non-invasiveness and high flexibility in contrasts, MRI is ideal for diagnostic purposes such as routine check-ups, initial diagnostics, follow-up scans and treatment efficacy monitoring.

Being just one among many other CVDs, internal carotid artery stenosis (ICAS) is a major public health issue and relates to 10-20% of all strokes [16]. Alongside several other severe complications, previous studies implied relations of chronic hypoperfusion with structural brain damage leading to cognitive impairments. However, hemodynamic imaging is not routinely in clinical protocols. Current diagnostics mainly rely on very simple extracranial flow imaging by Doppler ultrasonography rather than evaluating the complex local effects on the brain tissue. At the same time, treatment can reduce the stroke risks, but decisions are delicate due to potentially severe complications [17, 18]. Thus, ICAS may greatly benefit from novel multi-parametric quantitative hemodynamic MR imaging methods [9].

In order to enable more widespread oxygenation and perfusion imaging in ICAS, several challenges need to be overcome. First, clinically applicable methods with high sensitivity need to be developed first. Second, those methods need to be characterized in healthy controls and ICAS patients to probe their specificity and sensitivity to hemodynamic impairments. Thereby, deeper insights to physiological processes in normal function can be drawn to reliably differentiate ICAS related effects. Multi-parametric evaluations of novel methods with high sensitivity can also contribute to an improved understanding of the pathogenesis. Here, especially multi-parametric imaging can gain new information about pathophysiological impairments and their relations. And finally, the future potential to improve clinical ICAS diagnostics and treatment decisions has to be evaluated.

Apart from ICAS and other CVDs, quantitative hemodynamic MRI is highly promising for applications in many other pathologies as well as neuroscientific studies.

## 1.2 Thesis Purpose

In 2012, Bruce Pike as one of the leading experts in the field stated in a comprehensive review that "the challenge and opportunity during the coming years will be to improve the methods and realize their potential to provide robust quantitative individual assessments of baseline and activation induced responses for basic neuroscience and clinical applications" [19].

Aiming for this gap, this work is based on the symbiosis of perspectives from MR physics and medicine. Targeted by clinical implications, the processes of imaging methods development and clinical applications are merged from the beginning to meet clinical demands most effectively. On the one hand, it was necessary to implement clinically applicable quantitative hemodynamic MR imaging methods. This included MRI sequence modifications, development of specific post-processing programs for quantitative assessment of perfusion and oxygenation parameters and the design of a concluding database structure for combined evaluation of the multi-parametric data. On the other hand, it was necessary to apply the developed methods and analysis pipelines in targeted clinical studies. Thereby, potential benefits of the implemented methods for clinical applications were evaluated.

**Therefore, the main purpose of this work was to test the hypothesis that clinically applicable MRI-based quantitative perfusion and oxygenation imaging is sensitive to hemodynamic perturbations in asymptomatic ICAS patients. Furthermore, multi-parametric MRI was hypothesized to yield complementary information, thereby enabling new insights to the pathophysiology and offering auspicious perspectives to improve clinical diagnostics.**

## 1.3 Thesis Structure

The present cumulative thesis aims to describe the theoretical background and present the context of the four embedded journal publications with regards to existing literature. Basic physical principles of magnetic resonance imaging are introduced in Chapter 2. Fundamental hemodynamic parameters and relevant imaging techniques of the embedded publications are explained in Chapter 3. The clinical background of the cerebral blood supply under healthy conditions and in carotid artery stenoses are presented in Chapter 4. An introduction to the sophisticated data base framework for evaluations of the multi-parametric hemodynamic imaging data of the embedded publications is given in Chapter 5. Summaries and the full texts of the four embedded publications can be found in Chapter 7. Finally, these results are discussed in the context of existing literature and with regards to clinical novelty, limitations and future implications in Chapter 8.





## 2 Principles of Magnetic Resonance Imaging

This chapter briefly summarizes the physical background of magnetic resonance imaging (MRI), which is the preferred designation for the radiological application of nuclear magnetic resonance (NMR). After a brief description of the historical background, this chapter includes introductions to NMR in Section 2.1, to MRI in Section 2.2, to basic imaging techniques in Section 2.3 and to clinical MRI hardware components in Section 2.4, based on [2, 7, 20, 21].

An important early basis of NMR was the discovery of proton spins and explanations by quantum mechanical concepts by Stern, Gerlach, Rabi, Gorter et al. in the 1920's and 1930's [22, 23], for which Stern and Rabi were awarded with the Nobel prices in 1943 and 1944, respectively. The pioneer work by Bloch [24] and Purcell [25] in 1946 on spin precession measurements of liquids and solids was jointly awarded with a Nobel prize in 1952. In the 1950's Hahn [26] and Carr [27] published the first spin echo signal measurements and magnetic resonance spectra. Ivanov submitted a patent about the theory of spatial NMR encoding by magnetic field gradients in 1960, which was finally accepted decades later after it was first rejected and criticized as unviable [28]. Huge steps towards MRI were the first experimental demonstrations of spatially encoded NMR signals by Lauterbur [29] and their accelerations as well as mathematical signal analysis concepts by Mansfield in the 1970's [30], both were jointly awarded with a Nobel price in 2003. In the 1980's, first clinical MRI scanners were used and improved with fascinating advances in the ongoing hardware and pulse sequence developments. While those historical milestones only provide a brief overview, many more researchers greatly contributed. Nowadays, MRI is a clinical routine method with more than 80 Mio. performed examinations in 2018 within OECD member countries [31].

### 2.1 Physical principles of the NMR signal

The basis of MRI is the physical phenomenon of NMR. It is based on the excitation of atomic nuclei in a strong external magnetic field and subsequent measurements of the emitted electromagnetic energy during the relaxation process. In general, all isotopes with an odd nucleon number can be used for NMR. They have an intrinsic magnetic moment and angular momentum, which means they possess a nonzero nuclear spin. The  $^1\text{H}$  nuclei are by far most considered for clinical and research applications, as it is naturally abundant in the human body in water and other molecules - and applied for all imaging in this thesis. Imaging of other isotopes of various other elements with odd nucleon numbers is also possible with suitable hardware, but not widely established yet, e.g. due to lower signal to noise ratio (SNR).

The transitions between nuclear spin states can be measured in an NMR experiment, which is introduced in the following and principally consists of three main steps. First, precession of the sample's nuclear spins in an external constant main magnetic field  $B_0$  (see Section 2.1.1) and the formation of bulk magnetization (see Section 2.1.2). Second, excitation of the nuclear spins by an additional oscillating magnetic field  $B_1$  (see Section 2.1.3). And finally, measurement of the NMR signal via current induction in receive coils during the relaxation of the excited nuclear spins to thermal equilibrium (see Sections 2.1.4 and 2.1.5).

### 2.1.1 Precession

The physical description of NMR can either rely on classical or quantum mechanics. As MR experiments typically involve a spin ensemble, consisting of a large number of nuclei, classical mechanics is sufficient to explain most aspects and is used for the following description [32].

A fundamental property of isotopes with an odd nucleon number is that they possess an angular momentum  $\mathbf{J}$ , often called spin. The nuclei have electrical charges, rotate around their own axis and thereby create a magnetic field. The intrinsic angular momentum  $\mathbf{J}$  thus induces a magnetic moment  $\boldsymbol{\mu}$  according to

$$\boldsymbol{\mu} = \gamma \mathbf{J} \quad (2.1)$$

where  $\gamma$  is the gyromagnetic ratio of the specific isotope. For example, the gyromagnetic ratio of  $^1\text{H}$  nuclei is  $\gamma/2\pi = \gamma = 42.58 \text{ MHz T}^{-1}$ .

The direction of  $\boldsymbol{\mu}$  is completely random in the absence of external magnetic fields, due to thermal random motion. But in presence of an external magnetic field  $\mathbf{B}$ , the magnetic moment  $\boldsymbol{\mu}$  experiences a torque  $\boldsymbol{\tau}$  with

$$\boldsymbol{\tau} = \boldsymbol{\mu} \times \mathbf{B} = \frac{d\mathbf{J}}{dt} \quad (2.2)$$

The combination of equations 2.1 and 2.2 yields the equation of motion for isolated spins

$$\frac{d\boldsymbol{\mu}}{dt} = \gamma \boldsymbol{\mu} \times \mathbf{B} \quad (2.3)$$

In an external static magnetic field  $\mathbf{B}_0 = B_0 \mathbf{k}$ , the solution to the differential equation 2.3 describes a precession of  $\boldsymbol{\mu}$  about  $\mathbf{k}$ . The angular frequency  $\omega$  of this precession linearly depends on  $B_0$ , is known as the Larmor frequency  $\omega_0$  and calculated by

$$\omega_0 = \gamma B_0 \quad (2.4)$$

### 2.1.2 Bulk Magnetization

The collective behaviour of a spin ensemble with  $n$  nuclear spins is described by the macroscopic bulk magnetization vector  $\mathbf{M}$ , which is the sum of the magnetic moment vectors  $\boldsymbol{\mu}_n$  (Eq. 2.1). The equation of motion resulting from a spin ensemble in an external magnetic field  $\mathbf{B}$  is

$$\frac{d\mathbf{M}}{dt} = \gamma \mathbf{M} \times \mathbf{B} \quad (2.5)$$

While the absence of external magnetic fields results in  $\mathbf{M} = \mathbf{0}$ , a static magnetic field  $\mathbf{B}_0$  causes a net magnetization. Following the usual MR conventions,  $\mathbf{B}_0$  is defined parallel to the z-axis. The z-axis is called longitudinal axis and the x-y-plane is called transversal plane.

In thermal equilibrium, the transverse magnetization component  $\mathbf{M}_\perp$  is zero, due to random phases of the precessing magnetic moments, and the longitudinal component is  $M_\parallel = M_0$ . This amplitude of the spin ensemble's net magnetization  $M_0 = |\mathbf{M}|$  in equilibrium can be estimated based on first order approximation of the Boltzmann distribution resulting in

$$M_0 \approx \frac{\rho \gamma^2 \hbar^2 B_0}{4k_B T} \quad (2.6)$$

with the proton density  $\rho$ , the reduced Planck constant  $\hbar$ , the Boltzmann constant  $k_B$  and the temperature  $T$ .

### 2.1.3 Excitation

The aligned nuclear spins in a static field  $B_0$  can be excited by an additional oscillating magnetic field  $B_1$ . The  $B_1$  field is also referred to as radio frequency (RF) field. Its field strength is several orders of magnitudes smaller than  $B_0$ . The RF field has to oscillate with the Larmor frequency  $\omega_0$  (see equation 2.4) to meet the resonance condition

$$\omega_{RF} = \omega_0 \quad (2.7)$$

The combination of the constant magnetic field  $\mathbf{B}_0$  and the oscillating field  $\mathbf{B}_1(t)$ , applied in transversal plane, can be thus expressed as

$$\mathbf{B} = \begin{pmatrix} B_1 \cos(\omega_0 t) \\ -B_1 \sin(\omega_0 t) \\ B_0 \end{pmatrix} \quad (2.8)$$

To explain the following effects, it is helpful to use a rotating frame of reference. The frame rotates clockwise with the Larmor frequency about the z-axis, so that spins precessing with the Larmor frequency remain stationary in the rotating frame. Application of the RF-field causes perturbations of the equilibrium and tilts  $\mathbf{M}$  to the xy-plane. The flip angle  $\alpha$  between  $\mathbf{B}_0$  and  $\mathbf{M}$  depends on the gyromagnetic ratio, RF amplitude  $B_1$  and pulse duration  $\tau_p$

$$\alpha = \gamma B_1 \tau_p \quad (2.9)$$

When applied in thermal equilibrium ( $M_{\parallel} = M_0$  and  $M_{\perp} = 0$ ), a flip angle of  $\alpha = 90^\circ$  causes transversal precession with  $M_{\parallel} = 0$  and is thus also referred to as saturation pulse. And  $\alpha = 180^\circ$  causes an inversion with  $M_{\parallel} = -M_0$  and  $M_{\perp} = 0$ . In general, RF pulses are often named with the applied flip angle, e.g.  $90^\circ$  RF pulse.

### 2.1.4 Relaxation

After the nuclei absorbed energy during excitation by the  $B_1$  field, the spin system returns to thermal equilibrium. This process is characterized by precession of  $\mathbf{M}$  about  $\mathbf{B}_0$ . The longitudinal component of  $\mathbf{M}$  recovers and the transversal component decays. This return to the equilibrium state is phenomenologically described by two different types of relaxation:

- By spin-lattice interaction, the longitudinal magnetization component recovers exponentially with the characteristic relaxation time  $T_1$  towards its equilibrium state.
- By spin-spin interaction, the transverse magnetization component decays exponentially with the characteristic relaxation time  $T_2$  towards its equilibrium state.

The time-dependent behaviour of the net magnetization vector  $\mathbf{M}$  in the main magnetic field  $\mathbf{B}_0$  and the RF field  $\mathbf{B}_1$  (see equation 2.8) during excitation and relaxation is described by a set of differential equations, called Bloch equations

$$\frac{d\mathbf{M}}{dt} = \gamma \mathbf{M} \times \mathbf{B} + \begin{pmatrix} -\frac{M_x}{T_2} \\ -\frac{M_y}{T_2} \\ -\frac{M_z - M_0}{T_1} \end{pmatrix} \quad (2.10)$$

with the three net magnetization components  $M_x$ ,  $M_y$  and  $M_z$ .

If the system was initially in equilibrium ( $M_{\parallel} = M_0$  and  $M_{\perp} = 0$ ) and a  $90^\circ$  RF pulse was applied, the solution to equation 2.10 in the laboratory frame gives the result

$$\mathbf{M}(t) = M_0 \begin{pmatrix} \cos(\omega_0 t) e^{-\frac{t}{T_2}} \\ \sin(\omega_0 t) e^{-\frac{t}{T_2}} \\ 1 - e^{-\frac{t}{T_1}} \end{pmatrix} \quad (2.11)$$

Consequently, the x and y magnetization components oscillate at the Larmor frequency in the laboratory frame and decay with the time constant  $T_2$ , causing a decrease of transversal magnetization  $\mathbf{M}_{\perp}$ . The z magnetization component simultaneously recovers to equilibrium from 0 to  $M_0$  with the time constant  $T_1$ , causing an increase of  $M_{\parallel}$ . Both, the transverse magnetization decay and longitudinal recovery follow exponential functions, each, assuming spin systems with weak spin-spin interactions, which is appropriate for biological tissues.

Regarding sources of relaxation, the relaxation times are determined by the local environments of the samples molecules. In general, relaxation results from effects of fluctuating magnetic fields, caused by random thermal motion of molecules. Consequently, each nucleus is affected by fluctuating fields from the magnetic moments of surrounding nuclei in addition to  $B_0$ . The z-component of those additional fluctuating fields alter the precession rates around the z-axis (see equation 2.4), leading to increased phase dispersion and thereby cause  $T_2$  relaxation. But as precession around z-axis does not affect the magnetization vectors z-component, this effect does not contribute to  $T_1$  relaxation. To change the magnetization vectors z-component and thus affect  $T_1$  relaxation, magnetic field fluctuations must appear in the x-y-plane at the Larmor frequency. Those  $T_1$  relaxation processes additionally affect  $T_2$  relaxation. Thus,  $T_2$  is always shorter than  $T_1$ . For brain tissues,  $T_1$  is on the order of 10 times larger than  $T_2$ .  $T_1$  varies from approximately 0.2 - 4.0 s in the body at 3T and  $T_2$  of biological tissues is in the range of tens of ms. When increasing the field strength,  $T_1$  tends to increase, while  $T_2$  is relatively independent of  $B_0$ .

In practice, there is an additional dephasing effect, mainly related to static local field inhomogeneities  $\Delta B_i$ . Those dephasing effects cause a more rapid transverse magnetization decay, which is characterized by the decay time  $T_2'$ . As magnetic field inhomogeneities cause a range of precession rates (see equation 2.4), the spins become out of phase and the transverse magnetization decays faster. The combination of this reversible transverse relaxation time  $T_2'$  and the irreversible transverse relaxation time  $T_2$  (see Section 2.3.1) is given by the effective or apparent transverse relaxation time  $T_2^*$  (assuming Lorentzian distributions)

$$\begin{aligned} \frac{1}{T_2^*} &= \frac{1}{T_2} + \gamma \Delta B_i \\ &= \frac{1}{T_2} + \frac{1}{T_2'} \end{aligned} \quad (2.12)$$

The relaxation times can be also rewritten by their inverse as relaxation rates by

$$R_1 \equiv \frac{1}{T_1}, \quad R_2 \equiv \frac{1}{T_2}, \quad R_{2^*} \equiv \frac{1}{T_2^*}, \quad R_2' \equiv \frac{1}{T_2'} \quad (2.13)$$

As the external field inhomogeneities cause additional decay,  $R_{2^*} \geq R_2$  respectively  $T_2^* \leq T_2$ .

### 2.1.5 Signal Generation

After excitation, the transverse component of the net magnetization precesses about the z-axis and decays. This changing magnetic field induces an oscillating current (see Figure 2.1) in conducting materials nearby to the sample following Faraday's law. This measurable signal after excitation is called free induction decay (FID, see Section 2.3.1). It refers to the *free* precession of nuclear spins, causing a changing magnetic field which *induces* a measurable current to the receive coils during the transient signal *decay*. The receiver coils are orthogonally paired (quadrature detection) to detect the complex signal, which corresponds to  $\mathbf{M}_\perp(t)$  as a function of time. The measured signals oscillate with the Larmor frequency and are strongest in proximity to the sample. The FID signal in a magnetic field with inhomogeneities, which can be assumed for biological samples, decays with the time constant  $T_2^*$  (see Figure 2.1), related to spin dephasing by static local field disturbances

$$S(t) \propto e^{-i\omega_0 t} e^{-t/T_2^*} \quad (2.14)$$

### 2.1.6 Magnetic Susceptibility

When objects are placed in the  $B_0$  field, they cause field distortions as they become partly magnetized. This response of a material to an external magnetic field can be used for classification. Those magnetic properties of a uniform material in a uniform magnetic field  $\mathbf{B}$  can be quantified by the magnetic susceptibility  $\chi$  in

$$\mathbf{M}_{sample} = \chi \mathbf{B} \quad (2.15)$$

with the local magnetization inside the material  $\mathbf{M}_{sample}$ , which is different to the previously introduced net magnetization and relates to the density of magnetic dipoles from the atoms orbital electrons. Thus, electrons mainly determine a materials susceptibility. Specifically, three important types of magnetism for clinical imaging are diamagnetism with  $\chi < 0$ , paramagnetism with  $\chi > 0$  and ferromagnetism with  $\chi \gg 0$ .

Diamagnetic materials such as water have no unpaired electrons. Caused by effects of the magnetic field on the electrons orbital motions, the induced field inside the sample is in the opposite direction compared to the external field with  $\chi < 0$ . Paramagnetic materials, such as oxygen or commonly applied Gadolinium-based contrast agents, have unpaired electrons which align with the external field, which causes an increased magnetic field inside the sample with  $\chi > 0$ . And finally, electrons in ferromagnetic materials, such as iron, also align with the external field with additional coupling of the individual magnetic moments, resulting in fields with orders of magnitude larger compared to paramagnetic materials and with  $\chi \gg 0$ .

Thus, any object placed in the scanner will cause field distortions of  $B_0$ , which may affect the measured signals. Those distortions depend on several factors. First, the object's magnetic properties, e.g. its susceptibility. Second, the shape of an object influences field distortions, which are e.g. different for spherical objects compared to cylinders. Third, the orientation relative to  $\mathbf{B}_0$  can also affect the field distortions for non-spherical objects. Furthermore, heterogenous objects add additional macroscopic field inhomogeneities, especially at interfaces of materials with different susceptibilities. This specifically affects brain imaging, as the head is heterogenous and composes materials with different magnetic susceptibilities, such as for example cranial bone, brain tissue, iron depositions and air in the sinus cavities.

## 2.2 Magnetic Resonance Imaging

To use the signals from an NMR experiment for localized imaging, additional spatial encoding by magnetic field gradients is required (see Section 2.2.1) as well as transformation of measured signals to the image space (see Section 2.2.2). The intensity of each voxel in an MR image is directly proportional to the measured local signal. This MR signal depends on pulse sequence parameters, e.g. timings of the applied RF pulses and gradients, and on the sample's intrinsic tissue properties, such as proton density and relaxation times. Due to varying relaxation properties in different tissues, image contrast is generated.

### 2.2.1 Spatial encoding

While the main magnetic field  $B_0$  is static, additional spatially varying time dependent magnetic fields are applied to localize the MR signals. Those additional fields can be applied in all three orthogonal directions x, y, and z. These gradient fields are created by three orthogonal sets of gradient coils. The gradient coils in one axis apply a constant magnetic field gradient. By linear combinations of the three gradient axes, gradients can be also applied along any arbitrary direction. The overall magnetic field adds up to

$$\mathbf{B} = (B_0 + G_x x + G_y y + G_z z) \mathbf{k} \quad (2.16)$$

Spatial encoding in 2D imaging can be achieved in three steps corresponding to the three spatial directions with slice selection, phase and frequency encoding. Slice selection is applied by exciting only a single slice, with a typical thickness of 1 - 10 mm. During excitation by the RF pulse, a gradient is applied in z-direction perpendicular to the slice. Thereby, the field strength spatially linearly varies in z-direction. The Larmor frequency becomes slice dependent, as it is proportional to the magnetic field strength (see equation 2.4) with

$$\omega(z) = \omega_0 + \gamma G_z z \quad (2.17)$$

RF pulses with a limited bandwidth (centered around  $\omega_0$ ) are applied, so that they are only on resonance for a single slice in z-direction. The slice thickness then depends on the gradient strength  $G_z$ , as the resonance frequency becomes a steeper function of position in z-direction with an increasing gradient (see equation 2.17), and the RF pulse bandwidth. Furthermore, the RF pulse shape influences the slice excitation.

Within the excited slice, spatial encoding is applied by phase and frequency encoding in two orthogonal directions. For phase encoding, the gradient  $G_x$  is applied for the time interval  $T_{pe}$  after the RF pulse and before the readout. During gradient application, the transverse magnetization precession rate becomes position dependent along this phase encoding direction. After the gradient is switched off, the spins precess at the same rate again, but with different phase accumulations  $\Phi$ , which gives spatial information along this second axis according to

$$\Phi(x) = -\gamma G_x x T_{pe} \quad (2.18)$$

In direction of the third axis, the gradient  $G_y$  is applied during the signal readout for frequency encoding. Different frequencies of the nuclear spins give spatial information along this third axis with

$$\omega(y) = \gamma (B_0 + G_y y) \quad (2.19)$$

While those slice selective excitations are known as 2D imaging, as only signals from one slice are acquired at the same time, alternatively 3D imaging can be applied. Here, usually non-selective RF pulses are applied and spatial encoding can be achieved for example by phase encoding in two directions in addition to frequency encoding in the third direction. Furthermore, projection imaging with spatial encoding in just two directions and repeated acquisitions with a rotating projection axis can be used for certain applications. Besides spatial encoding, gradient coils can be also used for gradient echo imaging (see Section 2.3.2).

### 2.2.2 k-space

The complex signals of an MR experiment with phase and frequency encoding are obtained in the frequency domain, which is also known as k-space. To translate those signals from the frequency domain to usable MR images, Fourier transform is applied during image reconstruction in the post-processing. The Fourier transform is a mathematical transformation which translates measured signals from the frequency domain to the spatial domain, and vice versa. While different trajectories can be applied to sample signals in k-space, Cartesian sampling refers to a regular rectangular grid pattern. Cartesian k-space sampling is clinically most commonly applied and also used for all imaging sequences in this thesis. The acquired data with Cartesian k-space sampling can be reconstructed with discrete Fourier transform, in contrast to non-cartesian sampling, as for example spiral k-space trajectories.

## 2.3 Imaging Techniques

The flexibility to obtain different image contrasts in MRI is unique. Those contrasts depend on tissue properties and sequences parameters. The pulse sequences typically involve RF pulses, specific gradient waveforms and readout modules. Particular pulse sequences involve several parameters, which can adjust the image contrast. In clinical MRI, there are common trade-offs between scan time, spatial and temporal resolutions and acquired SNR. Most MRI sequences are based on acquisition of echo signals that are either generated by RF pulses generating spin echoes (see Section 2.3.1) or magnetic field gradients generating gradient echoes (see Section 2.3.2). Furthermore, another imaging technique called inversion recovery (see Section 2.3.3) is introduced. To accelerate the image acquisition, several fast imaging techniques can be additionally applied, as introduced in Section 2.3.4.

An important parameter is the repetition time (TR), which is the time interval in between two successive excitation RF pulses. Most pulse sequences consist of a repetitive pattern of excitations with signal readouts and are specifically designed for an image contrast, such as  $T_2$  weighting. Recently, a new technique called magnetic resonance fingerprinting (MRF) was introduced [33]. It employs pseudo-random imaging parameter variations in one acquisition to simultaneously generate images of several tissue property parameters via applications of a database, a so-called dictionary. As the MRF framework requires further validations for broad clinical usability, the imaging in this thesis relies on traditional MRI sequences.

### 2.3.1 Spin Echo

A spin echo (SE) can be generated by applying a  $90^\circ$  RF pulse to generate transverse magnetization followed by a  $180^\circ$  pulse after a certain time delay to refocus the dephasing spins and generate an echo, as shown in Figure 2.1. An advantage of SE sequences is their insensitivity to macroscopic magnetic field inhomogeneities and the SE signal decays with  $T_2$ .

In FID, the spins are in-phase after the  $90^\circ$  pulse, but subsequently precess at slightly different rates due to magnetic field inhomogeneities. The phase dispersion increases over time and the FID signal quickly decays with  $T_2^*$ . Whereas SE sequences are based on the formation of an echo. The time interval from an RF pulse to the echo is called echo time (TE). An additional inversion pulse is applied at TE/2 to convert the phase of each spin's magnetization vector to a negative phase. After the  $180^\circ$  pulse, the spins precess at the same rate as before and the phase dispersion decreases. As the phase accumulation is proportional to the elapsed time and the inversion pulse reverses the sign of the phase, the phase differences are zero again at TE and an echo signal is formed. Combinations of TR and TE can generate different image contrasts with weightings to  $T_1$ ,  $T_2$  or proton density (PD). For example,  $T_2$  weighted images ( $T_2w$ ) are acquired with long TR and TE (typically TR > 2000 ms and TE  $\approx T_2$ ).

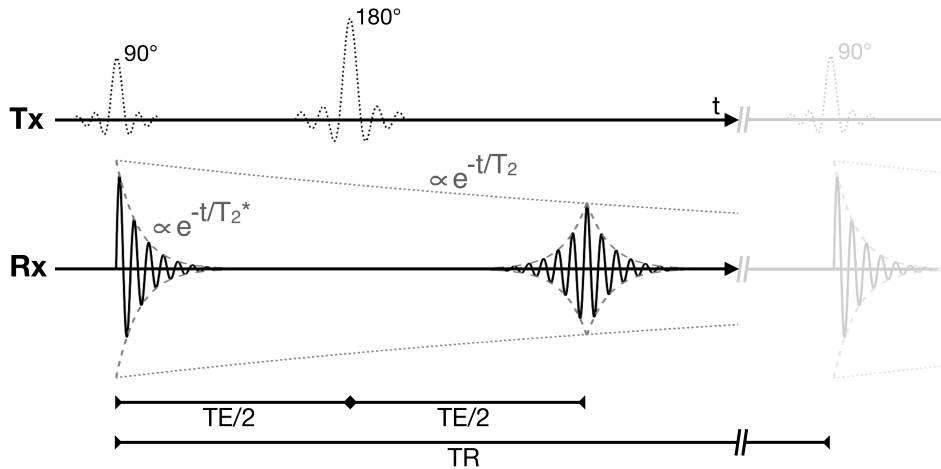


**Figure 2.1: Pulse sequence diagram of free induction decay (FID) and spin echo (SE).** After excitation with a  $90^\circ$  pulse, the FID signal decays with the time constant  $T_2^*$ . By application of a  $180^\circ$  inversion pulse at TE/2, the transversal magnetization vector recovers and a (primary) spin echo (SE) is generated at TE. The SE signal decays with the time constant  $T_2$ . The secondary echo is not shown. Note that oscillations with the Larmor frequency would be much faster. Abbreviations: Tx, transmission; Rx, reception; TE, echo time; TR, repetition time.

Spin echoes generally occur by refocussing pulses at any flip angle, but the echoes are strongest with inversion pulses. The described signal measurement during echo formation is referred to as symmetrical SE, which is the standard clinical implementation. Contrary, asymmetric SE (ASE) sequences do not acquire the signal during the echo peak, usually by shifting the refocussing pulse, to generate for example  $T_2'$  weighted images [34].

A multi-echo SE sequence can be applied by a repetitive pattern of inversion pulses, each after an additional TE, to create a train of echoes for each RF excitation pulse. Peaks of their envelopes will decay with  $T_2$ . By fitting the decay, quantitative  $T_2$  maps can be calculated.

To minimize  $B_1$  inhomogeneity effects and phase errors caused by imperfect inversion pulses, a modified SE sequence was proposed, called CPMG. It is named after Carr and Purcell, who proposed the initial SE sequence [35], as well as Meiboom and Gill, who proposed modifications by applying the inversion pulse orthogonally (e.g. along  $\pm y$ -axis) to the initial excitation pulse (along x-axis) [36]. Due to its robustness, CPMG is widely used in clinical SE sequences.



### 2.3.2 Gradient Echo

Another frequently used sequence to generate signal echoes are gradient recalled echoes (GRE). Instead of RF pulses in SE, time varying magnetic gradient fields are applied for refocussing in GRE. Those gradient fields are generated by the same gradient coils used for spatial encoding (see Section 2.2.1). However, GRE cannot refocus the phase offsets caused by static field inhomogeneities and the signal thus decays with  $T_2^*$ , as shown in Figure 2.2.

GRE sequences are based on the fact, that magnetic gradient fields can dephase and rephase the spins in a controlled fashion. After the excitation pulse with  $\alpha \leq 90^\circ$ , a gradient is applied. The gradient causes dephasing, as the loss of the spins phase coherence progresses. Subsequently, a gradient with opposite sign is applied. The second gradient causes a rephasing of the spins, as it unwinds the phase offsets, which were generated by the first dephasing gradient. An echo is formed during the rephasing gradient, when the integrals of the dephasing and rephasing gradients over time match. The second gradient is also used for the k-space sampling during the echo. In the presence of  $B_0$  inhomogeneities, the spins will not completely rephase and the signal at the echo carries a  $T_2^*$  weighting. Commonly, RF pulses with low flip angles  $\alpha < 90^\circ$  are applied for accelerated imaging, as a relatively high level of longitudinal magnetization remains, which allows shorter TR and thus, reduced scan time [37].

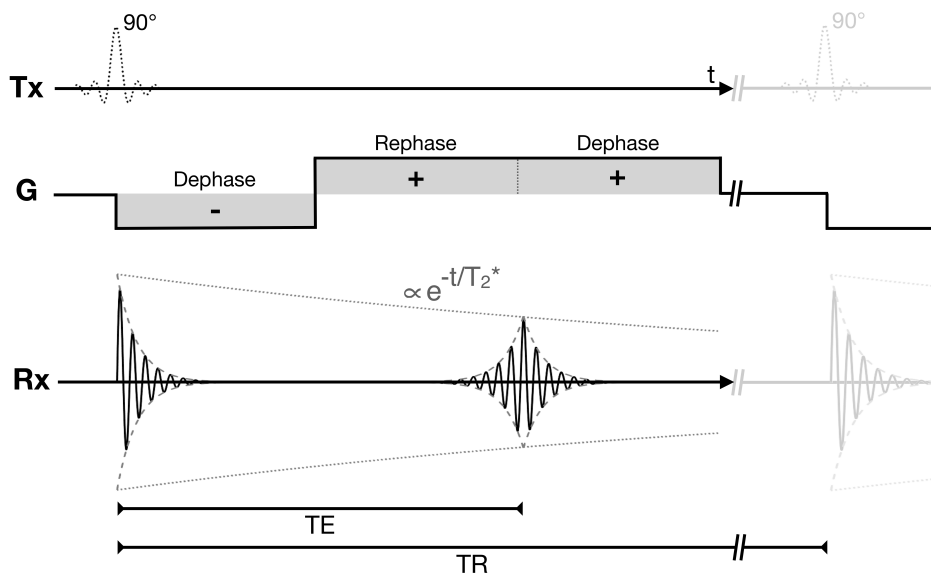


**Figure 2.2: Pulse sequence diagram of a gradient recalled echo (GRE).** After excitation with a  $90^\circ$  pulse, dephasing and rephasing gradients are subsequently applied to generate a GRE. Peaks of the GRE signal decay with the time constant  $T_2^*$ , when assuming magnetic field inhomogeneities. Additional GRE could be generated by adding a series of dephasing and rephasing gradients at multiples of TE. The higher order echoes are not shown. Note that oscillations with the Larmor frequency would be much faster. Abbreviations: Tx, transmission; G, gradient; Rx, reception; TE, echo time; TR, repetition time.

The GRE image weightings mainly depend on TE, TR,  $\alpha$  and the RF pulse and  $T_1w$  or  $T_2^*w$  images can be achieved. Multi-echo GRE can be acquired with one excitation by applying a series of dephasing and rephasing gradients per TR. The peak maxima decay with  $T_2^*$ .

### 2.3.3 Inversion Recovery

Another widely used pulse sequence is called inversion recovery (IR). It allows to introduce  $T_1$ w or minimize the signal contributions from specific tissues. A typical IR sequence begins with a  $180^\circ$  RF pulse to invert the longitudinal magnetization from equilibrium to  $M_z = -M_0$ . The longitudinal magnetization subsequently increases with  $T_1$ . During relaxation, the longitudinal magnetization becomes zero, which is called null point. After the inversion time (TI), an additional  $90^\circ$  RF pulse is typically applied, which flips the longitudinal magnetization at this time point to the transverse plane, which can be subsequently measured. Thus, the resulting signal depends on the previous signal recovery during the time interval TI. When the imaged sample contains tissues with different relaxation times, signals from specific tissues can be suppressed by adjusting the TI properly for the null point of this tissues relaxation time.

Similarly, inversion and saturation pulses can be also applied as preparation pulses for other sequences to suppress background signals. By applying a series of RF pulses with the timings adapted to the tissue specific  $T_1$  values, signals from different tissues can be simultaneously suppressed in the subsequently acquired signals, which is called background suppression.

### 2.3.4 Fast Imaging

Conventional imaging with the afore described basic sequences would be apparently slow, as each acquisition just includes one phase-encoding step and it needs to be repeated several times to acquire a whole image. Fast imaging is thus highly demanded for clinical applications, where routine examinations including several acquisitions with different image contrasts are usually planned in 20 minutes time slots. Furthermore, both, clinical and neuroscientific applications greatly benefit from dynamic imaging with high temporal resolutions.

The introduced basic GRE sequence with  $90^\circ$  excitation pulses requires long TR to allow longitudinal magnetization recovery. In 1985, considerable scan time shortening was introduced by eliminating waiting times with the so-called fast low-angle shot (FLASH) technique [37]. It is based on GRE with short TR (usually  $TR < T_1$ ) in combination with low flip angles, gaining maximum signal at the so-called Ernst angle. The longitudinal magnetization gets in a steady state and allows imaging with very short TR. FLASH can be combined with preparation experiments, e.g. inversion pulses, to achieve different image contrasts.

Another acceleration technique is called echo planar imaging (EPI). Here, the entire k-space is acquired after one excitation. This is referred to as single-shot imaging in contrast to segmented k-space acquisitions, which require multiple excitations for k-space sampling. It can be either combined with SE for  $T_2$ w or GRE for  $T_2^*$ w imaging. It relies on trains of gradient echoes to sample k-space lines with characteristic readout- and phase-encoding gradients, allowing slice acquisitions in less than 50 ms. Rectilinear k-space trajectories with blipped phase-encoding gradients are commonly applied to prevent phase accumulation effects. Even though EPI was already proposed in 1977 by Mansfield [38], the demanding hardware requirements of strong and fast switching gradients delayed wide applications. Nowadays, EPI is commonly applied, as for example in perfusion (see Section 3.2), diffusion (see Section 3.4.3) and oxygenation sensitive imaging (see Section 3.3). Its main advantages are the good  $T_2$  or  $T_2^*$  image contrast and the reduction of motion artefacts by the fast imaging. However, the high sensitivity to susceptibility artefacts causes well-known image distortions. Furthermore, EPI is prone to artefacts by off-resonances and gradient imperfections.

Another clinically applied technique is rapid acquisition with relaxation enhancement (RARE), which combines a CPMG sequence [35, 36] with phase encoding for each spin echo,

so that multiple k-space lines are sampled per excitation [39]. RARE is also known as turbo spin echo (TSE) or fast spin echo (FSE). The combination of EPI and RARE is called gradient and spin echo (GraSE), which is often used for  $T_2$ w and, with additionally required post-processing, quantitative  $T_2$  imaging [40].

Parallel imaging can further reduce the scan time by undersampling the k-space while considering spatial sensitivity information from multiple receive coil elements, as typical brain imaging coils have 16 to 64 elements. It considers prior knowledge about spatial coil element sensitivities during reconstruction of under-sampled k-space data. Two well known techniques are SENSE (sensitivity encoding) [41] and GRAPPA (generalized autocalibrating partial parallel acquisition) [42] based on data reconstruction in imaging respectively k-space domain.

Further accelerations can be achieved by simultaneous slice excitations. However, first implementations were impeded by strong artefacts [43]. The breakthrough was the combination of simultaneous slice excitation with coil sensitivity encoding of parallel imaging [44]. It is known as simultaneous multi-slice or multi-band (MB) imaging. With increasing availability, MB is more and more often applied in neuroscience [45] and also used in this thesis.

While the described techniques were explained on 2D imaging, non-slice selective excitations can be applied for 3D volume imaging (see Section 2.2.1). Main advantages are improved SNR, as signal from the whole volume are acquired at once, multi-planar reconstructions and reduced bias from imperfect slice selection pulses.

## 2.4 MR Hardware

The main component of an MR scanner is the magnet creating the static  $B_0$  field, which is used to polarize the nuclear spins in an object. Typical clinically applied whole body scanners feature bore diameters of 60 - 70 cm with field strengths ranging from 1 T to 1.5 T and 3 T. Higher field strength of 7 T up to 9.4 T for human use are occasionally used for research applications. The magnetic field is created by superconducting electromagnets at very low temperatures using cryogenic cooling such as liquid helium. Those fields are very strong compared to the magnitude of the Earth's magnetic field at its surface (0.25 - 0.65  $\mu$ T).

Additional MR system components are typically built into the bore of the main magnet. To correct for magnetic field distortions and improve the magnetic field homogeneity (see Section 2.1.6), additional shim coils are used. Shim coils in combination with metal plates permanently correct for imperfections of the  $B_0$  uniformity. Furthermore, shim coils are used to individually correct for intrinsic field inhomogeneities introduced by the imaged object.

Three sets of gradient coils are used for spatial encoding (see Section 2.2.1), echo generation in GRE (see Section 2.3.2) as well as other imaging purposes, such as diffusion encoding (see Section 3.4.3). Compared to the main magnetic field, magnetic gradient fields are much weaker with typical values of 10-45 mT/m. Another important gradient performance parameter is the slew rate describing the gradient switching speed with typical values of around 200 T/m/s.

The oscillating  $B_1$  field is usually created by body transmit coils. Although they could also be used for signal detection, separate receive coils are usually placed at the region of interest for increased SNR. Often applied multiple element phased-array receive coils enable parallel imaging. The entire scanner room is electromagnetically shielded by a Faraday cage to prevent electromagnetic interferences.

All experiments conducted in this thesis were performed on clinical whole-body 3 T MRI scanner (Ingenia, Philips Healthcare, The Netherlands) with 16 and 32 channel receive head and head-neck coils at the Klinikum rechts der Isar of the Technical University of Munich.



# 3 Quantification of Cerebral Perfusion, Oxygenation and Diffusion

This chapter introduces relevant MRI sequences applied in this thesis, including clinically established as well as state-of-the-art methods based on the descriptions from [20]. To introduce functional imaging from a physiological point of view, the neurovascular system is explained in Section 3.1. In MRI, the great flexibility of pulse sequence design allows to image the brain structure as well as a large variety of cerebral hemodynamic processes. Perfusion imaging is introduced in Section 3.2 and oxygenation sensitive imaging in Section 3.3. As brain function and structure are often closely related, structural imaging sequences applied in this thesis are additionally introduced in Section 3.4, including diffusion sensitive imaging. Each of these sections contains brief descriptions of the related physiology, applied imaging sequences and related signal post-processing.

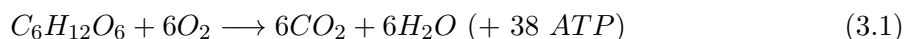
## 3.1 Neuro-Vascular System

The complex human nervous system is crucially dependent on the blood vessels in the neurovascular system. To maintain basic cell functions in the brain and satisfy increasing energy demands at neuronal activation, permanent energy supply is required. The energy is delivered via a complex blood vessel network. Oxygenated blood from the lungs is supplied to the brain from the arteries, passing the arterioles, through the capillary network and is drained via the venules and veins (see Figure 3.1A). The following description introduces neuronal signalling in Section 3.1.1, relevant hemodynamic parameters in Section 3.1.2 and the blood oxygenation level dependent (BOLD) effect in Section 3.1.3.

### 3.1.1 Neuro-Vascular Unit

The basis of every cognitive process is neuronal signalling. The human brain contains a highly complex network of more than 90 Billion neurons within grey matter (GM). Neurons communicate with each other via electrochemical processes with electrical nerve impulses, so-called action potentials, and neurotransmitters travelling through the synaptic gap to other neurons (see Figure 3.1B). Every neuron is supported by approximately 50 glia cells, which have various maintaining functions in the central nervous system, astrocytes for example form the blood brain barrier (BBB), regulate the chemical environment of neurons, recycle neurotransmitters and provide neurons with nutrients.

The brain requires energy for several processes, such as maintain basic cell functions, generate action potentials, recover the pre-synaptic side of the synapse, recovery from post-synaptic potentials and neurotransmitter recycling [49, 50]. The main cerebral source of energy is adenosine triphosphate (ATP), widely supplied by oxidative metabolism of glucose



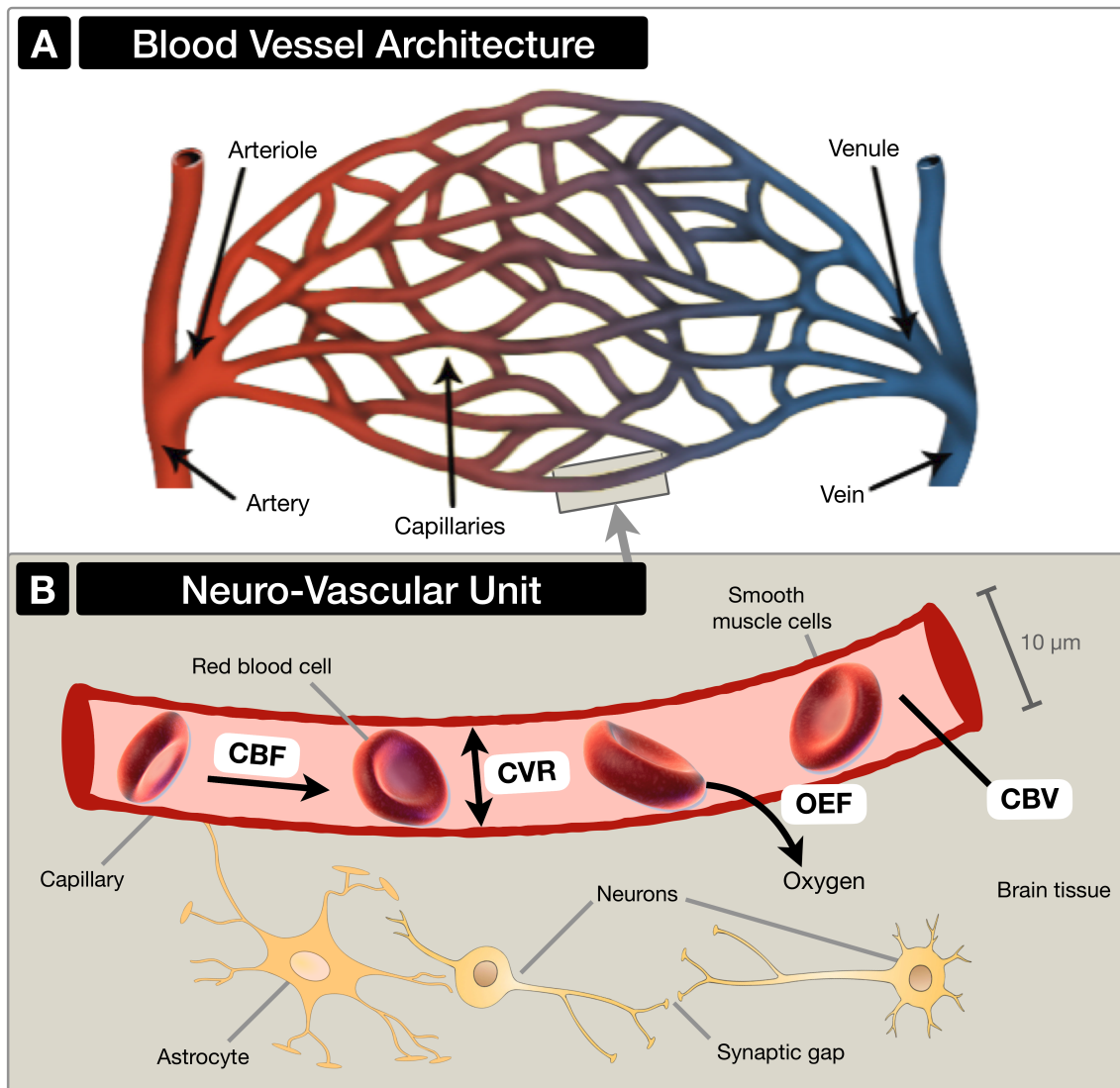


**Figure 3.1: Cerebral hemodynamic function.** (A) The vessels branch in the vascular tree to supply the capillaries with blood. (B) A magnified capillary shows the neuro-vascular unit. Red blood cells transport the oxygen, which diffuses through the vessel wall. Four major hemodynamic parameters are shown. The vessel diameter regulation by smooth muscle cells relates to the cerebrovascular reactivity (CVR), which affects the blood supply by cerebral blood flow (CBF) and the total cerebral blood volume (CBV), which can cause regulations of the oxygen diffusion to the tissue measured by the oxygen extraction fraction (OEF). Astrocytes extract glucose from the capillaries and supply the neurons with energy, which is required for neuronal signalling involving exchange of neurotransmitters through the synaptic gap. Images modified licensed under CC BY 3.0 from [46–48] and under public domain.

The neuro-vascular unit is an organisational entity with interactions between blood vessels, neurons and glia cells such as astrocytes [51, 52]. Oxygen and glucose are supplied via the blood vessels (see Figure 3.1A). Due to its low solubility in water and also blood, oxygen is transported from the lungs to the capillaries by the oxygen carrying molecule hemoglobin within red blood cells. Additional oxygen carrying contributions from blood plasma are usually very low. Oxygen diffuses through the vessel walls of the capillaries and arterioles by a passive process, driven by oxygen concentration gradients. At the same time, glucose is extracted from the blood to the surrounding brain tissue by the astrocytes (see Figure 3.1B). The resulting carbon dioxide (see eq. 3.1) diffuses out of the cells, into the blood and is cleared by the lungs. Contrary to oxygen, carbon dioxide has a high solubility in water.

### 3.1.2 Hemodynamic Regulation

The cerebral blood supply is related to several hemodynamic parameters. The nutritive delivery of arterial blood to the capillary bed and the brain tissue is described by the cerebral blood flow (CBF). It is the local delivery rate of arterial blood per mass of tissue and time, scaled in ml/100g/min. CBF is locally controlled by the vascular resistance, as the arterioles [53] and potentially also capillaries possess the ability to constrict or dilate their diameter [52] by smooth muscle cells within the vessel walls (see Figure 3.1B). While astrocytes are known to play a direct role in the vessel diameter regulations [54], the complex relations of arterial communication in terms of upstream dilation is not fully understood to date. For laminar fluid flow, the flow resistance depends by  $1/r^4$  on the vessel radius  $r$ . Autoregulation of the vessel diameter thereby allows to maintain CBF despite strong arterial blood pressure alternations and to support increases in metabolic activity caused by neural activation [55].

The blood is driven through the vascular tree by the cerebral perfusion pressure (CPP), which is the arterial versus venous pressure gradient. Another important hemodynamic parameter is the cerebrovascular reactivity (CVR). It relates to the capability of cerebral vessels to change their diameter in response to external requirements, e.g., neuronal stimulation or pathological changes (see Section 4.3) [56]. CVR can be measured as the cerebral blood vessels response to a vasoactive stimulus. CPP is directly related to CBF and CVR by

$$CPP = \frac{CBF}{CVR} \quad (3.2)$$

The tissue volume fraction occupied by blood vessels is quantified by the cerebral blood volume (CBV). Total CBV comprises all vessels within the vascular tree (see Figure 3.1A). It is also affected by autoregulation, as the blood volume increases with larger vessel diameter.

The net fraction of delivered oxygen that leaves the blood is measured by the oxygen extraction fraction (OEF). It is proportional to the oxygen pressure gradient between arteries and veins, see Figure 3.2. The oxygen is mainly extracted in the capillary bed and OEF can be calculated by the difference between arterial and venous oxygenation. While OEF relates to the consumed oxygen, there is permanent bidirectional oxygen diffusion between blood vessels and the surrounding brain tissue.

The extracted oxygen gets metabolized in the cells, which is quantified by the cerebral metabolic rate of oxygen consumption ( $CMRO_2$ ). It is proportional to the oxygen pressure gradient between capillaries and the brain tissue (see Figure 3.2). Following Fick's law,  $CMRO_2$  depends on CBF, OEF and the arterial oxygen concentration  $[O_2]_a$  according to

$$CMRO_2 = CBF \cdot OEF \cdot [O_2]_a \quad (3.3)$$

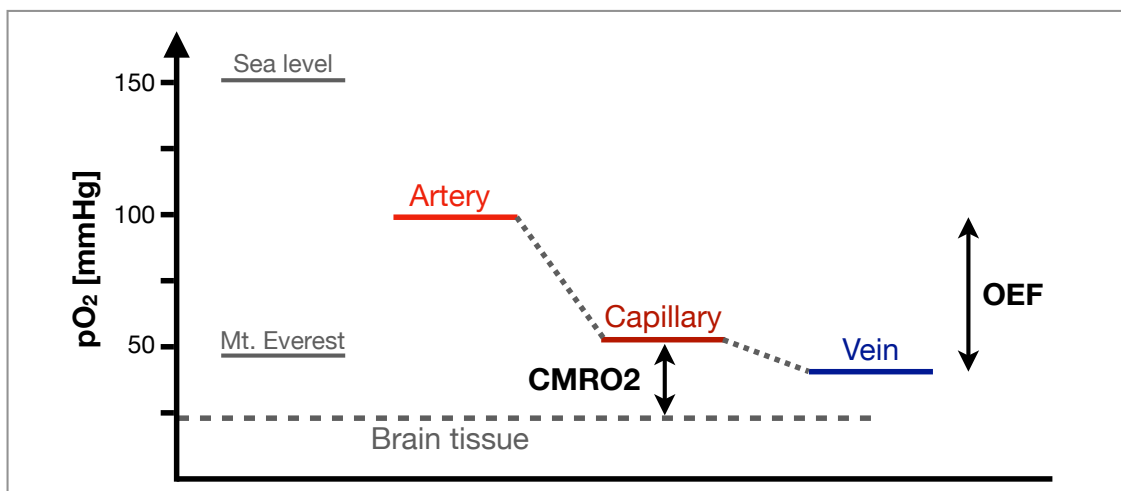


**Figure 3.2: Cerebral oxygen gradients.** Typical oxygen pressures in the blood compartments are illustrated. While the arterial oxygen pressure is fixed and determined by the lungs, oxygen pressure in the capillaries, veins and tissue can be modulated. For comparisons, atmospheric oxygen pressures are also shown. Image adapted from [20].

Consequently, CBF can influence the tissue's partial oxygen pressure. Changes of CBF during constant oxygen demands causes reverse OEF effects (see eq. 3.3), which changes the capillary oxygen pressure and thereby modulates the oxygen diffusion gradient [20].

Investigations of the local brain energy consumption are of highest interest to improve our still very limited understanding of healthy brain functions and offers high potential for improved diagnostics for large variety of brain pathologies (see Section 4.4.3). The energy consumption can be locally quantified either by the glucose metabolism rate ( $\text{CMRO}_{\text{Glc}}$ ) or the oxygen metabolism ( $\text{CMRO}_2$ ), see equation 3.1. Imaging of both processes is established by PET. The glucose metabolism can be assessed by radioactively labeled glucose [ $^{18}\text{F}$ ]-fluorodeoxyglucose (FDG) [57]. And the oxygen metabolism can be imaged by three separate PET measurements with different radioactive tracers, using  $^{15}\text{O}$  labeled  $\text{O}_2$  to assess  $\text{CMRO}_2$ ,  $^{15}\text{O}$  labeled water for CBF and  $^{15}\text{O}$  labeled carbon monoxide for CBV [58–60]. However, PET-based measurements are widely limited, due to radioactive tracer applications, required invasive arterial blood sampling and restricted availability of PET scanners with an onsite cyclotron. As more easily applicable alternatives, MRI-based imaging of perfusion (see Section 3.2) and oxygenation (see Section 3.3) were developed [61, 62].

### 3.1.3 BOLD Effect

Already in 1890, dependencies of local CBF with neural activity were proposed [63]. Since the first in-vivo MRI measurements of the BOLD effect in 1990 [64, 65], the field of functional MRI (fMRI) rapidly grew. The BOLD effect arises from the combination of a physiological and a physical effect [20]. From a physiology perspective, activations of brain areas cause moderate increases of the cerebral metabolic rate of oxygen  $\text{CMRO}_2$  (see eq. 3.1). At rest, OEF is relatively uniform across the brain at about 40%, while different levels of energy metabolism are adjusted by close coupling with changing CBF [66]. This neuro-vascular coupling (NVC) causes a substantial perfusion increase, exceeding the higher oxygen consumptions by a factor



of about 2-3 [67, 68]. Consequently, the OEF slightly decreases (see eq. 3.3) and leads to the paradox, that increased oxygen consumption by neuronal activity finally causes an increased oxygen saturation of hemoglobin. From a physics point of view, it is fascinating that the magnetic properties of hemoglobin depend on its oxygenation. While oxyhemoglobin is diamagnetic, deoxyhemoglobin is paramagnetic. Oxygenation level dependent magnetic properties of blood were already described in 1935 by Pauling [69]. In 1982, the sensitivity of MRI to in vitro blood sample oxygenation levels was shown by Thulborn et al. [70]. Finally, in 1992, Ogawa et al. first demonstrated the BOLD effect in the human brain [71]. Taken together, fMRI allows to non-invasively assess local signals related to neural activity to some degree [72, 73], as the flow response relates to the location [68] and degree of activations [74].

The majority of fMRI experiments nowadays rely on GRE sequences with EPI and MB accelerations to generate  $T_2^*$ w images with high temporal resolution (see Sections 2.3.2 and 2.3.4) [45]. While fMRI is widely applied in neuroscience, it has not been established in the clinics. This is also due to the simplification of acquiring  $T_2^*$ w images as an indirect measure of the highly complex relationships between the involved hemodynamic parameters (see Section 3.1.2) with counteracting effects of increasing CBF and CBV versus increasing CMRO<sub>2</sub> and OEF on the hemoglobin oxygenation [62]. Furthermore, as a general technical limitation, fMRI is impeded by macroscopic magnetic field inhomogeneities (see Section 2.1.4) [75] and hemodynamic response impairments in several pathologies [62]. To overcome those methodological limitations, the field of MRI-based quantitative hemodynamic imaging is rapidly evolving and gives new opportunities for future applications. Accounting for physiological variability, several calibrated BOLD implementations were proposed within the last years [61].

## 3.2 Perfusion Imaging

The hemodynamic relationships (see Section 3.1.2) are already highly complex under healthy conditions [76] (see Section 3.1.3) and become even more complicated in cerebrovascular pathologies [9] (see Section 4.4.3). Several parameters of the cerebral blood supply (see Section 3.1.2) can be measured with MR-based perfusion imaging. In this section, perfusion MRI will be described in two classes. First, a bolus tracking technique with intravenously applied exogenous contrast agents is introduced in Section 3.2.1 [77]. Second, non-invasive magnetic labeling of arterial blood water as an endogenous, freely-diffusible tracer is introduced in Sections 3.2.2 and 3.2.3 [78]. Furthermore, CVR imaging is introduced in Section 3.2.4.

### 3.2.1 Dynamic Susceptibility Contrast

Dynamic susceptibility contrast (DSC) is based on intravenous administration of contrast agent (CA) during MRI [77, 79]. The CA alters the relaxation times and the magnetic susceptibility of the blood [80]. A clinically commonly applied CA is gadolinium (Gd), as it is strongly paramagnetic with seven unpaired electrons (see Section 2.1.6). However, Gd is neurotoxic and can thus only be applied in humans when it is bound in molecule structures, such as Gd-linked diethylenetriaminepentaacetic acid (Gd-DTPA). In the healthy brain, Gd-DTPA does not cross the BBB and remains confined within the vasculature.

Regarding its magnetic properties, Gd-DTPA has two main effects on the blood. First, the local magnetic susceptibility is substantially altered, caused by its large magnetic moment. As CA remains confined in the blood vessels, microscopic magnetic field gradients arise between intra- and extravascular spaces (see Figure 3.1). Those field inhomogeneities shorten local

$T_2^*$  values and can be imaged by a  $T_2^*$ w GRE sequence. This  $T_2^*$  effect is the basis of DSC imaging, which is clinically commonly applied in several brain pathologies. As a second effect of Gd-DTPA, it reduces  $T_1$  when it is in direct contact with protons, which is used for another CA-based perfusion imaging technique called dynamic contrast enhanced (DCE) MRI. While DCE is more often applied in body applications, CA induced signal changes in the brain with intact BBB are rather small due to the CBV of only approximately 4% in GM.

### DSC Acquisition

Practically, DSC-MRI is applied by the injection of a sharp Gd-DTPA bolus, while its passage through the brains vasculature is traced by dynamic MRI. Typically, a GRE-EPI readout (see Sections 2.3.2 and 2.3.4) with TR around 1.5 s is applied according to current recommendations [80], which gives good temporal resolution and limits  $T_1$  bias. Typical voxel sizes are around  $2 \times 2 \times 3 \text{ mm}^3$ . The acquired 4D data allows to calculate tissue concentration-time curves of the CA bolus passage for each voxel (see Figure 3.3).

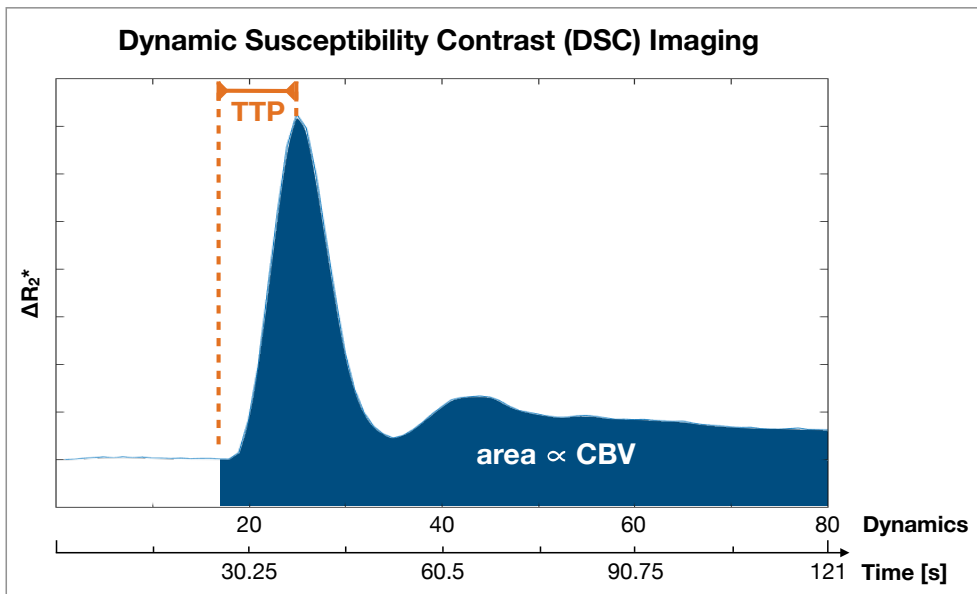


**Figure 3.3: Tissue concentration-time curve in DSC imaging.** Time-dependent tissue concentration curves are acquired for every imaging voxel in DSC. In this case, 80 dynamics were acquired with a TR of approximately 1.5 s. The cerebral blood volume (CBV) is proportional to the area under the curve (blue, full pass integration). Local perfusion delay information are derived by the time-to-peak (TTP) (orange).

### DSC Post Processing

Via post-processing of the DSC data, several perfusion related parameter can be calculated. The measured  $\Delta R_2^*$  time curve (see Figure 3.3) can be converted to a CA tissue concentration time curve by assuming a constant  $T_2^*$  relaxivity [81–83]. An established parameter is the cerebral blood volume (CBV). A robust and widely applied calculation method is integration of the tissue concentration curve. The area under the curve is proportional to the local CBV [84] (see Figure 3.3), when assuming an intact BBB [85]. As absolute CBV calculations remain

challenging, requiring information on the arterial input function, normalization to normal appearing white matter (NAWM) is commonly applied yielding relative CBV (rCBV) [86, 87].

Besides the local blood volume, the tissue concentration curves also contain relevant information on temporal perfusion characteristics. A robust and reliable parameter is the time-to-Peak (TTP). It describes the time interval between first arrival of the CA bolus to the peak, for each voxel (see Figure 3.3). Resulting TTP images give clinical important information on regional perfusion delays.

Recently, Jespersen and Østergaard proposed to gain additional information from perfusion data by parametric modelling of the residue function [88, 89]. They claimed to calculate additional hemodynamic parameters by sophisticated post-processing without requiring sequence modifications. Their model was applied to DSC data by Mouridsen et al. [90]. Based on Bayesian estimations, the capillary transit-time heterogeneity (CTH) is calculated as a marker of microvascular hemodynamic function, see Figure 3.4.

According to that, pathophysiological changes of the capillary morphology may cause CTH elevations. Those elevations might even result in reductions of oxygen availability via a reduced oxygen extraction capacity (OEC), which is also derived by the model. The authors proposed OEC to be the maximum possible oxygen extraction from the capillaries to the tissue [88]. Even though first applications of parametrically modelled DSC data in clinical studies were promising, further evaluations are demanded, especially in comparison with established hemodynamic parameters (see Section 3.1.2).

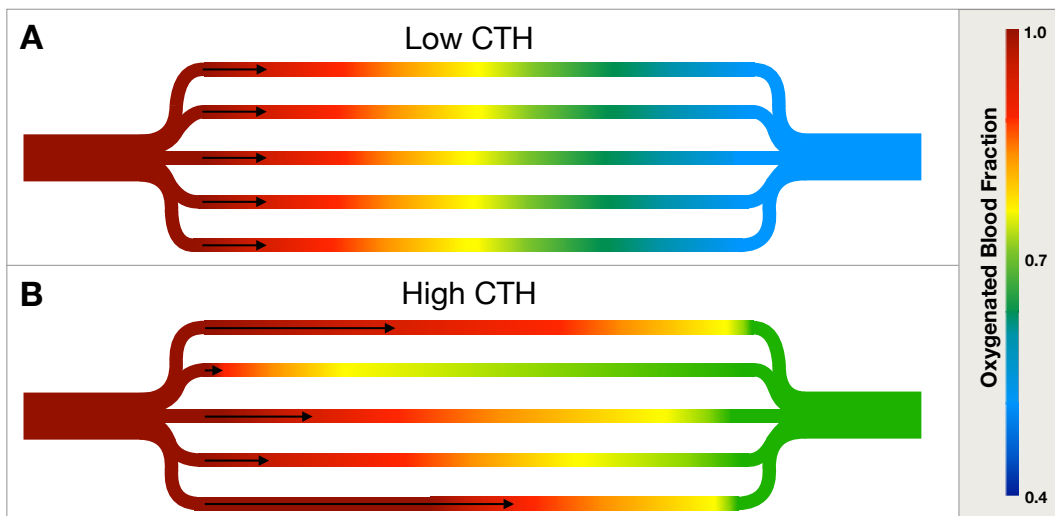


**Figure 3.4: Capillary transit time effects on capillary oxygen extraction.** During the passage of blood through the capillary bed, its oxygenation decreases (color coded). (A) Under healthy conditions, the flow is equally distributed across the capillaries with similar flow velocities (black arrows) with accordingly low capillary transit-time heterogeneity (CTH). (B) Contrary, several pathologies can cause CTH increases, which relates to varying flow velocities and oxygen extractions among capillaries. Note, that CTH can also affect the venous oxygen saturation. Figure adapted from [88, Fig.3].

Even though, CBF can be also estimated from DSC data [91, 92] based on the slope of the signal increase (see Figure 3.3), intravascular tracers have a generally limited reliability for CBF [20, 93]. Thus, CBF measurements are preferred by other techniques using freely diffusible tracers, such as ASL (see Section 3.2.2).

### DSC Applicability

Currently, DSC is widely clinically applied, especially in brain tumors and vascular diseases. In 2000, potential complications of Gd administration were found, causing nephrogenic systemic fibrosis (NSF). NSF is usually a fatal disease and can be caused by Gd-DTPA applications in patients with renal failure [94]. Since then, prior blood sample based estimations of the renal function are analyzed and allowed to effectively prevent NSF. Recently discovered long term Gd depositions are gaining high attention [10]. But no evidence for toxic effects caused by Gd accumulations was found yet. The applicable German law [11] follows the European Medicines Agency (EMA) report [12], stating that Gd-DTPA application remains recommended if clinically necessary, but only at lowest possible dose. To further minimize risks, the use macrocyclic Gd-based CA is compulsory for most applications. Those macrocyclic CA are considered to be chemically more stable compared to the previously more frequently applied linear molecule structures. The ongoing research on Gd accumulations led to a further increased clinical interest in non-invasive MRI-based perfusion imaging techniques (see Section 3.2.2).

### 3.2.2 Arterial Spin Labeling

A fundamentally different MRI-based approach to measure local perfusion effects is arterial spin labeling (ASL) [78]. It is based on magnetic labeling of the inflowing arterial blood water to the brain, as approximately 50% of the blood consists of water. Since blood water is used as a freely-diffusible tracer, ASL is ideal for CBF mapping. Regarding the imaging technique, perfusion information is isolated from static tissue water by image subtraction. *Label* images with magnetic blood labeling and *control* images without labeling are acquired, see Figure 3.5. As the static tissue water is assumed to remain unchanged between label and control images, the subtraction of both images yields the perfusion information.

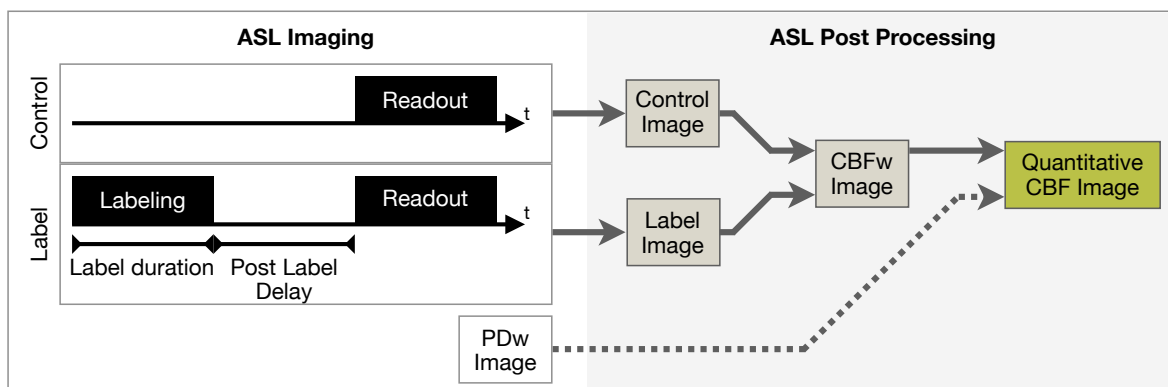


**Figure 3.5: Arterial spin labeling (ASL) workflow.** Control and label images, with labeling of inflowing arterial blood water, are acquired. During post processing, control and label images are subtracted to yield a cerebral blood flow weighted (CBFw) image. By an additionally acquired proton density weighted (PDw) image and further constants (see eq. 3.4), the quantitative CBF image is calculated.

### ASL Labeling Techniques

For labeling, basically three different approaches exist. The first two approaches were already proposed in the 1980's and 1990's, but both come with severe limitations. First, continuous ASL (CASL) was introduced, using continuous RF labeling of a thin slice at the neck [78, 95]. Within this labeling slab, all feeding arteries (see Section 4.1) are labeled at the same time by adiabatic inversion of the inflowing blood [96]. Adiabatic inversion relies on applying a constant RF field together with a constant field gradient in flow direction, so that the flowing blood sweeps through off-resonance and on-resonance and thereby inverts the magnetization. While CASL offers comparably good SNR, the labeling efficiency remains low and magnetization transfer effects caused by off-resonances effects impede the imaging. Often required separate labeling coils and high-power RF amplifiers are usually not compatible with clinical MR scanners and also increase the specific absorption rate (SAR).

The second approach called pulsed ASL (PASL) relies on inversion pulses applied within a 10-20 cm thick inversion plane at the neck. While no dedicated labeling coils are required for PASL, the SNR is lower, which impedes the usability within clinically feasible scan times. Even though several CASL and PASL optimizations were proposed, they were all limited by intrinsic disadvantages of the underlying approaches.

The break through for clinically applicable ASL was a third approach called pseudo-continuous ASL (pCASL). It was proposed by Dai et al. in 2008 as a hybrid of CASL and PASL [97]. A narrow labeling plane is applied similar to CASL for adiabatic inversion, but with a train of ultra short RF pulses of approximately 1 ms spacing. The SNR is better compared to PASL, while the labeling efficiency is superior to CASL. Furthermore, the much lower energy deposition in pCASL allows usage of the standard body coil and RF amplifier for labeling, being compatible with modern clinical MRI scanner hardware. The widespread availability of 3T MRI scanners nowadays is another relevant factor for broad future clinical applications, as ASL benefits from prolonged  $T_1$  of the labeled blood water and the higher SNR [98].

### pCASL Acquisition

To magnetically label the arterial blood-water, a train of inversion pulses is applied for 1-3 seconds in pCASL [98] in the neck region at the brain feeding arteries (see Section 4.1). The labeling plane should be individually planned based on an angiography scan with the following conditions: at straight vessel segments, above the carotid bifurcation at regions of laminar flow, oriented perpendicular to the arteries and without cutting any arterial loops (see Section 4.1).

To allow the labeled blood water to flow into the tissue element of interest, there is a certain time interval called post-label delay (PLD) between the labeling and the beginning of the MR imaging (see Figure 3.5). The PLD needs to be adapted to the investigated study cohort as a trade-off between two main factors. On the one hand, the PLD should be kept as short as possible. The tracer lifetime is limited, because the labeled blood decays with  $T_1$  in the range of 1300 - 1750 ms. On the other hand, the PLD needs to be sufficiently long that the labeled blood reaches the brain tissue, see Figure 3.6. Therefore, the PLD should be set according to the arterial transit time (ATT), which refers to the transport time of the labeled blood to the tissue volume of interest [99]. The normal range of ATT values can vary between 500-1500 ms and depends e.g. on the participants gender, differs among brain regions (see Section 4.2) and increases with age [100]. Furthermore, it can be severely prolonged by pathologies. Too short PLD can cause incomplete bolus arrival and thereby CBF underestimations. As a compromise, a PLD of 2000 ms is recommended for elderly participants and adult clinical

patients [98]. However, especially in cerebrovascular diseases, lower measured CBF could still be related to delayed perfusion with  $ATT > 2000 \text{ ms}$  rather than hypoperfusion. To overcome those limitations, future acquisitions of time-encoded ASL with multiple PLDs and tracer kinetic modeling [101] is highly promising, but currently remains difficult [102]. In addition to perfusion imaging, ASL can be also used for angiography with shorter PLDs.

For readout of the label and control images, 2D EPI or 3D GraSE are commonly used (see Sections 2.3.2 and 2.3.4). While 2D EPI offers higher temporal resolutions of approximately 10 seconds, segmented 3D GraSE offers optimal BGS for all slices. Both readout modules were applied in this thesis, but 3D GraSE was preferred based on initial comparisons in the conference contribution C19 and ISMRM perfusion study group recommendations [98]. Background suppression (BGS) of the static tissue signals is commonly applied (see Section 2.3.3), as the perfusion information relates only to 1-2% of the acquired signal in label and control images. Typical voxel sizes are around  $3 \times 3 \times 6 \text{ mm}^3$ .

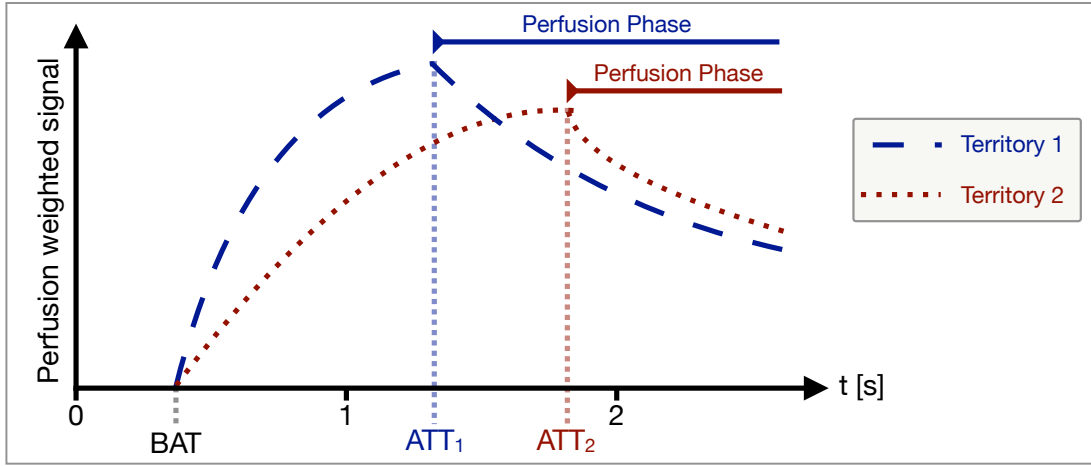


**Figure 3.6: ASL kinetic curves.** The time dependencies of perfusion weighted signals are illustrated in two brain regions with shorter arterial transit time  $ATT_1$  and longer  $ATT_2$ . CBF imaging is supposed in the perfusion phase after bolus arrival at  $PLD > ATT$ . In both regions, the bolus arrival time (BAT) is equal. Image adapted from [103, Fig.5].

### ASL Post Processing

By subtracting label and control images, perfusion weighted images are calculated, see Figure 3.5. A highly attractive feature of ASL is its ability to yield quantitative CBF maps. When assuming a single-compartment model and entire labeled bolus arrival, CBF results in

$$CBF = \frac{6000 \cdot \lambda \cdot (Control - Label) \cdot e^{\frac{PLD}{T_{1,blood}}}}{2 \cdot \alpha \cdot T_{1,blood} \cdot PDw \cdot \left(1 - e^{\frac{-\tau}{T_{1,blood}}}\right)} \quad [ml/100g/min] \quad (3.4)$$

with the brain/blood partition coefficient  $\lambda = 0.9 \text{ mL/g}$ ,  $T_{1,blood} = 1.65 \text{ s}$  at 3T, labelling efficiency  $\alpha = 0.85$ , label duration  $\tau = 1800 \text{ ms}$ , control, label and PDw images [98].

### ASL Applicability

Despite of extensive methodological improvements, researchers complained a "lack of enthusiasm from the clinical community" [104] for ASL applications and find "it is perplexing that ASL MRI has not really found its way into routine clinical practice" [105] in 2012. Even though ASL is yet not part of the clinical routine, the development of pCASL and the ISMRM perfusion study group consensus recommendations [98] were milestones for clinical applicability. Further pushed by Gd depositions in CA-based perfusion imaging (see Section 3.2.1), ASL as a non-invasive technique is gaining additional attention for potential future clinical applications in several pathologies, such as cerebrovascular diseases (see Section 4.4.3). However, remaining limitations of current pCASL implementations are the comparably low SNR, required user experience to set the labeling plane and potential delay effects with single-PLD acquisitions.

#### 3.2.3 Super-Selective Arterial Spin Labeling

While the afore introduced pCASL is based on labeling all brain feeding arteries (see Section 4.1) to locally quantify perfusion, sequence modifications even allow non-invasive mapping of perfusion territories. Rather than labeling a plane, in 2010, Helle et al. proposed to label just a spot to visualize perfusion territories of individual arteries (see Section 4.2). This so-called super-selective ASL (ss-ASL) is implemented via additional application of time-varying gradients during the RF labeling pulses. After each RF pulse, the directions of the additional gradient pulses are changed in a pseudorandomized fashion around a predefined centered target location with concomitant changes of the RF pulse phases. Thus, phase effects caused by these gradients are minimized just at the target location, leading to a locally maximized labeling efficiency. The labeling spot size in both dimensions perpendicular to the vessel are adjustable by the additionally applied gradient pulses (see Section 2.2.1).

Super-selective ASL includes all advantages of pCASL (see Section 3.2.2) and uses its standard 2D EPI or 3D GraSE readout modules. The availability of ss-ASL currently remains very limited, as it is still a research sequence requiring sequence programming modifications. But from a clinical perspective, ss-ASL is highly interesting [102]. First, knowledge about shifted perfusion territories has high diagnostic value in several cerebrovascular diseases (see Section 4.3). Second, it newly offers unique opportunity for non-invasive territory mapping with high potential for broader applications, as the only currently clinically established technique is based on invasive catheter angiography (see Section 4.4.3).

#### 3.2.4 Cerebrovascular Reactivity

Unlike steady state parameters such as CBF or OEF, which can be measured in the baseline state at rest (see Sections 3.2.2 and 3.3.1), CVR is usually measured by applying a vasodilatory stimulus. Dynamic MR images are acquired during baseline conditions and also during vasoactive stimulation. A potent vasodilatory stimulus is arterial carbon-dioxide ( $\text{CO}_2$ ). It is naturally involved in the cerebral energy metabolism (see eq. 3.1) and induces relaxation of vascular smooth muscle cells via chemoreceptor stimulation [106–108] (see Figure 3.1B).

Even though CVR is a highly promising parameter to detect hemodynamic impairments at early disease stages (see Section 4.4.3), the two most commonly applied methods for vasodilatory stimuli have severe disadvantages. First, exogenous drugs such as acetazolamide are intravenously applied prior to perfusion imaging. However, acetazolamide is not approved anymore for CVR imaging in Germany. Second, hypercapnic gas is applied via sealed face

masks supplying an increased ( $\text{CO}_2$ ) concentration in the inhaled air with additional endtidal gas monitoring. It is widely accepted as a reliable method in the CVR research community [109]. However, the tolerability by the participants is limited [110]. In addition, the setup is complicated and costly hardware is required, which severely impedes the overall clinical applicability. Furthermore, complicated experimental setups are hardly consistent with the efficient clinical MRI workflow. Recently, a non-invasive and easily applicable alternative was proposed, which uses breath-holds as vasodilatory stimuli during dynamic MRI [109].

### Breathhold-fMRI

Acquisitions of CVR by breathhold-fMRI (BH-fMRI) rely on imaging during a block design of alternating normal breathing and breath-holds, which lead to an increased arterial  $\text{CO}_2$  concentration. Breath-hold durations of 15 seconds were proposed to be tolerable for most participants [109], while causing sufficient  $\text{CO}_2$  increases for reproducible results [111]. For imaging, GRE-EPI readout with MB acceleration (see Sections 2.3.2 and 2.3.4) is usually applied for BOLD weighted imaging (see Section 3.1.3) with voxel volumes around  $3 \times 3 \times 3 \text{ mm}^3$ .

For post processing of BH-fMRI time series data, standard motion correction is followed by a regression analysis. Recently, the group of Jan Petr published a model-driven approach [112]. The acquired data is corrected for a global time delay and voxel wise correlation values are calculated by regression of a pre defined respiratory response function, see Figure 3.7 . Statistical beta values serve as a proxy of CVR. While the published results are promising, further clinical evaluations are clearly demanded to especially probe the reliability and sensitivity of BH-fMRI under healthy conditions and in cerebrovascular diseases (see Section 4.3).

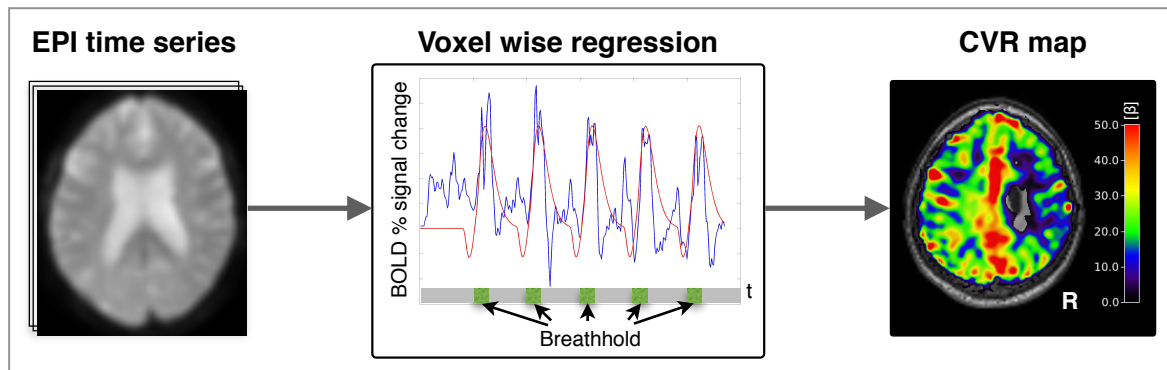


**Figure 3.7: Breathhold-fMRI post processing for cerebrovascular reactivity (CVR) mapping.** The time series of EPI images was acquired during a block design of 45 s normal breathing and 15 s breathhold with five repetitions. In model driven post-processing, regression analysis is applied with a respiratory response function for each voxel to calculate CVR maps [112]. Here, patient data with CVR impairments is shown, see Section 4.3. The locally reduced CVR indicates impaired hemodynamic function.



### 3.3 Oxygenation Imaging

Mapping of OEF is of high interest for neuroscientific applications, as the oxygen consumption relates to the neuronal activity (see Section 3.1.3) [76, 113–115]. Furthermore, OEF is highly promising to improve clinical diagnostics and treatment of several cerebrovascular diseases (see Section 4.4.3). Previous studies reported correlations between OEF increases and increased stroke risks [116–119]. However, established gold standard OEF measurements by PET are severely limited (see Section 3.1.2). Thus, alternative oxygenation sensitive imaging by MRI based on quantitative BOLD implementations is gaining high interest.

#### 3.3.1 Multi-Parametric Quantitative BOLD

While several MR-based methods for OEF imaging have been proposed (see Section 8.1.4) [19, 61, 62], an easily applicable technique with full brain coverage within clinically applicable scan times is called multi-parametric quantitative BOLD (mq-BOLD) [120]. It relies on the biophysical model of Yablonskiy and Haacke [121]. They model the blood vessel network by randomly oriented cylinders of infinite length and with homogenous magnetization.

The mq-BOLD implementation is based on calculating relative OEF (rOEF) from three separate MRI measurements of relative CBV (rCBV) and the quantitative transverse relaxation rates  $R_2^*$  and  $R_2$ . Maps of rCBV are obtained by DSC-MRI (see Section 3.2.1). Quantitative  $R_2^*$  imaging is applied by a multi-echo GRE sequence (see Section 2.3.2) with corrections for macroscopic background gradients [122, 123]. Quantitative  $R_2$  images are derived from a GraSE sequence with multiple echoes (see Section 2.3.4). Following the mq-BOLD approach [120], rOEF is calculated by

$$rOEF = \frac{R_2'}{c \cdot rCBV} \quad (3.5)$$

with the constant  $c = \gamma \cdot \frac{4}{3} \cdot \pi \cdot \Delta\chi \cdot B_0$  and  $B_0 = 3T$ . Here,  $\Delta\chi = \Delta\chi_0 \cdot Hct = 0.924 \cdot 10^{-7}$  is the susceptibility difference between oxygenated and deoxygenated blood. The susceptibility difference between fully deoxygenated and fully oxygenated hemoglobin is  $\Delta\chi_0 = 0.264 \cdot 10^{-6}$  [124, 125] and the small vessel hematocrit is  $Hct = 0.35$  [125].

Previous mq-BOLD applications in clinical studies showed promising results in several pathologies [126–129]. However, the usability was impeded and quantitative interpretations limited by systematically elevated rOEF values. Reported rOEF of 0.6-0.7 in GM [120] were much higher compared to physiologically expected values in the range of 0.35-0.56 based on PET reference measurements [9, 130]. Furthermore, rOEF evaluations were restricted to GM even though WM is particularly affected in many pathologies [131]. The increased vulnerability of WM to perfusion deficits is due to its more distal localization in the blood supply architecture [132]. However, the reliability of mq-BOLD-based rOEF values in WM is currently unknown. Well-known vasculature orientation effects [133, 134] contradict the model assumptions and related anisotropy effects of the underlying  $T_2$  [135, 136] and rCBV measurements [137] may further impede the validity of rOEF values in WM.

## 3.4 Structural Imaging

Besides the afore introduced functional mappings, structural imaging is of high importance in clinical MRI. Three widely used clinical imaging methods will be introduced, which allow classification of brain tissues (see Section 3.4.1), detection of microangiopathic changes (see Section 3.4.2) and measurement of white matter (WM) fiber orientation (see Section 3.4.3).

### 3.4.1 MP-RAGE

An MR sequence applied in almost every brain scan protocol is called magnetization prepared rapid gradient echo (MP-RAGE) [138]. It is a  $T_1$ w sequence, based on inversion preparation for enhancing  $T_1$ w contrast (see Section 2.3.3) in combination with rapid GRE readout (see Section 2.3.2). Images typically have high spatial resolution with voxel volumes of around  $1 \text{ mm}^3$ , covering the whole head in acquisition times of about five minutes. Based on the good GM-WM contrast, MR-RAGE data is widely used for image segmentation into the different tissue classes of GM, WM and cerebrospinal fluid (CSF). For segmentation and image processing, the statistical parametric mapping (SPM) toolbox is widely used in research applications and was also applied in this thesis [139]. Furthermore, spatial transformations of individual brain scans to a standardized brain atlas are often performed with SPM based on MP-RAGE images. A commonly used brain atlas for normalizations is the MNI template, named after the Montreal Neurological Institute at the McGill University in Montréal, Canada.

### 3.4.2 FLAIR

Another very common clinically applied sequence is called  $T_2$ w fluid attenuated inversion recovery (FLAIR) [140, 141]. It is based on an inversion preparation to suppress signals from fluids (see Section 2.3.3) with a  $T_2$ w FSE readout (see Sections 2.3.1 and 2.3.4) and typical voxel volumes around  $1 \text{ mm}^3$ . The suppression of hyperintense fluid signals, e.g. from CSF, improves the visibility of periventricular brain lesions. FLAIR imaging is sensitive to microangiopathic changes, which can arise in healthy ageing and may result in cognitive decline [142]. Furthermore, it is specifically sensitive to pathophysiological changes in several diseases, such as in multiple sclerosis (MS) [143]. For clinical diagnostics of vascular diseases, FLAIR lesions are graded by a radiologist using the Fazekas-score [144].

### 3.4.3 Diffusion Tensor Imaging

Another structural imaging technique is diffusion tensor imaging (DTI), which offers water diffusion sensitive contrast [20]. It is based on the application of magnetic gradient fields (see Section 2.2.1) to non-invasively measure the diffusion related signal attenuation in biological tissues [145, 146]. This images contrast relies on the fact that water molecules are not freely diffusing in tissues. Resulting restricted and directionality dependent diffusion thus gives important information on the local microscopic tissue architecture. DTI is appealing for studying brain structures in healthy ageing and is also clinically applied to study white matter diseases, such as for example Alzheimer's disease (AD) or strokes.

### WM Structure

In biological tissues, heterogenous structures can restrict the diffusion. In addition, tissues are often anisotropic, meaning that oriented structures cause direction dependent diffusion [20].

Specifically, WM mainly consists of myelinated axons. Those axons are nerve fibers and serve as messaging connections between GM regions, as they carry nerve impulses between neurones. Axons are wrapped by myelin sheaths, consisting of lipid bilayers in a laminar structure. Myelin acts as an insulator and increases the nerve signal's transmission speed. Nerve fibres are arranged in bundles, so called fibre tracts. Regarding diffusion, the laminar structure of myelinated axons causes anisotropic diffusion. It is highest along the fibre direction and most impeded perpendicular to the fibres [147].

### Diffusion MRI

From a physical perspective, diffusion can be seen as a random walk of molecules. Induced by random rotations and thermal motion, water molecules are permanently in motion, continuously tumbling and colliding with other molecules. The relative orientation of a molecule is permanently changing and it thus experiences fluctuations of the surrounding magnetic field. As motion of a nuclear spin in a non-uniform magnetic field causes changes in its precession rate, diffusion causes dephasing and finally affects the relaxation of nuclear spins, which can be measured by MRI (see Section 2.1.4). Diffusion processes are described by the diffusion coefficient  $D$ . While diffusion is isotropic in free water without preferential directions, this is not generally the case in tissues. Therefore,  $D$  is considered as a tensor in the DTI reconstruction with directionality dependent diffusion values. Historically, diffusion weighted imaging (DWI) with measurements in three directions was proposed first. It just gives a diffusion weighted image contrast, weighted by the trace of  $D$ , but the tensor itself remains unknown. Improvements by DTI with acquisitions of at least six different gradient directions allow to actually calculate local diffusion tensors and thereby enable to derive the preferred diffusion direction within each voxel [148].

For DTI, a strong bipolar magnetic field gradient (see Section 2.2.1) is applied after excitation and before image readout [145, 146]. The applied gradients are balanced, so that there is no net effect for stationary spins, but moving spins acquire a phase offset proportional to the travelled distance in the direction of the gradient. Thereby, the diffusion of water molecules is proportional to the nuclear spins's phase dispersion and the MR signal gets attenuated. In case of free diffusion, with a Gaussian distribution of spin phases, the attenuation exponentially depends on the tissue-related diffusion coefficient  $D$  as well as the sequence dependent gradient strength and gradient duration [149]. For readout, both, SE or GRE can be applied, which is often accelerated with EPI (see Section 2.3.4). A typical voxel size is  $2 \times 2 \times 2 \text{ mm}^3$ . The measurement is repeated in the different gradient encoding directions.

A commonly applied DTI post-processing tool is the FMRIB software library (FSL) [150]. It is named after the Oxford Centre for Functional MRI of the Brain at the University of Oxford and was also used in this work. Corrections for eddy current effects and motion are applied by the FMRIB's linear image registration tool (FLIRT) [151, 152], non-brain voxels removed by the brain extraction tool (BET) [115], and the tensor fitting applied by the FMRIB's diffusion toolbox (FDT) [153, 154].

An important parameter from DTI is the fractional anisotropy (FA) of WM [155]. It is a measure of the diffusion anisotropy, with values ranging between 0 and 1. Low FA values correspond to isotropic and high values to anisotropic diffusion. Furthermore, the main fibre orientation of each voxel can be calculated, derived from the diffusion tensor  $D$  by the eigenvector with the largest eigenvalue.



## 4 Clinical Background of Internal Carotid Artery Stenosis

This chapter provides an overview on cerebral blood supply under healthy conditions and impairments in carotid artery disease. The brain requires continuous blood supply, as it has high energy demands without storage capacities [156]. While the brain weights only 2 % of the whole body, it accounts for approximately 20 % of the total body energy consumption. Those high energy demands are remarkably constant over time, despite of known oxygen metabolism variations [157]. As the brain's main source of energy is the oxidative glucose metabolism (see Section 3.1.1), continuous supply with glucose and oxygen is required. They are delivered via a complex network of blood vessels (see Figure 4.1). Interruption of this cerebral energy supply have severe consequences after a few minutes already, causing cell death by strokes.

The following sections introduce the brain's vascular system starting with the blood passage from the major neck arteries in Section 4.1, via the principle intracranial arteries to the arterioles forming the vascular territories described in Section 4.2, based on the description in [158]. Pathophysiological blood supply disruptions by internal carotid artery stenoses are introduced in Section 4.3. Finally, currently applied clinical diagnostics, interventional options and the high potential of hemodynamic MRI applications are summarized in Section 4.4.

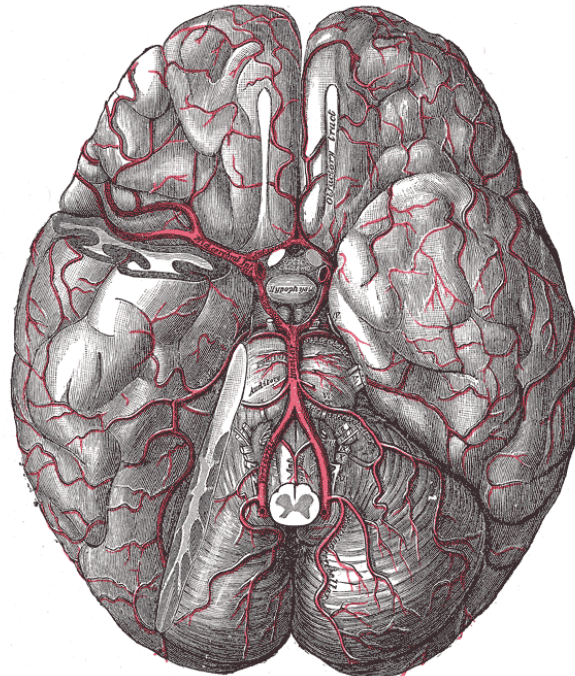


**Figure 4.1: Cerebral blood supply illustration.** Arteries (in red) show the blood passage from the two vertebral arteries in the neck, via principle intracranial arteries to arterial branching within the brain. Parts of the right hemisphere are not shown. Image under public domain from [158, Fig.516].

## 4.1 Anatomy of Major Neck Arteries

The brain is supplied with blood by four major arteries. There are two anterior internal carotid arteries (ICA) and two posterior vertebral arteries (VA), as shown in Figure 4.2. The left and right ICAs ascend in the front of the neck. Each of them arises from a common carotid artery, which bifurcates into the ICA and the external carotid artery (ECA). While the ICAs supply a great extent of the brain, the ECAs supply the exterior of the head, for example the face. The other two major brain supplying arteries are the left and right VAs, which course along the sides of the neck. Both VAs cranially merge to the basilar artery (BA).

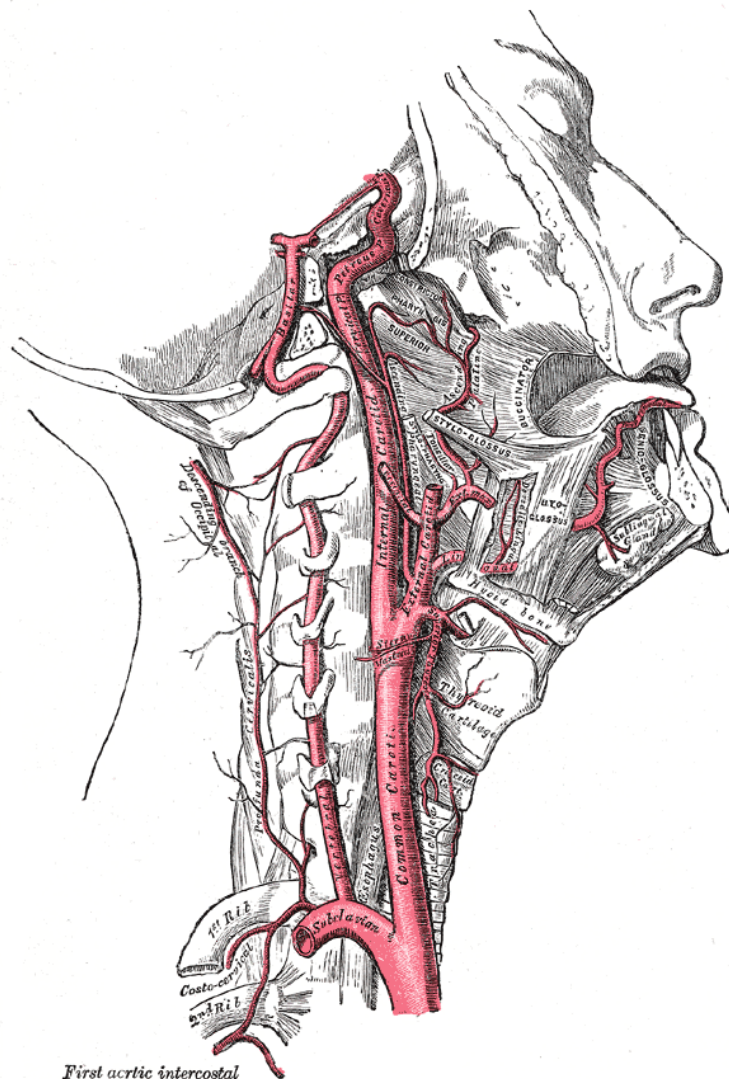


**Figure 4.2: The major arteries in the right side of the neck.** The common carotid artery bifurcates into the external carotid artery and internal carotid artery, which supplies the brain with blood. The vertebral artery courses along the side of the neck and unites with the contralateral vertebral artery to the basilar artery. Image under public domain from [158, Fig.513].

## 4.2 Cerebral Vascular Territories

The two ICAs and BA form a circle of interconnected arteries at the base of the brain, known as the circle of Willis (CoW) and shown in Figure 4.3. The ICAs and BA supply the CoW with blood. Within the CoW, ICAs can be connected by the anterior communicating artery (ACoMA). The posterior branches of the CoW can connect the BA via the posterior communicating artery (PCoMA). Thus, the CoW can provide connections between the anterior and posterior blood supply as well as between both hemispheres. However, the manifestation of the ACoMA and PCoMA can highly differ among individual subjects, being incomplete in about 60 % of the population. An incomplete CoW does not impair the regular cerebral blood supply, but becomes especially important in case of local blood supply disruptions, as they can be compensated via collateral blood flow in the CoW [159, pp. 55-56]. In general, varying locations and diameters of cerebral arteries under healthy conditions are known [160].

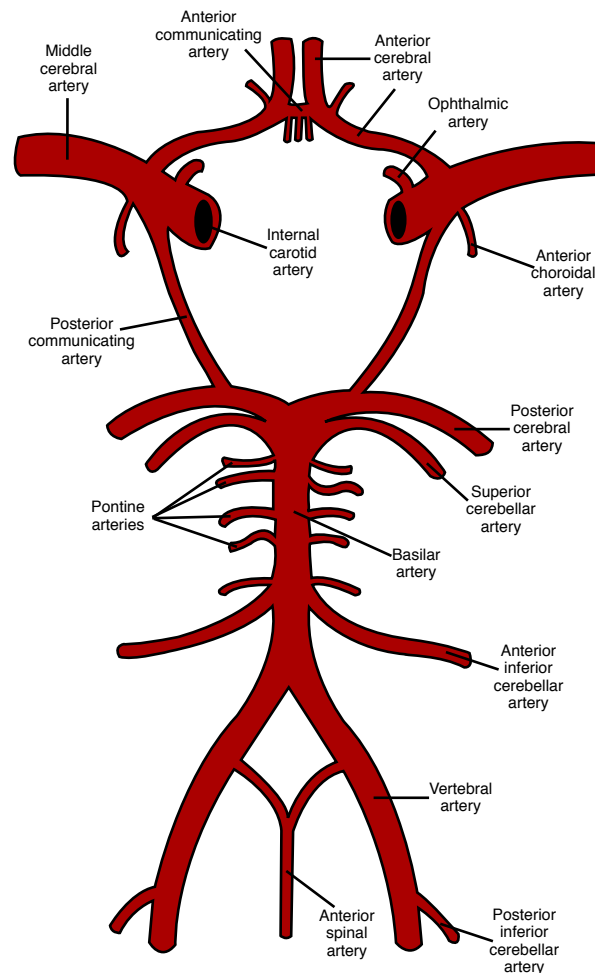


**Figure 4.3: Arterial circulation within the circle of Willis (CoW).** The internal carotid arteries and vertebral arteries can be connected via the anterior communicating artery and the posterior communicating arteries. Image under public domain from [161], adapted from image under public domain from [158, Fig.519].



Each of the brain feeding neck arteries supplies typical vascular territories, as shown in Figure 4.4. Those territories are related to the three arterial trunks within each hemisphere, which arise from the CoW (see Figure 4.3). Those three principle intracranial arteries are the anterior cerebral artery (ACA), middle cerebral artery (MCA) and posterior cerebral artery (PCA). The ACA is typically fed by an ICA and supplies the frontal lobes [159, p. 56]. Also fed by an ICA, the MCA supplies large parts of the brain including the lateral surface of temporal and parietal lobes [159, pp. 56-58]. The posterior cerebral artery (PCA) is usually fed by the BA and supplies the temporal and occipital lobes [159, pp. 58-62]. While those vascular territories are considered similar among a healthy population and symmetrical between hemispheres, variances have been previously presented even in a healthy cohort and attributed to the morphological variability of the previously introduced cerebral vascular system, e.g. by individual communicating arterial connection manifestations [162, 163].

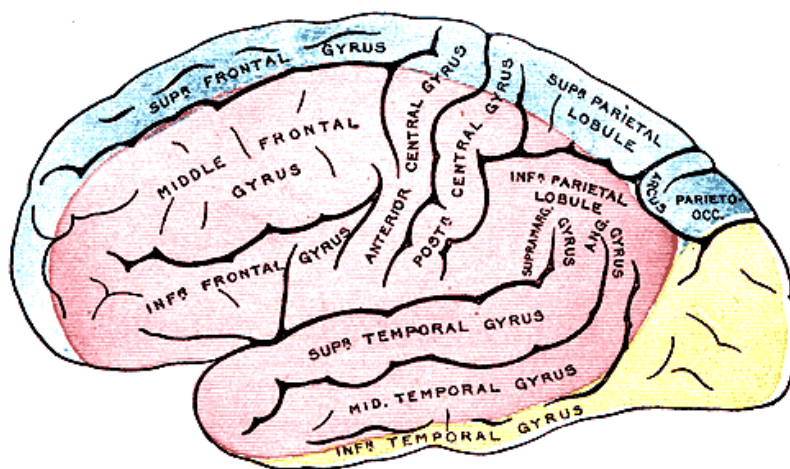


**Figure 4.4: Perfusion territories on the outer surface of the cerebral hemisphere.** Typical areas supplied by the anterior cerebral artery (ACA) are shown in blue, middle cerebral artery (MCA) in red and posterior cerebral artery (PCA) in yellow. Image under public domain from [158, Fig.517].

It is well known from stroke research, that the border zones between the ACA, MCA and PCA vascular territories (see Figure 4.4) are especially vulnerable for perfusion deficits [132, 164]. Those so-called watershed areas (WSA) are located most distal from the supplying arteries. Thus, impairments of the cerebral blood supply are likely to affect the watershed regions first [165, p. 105], for example by the stenosis of an ICA [117, 164].

### 4.3 Internal Carotid Artery Stenosis

Internal carotid artery stenosis (ICAS) is a narrowing of an ICA. It is usually caused by a plaque, which narrows the arterial lumen and is also known as atherosclerosis. The plaque is an accumulation at the inner arterial wall, consisting, inter alia, of lipids and fibrous tissue. The most common plaque location is the carotid bifurcation, as shown in Figure 4.5. Common risk factors for ICAS are hypertension, diabetes, smoking, age, gender and race [165, p. 109]. Epidemiological studies showed that approximately 1 million patients in Germany have ICAS [166, p. 2]. As the elderly population above 65 years is more likely to be affected by ICAS [167], a further increasing prevalence is predicted in view of demographic change.



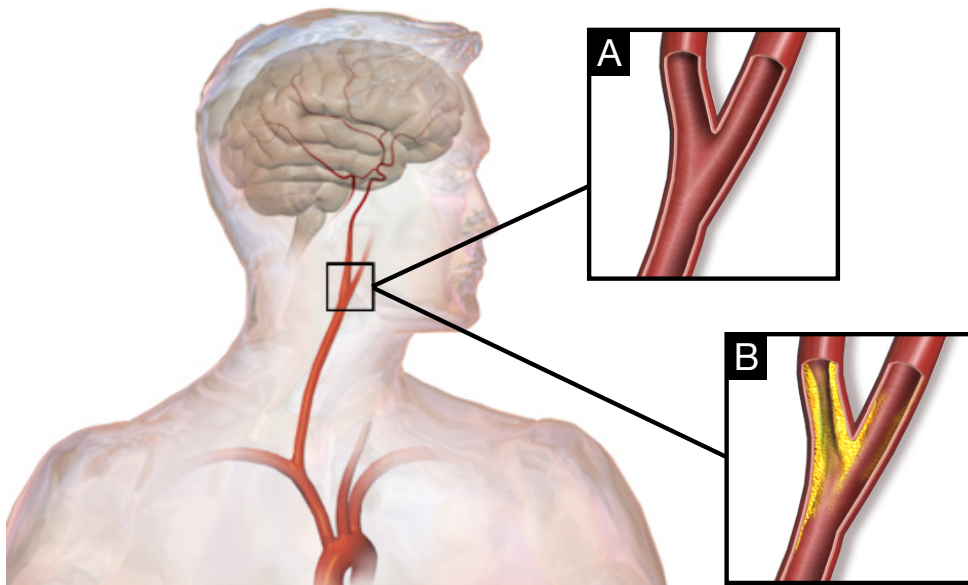


**Figure 4.5: Illustration of right sided internal carotid artery stenosis.** Magnifications of the common carotid artery bifurcation (black box) under healthy conditions (A) is compared to a plaque at the ICA (B), which narrows the arterial lumen. Image modified licensed under CC BY 3.0 from [168].

ICAS can cause various complications [166, p. 2]. Ischemic strokes can be caused by ruptured pieces of the plaque or blood clots, as a source of embolization [169]. This embolus is carried with the blood flow to the brain. As the vessel diameter decreases in arterial branching, the embolus can occlude smaller distal arteries. This occlusion interrupts the blood flow to the vascular territory that was previously supplied by this vessel, known as ischemic stroke. Approximately 10 - 20 % of all strokes are caused by ICAS [16]. Another complication are transient ischemic attacks (TIA), so-called mini-strokes, which are also often caused by blood clots [169, 170]. The permanently reduced blood supply of the brain by the plaque can also manifest in severe chronic perfusion deficits, causing for example cognitive decline [171].

## 4.4 Diagnosis and Treatment Options

### 4.4.1 Diagnosis of ICAS

The clinical patient management is based on the distinction between symptomatic and asymptomatic ICAS-patients [166, p. 18]. Symptomatic patients previously showed signs of permanent cerebral ischemia, TIA, or neurological symptoms [172, pp. 6-8] and thus, are usually diagnosed during examinations concerning those symptoms [173]. In contrast, asymptomatic ICAS does not cause obvious symptoms and is often detected as an incidental finding [167]. The initial ICAS diagnosis is often performed by non-invasive Doppler ultrasound of the ICAs [165, p. 109]. The blood flow velocity increases in the ICA at the location of the plaque and correlates with the narrowed arterial lumen. The degree of the stenosis is commonly estimated [174, p. 158] following the standardised NASCET criteria, based on the North American symptomatic carotid endarterectomy trial [173]. For further diagnostics, imaging of the major neck arteries is performed by either CT or MR angiography [175], following the current treatment guidelines [166, pp. 21-29].

### 4.4.2 Treatment Options in ICAS

The treatment aims to reduce the risk of stroke. Untreated symptomatic ICAS has a stroke rate of about 26 % after two years [176] and still 5 % per year in high-grade asymptomatic patients [177]. Non-invasive best medical treatment mainly relies on anti-platelet therapy for blood-thinning, statins for cholesterol lowering and anti-hypertensives to reduce the blood pressure and is also advised in lower-grade ICAS [174, 175, p. 163]. Alternatively, effective interventions are available either by carotid endarterectomy (CEA) or carotid artery stenting (CAS). CEA is an open surgery in the neck, where the ICA is sliced to remove the plaque [174, pp. 163-169]. More recently, CAS was introduced to permanently widen the arterial lumen by a stent, which is placed in a minimally invasive procedure [174, pp. 169-171]. However, both surgical treatment options come with substantial risks of intra- and postoperative complications, including strokes [17]. Those competing risks complicate treatment decisions, which are especially delicate in asymptomatic ICAS-patients [18]. While symptomatic high-graded patients often receive surgical treatment, it remains unclear whether high-grade asymptomatic patients would benefit from a more aggressive treatment by interventions [18, 175, 178].

### 4.4.3 Potential of Hemodynamic MRI in ICAS

Currently, treatment decisions are mainly based on the degree of the stenosis [167], but not on information about local hemodynamic impairments on a tissue level [179]. To generate additional evidence for treatment decisions, hemodynamic MRI is especially promising [9]. MRI offers the unique advantage to acquire a large variety of relevant hemodynamic parameters in the same scan-protocol (see Sections 3.2 and 3.3), in contrast to ultrasound or CT. However, there is a lack of clinically applicable methods and further validations are required [171].

Effective MRI-based hemodynamic imaging would be highly beneficial for periodical monitoring, as ICAS is a progressive disease. The disease progression of patients who received best medical treatment could be monitored to re-evaluate therapy decisions. After interventions, the treatment efficacy could be tested and long-term treatment effects screened, as plaques can regrow even after successful interventions [166, p. 22], especially when risk factors persist.

An important hemodynamic factor on the clinical manifestation in ICAS is the collateral blood supply. Decreased local perfusion pressure, caused by the plaque, can induce strong spatial variations of the perfusion territories [180]. Thereby, the typical vascular territories described in Section 4.2 can be widely shifted [181]. The capability of those collateral blood flow activations highly depends on the individual CoW configuration, with varying AComA and PComA manifestations (see Section 4.2). Even though knowledge about perfusion territory shifts could provide important information for treatment decisions, collateral flow is currently not commonly clinically evaluated, due to methodological limitations. While the anatomical CoW configuration can be imaged with CT or MRI, predictions of the actual vascular territories remain extremely difficult [182, p. 22]. Currently, the only clinically available imaging method to visualize vascular territories is digital subtraction angiography (DSA) [166, pp. 21-29]. In this invasive technique, contrast agent is injected to the major neck arteries with an arterial catheter from the femoral artery. X-ray projections are acquired during contrast agent administration to the catheter. DSAs are rarely acquired in ICAS [166, p. 22], as the procedure applies high effective ionizing radiation doses to the patient [183], have complication risks, high costs and includes inpatient admission [184]. Thus, clinically applicable non-invasive vascular perfusion territory mapping by MRI could provide relevant information about the individual vascular situation to support treatment decisions [9].

## 5 Database for Hemodynamic MRI Evaluation

This thesis mainly relies on multi-parametric in-vivo MRI-data. The introduced state-of-the-art hemodynamic imaging methods were applied in four prospective clinical studies, see Table 5.1. First, a clinical study was acquired to compare 29 patients with asymptomatic, unilateral and high-grade ICAS (see Chapter 4) to 30 age-matched healthy controls. Second, both groups were partly re-scanned, ICAS patients after intervention by CEA or CAS (see Section 4.4.2) and healthy controls with a similar time interval between both scans. The extensive MR imaging protocol included DSC,  $T_2$  GraSE,  $T_2^*$  GRE, pCASL, ss-ASL, BH-fMRI, DTI, MP-RAGE and FLAIR imaging (see Chapter 3). Third, pCASL was acquired in ten young healthy participants for comparisons with existing PET data, with additional FLAIR and MP-RAGE imaging. Finally, another 10 young healthy participants were scanned including DTI,  $T_2$  GraSE,  $T_2^*$  GRE, MP-RAGE and FLAIR for age-related comparisons.

Cohort	Number of participants N	Related Publications
ICAS patients	29	JP-I, JP-III, JP-IV, J3, J4
Elderly healthy	30	JP-I, JP-II, JP-III, JP-IV, J3, J4
ICAS follow-up	16	C1, C2, C5, C11
Elderly follow-up	17	JP-IV
Young healthy I	10	J4
Young healthy II	10	JP-II, JP-IV

**Table 5.1: Summary of in-vivo study participants.** For each cohort, the number of scanned participants, related publications and selected abstracts are noted.

The acquired multi-parametric in-vivo MR data relies on combined evaluations of several hemodynamic and structural imaging methods. To evaluate this comprehensive imaging data, a sophisticated fully-automated data processing pipeline was developed (see Figure 5.1), as introduced in Section 5.1. Its specific applications to the embedded journal publications JP-I, JP-II, JP-III and JP-IV as well as related publications J3 and J4 are described in Section 5.2.

### 5.1 Processing Pipeline

The image processing with in-house programs was implemented in Matlab 2016b (The Mathworks, Inc., Natick, Massachusetts, USA) using SPM12 [139] and FSL [150]. It consisted of three main steps, see Figure 5.1. First, data from the different MR imaging techniques was separately processed with specific programs. The resulting parameter maps were calculated in the individual subject’s space, as described in Section 5.1.1. Second, relevant resulting parameter maps of each participant were copied to generate a uniform data base, as described in Section 5.1.2. In this step, spatial coregistrations and MNI normalizations were applied. Third, group level evaluations of the multi-parametric data were implemented based on the unified data base structure, as described in Section 5.1.3.

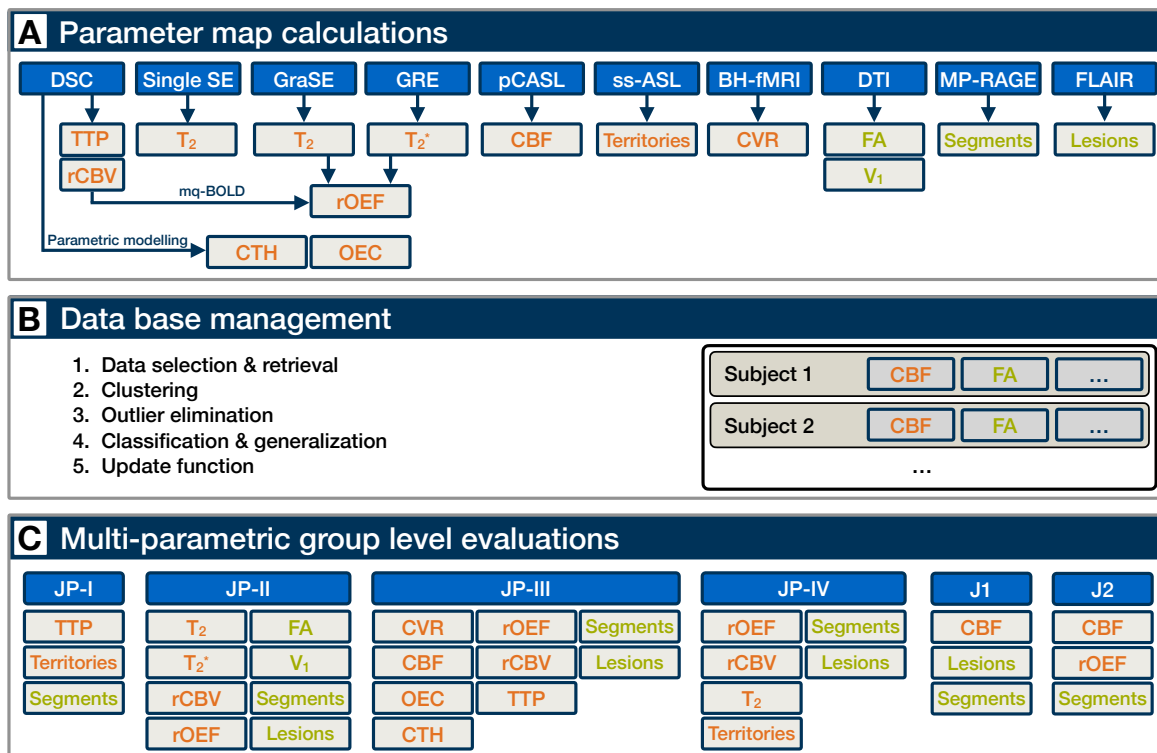


**Figure 5.1: Data processing pipeline.** (A) Based on the applied MRI sequences (light blue boxes), hemodynamic (orange) and structural parameter maps (green) were calculated with separate specific programs. (B) Those parameter maps were used to generate a uniform data base following the standardized brain imaging data structure (BIDS) structure. (C) Based on this data base, multi-parametric evaluations were performed on group level. For each journal publication, the evaluated parameters are summarized.

### 5.1.1 Parameter Map Calculations

In the first processing step, the MRI data of each sequence was processed with specific programs, as illustrated in Figure 5.1A. For this thesis and the related publications, fully automated pipelines were developed to process DSC (see Section 3.2.1), pCASL (see Section 3.2.2) including ss-ASL (see Section 3.2.3), breathhold-fMRI (see Section 3.2.4), mq-BOLD (see Section 3.3.1) and DTI (see Section 3.4.3) data. This also included typical pre-processing tasks, such as motion correction. Furthermore, tissue segments were derived from MP-RAGE (see Section 3.4.1) and lesions were segmented from FLAIR (see Section 3.4.2). The resulting parameter maps of each MRI sequence were saved for every participants. However, parameter maps of different sequences were saved in separate, independent, non-uniform folder structures. In general, orientations and spatial resolutions of the parameter maps differed as a consequence of individual MR-sequence settings. Moreover, the data was saved in the individual subject's space, depending on the respective field-of-view (FOV) planing during acquisition.

### 5.1.2 Data Base Management

In the second step, a uniform data base structure was automatically generated, as illustrated in Figure 5.1B and described in the following. Namely, the processed data of the individual

MRI methods (see Section 5.1.1) was scanned and relevant parameter maps copied during data selection and retrieval. The copied data was structured in a new unified data base in the clustering process. For example, acquisitions of different ASL sequences in the same participant were detected and grouped accordingly within the data base. The structure and naming of the new data base was set according to the standardized brain imaging data structure (BIDS) [185]. Artefact related outlier information, based on previous readings of experienced researchers in consensus, were automatically recognised and excluded from further evaluations. Parameter maps resulting from different MRI techniques with varying orientations and spatial resolutions were normalised to MNI-space during classification and generalization. Furthermore, coregistrations were performed to different target spaces, depending on the particular application. And to integrate newly acquired or re-processed imaging data to the existing data base structure, an incremental update function was implemented.

### 5.1.3 Multi-Parametric Group Level Evaluations

In the third step, multi-parametric group level evaluations were performed based on the unified data base structure (see Section 5.1.2), as illustrated in Figure 5.1C. Different kinds of correlations between the parameters were investigated, which are described in Section 5.2.

## 5.2 Applications in Journal Publications

The specific applications of the data base for the embedded journal publications JP-I, JP-II, JP-III and JP-IV are introduced in Sections 5.2.1, 5.2.2, 5.2.3 and 5.2.4 and for the related publications J3 and J4 in Sections 5.2.5 and 5.2.6, respectively, as illustrated in Figure 5.1C.

### 5.2.1 Database Application in JP-I

Specifically, JP-I required analysis of DSC (see Section 3.2.1) and ss-ASL data (see Section 3.2.3). Semi-automated segmentations were applied to TTP maps in the individual subject space. For validation purposes, perfusion territories from ss-ASL were additionally investigated and therefore coregistered to the DSC data. For comparisons on group level, the segmented masks were normalised to MNI space. By averaging the segmented and MNI-normalised masks, probability maps were calculated on group level.

### 5.2.2 Database Application in JP-II

Evaluations of JP-II required joint post-processing of DTI (see Section 3.4.3), MP-RAGE (see Section 3.4.1) and mq-BOLD data (see Section 3.3.1). Orientation information of each WM voxel was calculated from DTI and correlated with oxygenation information from mq-BOLD. Based on DTI data, main fiber orientation vectors  $\mathbf{V}_1$  were calculated (see Section 3.4.3). To assess orientation effects between the main fiber orientation  $\mathbf{V}_1$  and the main magnetic field  $\mathbf{B}_0$ , the rotation matrix depending on specific DTI FOV angulation was automatically extracted for each subject from the image data header. Thereby,  $\mathbf{V}_1$  was transformed from the DTI FOV coordinate system to the scanner coordinate system. Furthermore, the Cartesian coordinates of  $\mathbf{V}_1$  were transformed to spherical coordinates for each voxel. Orientation effects were only expected relative to  $\mathbf{B}_0$  (see Section 2.1.6), described by the polar angle, and not in the the plane perpendicular to  $\mathbf{B}_0$ , described by the azimuthal angle. To specifically select WM voxels, MP-RAGE was coregistered to DTI and segmented with subsequent thresholding

to yield WM masks. Additionally, voxels with a preferential orientation were selected based on thresholded FA maps from DTI. The mq-BOLD parameters  $T_2$ ,  $T_2^*$ ,  $R_2'$  and rOEF were coregistered to the DTI-data for each participant. For group-level evaluations, mq-BOLD parameters were correlated with fiber orientations within the oriented WM voxels.

### 5.2.3 Database Application in JP-III

In JP-III, multi-parametric information of six hemodynamic biomarkers was evaluated and the segmented masks from JP-I applied. Imaging data from pCASL (see Section 3.2.2), breath-hold fMRI (see Section 3.2.4), mq-BOLD (see Section 3.3.1) and parametric DSC modelling (see Section 3.2.1) were processed to calculate parameter maps of CBF, CVR, rCBV, rOEF, OEC and CTH in the individual subject space. The parameter maps were coregistered to the DSC data, each, for application of segmented masks based on TTP maps. In group level evaluations, average parameter values inside and outside of the segmented masks were separately calculated within GM and WM, based on segments from MP-RAGE (see Section 3.4.1). Furthermore, parameter lateralization between the hemispheres was compared.

### 5.2.4 Database Application in JP-IV

In JP-IV, mq-BOLD implementations (see Section 3.3.1) with different  $T_2$  mapping sequences were compared. The formerly applied 2D GraSE and two proposed 3D GraSE sequences (see Section 2.3.4) with optimized timings were applied and quantitative  $T_2$  maps calculated. With additionally acquired GRE as well as DSC data and based on the mq-BOLD model, maps of  $R_2'$  and rOEF were calculated for each GraSE sequence, respectively. Parameter maps of each participant were coregistered and compared for the different GraSE implementations, while applying GM masks based on MP-RAGE (see Section 3.4.1). To compare the locations of focal rOEF increases with perfusion territories, ss-ASL was applied (see Section 3.2.3). Furthermore, multiple single-echo spin echo acquisitions with varying echo times (see Section 2.3.1) were used as references in phantom scans to validate and compare the  $T_2$  maps from GraSE sequences.

### 5.2.5 Database Application in J3

In journal publication J3, the ICAS-related perfusion lateralization between hemispheres was correlated with cognitive impairments. CBF maps were calculated from pCASL (see Section 3.2.2), GM masks yielded from MP-RAGE (see Section 3.4.1) and lesions segmented based on FLAIR images (see Section 3.4.2). The resulting parameter maps were MNI normalized. On group level, CBF lateralization was correlated with hemispherical differences of visual attention deficits, based on separately conducted sophisticated psychological testings.

### 5.2.6 Database Application in J4

In journal publication J4, the oxygen metabolism was investigated. CBF maps were calculated from pCASL (see Section 3.2.2), rOEF maps by mq-BOLD (see Section 3.3.1) and GM masks from MP-RAGE (see Section 3.4.1). All parameter maps were MNI normalized. For group level evaluations, first, MRI-based CBF values were validated with available reference PET-based perfusion data (see Section 3.1.2) in two comparable cohorts of young healthy participants. Second, relative CMRO<sub>2</sub> maps were calculated from CBF and rOEF (see equation 3.3) to investigate ICAS-related inter-hemispheric flow-metabolism uncoupling (see Section 3.1.3).

## **6 Compliance with Ethical Standards**

All investigations performed in studies involving human participants were in accordance with the ethical standards of the institutional and/or national research committee and with the 1964 Helsinki declaration and its later amendments or comparable ethical standards. Informed consent was obtained from all individual participants included in the studies.





## 7 Journal Publications

This chapter includes four journal publications in Sections 7.1, 7.2, 7.3 and 7.4. Each publication is introduced, the respective copyright noted, the content summarised including a list of the author contributions and the full texts are embedded.

### 7.1 Journal Publication I: Increased variability of watershed areas in patients with high-grade carotid stenosis

The publication entitled *Increased variability of watershed areas in patients with high-grade carotid stenosis* was published in *Neuroradiology* (ISSN: 0028-3940) on 3 January 2018 [186]. The manuscript was authored by Stephan Kaczmarz, Vanessa Griese, Christine Preibisch, Michael Kallmayer, Michael Helle, Isabel Wustrow, Esben Thade Petersen, Hans-Henning Eckstein, Claus Zimmer, Christian Sorg, and Jens Goettler. It is available online (DOI: 10.1007/s00234-017-1970-4) under Copyright © by Springer-Verlag GmbH Germany. Preliminary results were also presented in the conference contribution C46, which was awarded with an ISMRM Magna Cum Laude Merit Award and invited for oral presentation at the ISMRM annual meeting 2017. A summary of the publication is provided in Section 7.1.1, the author contributions are listed in Section 7.1.2 and the full text is included subsequently on the following pages.

#### 7.1.1 Abstract

##### Purpose

Carotid artery stenosis is a major public health issue and can cause severe hemodynamic impairments. To increase the sensitivity to those impairments, detection of critically affected brain regions is of high clinical interest. In that regard, it is known that watershed areas (WSAs) of the brain are most susceptible to acute hypoperfusion due to their peripheral location between vascular territories. Despite of their high relevance for both research and clinical diagnostics, individual in vivo WSA definition is fairly limited to date. Thus, this study proposes a standardized semi-automated segmentation approach to delineate individual WSAs based on perfusion delay information from time-to-peak (TTP) maps and investigates the spatial variability of individual WSAs in ICAS patients in comparison with age-matched healthy controls.

##### Methods

MRI was performed on a clinical 3T scanner. We defined individual WSA (iWSA) masks based on relative TTP increases in 30 healthy elderly controls and 28 patients with unilateral, asymptomatic, high-grade carotid artery stenosis, being at risk for watershed area-related hemodynamic impairment. Determined iWSA locations of the healthy control group were

confirmed by an atlas from a published study based on time-encoded ASL [100]. For validation of iWSA locations in ICAS patients, perfusion territories were imaged with ss-ASL. We compared the spatial variability of iWSAs between groups and assessed TTP differences between hemispheres in individual and group-average watershed locations.

### **Results**

Patients showed significantly higher spatial variability of iWSA locations compared to healthy controls. Perfusion on the side of the stenosis was significantly delayed within iWSAs. This was independent from the grade of the stenosis and collateralization status of the circle of Willis. Contrary, application of a group-average WSA atlas was not sensitive to those perfusion impairments.

### **Conclusion**


Our results demonstrate the feasibility of individual delineation of iWSA masks based on TTP maps. We demonstrated the necessity of individual segmentation approaches to detect critical regions of impaired hemodynamics in patients with hemodynamic compromise, due to increased spatial variability of iWSA locations. Thus, individual WSA segmentation is highly promising to improve the sensitivity to hemodynamic impairments in cerebrovascular diseases. To probe this potential, future application to multi-parametric hemodynamic imaging is highly recommended.

#### **7.1.2 Author contributions**

The first author adapted the magnetic resonance pulse sequence (proprietary hardware specific libraries and software from Philips Medical Systems (Best, The Netherlands)), developed and implemented the processing pipeline, processed the data, developed and implemented the database to interpret the multi-parametric data using Matlab (Mathworks, Natick, MA); With the help and consultation from the coauthors: the first author designed the experiment, performed the experiments (MR measurements), segmented the data, interpreted the results, and wrote the paper.



## Increased variability of watershed areas in patients with high-grade carotid stenosis

Stephan Kaczmarz<sup>1,2</sup> · Vanessa Griese<sup>1,2</sup> · Christine Preibisch<sup>1,3</sup> · Michael Kallmayer<sup>4</sup> · Michael Helle<sup>5</sup> · Isabel Wustrow<sup>6</sup> · Esben Thade Petersen<sup>7,8</sup> · Hans-Henning Eckstein<sup>4</sup> · Claus Zimmer<sup>1</sup> · Christian Sorg<sup>1,2</sup> · Jens Göttler<sup>1,2</sup> 

Received: 5 September 2017 / Accepted: 19 December 2017 / Published online: 3 January 2018  
© Springer-Verlag GmbH Germany, part of Springer Nature 2018

### Abstract

**Purpose** Watershed areas (WSAs) of the brain are most susceptible to acute hypoperfusion due to their peripheral location between vascular territories. Additionally, chronic WSA-related vascular processes underlie cognitive decline especially in patients with cerebral hemodynamic compromise. Despite of high relevance for both clinical diagnostics and research, individual in vivo WSA definition is fairly limited to date. Thus, this study proposes a standardized segmentation approach to delineate individual WSAs by use of time-to-peak (TTP) maps and investigates spatial variability of individual WSAs.

**Methods** We defined individual watershed masks based on relative TTP increases in 30 healthy elderly persons and 28 patients with unilateral, high-grade carotid stenosis, being at risk for watershed-related hemodynamic impairment. Determined WSA location was confirmed by an arterial transit time atlas and individual super-selective arterial spin labeling. We compared spatial variability of WSA probability maps between groups and assessed TTP differences between hemispheres in individual and group-average watershed locations.

**Results** Patients showed significantly higher spatial variability of WSAs than healthy controls. Perfusion on the side of the stenosis was delayed within individual watershed masks as compared to a watershed template derived from controls, being independent from the grade of the stenosis and collateralization status of the circle of Willis.

**Conclusion** Results demonstrate feasibility of individual WSA delineation by TTP maps in healthy elderly and carotid stenosis patients. Data indicate necessity of individual segmentation approaches especially in patients with hemodynamic compromise to detect critical regions of impaired hemodynamics.

**Keywords** Carotid stenosis · Watershed area segmentation · Border zones · Time-to-peak · Super-selective arterial spin labeling

**Electronic supplementary material** The online version of this article (<https://doi.org/10.1007/s00234-017-1970-4>) contains supplementary material, which is available to authorized users.

✉ Jens Göttler  
jens.goettler@tum.de

<sup>1</sup> Department of Diagnostic and Interventional Neuroradiology, Klinikum rechts der Isar, Technische Universität München, Ismaninger Str. 22, 81675 Munich, Germany

<sup>2</sup> TUM Neuroimaging Center (TUM-NIC), Klinikum rechts der Isar, Technische Universität München, Munich, Germany

<sup>3</sup> Clinic for Neurology, Klinikum rechts der Isar, Technische Universität München, Munich, Germany

<sup>4</sup> Department of Vascular and Endovascular Surgery, Klinikum rechts der Isar, Technische Universität München, Munich, Germany

<sup>5</sup> Research Laboratories, Philips GmbH Innovative Technologies, Hamburg, Germany

<sup>6</sup> I. Medizinische Klinik und Poliklinik, Klinikum rechts der Isar, Technische Universität München, Munich, Germany

<sup>7</sup> Danish Research Centre for Magnetic Resonance, Centre for Functional and Diagnostic Imaging and Research, Copenhagen University Hospital Hvidovre, Copenhagen, Denmark

<sup>8</sup> Center for Magnetic Resonance, Department of Electrical Engineering, Technical University of Denmark, Kgs. Lyngby, Denmark

## Abbreviations

ATT	Arterial transit time
CoW	Circle of Willis
DSC	Dynamic susceptibility contrast
ICA	Internal carotid artery
ss-ASL	Super-selective arterial spin labeling
TTP	Time-to-peak
WSA	Watershed area
WSA <sub>H</sub>	Healthy controls' mean watershed template

## Introduction

Watershed areas (WSAs) of the brain are located along the border zones between the territories of major cerebral arteries, i.e., where most distal branches of these major arteries meet. WSAs are relevant for both clinical diagnostics and research. Specifically, WSAs are known to be most susceptible to reduced perfusion pressure as in high-grade carotid stenosis patients, accounting for approximately 10% of all ischemic strokes [1, 2]. Furthermore, chronic watershed-related vascular processes can lead to leukoaraiosis and silent microinfarcts, which contribute to cognitive decline and have shown to aggravate cognitive symptoms in Alzheimer's disease [3–5].

WSAs are located in the white matter along the ventricles and slightly above between the penetrating branches and the vascular territories of the anterior, middle, and posterior cerebral arteries (internal WSAs) and between the cortical territories of the major brain vessels (external WSAs) [1]. However, vascular territories and WSAs have variable spatial locations even in healthy people [6]. This variability might be even more pronounced under conditions of hemodynamic compromise as in patients with carotid steno-occlusive disease due to collateral flow and a resulting shift of perfusion territories [7–9].

Despite their high relevance for both clinical diagnostics and research, individual definition of WSAs remains challenging. Proposed in vivo methods are selective catheter angiography and arterial spin labeling (ASL)-based vascular territory mapping, such as super-selective arterial spin labeling (ss-ASL) that depict the downstream vascular territories by means of contrast agents and magnetically labeled blood, respectively [10, 11]. Another approach to identify WSAs takes advantage of delayed perfusion in WSAs due to their peripheral location at the edge of vascular territories. Based on this approach, ASL methods have shown to be able to delineate WSAs by measuring the increased arterial transit time (ATT) [12–14]. ASL is a non-invasive technique and does not require the application of contrast agent. However, it has a relatively low signal-to-noise ratio and does not yield reliable perfusion signal in deep white matter, where most of the volume of internal WSAs is located [15]. Furthermore, this

technique is highly susceptible to magnetic field inhomogeneities as for example caused by metal artifacts near the labeling plane at the neck resulting in a limited labeling efficiency in patients, e.g., after carotid stenting [16].

The current pilot study takes effort to overcome these limitations by suggesting a well-defined delineation of individual WSAs by an experienced operator using dynamic susceptibility contrast (DSC) based time-to-peak (TTP) maps [17], which can be calculated reliably and are very sensitive to perfusion delays in gray and white matter. They are therefore widely used for detection of cerebral malperfusion in acute stroke [18].

Here, we investigate the feasibility of a TTP-based WSA definition approach in healthy elderly and patients with unilateral, high-grade carotid artery stenosis, who are at high risk for WSA-related hemodynamic impairment. Location of determined WSAs was compared to an ASL-based ATT map from a previous study in 284 healthy young subjects, which can be regarded as a reasonable WSA reference atlas [14], and to individual vascular territory maps obtained by ss-ASL in patients [19]. Furthermore, we explored spatial variability of WSA location in both groups and analyzed TTP differences between hemispheres within individual WSAs and a standard watershed template to investigate the benefit of individual WSA definition.

## Material and methods

### Participants

Thirty healthy elderly (17 females, mean age  $70.3 \pm 4.8$  years) and 28 patients (9 females, mean age  $70.5 \pm 7.1$  years) with an asymptomatic, one-sided high-grade extracranial carotid artery stenosis (confirmed by duplex ultrasonography; all > 70% according to the NASCET criteria [20]) participated in this prospective study (Table 1). Patients were enrolled consecutively in the outpatient clinic for carotid stenoses of the Department of Vascular and Endovascular Surgery and Angiology of the Klinikum rechts der Isar, Technische Universität München, healthy participants by word-of-mouth advertisement from May 2015 until May 2017. Examination of every participant included medical history, basic neurological examination, and MRI. The study was approved by the medical ethical board of the Klinikum rechts der Isar, in line with Human Research Committee guidelines of Technische Universität München. All participants provided informed consent in accordance with the standard protocol approvals. Exclusion criteria for entry into the study were any neurological, psychiatric, or systemic diseases, clinically remarkable structural MRI (e.g., territorial stroke lesions, bleedings, or a history of brain surgery), visual impairments, severe chronic kidney disease, and MR contraindications.

**Table 1** Clinical characteristics

	Patients (n = 28)	Controls (n = 30)	p value
Age (years)	70.5 ± 7.1	70.3 ± 4.8	0.901
Female sex (no.) (%)	9 (32)	17 (57)	0.110
Stenotic degree (% NASCET criteria)	81.3 ± 10.3	–	
No. right-/left-sided stenosis	17/8	–	
No. right-/left-sided occlusions	1/2	–	
Anatomy of the circle of Willis			
Good collateralization (no.) (%)	17 (61)	18 (60)	0.956
Poor collateralization (no.) (%)	11 (39)	12 (40)	
Fazekas score of WMH (0–3°)	1.4 ± 0.9	1.0 ± 0.9	0.102
Smoking (no.) (%)	14 (50)	10 (33)	0.198
Mean pack-years in smokers	34.9 ± 21.9	21.1 ± 16.1	0.105
Hypertension (no.) (%)	22 (79)*	16 (53)*	0.043
Mean BP (mmHg, systolic/diastolic)	154 ± 23*/86 ± 10	140 ± 20*/84 ± 7	0.018/0.370
Body mass index	26.3 ± 4.8	26.6 ± 4.2	0.170
Diabetes (no.) (%)	8 (29)*	2 (7)*	0.027
Medication (no. of patients) (%)			
Antiplatelets	24 (86)*	6 (20)*	< 0.001
Statins	17 (61)*	7 (23)*	0.002
Antihypertensives	18 (64)*	12(40)*	0.034
CHD/PAOD (no.) (%)	16 (57)*	8 (27)*	< 0.001
MMSE	27.7 ± 2.8	28.6 ± 1.4	0.170
TMT-A (s)	50.9 ± 23.9	46.7 ± 29.7	0.699

Two-sample *t* test for age, Fazekas score, BP, body mass index, MMSE, and TMT-A. Chi-squared test for remaining group comparisons

BP blood pressure, WMH white matter hyperintensities, CHD coronary heart disease, PAOD peripheral artery occlusive disease, MMSE Mini-Mental State Examination, TMT-A Trail making test-A

\**p* ≤ 0.05, significant group differences

## Imaging data acquisition

Scanning was performed on a clinical 3-T Philips Ingenia MR-Scanner (Philips Healthcare, Best, The Netherlands) using a 16-channel head/neck-receive-coil. All participants underwent DSC and magnetization prepared rapid gradient echo (MP-RAGE) imaging. Furthermore, DWI and FLAIR sequences were conducted as a screening for ischemic brain lesions and to grade white matter hyperintensities by the Fazekas classification [21]. None of the participants had subacute or older territorial infarct lesions. Additionally, a contrast-enhanced angiography of the neck and the aortic arch vessels was performed. None of the healthy elderly showed relevant stenoses of the brain supplying arteries according to MRA. Additionally, five randomly chosen patients underwent an ss-ASL sequence with selective labeling of the left and right internal carotid artery (ICA).

The MR imaging parameters were as follows:

*DSC data* was obtained during a bolus injection of a weight-adjusted Gd-DOTA bolus (concentration, 0.5 mmol/ml; dose, 0.1 mmol/kg, at least 7.5 mmol per subject; flow rate, 4 ml/s; injection, 7.5 s after DSC imaging

started) using single-shot GE-EPI, TR = 1513 ms, TE = 30 ms,  $\alpha = 60^\circ$ , 80 repetitions, FOV 224 × 224 × 100 mm<sup>3</sup>, voxel size 2 × 2 × 3.5 mm<sup>3</sup>, and 26 slices

*MP-RAGE*: TI = 1000 ms, TR = 2300 ms, TE = 4 ms,  $\alpha = 9^\circ$ ; 170 slices covering the whole brain; FOV 240 × 240 × 170 mm<sup>3</sup>; voxel size 1.0 × 1.0 × 1.0 mm<sup>3</sup>

*ss-ASL* according to [10]: Planning of left and right ICA-labeling in the carotid stenosis patients was based on TOF angiography. ss-ASL with segmented 3D-GraSE readout, TR = 4403 ms, TE = 7.4 ms,  $\alpha = 90^\circ$ , FOV 220 × 220 × 104 mm<sup>3</sup>, voxel size 2.7 × 2.7 × 6 mm<sup>3</sup>, label duration 1800 ms, post-label delay 2000 ms, background suppression, 1 pair of label and control images (parameters according to the recommendations of the ISMRM perfusion study group [22])

## Data preprocessing

All processing procedures used MATLAB R2014a (MathWorks, Natick, MA, USA), Vinci (MPI for Neurological

Research, Cologne, Germany), and SPM12 (Wellcome Trust Centre for Neuroimaging, UCL, London, UK).

### TTP maps

DSC data was processed by a MATLAB-based software developed at our institution as described previously [23]. Accordingly, DSC data was filtered using a 3D Gaussian spatiotemporal filter-kernel of 3-mm Full Width at Half Maximum (FWHM) with time as the third dimension. Using SPM12 with default parameters, slice-timing correction was performed to account for temporal acquisition delays between neighboring slices due to interleaved slice acquisition order. The global bolus arrival time was automatically determined from the average signal of all brain voxels. TTP was then calculated as the interval between global bolus arrival time and each voxel's peak signal loss. Individual MP-RAGE images were spatially co-registered to the DSC data. TTP maps were smoothed using an isotropic Gaussian kernel of 6-mm FWHM.

### ss-ASL maps

Perfusion-weighted images of the left and right ICA-territory were calculated by custom MATLAB programs using SPM12. Label and control images were motion corrected, averaged, subtracted, and normalized by a PDw image following [22]. Resulting images were smoothed with an isotropic Gaussian kernel of 6-mm FWHM.

## Data analysis

### Definition of individual watershed areas

An overview of applied imaging sequences and the processing pipeline is given in Fig. 1. Each participant's TTP map was thresholded at the 90th percentile of the whole brain histogram using the contour and threshold tool of Vinci (Fig. 2, column 2) resulting in a raw watershed mask. This initial watershed mask was further manually modified according to the following segmentation guideline: (1) exclusion of brain regions outside the frontal lobe, occipital lobe, parietal lobe, and the temporo-parietal junction from the watershed area segmentation procedure to avoid influence of susceptibility artifacts in the DSC sequence; (2) adjust watershed masks to achieve a similar volume for each side (width: approx. 1 cm); (3) anterior circulation: in subjects with asymmetrically increased TTP in the anterior circulation, application of different TTP windows for each hemisphere to obtain an appropriate contrast for all watershed and non-watershed regions (Fig. 3), anterior watershed areas: connecting peak TTP values in the anterior frontal cortex and adjacent white matter along the ventricles and slightly above with the initial mask (Fig. 2,

arrow 1), application of different TTP windows to identify local TTP increases if necessary; (4) removal of regions from the initial mask that overlap with the dural venous sinuses or superficial/deep veins (Fig. 2, arrow 2); (5) removal of areas with increased TTP values in the ventricular system (Fig. 2, arrow 3); and (6) posterior watershed regions: adjustment of TTP windows to generally increased TTP in posterior circulation to be able to identify TTP increases in typical watershed areas, i.e., between the posterior parts of the lateral ventricles to the occipital cortex and temporo-parietal junction. Removal of segmented areas from the initial watershed mask that do not overlap with peak TTP increases in the posterior circulation (Fig. 2, arrow 4).

### Inter-rater reliability study

This procedure was conducted by two operators (J.G. and S.K., both with 3 years of experience in cerebrovascular research; WSAs of J.G. were used for all further analyses). Inter-rater reliability was assessed according to [24]. The consistency of WSA volumes between the two operators was measured by the intra-class correlation coefficient (ICC) using SPSS (SPSS Inc., Chicago, IL, version 24.0). The ICC variant that measured absolute agreement under a two-way random analysis of variance model was used. Spatial overlap of the corresponding watershed masks was calculated by the Jaccard index ( $JI(A, B) = \frac{A \cap B}{A \cup B}$ , with  $A$  and  $B$  being the watershed masks segmented by operators 1 and 2, respectively) using MATLAB. The JI reaches from 0 (no overlap) to 1 (complete congruence).

### Probability masks of watershed areas

All individual masks were normalized to Montreal Neurological Institute (MNI) space using SPM12. Voxel-wise probability as well as standard deviation maps were calculated for each group. Probability maps represent each voxel's probability to be defined as a WSA across subjects and standard deviation maps depict their inter-subject variability. The spatially normalized probability map of controls was thresholded at 0.75 to generate a standard WSA template ( $WSA_H$ ). The threshold was adjusted to match the  $WSA_H$  volume to the average volume of the controls' individual WSAs in MNI space ( $iWSA_{MNI}$ ). The average volume of healthy controls'  $iWSA_{MNI}$  was 11,422 voxels. By applying a threshold of 0.75 to the probability map, resulting  $WSA_H$  yielded a total of 11,779 voxels.

TTP differences ( $\Delta TTP$ ) between the unaffected vs. the affected hemisphere in patients and the left vs. right hemisphere in controls, respectively, were calculated within  $WSA_H$  and the individually defined WSAs in each subject in native space.



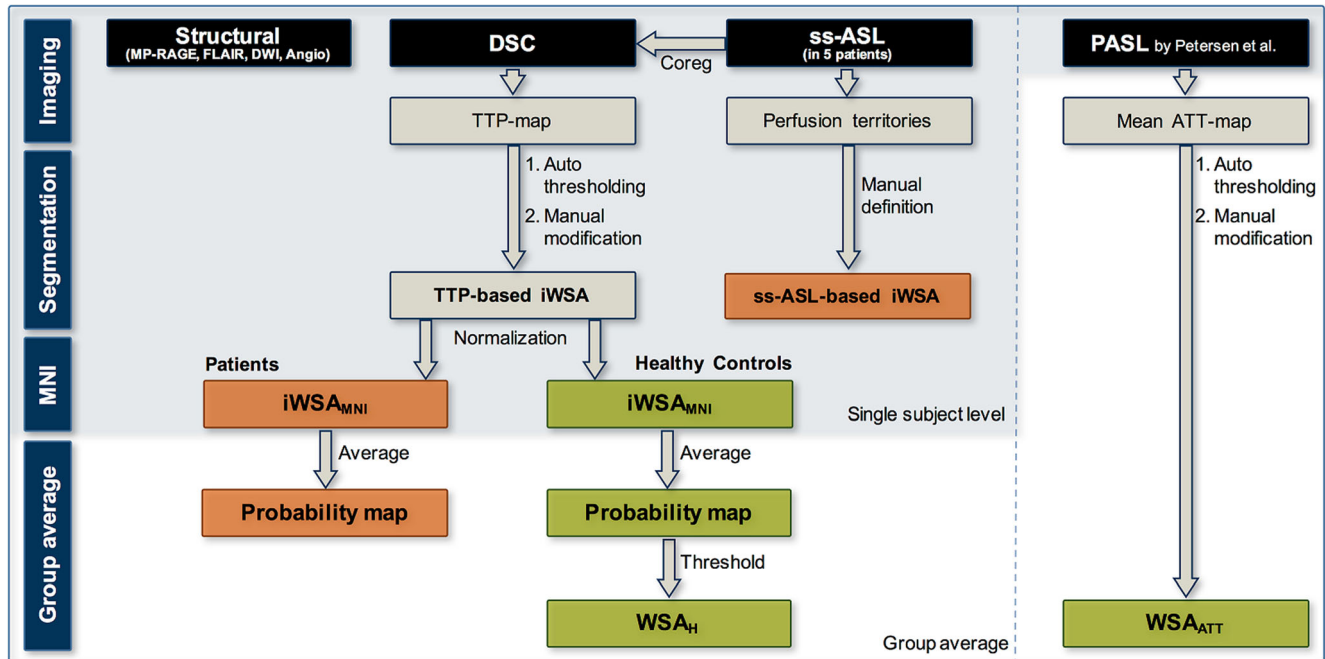


**Fig. 1** Overview of imaging sequences and processing pipeline. Acquired sequences are shown in the top row (black). Structural imaging comprised MP-RAGE, FLAIR, DWI, and contrast-enhanced angiography of the head and neck. Processing steps are noted next to the arrows indicating the workflow. The light-blue background indicates processing steps, which are performed on a single-subject level. DSC-derived TTP maps were segmented in two steps for each participant. A threshold was automatically applied at the 90th percentile of the TTP maps and followed by a manual modification, resulting in individual watershed masks (TTP-based iWSA). Those individual masks were separately normalized to MNI space ( $iWSA_{MNI}$ ) for patients

(orange) and healthy controls (green). On the group level, WSA probability maps were calculated for both groups. A group-average WSA was generated for healthy controls ( $WSA_H$ ). In five randomly chosen patients, ss-ASL was additionally acquired and co-registered to DSC. WSAs were manually segmented along the border zones between vascular territories (ss-ASL-based iWSA) and compared with corresponding TTP-based WSAs. Furthermore, we analyzed the mean of ATT maps acquired by PASL in 284 healthy controls from another study [14]. Based on this mean ATT map, we segmented a watershed mask ( $WSA_{ATT}$ ) according to our proposed watershed segmentation procedure and spatially compared it to the mean TTP-based watershed mask of our healthy controls

**Validation of WSA location**

To evaluate whether determined WSAs of healthy controls were reasonably located and in line with ASL-derived WSA definition methods, we compared our TTP-based watershed regions with the mean ATT template of the QUASAR reproducibility study by Petersen et al., which was created from 284 healthy volunteers (mean age  $33.7 \pm 8.9$  years; 120 females) [14]. We segmented WSAs in the ATT atlas according to our proposed method applying the 90th percentile followed by manual modification according to the mentioned guideline (Fig. 4). The mean TTP map of healthy controls was thresholded at the 90th percentile. We spatially compared resulting watershed masks by the JI.

Furthermore, we investigated whether individual WSAs of patients were located within border zones as indicated by ss-ASL, i.e., where two different vascular territories meet [25]. Due to restricted availability, ss-ASL could only be conducted in five randomly chosen patients. To verify that individual WSAs defined by TTP were correctly located in those patients, we spatially

compared them with the segmented border zones based on ss-ASL. Segmentation of border zones based on ss-ASL was conducted by J.G. using Vinci in five meeting left and right ICA territories and seven meeting ICA and posterior circulation territories (in three cases, the ICA supplied the complete posterior supratentorial hemisphere), resulting in 12 watershed masks (Fig. 5). To test for spatial similarity of those twelve ss-ASL-derived border zones and corresponding TTP-based WSAs, we calculated the JI.

**Evaluation of the collateralization of the circle of Willis and Fazekas score**

Collateralization status was rated according to the anatomy of the circle of Willis (CoW) by J.G. and V.G. in consensus. Good collateral flow was defined as a complete CoW, i.e., patent anterior communicating artery and both posterior communicating arteries. Poor collateral flow was defined as an incomplete CoW, i.e., at least one atretic anterior or posterior communicating artery. The same raters also evaluated white

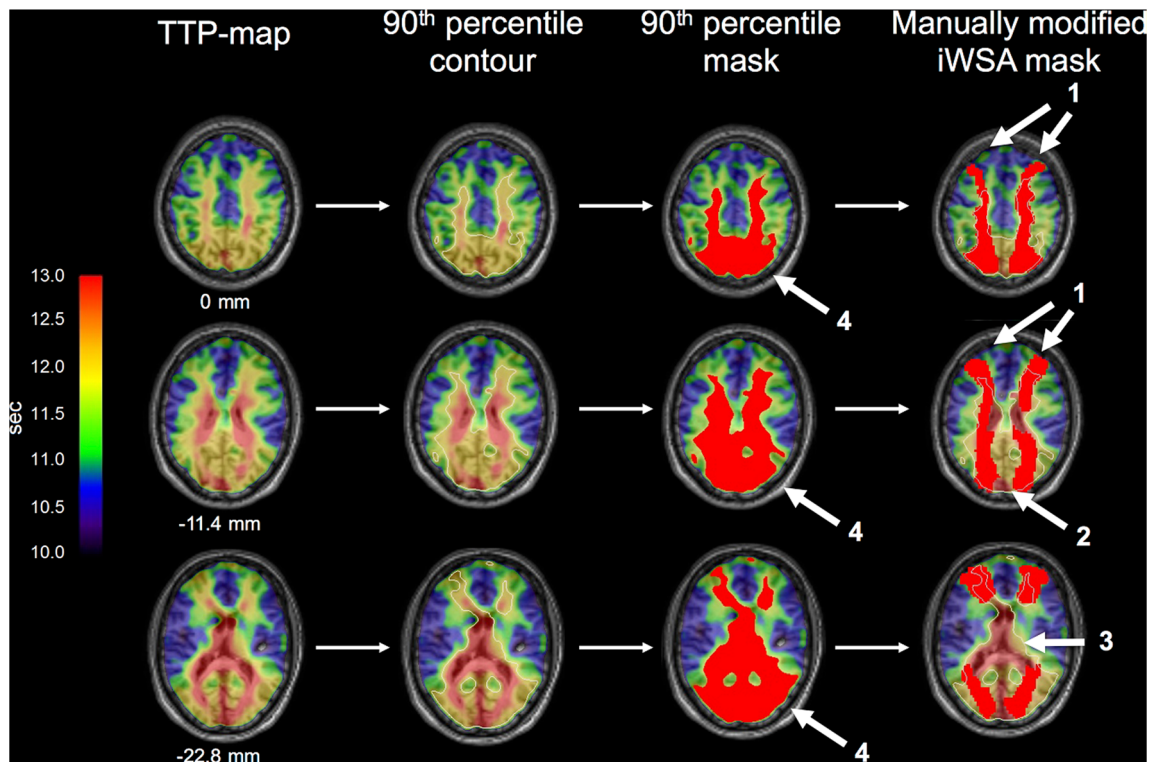


**Fig. 2** Procedure scheme of watershed area segmentation by TTP maps in healthy elderly. *Column 1*: TTP-map overlaid on a MP-RAGE image of a healthy participant. High TTP is depicted in red, low TTP in blue (colorbar). *Columns 2 and 3*: Contouring of the 90th percentile of the whole brain histogram (white line) and masking of all voxels above this threshold (red). *Column 4*: Manual modification of the initial mask in order to include external/cortical watershed zones (arrows 1) and to

exclude venous blood sinuses/vessels (arrow 2) as well as the ventricular system and choroid plexus (arrow 3). Note that the posterior circulation exhibits generally increased TTP values, resulting in large segmented areas in initial watershed mask (arrow 4). Therefore, segmented areas of the initial watershed mask that do not overlap with peak TTP increases in the posterior circulation have to be removed manually

matter hyperintensity load by the Fazekas score using FLAIR imaging in each subject [21].

### Statistics

Subject characteristics were compared between groups by two-sample *t* tests and chi-squared tests where applicable. Two-sample *t* tests were applied to compare TTP values in individual WSA and WSA<sub>H</sub> between patients and controls and in individual WSAs between patients with good/poor collateralization and male/female patients. Grade of the stenosis and age were associated with TTP values in individual WSAs by Pearson correlation. A *p* value  $\leq 0.05$  was considered statistically significant. SPSS was used for statistical analyses.

### Results

TTP maps in healthy subjects could be reliably segmented in fronto-parieto-occipital regions resulting in individual WSAs. All individual TTP-based watershed masks of healthy subjects are depicted in the Online Resource 1.

To test inter-rater reliability of the WSA segmentation approach in two operators, we compared the consistency of the absolute WSA volume (estimated by the ICC) and the overlap of watershed masks (calculated by the JI). The overall ICC of segmented WSA volumes was 0.86. ICC was slightly lower in patients (ICC = 0.82) compared to the controls (ICC = 0.89). The overall mean JI was  $0.75 \pm 0.11$ , again marginally lower in patients (JI =  $0.71 \pm 0.13$ ) as compared to controls (JI =  $0.78 \pm 0.07$ ). These results demonstrate good inter-rater agreement and support the reliability of the proposed WSA segmentation approach.

We compared the spatial congruency of WSAs based on our TTP-based approach and the mean ATT template of the QUASAR study (Fig. 4) [14]. Overlapping WSA maps yielded a JI of 0.44, suggesting a similar spatial extent and reasonable overlap of WSAs derived by both definition methods.

Twenty-two out of 28 patients (approx. 79%) exhibited large brain areas of asymmetrically increased TTP values distal to the stenosis (Fig. 3). Of those, a larger portion of the affected hemisphere lay within the initial 90th percentile mask, resulting in a considerable asymmetry between hemispheres (Fig. 3). However, WSAs could still be defined



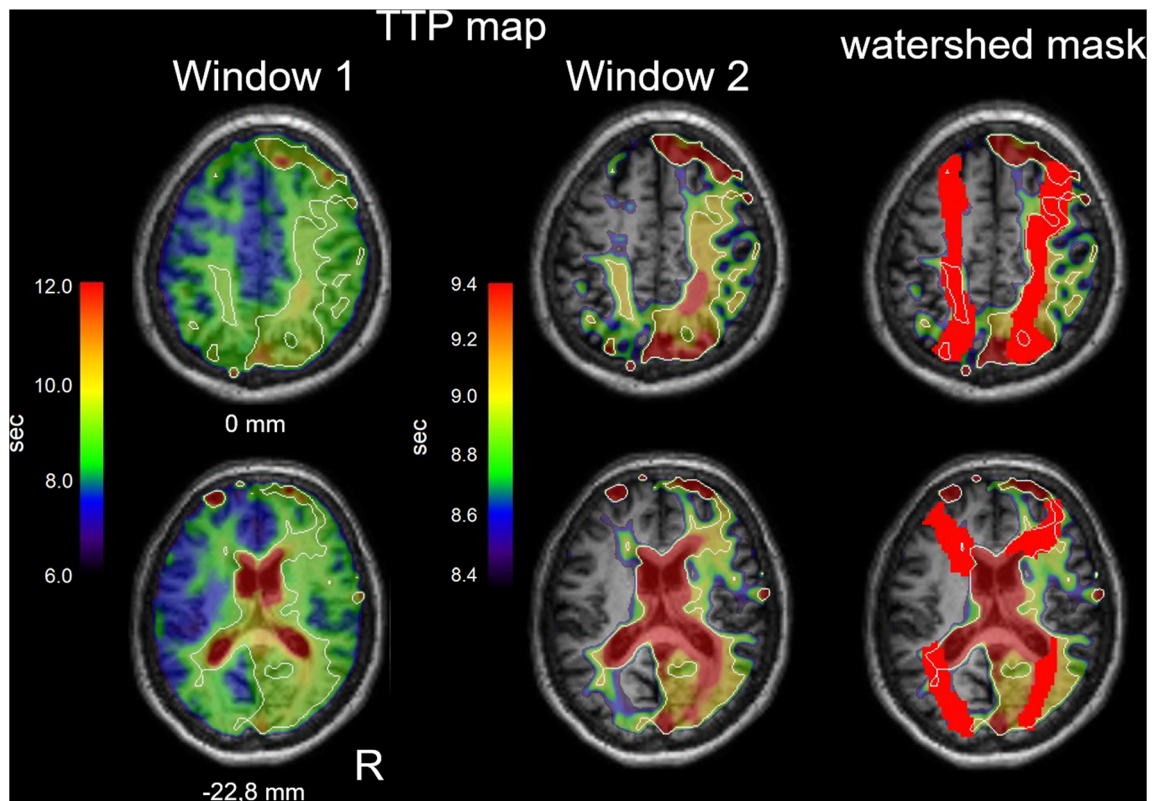


**Fig. 3** Watershed area definition by TTP maps in a patient with high-grade carotid stenosis. *Columns 1 and 2:* TTP-map with 90th percentile segmentation (white line) projected onto a MP-RAGE image of a patient with right-sided carotid stenosis at different TTP windows. This was done

to visualize relative TTP increases within the large right-sided 90th percentile in order to segment WSAs. High TTP is depicted in red, low TTP in blue (respective colorbar). *Column 3:* Additional overlay of resulting watershed mask (red) after manual correction

along peak TTP values of the affected and unaffected hemispheres, respectively, by using different TTP windows (Fig. 3, columns 1 and 2).

Furthermore, we spatially compared individual WSAs defined by TTP with the segmented border zones based on ss-ASL in five patients. Mean JI was  $0.64 \pm 0.05$  across all five patients (Fig. 5), suggesting that TTP-based and ss-ASL-based watershed masks show good spatial correspondence. The mean JI was  $0.67 \pm 0.04$  for the anterior WSAs and  $0.62 \pm 0.05$  for the posterior WSA (two-sample *t* test:  $p = 0.104$ ), indicating that accuracy of WSA definition did not significantly differ between anterior and posterior watershed regions.

To estimate spatial variability of WSAs in both groups, we compared their respective maps of spatial probability and standard deviation (Fig. 6). In patients, WSAs showed higher spatial variability as indicated by lower probability values and higher standard deviation values as compared to controls (Fig. 6).

To further support the benefit of individualized segmentation of WSAs, we compared TTP values of the affected and unaffected hemispheres in individual watershed masks and the healthy controls' standard template WSA<sub>H</sub>. In both groups,

variances of  $\Delta$ TTP values were lower in individual WSAs as compared to WSA<sub>H</sub> (Fig. 7). Patients showed significantly increased TTP values in the hemisphere ipsilateral to the stenosis only in individual watershed masks (mean  $\Delta$ TTP = 0.50 s, one-sample *t* test:  $p < 0.001$ ) being significantly different from  $\Delta$ TTP within WSA<sub>H</sub> (two-sample *t* test:  $p = 0.010$ ; Fig. 7). Mean  $\Delta$ TTP of controls did not differ between individual WSAs and WSA<sub>H</sub>.

White matter hyperintensity burden estimated by the Fazekas score did not differ significantly between groups (Table 1). Grade of the stenosis ( $r = 0.275$ ,  $p = 0.166$ ) and collateralization status of the CoW (good/poor collateralization:  $n = 17/11$ ; two-sample *t* test:  $p = 0.455$ ) were not significantly associated with  $\Delta$ TTP values in individual WSAs in patients. Furthermore, no effects on  $\Delta$ TTP in patients' individual WSAs were observed for age ( $r = 0.016$ ,  $p = 0.937$ ) and sex (two-sample *t* test:  $p = 0.255$ ).

## Discussion

The aim of this study was to investigate the TTP-based individual WSA delineation and variability in healthy controls

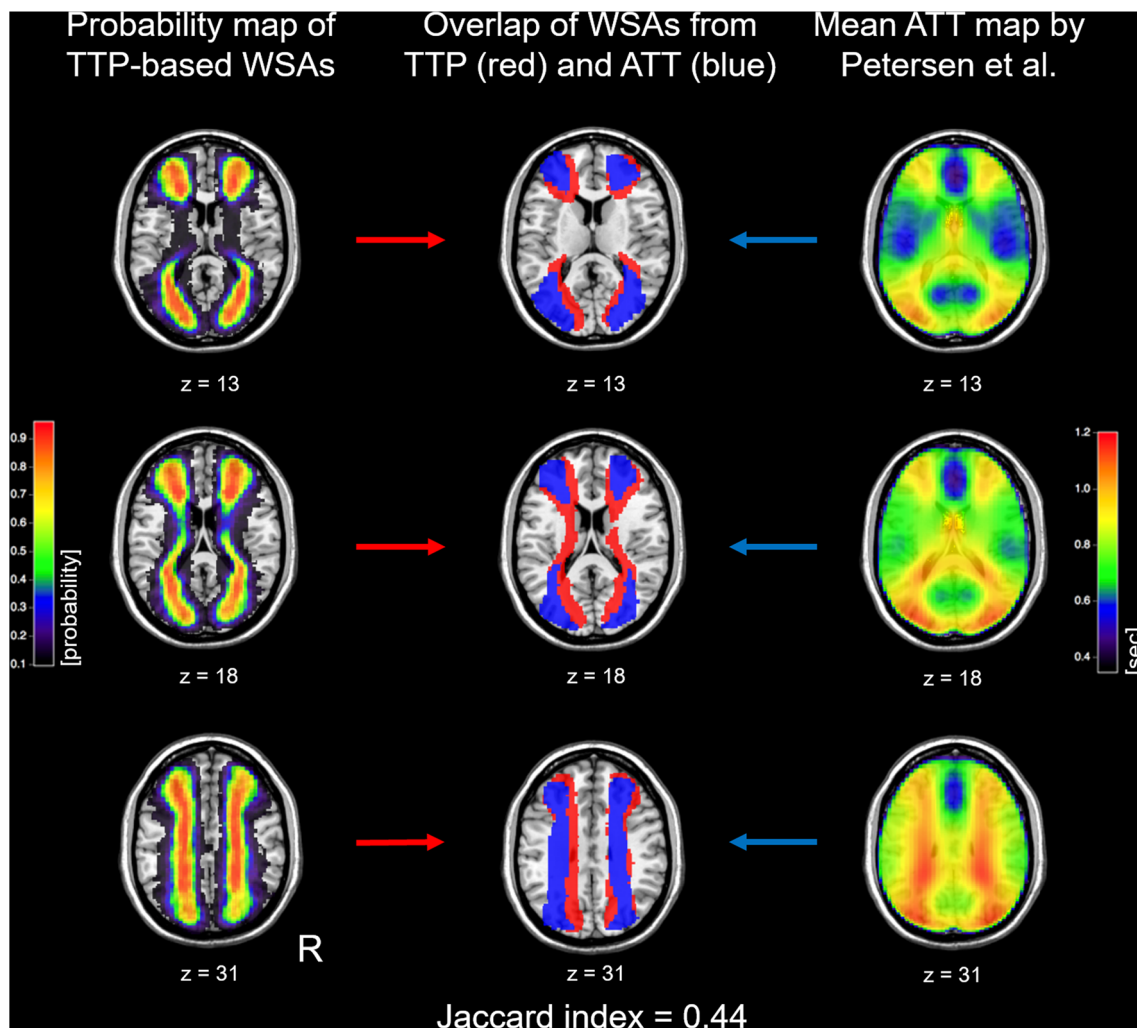


**Fig. 4** Comparison of TTP-based watershed masks and ASL-derived ATT maps in healthy participants. Comparison of probability maps of individual TTP-based watershed masks of healthy controls (left) and a mean ATT map of a publication by Petersen et al. [14] created from 284 healthy young subjects (right). High voxelwise probability of watershed masks location/mean ATT is depicted in red, low probability/ATT in blue

(left/right colorbar). Watershed masks derived from TTP (red) and ATT (blue) were segmented according to our proposed procedure and overlapped (middle). Note spatial similarity of watershed masks of both modalities in most corresponding brain regions yielding a Jaccard index of 0.44. All normalized maps are projected onto a T1-weighted image in MNI space

and patients with high-grade carotid stenosis. WSA segmentation based on the proposed guideline was feasible and showed good inter-rater agreement. In controls, correct localization of internal and external WSAs was confirmed by comparison with an ATT template of a previously published study [14]. In patients, WSA delineation needed more manual modification of the initial mask as compared to healthy controls. Resulting watershed masks were correctly located as confirmed by ss-ASL in a subgroup and showed higher spatial variability. TTP increases ipsilateral to the stenosis were specific for individual watershed masks (in contrast to the averaged watershed mask of controls) and independent from the grade of the stenosis, collateralization status of the CoW, age, and sex. Taken together, these results indicate that our WSA segmentation approach based on TTP maps facilitates reliable

mapping of variable WSAs in healthy elderly and hemodynamically compromised patients.

Based on the assumption that perfusion is slightly delayed in WSAs, we segmented individual WSAs along relatively increased TTP values in healthy elderly. We chose TTP instead of mean transit time (MTT) maps due to a higher contrast between WSA and non-WSA areas. Moreover, this simple measure is less sensitive to noise-compared to MTT which is derived via singular value decomposition. To validate our TTP-based approach, we compared controls' mean WSAs to the mean WSAs from an ASL-based mean ATT map from a previous publication (Fig. 4) [14]. WSAs based on both methods had a similar spatial extent and location ( $JI = 0.44$ ), even though the subjects in the study of Petersen et al. were much younger

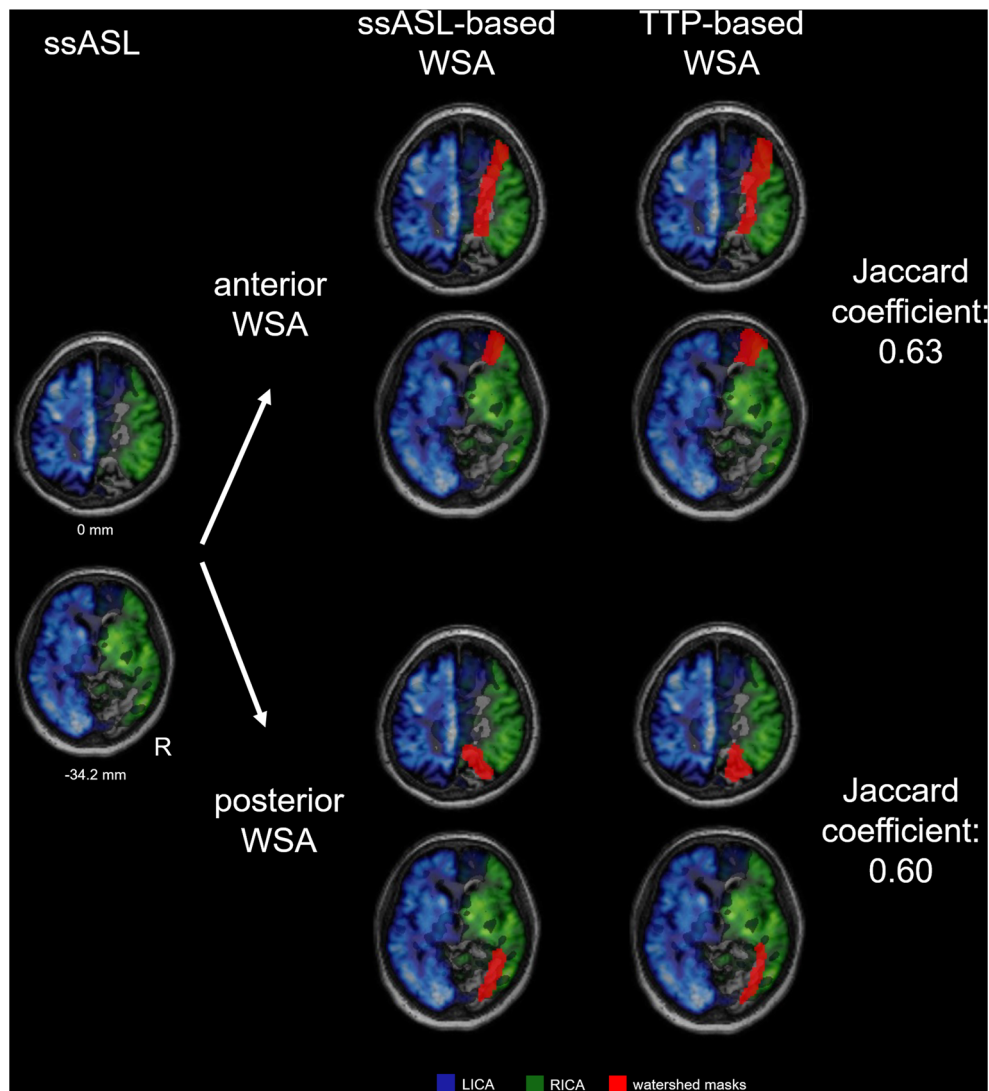


**Fig. 5** Spatial correspondence of TTP-based watershed masks and ss-ASL-derived border zones in a patient. *Left column:* ss-ASL maps of labeled left and right internal carotid artery (LICA territory in blue and RICA territory in green) in a patient with right-sided carotid artery stenosis. Here, the LICA supplies parts of the anterior cerebral artery territory on the right side resulting in a cleft between the perfusion signal of the LICA and RICA, most likely coinciding with the anterior WSA. The posterior circulation was not labeled. Maps are projected onto an individual MP-RAGE image in native space. *Middle and right*

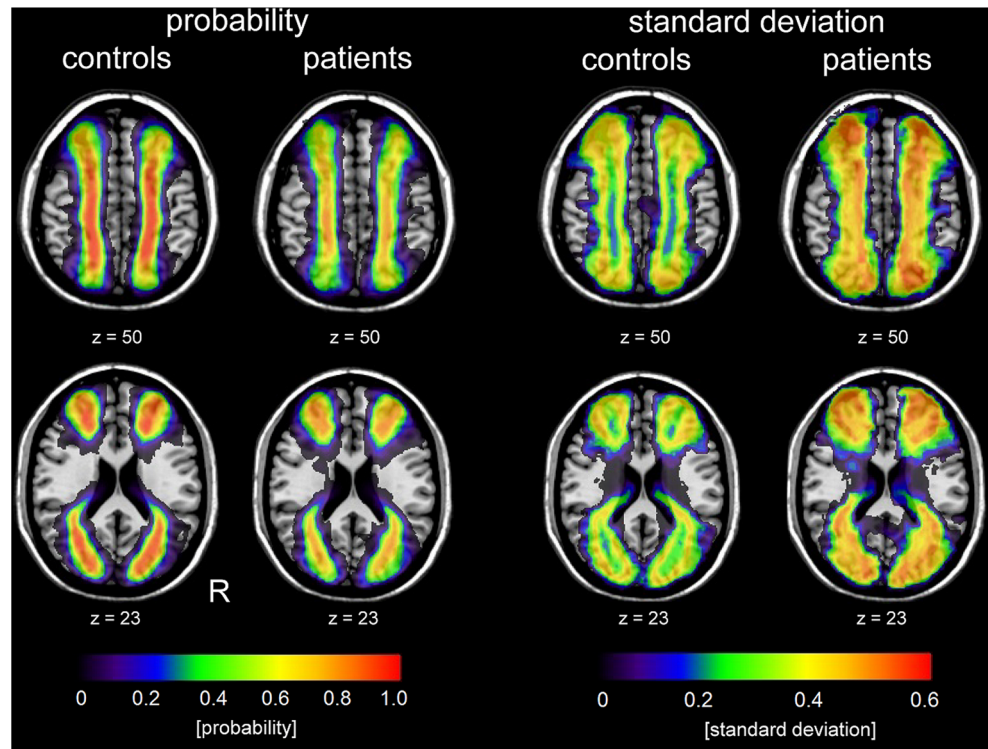
*column:* Manual segmentation of the anterior WSAs (i.e., between the left and right anterior circulation) and posterior WSAs (i.e., between the right anterior and posterior circulation) based on ss-ASL maps and TTP maps. Both WSAs (red) are overlaid onto the perfusion territories (middle column: ss-ASL-based; right column: TTP-based). Note good correspondence of watershed masks derived from two different modalities along the border zones between the LICA and RICA territory (Jaccard index in this patient:  $JI = 0.63$ ) as well as between the RICA territory and posterior circulation ( $JI = 0.60$ )

(mean age 33.7 years as compared to 70.3 years in our cohort). This finding demonstrates that the ATT- and TTP-based approach yield similar WSAs in a larger group of healthy subjects. However, as current ASL techniques are known to exhibit a lower signal-to-noise ratio especially in white matter as compared to DSC, we hypothesize that watershed definition based on TTP maps from DSC should be more reliable in the individual subject. Therefore, our proposed procedure is a fair alternative to ATT maps derived by ASL with multiple post-label delays or time encoded ASL approaches. DSC is widely used in

clinical practice due to its robustness and ease of application. As opposed to ASL, it also enables reliable measures in deep white matter being crucial especially for the delineation of internal WSAs. A disadvantage of DSC is the administration of gadolinium-based contrast agent, which has been shown to deposit in the brain tissue after serial use even in subjects with normal renal function [26]. However, this is not the case when using macrocyclic agents as in our study [27, 28]. Therefore, we are confident that DSC-based WSA definition is well justifiable in hemodynamically impaired patients.



**Fig. 6** Increased variability of watershed areas in patients. *Left:* Probability maps of normalized individual TTP-based watershed masks across subjects of each group (see colorbar). Spatial patterns of the mean masks are similar for both groups, whereas controls show higher probability of watershed masks being located in core watershed regions. *Right:* Maps depict the standard deviation of normalized individual watershed masks across subjects of each group. Both groups show a wide spatial extent of individual masks with a higher variability in patients. Note that standard deviation is decreased in core watershed regions only in healthy controls. All maps are projected onto a normalized single-subject T1-weighted MP-RAGE image in the MNI space



WSA definition in patients with carotid stenosis was more challenging as 79% of them exhibited an asymmetric TTP increase in the hemisphere ipsilateral to the stenosis. To not include large parts of the ipsilateral hemisphere, which most likely do not coincide with WSAs, we focused on peak TTP increases being pronounced in core regions of WSAs and adjusted the initial masks accordingly. This procedure resulted in rather slim watershed masks of similar volume on each side (Fig. 3). As no comparable watershed atlases in hemodynamically compromised patients exist in the literature to date, we confirmed patients' watershed mask localizations by individual mapping of vascular territories using ss-ASL in a subgroup. In those, TTP-based watershed masks and border zones of two adjacent vascular territories defined by ss-ASL showed high spatial congruency with a mean JI of  $0.64 \pm 0.05$ . This supports reliability of our approach also in patients with hemodynamic compromise. However, vascular territory mapping approaches can only delineate WSAs that lie between different labeled territories. As labeling of the intracranial vessels is challenging, WSAs between the anterior and middle cerebral artery cannot be defined reliably (as, e.g., in the anterior left hemisphere in Fig. 5). Furthermore, if the ICA supplies the whole hemisphere, e.g., via a fetal posterior communicating artery, it is also not possible to delineate the posterior watershed region on this side (as in the posterior left hemisphere in Fig. 5). Therefore, perfusion delay-based WSA methods, such as TTP maps, might serve as more reliable tools for individual WSA definition as compared to vascular territory mapping approaches.

Our analysis revealed a higher spatial variability of WSAs in patients compared to age-matched healthy controls, supporting the need of individual WSA segmentation in hemodynamic compromise (Fig. 6). Variance of TTP differences between hemispheres was lower in individual WSAs as compared to the normalized standard watershed template of controls in both groups. Moreover, only in patients' individual watershed masks, TTP increases have been observed ipsilaterally to the stenosis when compared to the standard watershed template of controls indicating higher accuracy of individual WSA definition (Fig. 7). The grade of the stenosis and collateralization status of the CoW were not associated with increased lateralization of TTP values, implying that the anatomy of the stenosis and the CoW do not further contribute to hemodynamic compromise in these patients. Furthermore, we did not observe a relevant shift of the WSAs ipsilateral to the stenosis as a function of the anatomy of the CoW, e.g., we did not find an anterior shift of the posterior WSA in patients with a patent P1-segment and atretic PcomA on the side of the stenosis. Accordingly, it has been shown that a shift of vascular territories and recruitment of collateral flow in case of tight carotid stenosis or occlusion was not predictable by the anatomy of the CoW [25, 29]. These studies and our own data indicate that the individual segmentation of WSAs is crucial, especially in patients with stenoses of the brain supplying arteries, since their vascular supply situation does not really match standard WSA templates.

Localizing WSAs in hemodynamically compromised patients is especially important, since most severe hemodynamic changes, such as increased oxygen extraction fraction and

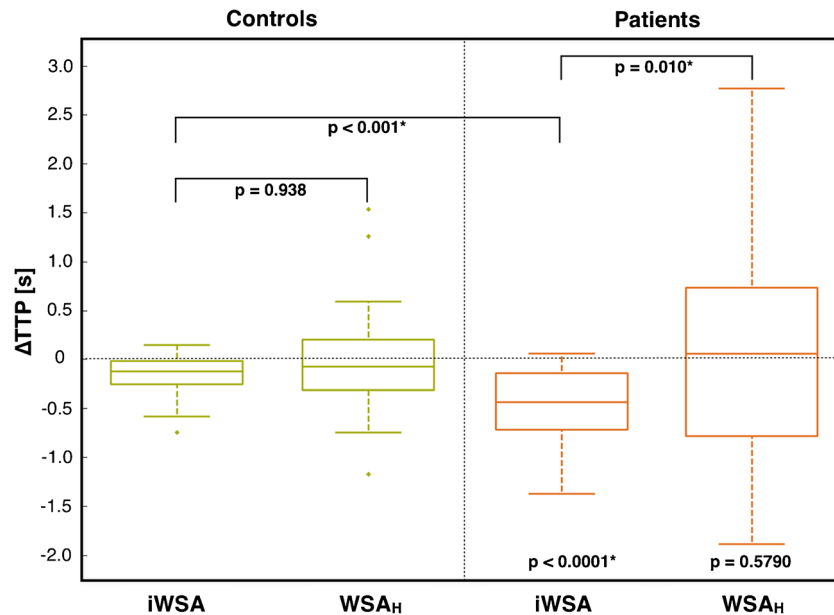


**Fig. 7** TTP increases only within individually defined WSAs of patients. Comparison of TTP differences ( $\Delta$ TTP) between the left vs. right hemisphere in healthy controls and the unaffected vs. affected hemispheres for patients, respectively, within individual watershed masks (iWSA) and controls' mean watershed template ( $WSA_H$ ). Variance of  $\Delta$ TTP was generally increased within  $WSA_H$  compared to iWSA (patients, 1.32 s vs. 0.15 s; controls, 0.85 s vs. 0.05 s; indicated by the range of boxplots). No differences of  $\Delta$ TTP have been found between healthy controls'  $WSA_H$  and iWSA (two-sample *t* test:  $p = 0.938$ ).

However, patients exhibit a significant lateralization with prolonged TTP ipsilaterally to the stenosis only in the iWSA (two-sample *t* test:  $p = 0.010$ ). Results suggest that individual watershed segmentation is necessary to account for individual spatial variability of WSAs and to detect a lateralization of perfusion delay especially in patients with hemodynamic compromise. The boxes contain all values between the first and third quartile, the line inside marks the median, and the whiskers reach from minimum to maximum not including outliers. Asterisk indicates significant  $p \leq 0.05$ .

reduced cerebrovascular reactivity, occur in those regions [30, 31]. These hemodynamic alterations have been shown to be associated with increased stroke risk [32, 33]. This particularly applies to internal WSAs, where infarcts of hemodynamic as well as microembolic origin occur, whereas infarcts in external WSAs are rather solely embolic in carotid stenosis patients [34]. Therefore, using individually defined internal WSAs as volume-of-interests for assessing abovementioned hemodynamic variables could be expected to increase the predictive accuracy for stroke risk as compared to whole brain averaging.

Moreover, there are hints that chronic hypoperfusion and hypoxia within WSAs may also have harmful effects on brain tissue in elderly people. Confluent as compared to punctate leukoaraiosis is associated with cerebral hypoperfusion [35] and is more likely to occur in WSAs [3]. Confluent white matter lesions are linked with cognitive symptoms as reduced mental processing speed and memory performance [36, 37]. Furthermore, not only white matter hyperintensities but also microinfarcts within WSAs have been shown to contribute to dementia symptoms in AD patients [4, 5]. Therefore, reliable WSA segmentation—as proposed here—is warranted to further explore WSA-related vascular processes and their cognitive implications as well as to ultimately identify and treat harmful perfusion states leading to progressive cognitive decline.

The following limitations apply to this study: First, our comparison of TTP-based WSAs with ss-ASL in five patients shows promising spatial correspondence; however, due to the relatively low number of 12 WSAs compared in this sample, it is certainly difficult to draw conclusions for the whole study cohort. Therefore, further validation studies comparing the TTP-based to ss-ASL and ASL-based ATT approaches in the same subjects are needed to confirm the reliability of our procedure. Second, our injection rate of 4 ml/s lay within recommended limits for DSC imaging. A slightly higher rate may have further improved bolus reliability, ideally in combination with an increased temporal sampling rate. Third, we did not define WSAs in the temporal lobe as segmentation in this brain region is often hindered by susceptibility artifacts. Fourth, cardiovascular risk factors, such as diabetes and hypertension, have been shown to affect cerebral hemodynamics [38–40]. These factors were more common in the patient group as compared to the controls (Table 1). Although no study has linked these factors with a shift of WSAs so far, we cannot exclude that they are independent confounding factors that increase variability of the WSAs via impaired hemodynamics. Therefore, it would be important to compare variability of WSAs in people with present cardiovascular risk factors to a healthy control cohort in a future study. Lastly, the proposed WSA segmentation approach is clearly operator dependent. However,

inter-operator reliability of WSA volume and WSA overlap was reasonable. As WSAs do not exhibit circumscribed borders, our approach can be expected to embody a fair estimation of WSAs' locations.

## Conclusions

This is the first study systematically evaluating variability of TTP-based watershed masks in patients with high-grade carotid artery stenosis and healthy controls. WSA segmentation was reliably feasible in both groups and showed high inter-operator reliability. Patients exhibited increased spatial variability of WSAs compared to controls. Furthermore, TTP increases on the side of the stenosis were only detectable within individual watershed masks as compared to an averaged watershed template obtained from controls. These TTP increases were independent from the degree of the stenosis and the individual collateralization of the CoW. Results indicate that individual WSA segmentation is necessary to detect critical regions of impaired WSA-related vascular processes especially in cerebrovascular disease.

## Compliance with ethical standards

**Funding** This study was funded by the Faculty of Medicine of the Technische Universität München (JG: KKF E12) and by the Dr.-Ing. Leonhard Lorenz-Stiftung (JG: 915/15).

**Conflict of interest** MH is employed by Philips Research.

**Ethical approval** All procedures performed in studies involving human participants were in accordance with the ethical standards of the institutional committee of Technische Universität München and with the 1964 Helsinki declaration and its later amendments or comparable ethical standards.

**Informed consent** Informed consent was obtained from all individual participants included in the study.

## References

- Momjian-Mayor I, Baron JC (2005) The pathophysiology of watershed infarction in internal carotid artery disease: review of cerebral perfusion studies. *Stroke* 36(3):567–577. <https://doi.org/10.1161/01.STR.0000155727.82242.e1>
- D'Amore C, Paciaroni M (2012) Border-zone and watershed infarctions. *Front Neurol Neurosci* 30:181–184. <https://doi.org/10.1159/000333638>
- Enzinger C, Smith S, Fazekas F, Drevin G, Ropele S, Nichols T, Behrens T, Schmidt R, Matthews PM (2006) Lesion probability maps of white matter hyperintensities in elderly individuals: results of the Austrian stroke prevention study. *J Neurol* 253(8):1064–1070. <https://doi.org/10.1007/s00415-006-0164-5>
- Brundel M, de Bresser J, van Dillen JJ, Kappelle LJ, Biessels GJ (2012) Cerebral microinfarcts: a systematic review of neuropathological studies. *J Cereb Blood Flow Metab* 32(3):425–436. <https://doi.org/10.1038/jcbfm.2011.200>
- Suter OC, Sunthorn T, Kraftsik R, Straubel J, Darekar P, Khalili K, Miklossy J (2002) Cerebral hypoperfusion generates cortical watershed microinfarcts in Alzheimer disease. *Stroke* 33(8):1986–1992. <https://doi.org/10.1161/01.STR.0000024523.82311.77>
- van der Zwan A, Hillen B, Tulleken CA et al (1992) Variability of the territories of the major cerebral arteries. *J Neurosurg* 77(6):927–940. <https://doi.org/10.3171/jns.1992.77.6.0927>
- Van Laar PJ, Hendrikse J, Mali WP et al (2007) Altered flow territories after carotid stenting and carotid endarterectomy. *J Vasc Surg* 45(6):1155–1161. <https://doi.org/10.1016/j.jvs.2006.11.067>
- Hendrikse J, van der Zwan A, Ramos LM et al (2005) Altered flow territories after extracranial-intracranial bypass surgery. *Neurosurgery* 57(3):486–494. <https://doi.org/10.1227/01.NEU.0000170563.70822.10>
- Wu B, Wang X, Guo J, Xie S, Wong EC, Zhang J, Jiang X, Fang J (2008) Collateral circulation imaging: MR perfusion territory arterial spin-labeling at 3T. *AJNR Am J Neuroradiol* 29(10):1855–1860. <https://doi.org/10.3174/ajnr.A1259>
- Helle M, Rufer S, van Osch MJ et al (2013) Superselective arterial spin labeling applied for flow territory mapping in various cerebrovascular diseases. *J Magn Reson Imaging* 38(2):496–503. <https://doi.org/10.1002/jmri.24041>
- Arteaga DF, Strother MK, Davis LT, Fusco MR, Faraco CC, Roach BA, Scott AO, Donahue MJ (2017) Planning-free cerebral blood flow territory mapping in patients with intracranial arterial stenosis. *J Cereb Blood Flow Metab* 37(6):1944–1958. <https://doi.org/10.1177/0271678X16657573>
- Hendrikse J, Petersen ET, van Laar PJ, Golay X (2008) Cerebral border zones between distal end branches of intracranial arteries: MR imaging. *Radiology* 246(2):572–580. <https://doi.org/10.1148/radiol.2461062100>
- Mildner T, Muller K, Hetzer S et al (2014) Mapping of arterial transit time by intravascular signal selection. *NMR Biomed* 27(5):594–609. <https://doi.org/10.1002/nbm.3098>
- Petersen ET, Mouridsen K, Golay X, all named co-authors of the QUASAR test-retest study (2010) The QUASAR reproducibility study, part II: results from a multi-center arterial spin labeling test-retest study. *NeuroImage* 49(1):104–113. <https://doi.org/10.1016/j.neuroimage.2009.07.068>
- van Osch MJ, Teeuwisse WM, van Walderveen MA et al (2009) Can arterial spin labeling detect white matter perfusion signal? *Magn Reson Med* 62(1):165–173. <https://doi.org/10.1002/mrm.22002>
- Chen DY, Kuo YS, Hsu HL et al (2016) Loss of labelling efficiency caused by carotid stent in pseudocontinuous arterial spin labelling perfusion study. *Clin Radiol* 71(1):e21–e27. <https://doi.org/10.1016/j.crad.2015.10.004>
- Nasel C, Azizi A, Wilfort A, Mallek R, Schindler E (2001) Measurement of time-to-peak parameter by use of a new standardization method in patients with stenotic or occlusive disease of the carotid artery. *AJNR Am J Neuroradiol* 22(6):1056–1061
- Neumann-Haefelin T, Wittsack HJ, Wenserski F, Siebler M, Seitz RJ, Modder U, Freund HJ (1999) Diffusion- and perfusion-weighted MRI. The DWI/PWI mismatch region in acute stroke. *Stroke* 30(8):1591–1597. <https://doi.org/10.1161/01.STR.30.8.1591>
- Helle M, Norris DG, Rufer S et al (2010) Superselective pseudocontinuous arterial spin labeling. *Magn Reson Med* 64(3):777–786. <https://doi.org/10.1002/mrm.22451>
- North American Symptomatic Carotid Endarterectomy Trial (1991) Methods, patient characteristics, and progress. *Stroke* 22:711–720



21. Fazekas F, Chawluk JB, Alavi A, Hurtig HI, Zimmerman RA (1987) MR signal abnormalities at 1.5 T in Alzheimer's dementia and normal aging. *AJR Am J Roentgenol* 149(2):351–356. <https://doi.org/10.2214/ajr.149.2.351>
22. Alsop DC, Detre JA, Golay X, Günther M, Hendrikse J, Hernandez-Garcia L, Lu H, MacIntosh BJ, Parkes LM, Smits M, van Osch MJP, Wang DJJ, Wong EC, Zaharchuk G (2015) Recommended implementation of arterial spin-labeled perfusion MRI for clinical applications: a consensus of the ISMRM perfusion study group and the European consortium for ASL in dementia. *Magn Reson Med* 73(1):102–116. <https://doi.org/10.1002/mrm.25197>
23. Kluge A, Lukas M, Toth V et al (2015) Analysis of three leakage-correction methods for DSC-based measurement of relative cerebral blood volume with respect to heterogeneity in human gliomas. *Magn Reson Imaging* 34:410–421
24. John JP, Wang L, Moffitt AJ, Singh HK, Gado MH, Csernansky JG (2006) Inter-rater reliability of manual segmentation of the superior, inferior and middle frontal gyri. *Psychiatry Res* 148(2-3):151–163. <https://doi.org/10.1016/j.psychres.2006.05.006>
25. Richter V, Helle M, van Osch MJ et al (2017) MR imaging of individual perfusion reorganization using superselective pseudo-continuous arterial spin-labeling in patients with complex extracranial steno-occlusive disease. *AJNR Am J Neuroradiol* 38(4):703–711. <https://doi.org/10.3174/ajnr.A5090>
26. Kanda T, Ishii K, Kawaguchi H, Kitajima K, Takenaka D (2014) High signal intensity in the dentate nucleus and globus pallidus on unenhanced T1-weighted MR images: relationship with increasing cumulative dose of a gadolinium-based contrast material. *Radiology* 270(3):834–841. <https://doi.org/10.1148/radiol.13131669>
27. Kanda T, Oba H, Toyoda K, Furui S (2016) Macrocytic gadolinium-based contrast agents do not cause hyperintensity in the dentate nucleus. *AJNR Am J Neuroradiol* 37(5):E41. <https://doi.org/10.3174/ajnr.A4710>
28. Radbruch A, Haase R, Kieslich PJ, Weberling LD, Kickingeder P, Wick W, Schlemmer HP, Bendszus M (2017) No signal intensity increase in the dentate nucleus on unenhanced T1-weighted MR images after more than 20 serial injections of macrocytic gadolinium-based contrast agents. *Radiology* 282(3):699–707. <https://doi.org/10.1148/radiol.2016162241>
29. van Laar PJ, Hendrikse J, Klijn CJ et al (2007) Symptomatic carotid artery occlusion: flow territories of major brain-feeding arteries. *Radiology* 242(2):526–534. <https://doi.org/10.1148/radiol.2422060179>
30. Fisher JA, Sobczyk O, Crawley A, Poulblanc J, Dufort P, Venkatraghavan L, Sam K, Mikulis D, Duffin J (2017) Assessing cerebrovascular reactivity by the pattern of response to progressive hypercapnia. *Hum Brain Mapp* in press. <https://doi.org/10.1002/hbm.23598>
31. Xie S, Hui LH, Xiao JX, Zhang XD, Peng Q (2011) Detecting misery perfusion in unilateral steno-occlusive disease of the internal carotid artery or middle cerebral artery by MR imaging. *AJNR Am J Neuroradiol* 32(8):1504–1509. <https://doi.org/10.3174/ajnr.A2523>
32. Derdeyn CP, Videen TO, Grubb RL Jr et al (2001) Comparison of PET oxygen extraction fraction methods for the prediction of stroke risk. *J Nucl Med* 42(8):1195–1197
33. Silvestrini M, Vernieri F, Pasqualetti P, Matteis M, Passarelli F, Troisi E, Caltagirone C (2000) Impaired cerebral vasoreactivity and risk of stroke in patients with asymptomatic carotid artery stenosis. *JAMA* 283(16):2122–2127. <https://doi.org/10.1001/jama.283.16.2122>
34. Moustafa RR, Momjian-Mayor I, Jones PS, Morbelli S, Day DJ, Aigbirhio FI, Fryer TD, Warburton EA, Baron JC (2011) Microembolism versus hemodynamic impairment in rosary-like deep watershed infarcts: a combined positron emission tomography and transcranial Doppler study. *Stroke* 42(11):3138–3143. <https://doi.org/10.1161/STROKEAHA.111.616334>
35. ten Dam VH, van den Heuvel DM, de Craen AJ, Bollen EL, Murray HM, Westendorp RG, Blauw GJ, van Buchem MA (2007) Decline in total cerebral blood flow is linked with increase in periventricular but not deep white matter hyperintensities. *Radiology* 243(1):198–203. <https://doi.org/10.1148/radiol.2431052111>
36. Schmidt R, Petrovic K, Ropele S, Enzinger C, Fazekas F (2007) Progression of leukoaraiosis and cognition. *Stroke* 38(9):2619–2625. <https://doi.org/10.1161/STROKEAHA.107.489112>
37. van den Heuvel DM, ten Dam VH, de Craen AJ, Admiraal-Behloul F, Olofsen H, Bollen EL, Jolles J, Murray HM, Blauw GJ, Westendorp RG, van Buchem MA (2006) Increase in periventricular white matter hyperintensities parallels decline in mental processing speed in a non-demented elderly population. *J Neurol Neurosurg Psychiatry* 77(2):149–153. <https://doi.org/10.1136/jnnp.2005.070193>
38. Mortby ME, Janke AL, Anstey KJ, Sachdev PS, Cherbuin N (2013) High "normal" blood glucose is associated with decreased brain volume and cognitive performance in the 60s: the PATH through life study. *PLoS One* 8(9):e73697. <https://doi.org/10.1371/journal.pone.0073697>
39. Aanerud J, Borghammer P, Chakravarty MM, Vang K, Rodell AB, Jónsdóttir KY, Møller A, Ashkanian M, Vafaei MS, Iversen P, Johannsen P, Gjedde A (2012) Brain energy metabolism and blood flow differences in healthy aging. *J Cereb Blood Flow Metab* 32(7):1177–1187. <https://doi.org/10.1038/jcbfm.2012.18>
40. Alosco ML, Gunstad J, Xu X, Clark US, Labbe DR, Riskin-Jones HH, Terrero G, Schwarz NF, Walsh EG, Poppas A, Cohen RA, Sweet LH (2014) The impact of hypertension on cerebral perfusion and cortical thickness in older adults. *J Am Soc Hypertens* 8(8):561–570. <https://doi.org/10.1016/j.jash.2014.04.002>

## 7.2 Journal Publication II: Characterizing white matter fiber orientation effects on multi-parametric quantitative BOLD assessment of oxygen extraction fraction

The publication entitled *Characterizing white matter fiber orientation effects on multi-parametric quantitative BOLD assessment of oxygen extraction fraction* was published in the Journal of Cerebral Blood Flow and Metabolism (JCBFM, ISSN: 1559-7016) electronically on 5 April 2019 [187]. The manuscript was authored by Stephan Kaczmarz, Jens Goetler, Claus Zimmer, Fahmeed Hyder and Christine Preibisch. It is available online (DOI: 10.1177/0271678X19839502) under Copyright © by the Authors. Preliminary results were also presented in conference contributions C9 and C14, awarded with the ISMRM Magna Cum Laude Merit Award and ISCBFM Early Career Investigator Travel Award as well as invited for oral presentation at the ISMRM annual meeting 2018. A summary of the publication is provided in Section 7.2.1, the author contributions are listed in Section 7.2.2 and the full text is included subsequently on the following pages.

### 7.2.1 Abstract

#### Purpose

Relative oxygen extraction fraction (rOEF) is a fundamental indicator of cerebral hemodynamic function. The MRI-based multi-parametric quantitative blood oxygenation level dependent (mq-BOLD) technique facilitates rOEF mapping based on three separate acquisitions of the transverse relaxation times  $T_2$  and  $T_2^*$  as well as the relative cerebral blood volume (rCBV) based on dynamic susceptibility contrast (DSC) imaging. While the underlying model assumptions of randomly oriented structures are reasonable in GM, known anisotropy effects in WM contradict them. Those anisotropy effects are known to affect transverse relaxation as well as rCBV and are thus expected to also impede mq-BOLD-based rOEF images. At the same time, rOEF imaging in WM has high clinical relevance, as WM is known to be particularly affected by many vascular pathologies. Thus, rOEF mapping in WM has high potential to increase the sensitivity to hemodynamic impairments and improve their detection at early disease stages at the same time. However, no evaluations of anisotropy effects on rOEF by mq-BOLD in WM have been performed before. The aim of our methodological study was therefore to characterize fiber orientation related anisotropy effects of rOEF in WM. The rOEF mapping by mq-BOLD was combined with fiber orientation information from diffusion tensor imaging (DTI).

#### Methods

MRI was performed on a 3T clinical scanner. The mq-BOLD related parameters  $T_2$ ,  $T_2^*$ ,  $R_2'$ , rCBV, rOEF were correlated with DTI-based fiber orientation information in 30 healthy volunteers. Main fibre orientations towards the main magnetic field  $B_0$  were derived from DTI for each WM voxel and transformed to spherical coordinates. The orientation dependencies of mq-BOLD parameters were evaluated by voxel-wise correlations of the mq-BOLD parameter values and the orientation information from DTI. To investigate the origins of anisotropy effects, different models were fitted to the data and compared.



## Results

Strong dependencies of transverse relaxation and rCBV on the nerve fiber orientation towards  $B_0$  were confirmed, with anisotropy-driven variations up to 37 %. Due to partially counteracting influences of  $R'_2$  and rCBV effects, the average rOEF orientation-dependent variation was comparably weak (3.8 %). Model fittings indicate that observed  $T_2$  anisotropy effects are mainly driven by diffusion, while major contributions to  $T_2^*$  and rCBV orientation effects are expected due to highly ordered myelinated fiber structures and known preferential vasculature orientations in WM.

## Conclusion

The results demonstrate the reliable in vivo characterization of WM anisotropy effects in mq-BOLD imaging with high sensitivity at reasonable scan time. Strong dependencies of transverse relaxation and rCBV on the nerve fiber orientation towards  $B_0$  were confirmed. In contrast, observed orientation effects in rOEF values were comparably weak in the healthy cohort with an average orientation induced variation of just 3.8%. This is due to counteracting anisotropy effects of  $R'_2$  and rCBV in the rOEF calculation. Thus, rather minor influences of orientation effects on mq-BOLD-derived rOEF in WM are indicated.

### 7.2.2 Author contributions

The first author designed the experiment, adapted the magnetic resonance pulse sequence (proprietary hardware specific libraries and software from Philips Medical Systems (Best, The Netherlands)), developed and implemented the processing pipeline, processed the data, developed and implemented the database to interpret the multi-parametric data using Matlab (Mathworks, Natick, MA); With the help and consultation from the coauthors: performed the experiments (MR measurements), evaluated the data, interpreted the results, and wrote the paper.

# Characterizing white matter fiber orientation effects on multi-parametric quantitative BOLD assessment of oxygen extraction fraction

Journal of Cerebral Blood Flow & Metabolism  
2020, Vol. 40(4) 760–774  
© Author(s) 2019  
Article reuse guidelines:  
sagepub.com/journals-permissions  
DOI: 10.1177/0271678X19839502  
journals.sagepub.com/home/jcbfm



Stephan Kaczmarz<sup>1,2,3</sup> , Jens Göttler<sup>1,2,3,4</sup> , Claus Zimmer<sup>1</sup>,  
Fahmeed Hyder<sup>3</sup> and Christine Preibisch<sup>1,2,5</sup> 

## Abstract

Relative oxygen extraction fraction (rOEF) is a fundamental indicator of cerebral metabolic function. An easily applicable method for magnetic resonance imaging (MRI) based rOEF mapping is the multi-parametric quantitative blood oxygenation level dependent (mq-BOLD) approach with separate acquisitions of transverse relaxation times  $T_2^*$  and  $T_2$  and dynamic susceptibility contrast (DSC) based relative cerebral blood volume (rCBV). Given that transverse relaxation and rCBV in white matter (WM) strongly depend on nerve fiber orientation, mq-BOLD derived rOEF is expected to be affected as well. To investigate fiber orientation related rOEF artefacts, we present a methodological study characterizing anisotropy effects of WM as measured by diffusion tensor imaging (DTI) on mq-BOLD in 30 healthy volunteers. Using a 3T clinical MRI-scanner, we performed a comprehensive correlation of all parameters ( $T_2^*$ ,  $T_2$ ,  $R_2'$ , rCBV, rOEF, where  $R_2' = 1/T_2^* - 1/T_2$ ) with DTI-derived fiber orientation towards the main magnetic field ( $B_0$ ). Our results confirm strong dependencies of transverse relaxation and rCBV on the nerve fiber orientation towards  $B_0$ , with anisotropy-driven variations up to 37%. Comparably weak orientation-dependent variations of mq-BOLD derived rOEF (3.8%) demonstrate partially counteracting influences of  $R_2'$  and rCBV effects, possibly suggesting applicability of rOEF as an oxygenation sensitive biomarker. However, unresolved issues warrant caution when applying mq-BOLD to WM.

## Keywords

Anisotropy, diffusion tensor imaging, multi-parametric quantitative BOLD, oxygen extraction fraction, white matter

Received 7 May 2018; Revised 23 January 2019; Accepted 22 February 2019

## Introduction

The oxygen extraction fraction (OEF) is a fundamental marker of cerebral metabolic function, which is widely considered as an important indicator of brain health and tissue viability. For rapid in vivo assessment of regional OEF, the magnetic resonance imaging (MRI) based multi-parametric quantitative BOLD (mq-BOLD) approach is highly promising. In mq-BOLD, three separate measurements are conducted to obtain maps of the relative cerebral blood volume (rCBV) as well as the quantitative transverse relaxation rates  $R_2^*$  and  $R_2$ . The rCBV is measured by dynamic susceptibility contrast (DSC) and the relaxation rates by gradient-echo (GRE) ( $R_2^* = 1/T_2^*$ ) and gradient spin-echo (GraSE) MRI ( $R_2 = 1/T_2$ ). Based on those three parameter-maps, the semi-quantitative relative oxygen extraction

<sup>1</sup>Department of Diagnostic and Interventional Neuroradiology, Klinikum rechts der Isar, Technical University of Munich, Munich, Germany

<sup>2</sup>TUM Neuroimaging Center (TUM-NIC), Klinikum rechts der Isar, Technical University of Munich, Munich, Germany

<sup>3</sup>Departments of Radiology & Biomedical Imaging and of Biomedical Engineering, Magnetic Resonance Research Center, Yale University, New Haven, CT, USA

<sup>4</sup>Department of Diagnostic and Interventional Radiology, Klinikum rechts der Isar, Technical University of Munich, Munich, Germany

<sup>5</sup>Clinic for Neurology, Klinikum rechts der Isar, Technical University of Munich, Munich, Germany

### Corresponding author:

Stephan Kaczmarz, Dipl. Phys (Univ.), Department of Diagnostic and Interventional Neuroradiology, Klinikum rechts der Isar, Technical University of Munich, Ismaninger Str. 22, München 81675, Germany.  
Email: stephan.kaczmarz@tum.de

fraction (rOEF) is calculated voxel-wisely.<sup>1,2</sup> However, derived values are considered to measure semi-quantitative, relative OEF, as relative CBV instead of venous CBV is used for calculation and obtained values are systematically elevated.<sup>1</sup> Compared to positron emission tomography (PET), the mq-BOLD technique is patient-friendly and easy to apply, as neither ionizing radiation nor arterial blood sampling are required.<sup>3</sup> The technique has already been successfully applied in several studies comprising patients with glioma,<sup>4–6</sup> stroke<sup>7</sup> and carotid artery stenosis.<sup>8</sup>

The mq-BOLD approach is based on a model representing a network of randomly oriented blood vessels by infinite length cylinders that possess homogenous magnetization and infinite length.<sup>1,9</sup> While these model assumptions are reasonable in gray matter (GM), known anisotropy effects in white matter (WM) contradict them. Anisotropy effects primarily arise from the highly oriented myelin sheaths within nerve fibers.<sup>10</sup> Moreover, blood vessels are also expected to contribute to orientation effects,<sup>11,12</sup> because preferential orientation of blood vessels in WM parallel the fiber tracts.<sup>13,14</sup> As corroborated by simulations, the results of Hernández-Torres et al.<sup>12</sup> are in agreement with oriented vessels occupying about one-third of the vascular volume in WM. Thus, mq-BOLD application in highly ordered WM structures raises questions about its reliability.<sup>1</sup> Since WM is particularly affected by many vascular pathologies such as stroke and small vessel diseases,<sup>15</sup> a deeper understanding of factors influencing mq-BOLD-derived rOEF values in WM as high clinical relevance.

Fiber bundles in WM consist of axons, running mainly parallel to each other, being wrapped by myelin. The surrounding myelin sheaths consist of lipid bilayers organized in a lamellar structure with alternating layers of lipid and water.<sup>16</sup> Strong effects of the nerve fiber orientation towards the main static magnetic field ( $B_0$ ) on effective transverse relaxation are well known and have been investigated extensively<sup>11,16–31</sup> and also demonstrated in the context of DSC-based perfusion imaging.<sup>12</sup> In addition, spin echo-derived  $T_2$  was found to be affected by fiber orientation effects,<sup>20</sup> which was attributed to diffusion.<sup>18</sup>

Fiber orientation effects have been studied by different methods, including *in vitro* samples<sup>20,23,24,26,31</sup> and scanning in different head positions.<sup>11,18</sup> However, determining fiber orientation via diffusion tensor imaging (DTI)<sup>32</sup> allows voxelwise correlations with the parameter values,<sup>11,12,17,19,28,29</sup> and thus appears most suitable for accurate *in vivo* measurements.

A number of studies attempted to characterize the  $T_2^*$ -related orientation effects employing different models.<sup>9,16,20,22,24,27,28,31,33,34</sup> Based on analytical modeling of highly aligned parallel cylinders with

susceptibility differences to the surrounding tissue, it has been derived that  $R_2^*$  and  $R_2'$ , defined as  $R_2^* - R_2$ , are modulated by  $\sin^2(\theta)$  depending on their angle  $\theta$  towards  $B_0$ .<sup>9,34</sup> However, more detailed experimental analyses of  $R_2^*$  revealed deviations from this  $\sin^2(\theta)$  term points to additional influences.<sup>17,20,24,29,31</sup> This additional component was suspected to arise from susceptibility anisotropy<sup>23,24,35</sup> of myelin<sup>30</sup> and modeled by a  $\sin^4(\theta)$  term.<sup>24</sup> To this end, the hollow cylinder fiber model (HCFM) with anisotropic magnetic susceptibility in the annular region was used to represent myelin sheaths surrounding the axons.<sup>27</sup> Alternative explanations for the additional orientation influences could be magic angle effects, arising from dipole–dipole interactions, which have been demonstrated in tendons and peripheral nerves with much thicker fiber bundles.<sup>36</sup> A detailed study compared both possible explanations and concluded that  $R_2$  and  $R_2^*$  orientation effects most likely originate from anisotropic susceptibility rather than magic angle effects.<sup>20</sup>

Even though, the orientation effects of  $T_2^*$ ,  $T_2$  and DSC-based rCBV in WM are well known, and complex effects on mq-BOLD-derived parameters are expected, their impact on mq-BOLD based rOEF measurements is unclear. Therefore, the aim of our study was to characterize the influence of orientation effects in WM on the calculated parameter values of mq-BOLD derived rOEF. To this end, we performed separate measurements of  $T_2^*$ ,  $T_2$  and DSC-based rCBV in 30 healthy volunteers and assessed the angular dependencies of all parameters with respect to the main static magnetic field  $B_0$  using DTI.

## Material and methods

### Participants

Thirty healthy elderly (17 females; mean age  $70.3 \pm 4.8$  years; see Supplemental Table 1 for more details; normal test results in MMSE, STAI, BDI) participated in this prospective study. Participants were enrolled by word-of-mouth advertisement from May 2015 until May 2017. Examination of every participant included medical history, basic neurological examination and MRI. The study was approved by the medical ethical board of the Klinikum rechts der Isar, in line with Human Research Committee guidelines of the Technical University of Munich. All participants provided informed consent in accordance with the standard protocol approvals. Exclusion criteria for entry into the study were any neurological, psychiatric or systemic disease, clinically remarkable structural MRI (e.g. territorial stroke lesions, bleedings, or a history of brain surgery), severe chronic kidney disease or MR contraindications.

### Imaging data acquisition

Scanning was performed on a clinical 3T Philips Ingenia MR-Scanner (Philips Healthcare, Best, The Netherlands) using a 16-channel head/neck-receive-coil. The Omega HP gradients allow a maximum amplitude of 45 mT/m and slew rate of 200 T/m/s. In order to calculate mq-BOLD-derived rOEF, the MRI protocol comprised quantitative mapping of intrinsic and effective transverse relaxation times  $T_2$  and  $T_2^*$  together with DSC MRI for rCBV assessment<sup>37,38</sup> as described previously.<sup>1</sup>  $T_1$ -weighted magnetization prepared rapid gradient echo (MPRAGE) and  $T_2$ -weighted fluid-attenuated inversion recovery (FLAIR) data were acquired to facilitate brain tissue segmentation and screening for lesions, respectively. Additionally, a contrast-enhanced angiography of the arteries of the neck and the aortic arch was performed to exclude relevant stenoses of the brain supplying arteries. DTI was performed to obtain fiber orientation within WM<sup>39</sup> and to assess orientation dependencies of the mq-BOLD related parameters (Figure 1).

$T_2^*$ -mapping used a 12 echo gradient echo (GRE) sequence featuring exponential excitation pulses to facilitate correction of magnetic background gradients<sup>40,41</sup> and duplicate acquisition of k-space center for motion correction<sup>42</sup> with the following imaging parameters:  $TE_1 = \Delta TE = 5$  ms,  $TR = 1950$  ms,  $\alpha = 30^\circ$ , mono-polar readout, 30 slices, matrix  $112 \times 92$ , voxel size  $2.0 \times 2.0 \times 3.0$  mm<sup>3</sup>, total acquisition time 6:08 min.

$T_2$ -mapping was based on an eight echo gradient-spin-echo (GraSE) sequence:  $TE_1 = \Delta TE = 16$  ms,  $TR = 8596$  ms, echo planar imaging (EPI) factor = 7, 30 slices, gap 0.3 mm, matrix  $112 \times 91$ , voxel size  $2.0 \times 2.0 \times 3.0$  mm<sup>3</sup>, acquisition time 2:23 min.

*DSC-imaging* used dynamic acquisition of 80 single-shot gradient-echo EPI volumes during injection of a weight-adjusted Gd-DOTA bolus (concentration 0.5 mmol/ml, dose 0.1 mmol/kg, at least 7.5 mmol per subject, flow rate 4 ml/s, injection 7.5 s after DSC imaging onset) with  $TE = 30$  ms,  $TR = 1513$  ms,  $\alpha = 60^\circ$ , 26 slices, voxel size  $2.0 \times 2.0 \times 3.5$  mm<sup>3</sup>, acquisition time 2:01 min, following the ASFNR recommendations.<sup>43</sup>

*DTI* used spin-echo EPI with 32 gradient directions,  $b = 800$  s/mm<sup>2</sup>,  $TE = 61$  ms,  $TR = 12.9$  s, Halfscan = 0.7, SENSE = 2, 60 slices, matrix  $112 \times 110$ , voxel size  $2.0 \times 2.0 \times 2.0$  mm<sup>3</sup>, NSA = 2, acquisition time 15:30 min. The DTI field-of-view (FOV) was individually aligned to the interhemispheric gap in the axial plane and tilted in the sagittal plane to exclude the participant's eyes.

*Structural imaging* comprised MPRAGE ( $TE = 4$  ms,  $TR = 9$  ms,  $\alpha = 8^\circ$ ,  $TI = 1000$  ms, shot interval 2300 ms, SENSE AP = 1.5, SENSE RL = 2.0, 170 slices, matrix  $240 \times 238$ , voxel size  $1.0 \times 1.0 \times 1.0$  mm<sup>3</sup>, acquisition time 5:59 min) and FLAIR ( $TE = 289$  ms,  $TR = 4800$  ms,  $\alpha = 90^\circ$ , inversion delay 1650 ms,  $\alpha = 90^\circ$ , TSE factor = 167, 163 slices, matrix  $224 \times 224$ , voxel size  $1.12 \times 1.12 \times 1.12$  mm<sup>3</sup>, acquisition time 4:34 min). Screening for ischemic brain lesions and grading of white matter hyper-intensities were based on diffusion-weighted imaging and FLAIR. The FLAIR lesions were graded by the Fazekas-score<sup>44</sup> (Rater: JG).

### Data preprocessing and parameter calculation

All processing procedures used FMRIB Software Library<sup>45</sup> (FSL), SPM12<sup>46</sup> (Wellcome Trust Centre for Neuroimaging, UCL, London, UK) and custom programs in MATLAB R2016b (The MathWorks,

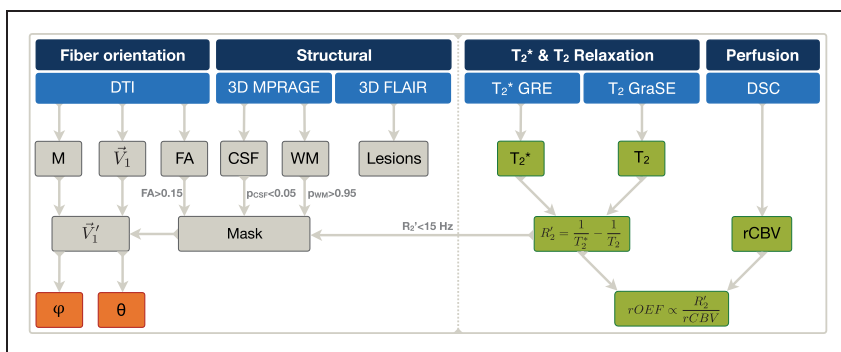


**Figure 1.** Overview of MRI protocol and derived parameters. DTI was used to derive the rotation matrix  $\mathbf{M}$ , the main nerve fiber orientation vector-maps  $\mathbf{V}_1$  and the fractional anisotropy (FA). MPRAGE was used for CSF and WM mask generation. FLAIR was used for structural lesion detection. The rotation matrix  $\mathbf{M}$  was applied to transform  $\mathbf{V}_1$  vector-maps to the scanner coordinate system resulting in  $\mathbf{V}'_1$ . After application of a mask, selecting only oriented WM and excluding iron artefact related voxels ( $FA > 0.15$ ,  $P_{CSF} < 0.05$ ,  $P_{WM} > 0.95$ ,  $R_2' < 15$  Hz), the spherical angles  $\varphi$  and  $\theta$  (azimuthal and polar angles, respectively, between the main nerve fiber orientation and  $B_0$ ) were calculated voxel-wisely (orange). The dependencies of the calculated mq-BOLD-related parameters (green) on  $\varphi$  and  $\theta$  were analyzed in bins of  $5^\circ$ , each for  $\varphi$  and  $\theta$ .

Natick, MA, USA). MPRAGE data were segmented by SPM12 using six tissue classes and default settings for generation of a WM mask by applying a probability threshold of  $P_{WM} > 0.95$ . To reduce influences of partial volume effects, cerebrospinal fluid (CSF) was additionally excluded by applying a threshold of  $P_{CSF} < 0.05$  (Figure 1).

**mq-BOLD parameter maps.** Multi-echo GRE data were corrected for macroscopic background gradients<sup>40,41</sup> and motion<sup>42</sup> and subsequently fitted mono-exponentially for  $T_2^*$  as described previously.<sup>1</sup> Quantitative  $T_2$  parameter maps were derived by mono-exponential fitting of the even-echoes GraSE data to reduce the influence of stimulated echoes.<sup>1,5</sup>  $T_2^*$ -maps were coregistered to the first echo of the  $T_2$  GraSE sequence and visually checked (CP, SK). Both,  $T_2^*$  and  $T_2$  were smoothed with a 3D Gaussian filter-kernel of 3-mm prior to calculation of

$$R_2' = \frac{1}{T_2^*} - \frac{1}{T_2} \quad (1)$$

Since iron depositions are known to increase  $R_2'$ , an empirically set threshold of  $R_2' < 15$  Hz was applied and carefully checked (CP, SK) to exclude iron induced focal increases of  $R_2'$ . As macroscopic background, gradients up to about  $250 \mu\text{T/m}$  can be corrected<sup>40</sup> and areas with higher gradients can also be removed via  $R_2'$  thresholding,<sup>1</sup> remaining  $R_2'$  was assumed to mainly reflect subvoxel susceptibility perturbations.<sup>18</sup> DSC data were corrected for leakage contributions based on a reference curve technique<sup>47</sup> and processed as described previously.<sup>37,38</sup> Accordingly, DSC data were filtered using a 3D Gaussian spatiotemporal filter-kernel of 3-mm full width at half maximum (FWHM) with time as the third dimension. Relative CBV (rCBV) was calculated by first-pass integration of the area under the leakage corrected  $\Delta R_2^*(t)$  curve.<sup>37</sup> Subsequently, rCBV was normalized to 2.5% in normal appearing WM.<sup>3,48</sup> Following the mq-BOLD approach,<sup>1</sup> relative oxygen extraction fraction (rOEF) was calculated as

$$rOEF = \frac{R_2'}{c \cdot rCBV} \quad (2)$$

where  $c = \gamma \cdot \frac{4}{3} \cdot \pi \cdot \Delta\chi \cdot B_0$  and  $B_0 = 3T$ . Here,  $\Delta\chi = \Delta\chi_0 \cdot \text{Hct} = 0.924 \times 10^{-7}$  is the susceptibility difference between oxygenated and deoxygenated blood with the susceptibility difference between fully deoxygenated and fully oxygenated hemoglobin  $\Delta\chi_0 = 0.264 \times 10^{-6}$ <sup>49,50</sup> and the small-vessel hematocrit  $\text{Hct} = 0.35$ .<sup>50</sup> The gyromagnetic ratio is  $\gamma = 2.675 \times 10^8 \text{ s}^{-1} \text{ T}^{-1}$ . For quality assessment,  $T_2^*$ ,  $T_2$ , rCBV and rOEF parameter maps were screened especially for motion artefacts (raters CP,

SK). Based on these ratings, two subjects were excluded from the final evaluation.

**DTI-based fiber orientation mapping.** DTI-data were processed using FSL.<sup>45</sup> Eddy current effects and motion were corrected by the FSL FLIRT toolbox<sup>51,52</sup> and non-brain voxels removed by the FSL brain extraction tool.<sup>53</sup> Eigenvalues and corresponding eigenvectors were calculated with the tensor fitting routine of FSL FDT.<sup>54,55</sup> Fractional anisotropy (FA) values were calculated and thresholded at  $FA > 0.15$  to exclude voxels with isotropic structures. We assumed the nerve-fibers to be collinear with the main eigenvector, which is associated with the highest eigenvalue.<sup>10</sup> Thereby, the tensor fitting revealed voxelwise vectors  $V_1$  describing the main nerve fiber orientation within the coordinate system defined by the DTI-FOV (Figure 2).

**Spatial coregistration.** For further evaluation, all individual MR images and parameter maps (MPRAGE, tissue segments,  $T_2^*$ ,  $T_2$ ,  $R_2'$ , rCBV- and rOEF-maps) were spatially coregistered to the individual participant's DTI-data using SPM12 and very carefully checked for transformation-related artefacts by two experienced researchers (CP, SK).

**Angulation processing.** The orientation information about the DTI-FOV was extracted from the DTI nifti headers. The resulting matrix  $M$  describes the rotation between the DTI-FOV and the MR-scanner coordinate system and was applied to the main nerve fiber orientation vectors  $V_1$  resulting in  $V_1'$  (Figure 2).<sup>30,56</sup> Thereby, each voxel's  $V_1$  vector was rotated to the scanner coordinate system with  $z' \parallel B_0$ . Subsequently,  $V_1'$  vectors were transformed from Cartesian to spherical coordinates. The resulting polar angle  $\theta$  describes the angulation between the main nerve fiber orientation and  $B_0$ . The azimuthal angle  $\phi$  describes the orientation of  $V_1'$  projected onto the  $x'$ - $y'$ -plane ( $\perp B_0$ ) (Figure 2). As fiber-direction is irrelevant, we analyzed angle ranges from  $\theta = 0^\circ$  to  $90^\circ$ <sup>11,12,17</sup> and  $\phi = -90^\circ$  to  $90^\circ$ . Further analysis was restricted to oriented WM voxels outside of regions with iron-artefacts or uncorrectable macroscopic magnetic field gradients, defined by  $FA > 0.15$ ,  $p_{WM} > 0.95$ ,  $p_{CSF} < 0.05$  and  $R_2' < 15$  Hz. Within this mask, anisotropy effects of the individual parameters  $T_2^*$ ,  $T_2$ ,  $R_2'$ , rCBV and rOEF were evaluated in  $5^\circ$  bins. All previously described processing was conducted individually for each participant. On the group-level, median values were calculated within a given angle-bin for each parameter. Standard deviations (SDs) of the parameters were calculated by dividing the SD of all voxels and all participants within a given angle-bin by the square-root of the number of evaluated participants. Histograms of  $T_2^*$ ,  $T_2$ ,  $R_2'$ ,



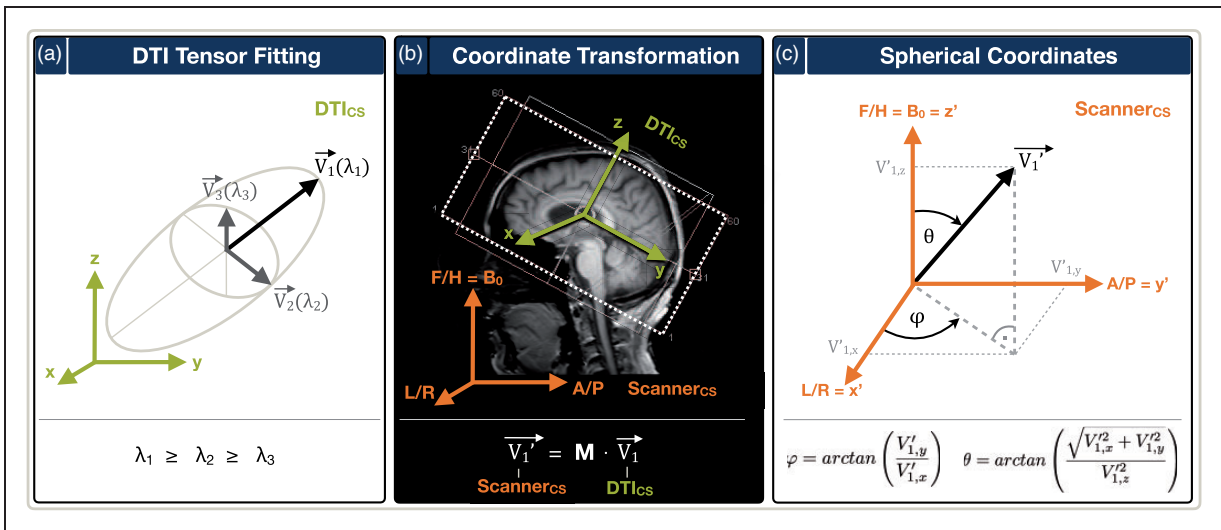


**Figure 2.** Overview of main nerve fiber vector map calculation and angular transformations. (a) Tensor fitting of the DTI-data within the DTI-FOV coordinate system ( $DTI_{CS}$ , green) revealed the main nerve fiber orientation for each voxel, described by the vector  $V_1$  corresponding to the largest eigenvalue  $\lambda_1$ . (b) The rotation matrix  $M$ , individually derived from the DTI image header for each participant, was applied to transform the  $V_1$  vector-maps to the MRI-scanner coordinate system ( $Scanner_{CS}$ , orange) resulting in  $V_1'$  vector-maps. (c) Vector-maps of  $V_1'$  were transformed to spherical coordinates, yielding the polar angle  $\theta$  and the azimuthal angle  $\phi$  for each voxel.

rCBV and rOEF maps vs.  $\theta$  and  $\phi$  were prepared using median values and SDs across all oriented WM voxels from all participants.

### Fitting model

Recently, Lee et al.<sup>24</sup> proposed a model for highly aligned networks of parallel fibers including anisotropy of magnetic susceptibility to describe  $R_2^*$  orientation effects depending on the polar angle  $\theta$ . According to that, the orientation dependence of the measured signal was fitted by

$$S(\theta) = c_0 + c_1 \sin(2\theta + \phi_0) + c_2 \sin(4\theta + \phi_1) \quad (3)$$

with the orientation-independent coefficient  $c_0$ , the two orientation-dependent coefficients  $c_1$  and  $c_2$  and two sinusoids to account for highly non-random, non-isotropic perturber distributions and magnetic susceptibility anisotropy. The model can be applied to  $R_2(\theta)$ <sup>20</sup> and  $R_2'(\theta)$ .<sup>34</sup> In this work, we also analyzed whether this model is capable to describe rCBV( $\theta$ ) and rOEF( $\theta$ ) orientation effects. All fits were performed by the least-square curve fitting routine 'lsqcurvefit' (MATLAB R2016b, The MathWorks, Natick, MA, USA) with default settings.

## Results

The calculated maps of the polar angle  $\theta$  and azimuthal angle  $\phi$  show excellent agreement with the expected fiber tract directions as demonstrated in Figure 3,

showing data from a prototypical participant (see Supplemental Figure 1 for more details).

On group level,  $T_2^*$  median values strongly depended on  $\theta$  with  $T_2^*(\theta)$  ranging from 48.2 ms to 54.7 ms, which corresponded to an absolute difference of  $\Delta T_2^*(\theta) = 6.5$  ms and a variation of 13.5% between fibers parallel and perpendicular to  $B_0$  (Figure 4(a)). Accordingly,  $R_2^*(\theta)$  median values were measured within the range of  $R_2^*(\theta) = [18.3-20.8]$  Hz and  $\Delta R_2^*(\theta) = 2.5$  Hz (data not shown). Analysis of  $T_2$  revealed an angulation-dependent range of median values  $T_2(\theta) = [78.4-84.3]$  ms corresponding to  $\Delta T_2(\theta) = 5.9$  ms and a variation of 7.5% (Figure 4(c)) or  $\Delta R_2(\theta) = 0.9$  Hz (data not shown). Both,  $T_2^*$  and  $T_2$  were almost independent of the orientation within the plane perpendicular to  $B_0$ , described by the azimuthal angle  $\phi$  (Figure 4(b) and (d)).  $R_2'$  yielded a  $\theta$ -dependent range of median values  $R_2'(\theta) = [6.5-8.2]$  Hz corresponding to a variation of 26.5% (Figure 5(a)). Relative CBV median values varied between rCBV( $\theta$ ) = [2.0-2.8]%, representing a variation of 37.1% (Figure 5(c)). The resulting range of rOEF median values was rOEF( $\theta$ ) = [0.94-1.09] corresponding to a variation of 15.0% between lowest and highest values (Figure 5(e)). Similar to  $T_2^*$  and  $T_2$ , the median values of  $R_2'$ , rCBV and rOEF were almost independent of  $\phi$  (Figure 5(b), (d) and (f)).

The distribution of the number of voxels within oriented WM contributing to the presented median values within the  $\theta$  bins of  $5^\circ$  was well described by a sinusoidal curve (Figure 6(a)), indicating that fiber orientations towards the main magnetic field are almost homogeneously distributed within the investigated

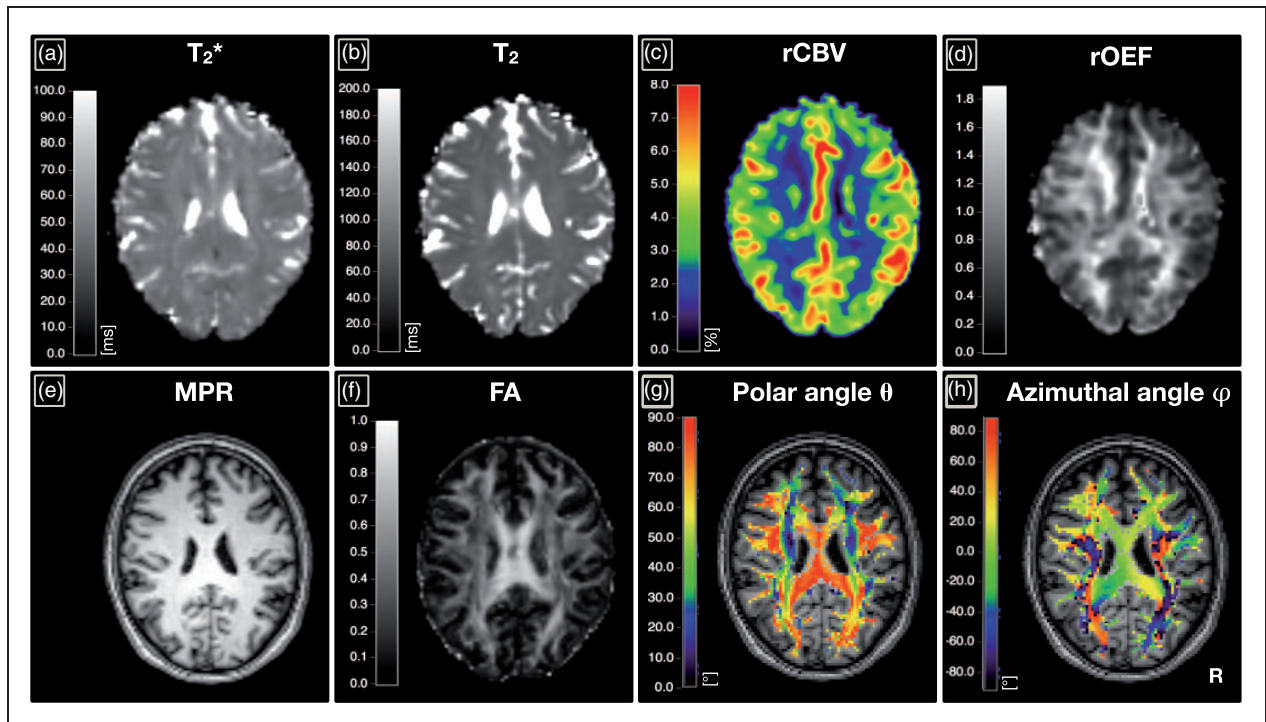


**Figure 3.** Exemplary parameter maps of a healthy volunteer in one axial slice.  $T_2^*$  (a),  $T_2$  (b), rCBV (c), rOEF (d), MPRAGE (e), FA (f), the polar angle  $\theta$  (g) and the azimuthal angle  $\varphi$  (h) overlaid on MPRAGE. The mask of oriented WM was already applied to the orientation maps (g, h). Fibers in FH-direction correspond to  $\theta = 0^\circ$  in case of small DTI-FOV angulations. Fibers in AP-direction correspond then to  $\theta = 90^\circ$  and  $\varphi = \pm 90^\circ$ . Fibers in LR-direction correspond to  $\theta = 90^\circ$  and  $\varphi = 0^\circ$ .

volumes. Conversely, the voxel distribution depending on the azimuthal angle  $\varphi$  was almost constant, also indicating a homogenous distribution, with a slight preference for left-right and anterior-posterior orientations (Figure 6(b)).

Although the Fazekas-scores revealed a mean of  $1.0 \pm 0.9$  (range 0–3, for details see Supplemental Table 1) indicating minor microangiopathic changes, none of the participants had subacute or older territorial infarct lesions. Including participants with Fazekas-scores above 1 had no obvious effect on the observed orientation dependencies (Supplemental Figure 2). Separate evaluations of the data from female and male participants did not reveal significant effects of gender on rOEF( $\theta$ ) (Supplemental Figure 3). Additional measurements of  $T_2^*$ ,  $T_2$  and DTI in a small cohort of young healthy controls provided evidence that observed orientation dependencies were not influenced by age (Supplemental Figure 4).

Fitting of Lee's model (equation (3)) to the median values of  $T_2^*(\theta)$  revealed excellent agreement ( $R^2 > 0.999$ , Figure 7(a)), with the two fitted sinusoidal components being incoherent in phase (Figure 7(b)). Accordingly, fitting of  $R_2^*(\theta)$  revealed  $c_0 = 19.54$  Hz,  $c_1 = 1.11$  Hz,  $\Phi_0 = 67.33^\circ$ ,  $c_2 = 0.07$  and  $\Phi_1 = 0.61^\circ$  (data not shown). Applying the same model (equation (3)) to  $T_2(\theta)$ ,  $R_2'(\theta)$  and rCBV( $\theta$ ) median values, showed

excellent agreement ( $R^2 > 0.997$ , Figure 7(c) to (f)) as well. Even fitting of rOEF( $\theta$ ) shows very good agreement to Lee's model (equation (3)) ( $R^2 > 0.991$ , Figure 7(f)).

## Discussion

In this study, we presented a DTI-based quantitative orientation analysis method using an automated coordinate system transformation to spherical coordinates and applied it to characterize anisotropy effects of mq-BOLD related parameter maps in WM. Orientation effects were measured for multiple parameters, namely  $T_2^*$ ,  $T_2$ , rCBV and rOEF. Using DTI-derived nerve fiber orientations, tissue orientation effects were quantified along the polar angle  $\theta$  towards  $B_0$ . Observed dependencies of  $T_2^*(\theta)$ ,  $T_2(\theta)$  and rCBV( $\theta$ ) are in excellent agreement with the literature.<sup>11,12,17–21,24,28,29</sup> In addition, orientation effects of rOEF( $\theta$ ) were demonstrated and quantified. All observed angular dependencies could be well described by fitting a model including susceptibility anisotropy (equation (3)) in good agreement with previous reports.<sup>20,21,24,28,29</sup> Contrary to intuition, the impact of WM orientation on calculated parameter values of rOEF is comparably weak because contributions of  $R_2'$  and rCBV partly compensate.

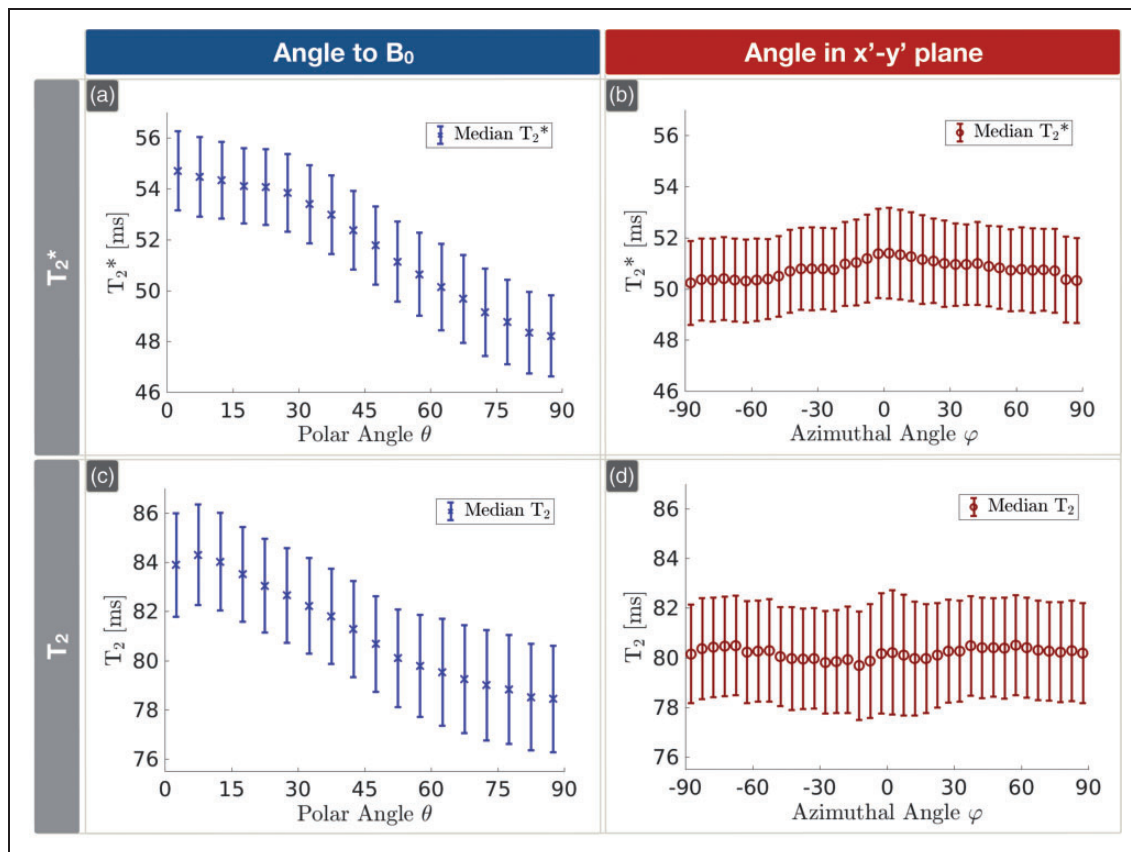


**Figure 4.** Orientation dependencies of  $T_2^*$  and  $T_2$  on group level. The dependencies of  $T_2^*$  (a, b) and  $T_2$  (c, d) on polar angle  $\theta$  (a, c) and azimuthal angle  $\varphi$  (b, d) are depicted (median across all participants  $\pm$  SD). Parameter values were evaluated within  $5^\circ$  bins. The plots show a clear orientation dependency of  $T_2^*$  (a) and  $T_2$  (c) on  $\theta$ , which describes the fiber orientation relative to  $B_0$ . As expected, no major angle dependencies of any parameter were observed in the  $x'$ - $y'$  plane perpendicular to  $B_0$  (b, d).

### Influence of WM orientation on $T_2^*$

Our measured differences  $\Delta T_2^*(\theta) = 6.5$  ms or  $\Delta R_2^*(\theta) = 2.5$  Hz fully agree with previously reported in vivo measurements.<sup>11,17–21,24,28,29</sup> The details of  $T_2^*(\theta)$  and  $R_2^*(\theta)$  angular dependencies (Figure 4(a)) resemble those observed in previous studies.<sup>11,28,29</sup> Though, our measured  $T_2^*(\theta)$  dependency appears more pronounced than demonstrated by Denk et al.,<sup>17</sup> which might be explained by our improved, automated coordinate system transformation and rigorous thresholding to exclude artefacts.

The major contributors to anisotropy effects driving orientation dependencies of effective transverse relaxation are still under discussion. Most likely, the angular dependencies are caused by sub-voxel susceptibility effects arising from anisotropic sources, namely highly ordered myelin-fiber structures<sup>12,17–24,57</sup> and effects of oriented WM vasculature<sup>11,12,22</sup> being preferentially aligned parallel to axonal-fibers.<sup>12–14</sup>

Lee's model (equation (3)) includes highly oriented cylinders, which can represent the fibers and vessels, as well as anisotropic susceptibility in the annular region,

representing myelin.<sup>24</sup> Fitting Lee's model (equation (3)) to  $T_2^*(\theta)$  reveals excellent agreement (Figure 7(a)) in accordance with the literature.<sup>20,24,29,57</sup> While the fitted  $T_2^*(\theta)$  curve closely resembles the data, we did not observe phase coherence of the two sinusoidal components (Figure 7(b)), which represent influences by highly non-random, non-isotropic perturbers and magnetic susceptibility anisotropy, in contrast to Lee et al.<sup>24</sup> Other studies applied a similar model without sinusoidal phase shifts to  $R_2^*(\theta)$ , yielding very similar results.<sup>29,57</sup> Our results are, therefore, in accordance with assuming major contributions to  $T_2^*(\theta)$  orientation effects from highly ordered myelinated fiber structures and the vasculature.

### Influence of WM orientation on $T_2$

We also observed a strong  $T_2(\theta)$  orientation effect with  $\Delta T_2(\theta) \approx 6$  ms or  $\Delta R_2(\theta) \approx 1$  Hz in accordance with Oh et al.<sup>20</sup> Minor discrepancies to their ex vivo study can be explained by cell swelling as well as further molecular changes<sup>18</sup> in their formalin fixed tissue samples scanned at room temperature, which also



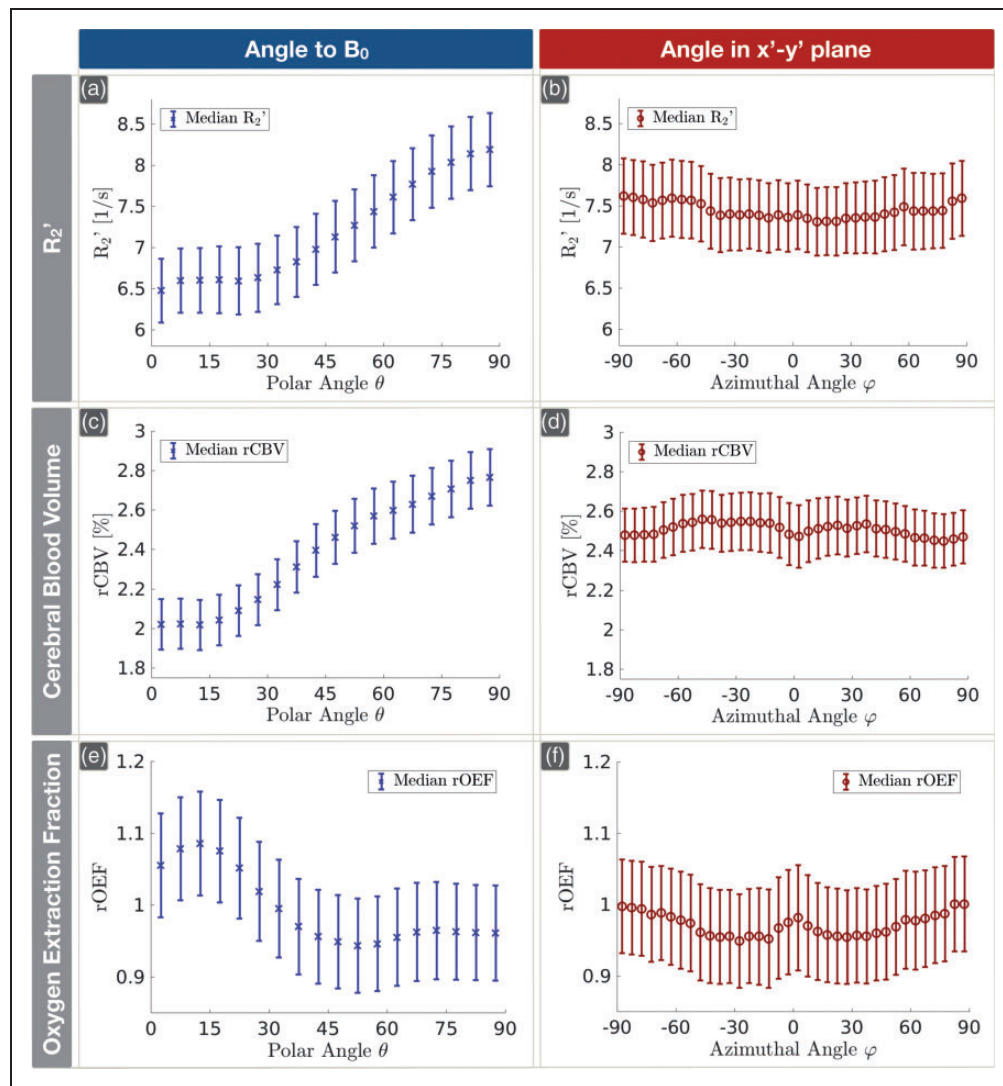


**Figure 5.** Orientation dependencies of  $R_2'$ , rCBV and resulting rOEF on group level. Plots of  $R_2'$  (a, b), rCBV (c, d) and rOEF (e, f) are shown (median across all participants  $\pm$  SD) depending on the polar angle  $\theta$  (a, c, e) and the azimuthal angle  $\varphi$  (b, d, f). Parameter values were evaluated within  $5^\circ$  bins.  $R_2'$  was derived from  $T_2^*$  and  $T_2$  and shows strong orientation dependence on  $\theta$  (a). Relative CBV shows a similar behavior with an even stronger dependence on  $\theta$  (c). As rOEF is proportional to the ratio of  $R_2'$  and rCBV (equation (2)), the resulting anisotropy artefacts of rOEF are driven by the different slopes of  $R_2'$  (a) and rCBV (c). Thereby, rOEF shows a lower dependency on  $\theta$  (e). In the  $x'-y'$  plane perpendicular to  $B_0$ , no major angular dependency effects were observed (b, d, f).

influences the transverse relaxation rates.<sup>20</sup> Moreover, their study was conducted at 7T and they averaged over larger ROIs without actually measuring fiber orientation. While orientation dependencies can be expected to be more prominent at higher field strength, the latter rather decreases the observed effects.

Regarding origins of  $T_2(\theta)$  orientation effects, contributions from susceptibility effects are actually expected to be minimized by the GraSE refocusing pulses, in contrast to GRE-based  $T_2^*$  mapping.<sup>20</sup> However, mediated by diffusion, the same susceptibility gradients causing  $T_2^*$  decay are expected to

decrease  $T_2$ .<sup>18,20</sup> The signal decay due to diffusion of spins through inhomogeneous magnetic fields can be modeled with the Carr-Purcell method by adding a diffusion term to the intrinsic spin-spin dephasing. This additional exponential term, representing the signal decay due to diffusion, can be approximated by a Taylor expansion resulting in a sum of  $\sin(2\theta)$  and  $\sin(4\theta)$  terms. For a rough estimate of diffusion effects on  $T_2(\theta)$ , we rely on Le Bihan et al.,<sup>10</sup> who analyzed anisotropic diffusion in WM<sup>58</sup> and found diffusion perpendicular to nerve fibers to be impeded by approximately 60%. Based on this, the maximum

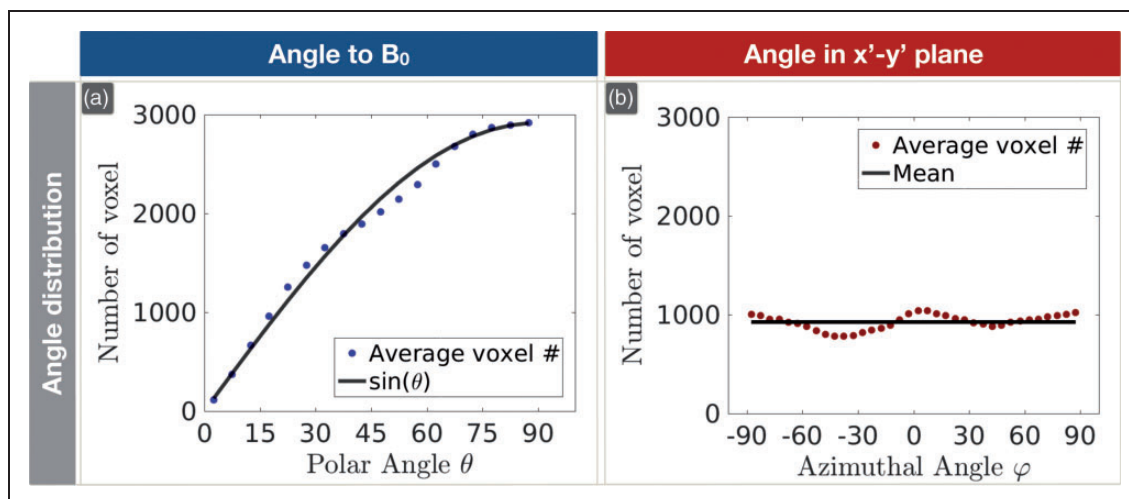


**Figure 6.** Histograms of the numbers of contributing voxels depending on the polar angle  $\theta$  and the azimuthal angle  $\varphi$ . The dotted blue line represents the average number of measured voxels per participant depending on  $\theta$  (a). For comparison, the solid black line indicates equally populated orientations (a). The average number of voxels per participant depending on  $\varphi$ , perpendicular to  $B_0$ , is shown by the red dotted line and compared to the mean of all voxels, represented by the solid black line (b).

strength of the GraSE sequence's readout gradients ( $\approx 20$  mT/m) could well explain  $T_2$  orientation effects within the observed range. Since fitting of Lee's model (equation (3)) to  $T_2(\theta)$  shows excellent agreement (Figure 7(c)), it appears reasonable to attribute dependencies of  $T_2$  on  $\theta$  to diffusion effects.

Application of Lee's model (equation (3)) to  $T_2(\theta)$  was further supported by Oh et al.,<sup>20</sup> who compared the anisotropic susceptibility model with pure magic angle effects of  $R_2(\theta)$  as well as a model of isotropic susceptibility in superposition with magic angle effects. In agreement with their data, pure magic angle effects cannot explain our measured  $T_2(\theta)$  dependency (see Figure 7(c)). In general, our fittings of  $T_2^*$  and  $T_2$  resemble their findings. However, as differences of the models including higher order terms are very subtle, we cannot exclude some additional influences of magic angle effects based on our data.

### Influence of WM orientation on $R_2'$

Since, in our approach,  $R_2'(\theta)$  is calculated from  $T_2^*$  and  $T_2$  (equation (1)), a strong orientation effect of approximately 27% was found, according to expectations (Figure 5(a)). Again, fitting of the model (equation (3)) is in excellent agreement with the measured  $R_2'(\theta)$  dependency (Figure 7(d)).

### Influence of WM orientation on rCBV

As could be expected from the fact that DSC-MRI is based on  $T_2^*$ -weighted EPI, our measurements revealed a pronounced dependency of rCBV on  $\theta$ . This

dependency is characterized by an almost angulation independent section for  $\theta = [0^\circ - 15^\circ]$  followed by a steep increase of rCBV for  $\theta = [15^\circ - 90^\circ]$  (Figure 5(c)). These findings are in full accordance with a previous study by Hernández-Torres et al.,<sup>12</sup> who analyzed DSC-based rCBV with a very similar methodology. The authors concluded anisotropic vascular architecture to significantly contribute to the observed CBV orientation effects, as histological staining demonstrated blood vessels running preferentially parallel to WM fibers.<sup>13,14</sup> Furthermore, via simulations they found evidence that one-third of the WM vascular volume is comprised of vessels aligned to the fiber tracts.<sup>12</sup>

Again, fitting Lee's model (equation (3)) to rCBV( $\theta$ ) revealed excellent agreement (Figure 7(e)). Interestingly, the ratio of the orientation-dependent fit coefficients  $c_1$  and  $c_2$  to the orientation independent coefficient  $c_0$  is much higher for the rCBV( $\theta$ ) fitting compared to  $T_2^*(\theta)$  and  $T_2(\theta)$  (Figure 7(a), (c) and (e)). This is related to the very strong orientation dependence of rCBV( $\theta$ ) ( $\approx 37\%$ ) and implies enhanced effects due to oriented vasculature in contrast agent-based DSC-imaging.

### Distribution of orientations

Even though the subvoxel WM structures are highly anisotropic, as indicated by high FA values within oriented WM (Figure 3), the orientations across all WM voxels are almost equally populated (Figure 6). Regarding the polar angle  $\theta$ , measured voxel distributions closely resemble a sinusoidal shape, representing

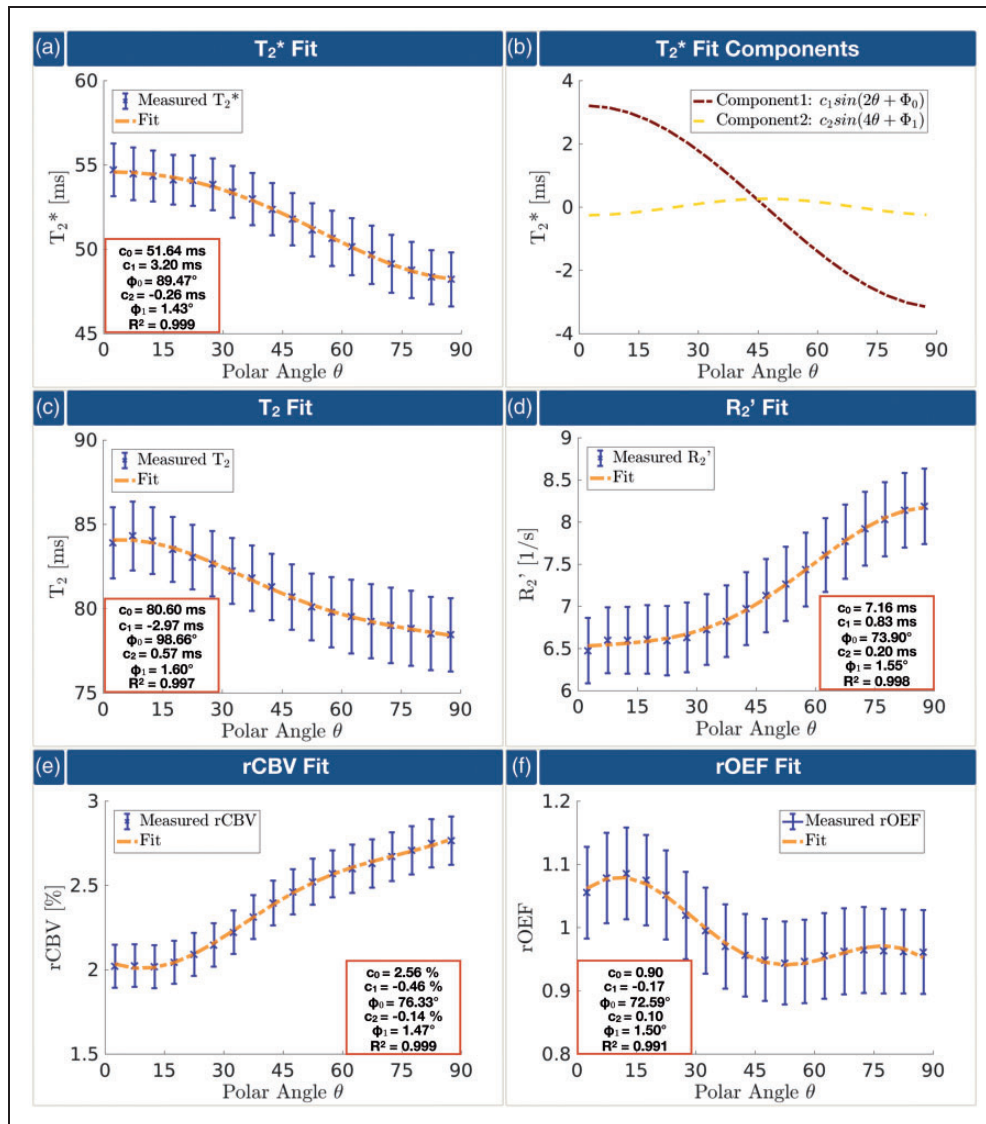


**Figure 7.** Fittings of all mq-BOLD-related parameters. All parameters were fitted with the same function (equation (3)). Median values on group-level and SDs are shown in blue, fitted curves are indicated by dashed orange lines. The fit parameters are noted in the red framed boxes (a, c–f). Analysis of the two sinusoidal fit components of  $T_2^*$  shows phase incoherence (b). All fittings of  $T_2^*$  (a),  $T_2$  (c),  $R_2'$  (d), rCBV (e) and rOEF (f) reveal excellent agreement with sum-of-squared-errors  $R^2 > 0.99$ .

equal populations (Figure 6(a)). Those results are in accordance with data from a similar approach by Denk et al.<sup>17</sup> However, our results are even closer to equal population, which might be due to different FA thresholds, our additional WM and CSF thresholds, larger sample size, higher number of DTI gradient directions and improved, automated coordinate transformation. Analysis of the voxel distribution with respect to the azimuthal angle  $\varphi$  reveals almost equal population, too (see Figure 6(b)). However, angles around  $\varphi = 0^\circ$  and  $\varphi = \pm 90^\circ$  tend to be somewhat higher populated indicating a slight preference for fiber orientations in right-left and anterior–posterior

orientations. Those findings are in accordance with DTI and histological examination of highly ordered structures such as the corpus callosum.<sup>59</sup>

Previous studies analyzing orientation effects by voxel-wise parameter correlations with DTI investigated either only the polar angle<sup>12,17,29</sup> or showed somewhat contra intuitive dependencies on the Euler angles relative to the x-axis and y-axis.<sup>11</sup> Those uncertainties could be resolved in our study by introducing spherical coordinates to describe the fiber orientation within the scanner coordinate system. Overall, the distribution of orientations underlines the successful implementation of the introduced automated coordinate system

transformation. Moreover, it strongly indicates the validity of our DTI-based orientation analysis.

### Influence of WM orientation on rOEF

A pronounced dependence of mq-BOLD-derived rOEF on  $\theta$  was expected, since the contributing parameters  $R_2'$  and rCBV demonstrate a distinct anisotropy in WM. However, the observed variation between lowest and highest values of 15% is rather weak compared to the strong variations of  $R_2'(\theta)$  ( $\approx 27\%$ ) and rCBV( $\theta$ ) ( $\approx 37\%$ ). Interestingly, rOEF( $\theta$ ) shows an angular dependency that appears distinctly different from the  $R_2'(\theta)$  and rCBV( $\theta$ ). This is due to counteracting influences of  $R_2'$  and rCBV, causing rOEF orientation artefacts to depend on their different slopes in the ratio of  $R_2'(\theta)$  and rCBV( $\theta$ ) (equation (2)) (Figure 5(a), (c) and (e)). Moreover, a closer analysis reveals that average orientation induced variation of rOEF( $\theta$ ) is rather low when accounting for the voxel distribution depending on  $\theta$ . The highest orientation induced variation of rOEF( $\theta$ ) was observed at low angles  $\theta < 30^\circ$  (Figure 5(e)), which actually corresponds to a small fraction of voxels (Figure 6(a)). Thus, the average variation, calculated via bin-wise deviations from the overall mean rOEF and weighting by the number of voxels within each angle-bin, is 3.8%. Those findings imply that mean values of WM rOEF are only weakly affected by orientation effects. Interestingly, fitting Lee's model (equation (3)) to rOEF( $\theta$ ) shows good agreement (Figure 7(f)) even if the underlying orientation effects of  $T_2^*$ ,  $T_2$  and rCBV are expected to arise from different origins and form complex superpositions within the mq-BOLD model (equation (2)).

### Possible limitations

Values of rOEF derived by mq-BOLD are systematically elevated, as previously reported.<sup>1,4,7,60</sup> Furthermore, WM values (average rOEF<sub>WM</sub> = 0.94) are elevated compared to GM values (average rOEF<sub>GM</sub> = 0.60; for more details, see Supplemental Table 2). This contradicts PET-based OEF measurements, and primarily arises from systematic errors of the mq-BOLD method. While approximating the venous CBV by total DSC-based CBV certainly contributes to GM-WM contrast, systematic bias in  $T_2$  measurement mainly causes general overestimation.<sup>1</sup> Improved quantitative  $T_2$  mapping has already been demonstrated to statistically significantly reduce rOEF elevations towards lower, physiologically more realistic values.<sup>61</sup> In this study, we could demonstrate that orientation effects do not primarily contribute to neither rOEF elevations nor the GM-WM contrast. Despite of this and successful applications of mq-BOLD in different pathologies,<sup>1,4,7,60</sup> future studies are

necessary to further validate and improve the method. Furthermore, observed diffusion-dependent  $T_2(\theta)$  orientation effects indicate that the assumption of static dephasing in mq-BOLD might be violated. In any case, caution should be exercised when evaluating rOEF by mq-BOLD in WM. To minimize detrimental influences of unphysiological GM-WM contrast, mq-BOLD evaluations should not mix values from GM and WM.

Generally, the large variations of  $T_2^*$ ,  $T_2$  and  $R_2'$  values and error propagation due to mq-BOLD modeling<sup>2</sup> limit the ability to differentiate between the different origins of anisotropy (see Appendix 1). The observed non-orientation-dependent parameter variations can be explained by further factors influencing transverse relaxation such as insufficiently corrected macroscopic magnetic background gradients, myelination and non-heme iron content or physiological differences.<sup>11,17</sup> Nevertheless, orientation effects of all investigated parameters could be clearly extracted by the presented methodology of automated coordinate system transformation, rigorous thresholding and averaging of all participant's data to minimize potential systematic errors.

Further limitations may apply. Measurements of  $T_2^*$  and  $T_2$  are known to depend on the echo sampling.<sup>62,63</sup> In addition, mono-exponential fitting to compute  $T_2^*$  and  $T_2$ -maps is a simplification as multi-compartmental effects in WM are well known.<sup>18,27,28,64</sup> But even if multi-exponential relaxation was contributing, our analysis depicts the dominant term.

Influences of age and WM pathology on the observed orientation effects may be suspected. To limit application of contrast agent in DSC-imaging, we investigated orientation effects in the elderly control group, which was also acquired for a physiological MRI study.<sup>8</sup> Additional control analyses revealed that higher Fazekas-scores of some of our elderly participants have no obvious impact on the observed orientation effects (Supplemental Figure 2). This is in accordance with Haller et al. who concluded that periventricular FLAIR hyperintensities are in many cases not associated with demyelination.<sup>65</sup> In order to control for age effects on  $T_2^*(\theta)$ ,  $T_2(\theta)$  and  $R_2(\theta)$  orientation dependencies, we compared the presented data to those of young healthy participants and found the same orientation dependencies, independent of age (Supplemental Figure 4).

Anisotropy effects of oriented susceptibility perturbations also depend on the magnetic field strength, where we expect stronger orientation dependencies with increasing  $B_0$ . Furthermore, sequence-dependent influences may for example arise from the voxel size, as the aspect ratio in GRE was found to affect the sensitivity to veins and may thereby also influence measured orientation dependencies.<sup>17</sup>



Another potential limitation is the scanning at only one head orientation. However, in vivo scanning at different head positions is experimentally very challenging and limited on both, reachable angles and the number of scanned angles.<sup>17</sup> In contrast, our investigation of tissue orientation effects based on analysis of DTI-data requires scanning at only one head position while deriving precise information about voxel-wise fiber orientations. Even though errors of DTI-based fiber orientation mapping induced by crossing fibers within single voxels cannot be corrected with the presented methodology,<sup>32</sup> thresholding of FA values reduced errors by excluding isotropic voxels.

A disadvantage of the DTI-based method may arise from patient movement between the mq-BOLD and the DTI acquisitions, but careful immobilization of the participant's head with foam pads and image coregistration could minimize motion-related errors. But in spite of careful inspection, small misalignments after coregistration cannot be ruled out completely. Nevertheless, the validity of the results is strongly supported by the excellent agreement of  $\theta$  dependent fittings with previous studies.

Analysis of orientation effects assumes  $B_0$  to be parallel to the  $z'$ -axis in our as well as previous studies.<sup>11,12,17,28,29</sup> However, magnetic field inhomogeneities, shimming and measurements off the iso-center may violate this assumption. Nevertheless, analysis of the azimuthal angle  $\phi$  revealed independence on the fiber orientation perpendicular to  $B_0$ , strongly indicating correct orientation analyses and generally high consistency of the presented data.

Partial volume effects are another potential error source affecting both, DTI orientation analysis and the mq-BOLD parameter estimates. However, those influences could be reduced by rigorous application of individual oriented WM masks excluding CSF.

### Impact of orientation effects

Tissue microstructure orientation effects may have far reaching consequences on many MRI parameters in WM. While we demonstrated mq-BOLD-derived rOEF to be only moderately affected by WM orientation effects,  $T_2^*$ ,  $T_2$ ,  $R_2'$  and rCBV strongly depend on the orientation. Moreover, orientation effects in WM are also known to affect arterial spin labeling and functional connectivity imaging.<sup>66</sup> Due to pial vessels orientation effects in the cortex, orientation dependencies were shown in GM, too.<sup>67</sup> Pathologies affecting the vessel architecture or the myelinisation may have additional influences, also by changing orientation effects regionally. This needs to be considered, especially when comparing different brain regions or hemispheres.

A promising method to further disentangle orientation effect origins by myelinated nerve fibers and oriented vessels is cortical surface modeling of GM.<sup>67</sup> Veins can be modelled depending on the cortical surface orientation to exclusively characterize vessel-related orientation effects.

### Conclusion

Our results demonstrate reliable in vivo characterization of WM anisotropy effects in mq-BOLD imaging with high sensitivity at reasonable scan time. We confirmed strong dependencies of transverse relaxation and rCBV on the nerve fiber orientation towards  $B_0$ . In contrast, observed orientation effects in rOEF values are comparably low in our healthy, elderly cohort indicating an average orientation induced variation of 3.8%. This is due to a partial compensation of anisotropy effects in  $R_2'$  and rCBV and indicates rather minor influences of orientation effects on mq-BOLD-derived rOEF in WM. In any case, caution should be exercised when evaluating mq-BOLD-derived rOEF in WM and further mq-BOLD validations are clearly necessary.

### Funding

The author(s) disclosed receipt of the following financial support for the research, authorship, and/or publication of this article: This work was supported by the Friedrich-Ebert-Stiftung (grant to SK), the Dr.-Ing. Leonhard Lorenz-Stiftung (grant to JG: 915/15), by the Faculty of Medicine of the Technical University of Munich (grant to JG: KKF E12), by a postdoc fellowship of the German Academic Exchange Service (DAAD) (grant for JG) and the German Research Foundation (DFG) – Project number PR 1039/6-1 (grant to CP). FH was supported by NIH grants (R01 MH-067528, R01 NS-100106, P30 NS-052519).

### Acknowledgements

We thank Andreas Hock (Philips Healthcare, Hamburg, Germany) for his support with the DTI orientation transformation.

### Declaration of conflicting interests

The author(s) declared no potential conflicts of interest with respect to the research, authorship, and/or publication of this article.

### Author's contributions

SK: study design, data acquisition, data analysis, interpretation of the results, manuscript writing.

JG: data acquisition, data analysis, interpretation of the results, manuscript editing.

CZ: study design, study supervision.

FH: interpretation of the results, manuscript editing.


CP: study design, study supervision, interpretation of the results, manuscript editing.


## Supplemental material

Supplemental material for this paper can be found at the journal website: <http://journals.sagepub.com/home/jcb>

## ORCID iDs

Stephan Kaczmarz  <http://orcid.org/0000-0001-7694-7012>

Jens Göttler  <http://orcid.org/0000-0002-5746-2156>

Christine Preibisch  <http://orcid.org/0000-0003-4067-1928>

## References

- Hirsch NM, Toth V, Forschler A, et al. Technical considerations on the validity of blood oxygenation level-dependent-based MR assessment of vascular deoxygenation. *NMR Biomed* 2014; 27: 853–862.
- Christen T, Schmiedeskamp H, Straka M, et al. Measuring brain oxygenation in humans using a multi-parametric quantitative blood oxygenation level dependent MRI approach. *Magn Reson Med* 2012; 68: 905–911.
- Leenders KL. PET: blood flow and oxygen consumption in brain tumors. *J Neurooncol* 1994; 22: 269–273.
- Preibisch C, Shi K, Kluge A, et al. Characterizing hypoxia in human glioma: a simultaneous multimodal MRI and PET study. *NMR Biomed* 2017; 30: e3775.
- Toth V, Forschler A, Hirsch NM, et al. MR-based hypoxia measures in human glioma. *J Neurooncol* 2013; 115: 197–207.
- Stadlbauer A, Zimmermann M, Kitzwogger M, et al. MR Imaging-derived oxygen metabolism and neovascularization characterization for grading and IDH gene mutation detection of gliomas. *Radiology* 2017; 283: 799–809.
- Gersing AS, Ankenbrank M, Schwaiger BJ, et al. Mapping of cerebral metabolic rate of oxygen using dynamic susceptibility contrast and blood oxygen level dependent MR imaging in acute ischemic stroke. *Neuroradiology* 2015; 57: 1253–1261.
- Göttler J, Kaczmarz S, Kallmayer M, et al. Flow-metabolism uncoupling in patients with asymptomatic unilateral carotid artery stenosis assessed by multi-modal magnetic resonance imaging. *J Cereb Blood Flow Metab*. Epub ahead of print 3 July 2018. DOI: 10.1177/0271678X18783369.
- Yablonskiy DA and Haacke EM. Theory of NMR signal behavior in magnetically inhomogeneous tissues: the static dephasing regime. *Magn Reson Med* 1994; 32: 749–763.
- Le Bihan D, Mangin JF, Poupon C, et al. Diffusion tensor imaging: concepts and applications. *J Magn Reson Imag* 2001; 13: 534–546.
- Bender B and Klose U. The in vivo influence of white matter fiber orientation towards B(0) on T2\* in the human brain. *NMR Biomed* 2010; 23: 1071–1076.
- Hernández-Torres E, Kassner N, Forkert ND, et al. Anisotropic cerebral vascular architecture causes orientation dependency in cerebral blood flow and volume measured with dynamic susceptibility contrast magnetic resonance imaging. *J Cereb Blood Flow Metab* 2017; 37: 1108–1119.
- Nonaka H, Akima M, Hatori T, et al. Microvasculature of the human cerebral white matter: arteries of the deep white matter. *Neuropathology* 2003; 23: 111–118.
- Cavaglia M, Dombrowski SM, Drazba J, et al. Regional variation in brain capillary density and vascular response to ischemia. *Brain Res* 2001; 910: 81–93.
- Mangla R, Kolar B, Almast J, et al. Border zone infarcts: pathophysiologic and imaging characteristics. *Radiographics* 2011; 31: 1201–1214.
- Lee J, Nam Y, Choi JY, et al. Mechanisms of T2\* anisotropy and gradient echo myelin water imaging. *NMR Biomed* 2017; 30: e3513.
- Denk C, Torres EH, MacKay A, et al. The influence of white matter fibre orientation on MR signal phase and decay. *NMR Biomed* 2011; 24: 246–252.
- Sati P, Silva AC, van Gelderen P, et al. In vivo quantification of T2\* anisotropy in white matter fibers in marmoset monkeys. *Neuroimage* 2012; 59: 979–985.
- Cherubini A, Peran P, Hagberg GE, et al. Characterization of white matter fiber bundles with T2\* relaxometry and diffusion tensor imaging. *Magn Reson Med* 2009; 61: 1066–1072.
- Oh S-H, Kim Y-B, Cho Z-H and Lee J. Origin of B(0) orientation dependent R(2)(\*) (=1/T(2)(\*)) in white matter. *Neuroimage* 2013; 73: 71–79.
- Lee J, Shmueli K, Kang BT, et al. The contribution of myelin to magnetic susceptibility-weighted contrasts in high-field MRI of the brain. *Neuroimage* 2012; 59: 3967–3975.
- He X and Yablonskiy DA. Biophysical mechanisms of phase contrast in gradient echo MRI. *Proc Natl Acad Sci U S A* 2009; 106: 13558–13563.
- Lee J, Shmueli K, Fukunaga M, et al. Sensitivity of MRI resonance frequency to the orientation of brain tissue microstructure. *Proc Natl Acad Sci U S A* 2010; 107: 5130–5135.
- Lee J, van Gelderen P, Kuo LW, et al. T2\*-based fiber orientation mapping. *Neuroimage* 2011; 57: 225–234.
- Li TQ, van Gelderen P, Merkle H, et al. Extensive heterogeneity in white matter intensity in high-resolution T2\*-weighted MRI of the human brain at 7.0 T. *Neuroimage* 2006; 32: 1032–1040.
- Li TQ, Yao B, van Gelderen P, et al. Characterization of T(2)\* heterogeneity in human brain white matter. *Magn Reson Med* 2009; 62: 1652–1657.
- Wharton S and Bowtell R. Fiber orientation-dependent white matter contrast in gradient echo MRI. *Proc Natl Acad Sci U S A* 2012; 109: 18559.
- Chen WC, Foxley S and Miller KL. Detecting microstructural properties of white matter based on compartmentalization of magnetic susceptibility. *Neuroimage* 2013; 70: 1–9.
- Hernandez-Torres E, Wiggermann V, Hametner S, et al. Orientation dependent MR signal decay differentiates between people with MS, their asymptomatic siblings and unrelated healthy controls. *PLoS One* 2015; 10: e0140956.
- Li W, Wu B, Avram AV and Liu C. Magnetic susceptibility anisotropy of human brain in vivo and its molecular underpinnings. *Neuroimage* 2012; 59: 2088–2097.

31. Wharton S and Bowtell R. Gradient echo based fiber orientation mapping using R2\* and frequency difference measurements. *Neuroimage* 2013; 83: 1011–1023.
32. Schilling KG, Janve V, Gao Y, et al. Histological validation of diffusion MRI fiber orientation distributions and dispersion. *Neuroimage* 2018; 165: 200–221.
33. Yablonskiy DA and Sukstanskii AL. Generalized Lorentzian tensor approach (GLTA) as a biophysical background for quantitative susceptibility mapping. *Magn Reson Med* 2015; 73: 757–764.
34. Yablonskiy DA, Reinos WR, Stark H, et al. Quantitation of T2' anisotropic effects on magnetic resonance bone mineral density measurement. *Magn Reson Med* 1997; 37: 214–221.
35. Liu C. Susceptibility tensor imaging. *Magn Reson Med* 2010; 63: 1471–1477.
36. Chappell KE, Robson MD, Stonebridge-Foster A, et al. Magic angle effects in MR neurography. *AJNR Am J Neuroradiol* 2004; 25: 431–440.
37. Kluge A, Lukas M, Toth V, et al. Analysis of three leakage-correction methods for DSC-based measurement of relative cerebral blood volume with respect to heterogeneity in human gliomas. *Magn Reson Imaging* 2016; 34: 410–421.
38. Hedderich D, Kluge A, Pyka T, et al. Consistency of normalized cerebral blood volume values in glioblastoma using different leakage correction algorithms on dynamic susceptibility contrast magnetic resonance imaging data without and with prebolus. *J Neuroradiology* 2019; 46: 44–51.
39. Soares JM, Marques P, Alves V, et al. A hitchhiker's guide to diffusion tensor imaging. *Front Neurosci* 2013; 7: 31.
40. Hirsch NM and Preibisch C. T2\* mapping with background gradient correction using different excitation pulse shapes. *AJNR Am J Neuroradiol* 2013; 34: E65–E68.
41. Baudrexel S, Volz S, Preibisch C, et al. Rapid single-scan T2\*-mapping using exponential excitation pulses and image-based correction for linear background gradients. *Magn Reson Med* 2009; 62: 263–268.
42. Magerkurth J, Volz S, Wagner M, et al. Quantitative T2\*-mapping based on multi-slice multiple gradient echo flash imaging: retrospective correction for subject motion effects. *Magn Reson Med* 2011; 66: 989–997.
43. Welker K, Boxerman J, Kalnin A, et al. ASFN recommendations for clinical performance of MR dynamic susceptibility contrast perfusion imaging of the brain. *AJNR Am J Neuroradiol* 2015; 36: E41–E51.
44. Fazekas F, Chawluk JB, Alavi A, et al. MR signal abnormalities at 1.5 T in Alzheimer's dementia and normal aging. *AJR Am J Roentgenol* 1987; 149: 351–356.
45. Woolrich MW, Jbabdi S, Patenaude B, et al. Bayesian analysis of neuroimaging data in FSL. *Neuroimage* 2009; 45: S173–S186.
46. Penny WD, Friston KJ, Ashburner JT, et al. *Statistical parametric mapping: the analysis of functional brain images*. Amsterdam: Elsevier Science, 2011.
47. Boxerman JL, Schmainda KM and Weisskoff RM. Relative cerebral blood volume maps corrected for contrast agent extravasation significantly correlate with glioma tumor grade, whereas uncorrected maps do not. *AJNR Am J Neuroradiol* 2006; 27: 859–867.
48. Mineura K, Sasajima T, Kowada M, et al. Perfusion and metabolism in predicting the survival of patients with cerebral gliomas. *Cancer* 1994; 73: 2386–2394.
49. Spees WM, Yablonskiy DA, Oswood MC, et al. Water proton MR properties of human blood at 1.5 Tesla: magnetic susceptibility, T(1), T(2), T\*(2), and non-Lorentzian signal behavior. *Magn Reson Med* 2001; 45: 533–542.
50. Silvennoinen MJ, Clingman CS, Golay X, et al. Comparison of the dependence of blood R2 and R2\* on oxygen saturation at 1.5 and 4.7 Tesla. *Magn Reson Med* 2003; 49: 47–60.
51. Jenkinson M and Smith S. A global optimisation method for robust affine registration of brain images. *Med Image Anal* 2001; 5: 143–156.
52. Jenkinson M, Bannister P, Brady M, et al. Improved optimization for the robust and accurate linear registration and motion correction of brain images. *Neuroimage* 2002; 17: 825–841.
53. Smith SM. Fast robust automated brain extraction. *Hum Brain Mapp* 2002; 17: 143–155.
54. Behrens TE, Woolrich MW, Jenkinson M, et al. Characterization and propagation of uncertainty in diffusion-weighted MR imaging. *Magn Reson Med* 2003; 50: 1077–1088.
55. Behrens TE, Berg HJ, Jbabdi S, et al. Probabilistic diffusion tractography with multiple fibre orientations: what can we gain?. *Neuroimage* 2007; 34: 144–155.
56. Li X, Vikram DS, Lim IA, et al. Mapping magnetic susceptibility anisotropies of white matter in vivo in the human brain at 7 T. *Neuroimage* 2012; 62: 314–330.
57. Lee J, Shin HG, Jung W, et al. An R2\* model of white matter for fiber orientation and myelin concentration. *Neuroimage* 2017; 162: 269–275.
58. Le Bihan D, Turner R and Douek P. Is water diffusion restricted in human brain white matter? An echo-planar NMR imaging study. *Neuroreport* 1993; 4: 887–890.
59. Mollink J, Kleinnijenhuis M, Cappellen van Walsum A-Mv, et al. Evaluating fibre orientation dispersion in white matter: comparison of diffusion MRI, histology and polarized light imaging. *Neuroimage* 2017; 157: 561–574.
60. Wiestler B, Kluge A, Lukas M, et al. Multiparametric MRI-based differentiation of WHO grade II/III glioma and WHO grade IV glioblastoma. *Sci Rep* 2016; 6: 35142.
61. Kaczmarz S, Goettler J, Hock A, et al. Reducing T2-related bias in mq-BOLD derived maps of Oxygen Extraction Fraction by 3D acquisition. In: *Proceedings of the international society of magnetic resonance in medicine*, Paris, France, 26 June 2018.
62. Stefanovic B, Sled JG and Pike GB. Quantitative T2 in the occipital lobe: the role of the CPMG refocusing rate. *J Magn Reson Imaging* 2003; 18: 302–309.
63. Bartha R, Michaeli S, Merkle H, et al. In vivo 1H2O T measurement in the human occipital lobe at 4T and 7T by Carr-Purcell MRI: detection of microscopic susceptibility contrast. *Magn Reson Med* 2002; 47: 742–750.

64. Du YP, Chu R, Hwang D, et al. Fast multislice mapping of the myelin water fraction using multicompartiment analysis of  $T_2^*$  decay at 3T: a preliminary postmortem study. *Magn Reson Med* 2007; 58: 865–870.
65. Haller S, Kövari E, Herrmann FR, et al. Do brain  $T_2$ /FLAIR white matter hyperintensities correspond to myelin loss in normal aging? A radiologic-neuropathologic correlation study. *Acta Neuropathol Commun* 2013; 1: 14.
66. Aslan S, Huang H, Uh J, et al. White matter cerebral blood flow is inversely correlated with structural and functional connectivity in the human brain. *Neuroimage* 2011; 56: 1145–1153.
67. Gagnon L, Sakadzic S, Lesage F, et al. Validation and optimization of hypercapnic-calibrated fMRI from oxygen-sensitive two-photon microscopy. *Philos Trans R Soc Lond B Biol Sci* 2016; 371: 20150359.

## Appendix

To estimate errors of mq-BOLD-derived rOEF, linear error propagation was performed. The function  $f(T_2, T_2^*, rCBV)$  describes the mq-BOLD-based rOEF calculation

$$f(T_2, T_2^*, rCBV) = \frac{\frac{1}{T_2^*} - \frac{1}{T_2}}{c \cdot rCBV} \quad (4)$$

Linear error propagation of the function  $f$  depending on  $T_2$ ,  $T_2^*$  and  $rCBV$  leads to

$$\Delta f = \left| \frac{\partial f(T_2, T_2^*, rCBV)}{\partial T_2} \right| \cdot \Delta T_2 + \left| \frac{\partial f(T_2, T_2^*, rCBV)}{\partial T_2^*} \right| \cdot \Delta T_2^* + \left| \frac{\partial f(T_2, T_2^*, rCBV)}{\partial rCBV} \right| \cdot \Delta rCBV \quad (5)$$

with the partial derivatives

$$\left| \frac{\partial f(T_2, T_2^*, rCBV)}{\partial T_2} \right| = \frac{1}{c \cdot T_2^2 \cdot rCBV} \quad (6)$$

$$\left| \frac{\partial f(T_2, T_2^*, rCBV)}{\partial T_2^*} \right| = \frac{1}{c \cdot T_2^{*2} \cdot rCBV} \quad (7)$$

$$\left| \frac{\partial f(T_2, T_2^*, rCBV)}{\partial rCBV} \right| = \frac{\frac{1}{T_2^*} - \frac{1}{T_2}}{c \cdot rCBV^2} \quad (8)$$

Assuming rounded WM median values of  $T_2 = 80$  ms,  $T_2^* = 50$  ms,  $rCBV = 2.5\%$  yielded an absolute value of  $rOEF = f(T_2 = 80$  ms,  $T_2^* = 50$  ms,  $rCBV = 2.5\%) = 0.97$  (equation (4)). Those values were applied to the partial derivatives (equations (6) to (8)) to estimate the absolute rOEF error in healthy participants (equation (5)), while statistical errors of 2.5% each for  $T_2$  and  $T_2^*$  and 5% for  $rCBV$  were assumed according to recent publications,<sup>1,61</sup> resulting in  $\Delta rOEF = \Delta f(T_2 = 80$  ms  $\pm 2.5\%$ ,  $T_2^* = 50$  ms  $\pm 2.5\%$ ,  $rCBV = 2.5\% \pm 5\%) = 0.15$ . To account for those approximated rOEF errors of 15%, orientation effects were averaged over all oriented WM voxels of all 28 evaluated participants within 5° bins.



## 7.3 Journal Publication III:

### Hemodynamic impairments within individual watershed areas in asymptomatic carotid artery stenosis by multimodal MRI

The publication entitled *Hemodynamic impairments within individual watershed areas in asymptomatic carotid artery stenosis by multimodal MRI* was published in the Journal of Cerebral Blood Flow and Metabolism (JCBFM, ISSN: 1559-7016) electronically on 1 April 2020 under the Creative Commons licence BY-NC 4.0 [188]. The manuscript was authored by Stephan Kaczmarz, Jens Goettler, Jan Petr, Mikkel Bo Hansen, Kim Mouridsen, Claus Zimmer, Fahmeed Hyder and Christine Preibisch. It is available online (DOI: 10.1177/0271678X19839502) under Copyright © by the Authors. Preliminary results were also presented in conference contributions C6, C7, C8 and C13, awarded with an ISMRM Magna Cum Laude Merit Award and ESMRMB Student Support Programme as well as invited for oral presentation at the ESMRMB annual meeting 2019, the BRAIN & BRAIN PET biannual meeting 2019 and DGNR annual meeting 2019, each. A summary of the publication is provided in Section 7.3.1, the author contributions are listed in Section 7.3.2 and the full text is included subsequently on the following pages.

#### 7.3.1 Abstract

##### Purpose

Improved understanding of complex hemodynamic impairments in asymptomatic internal carotid artery stenosis (ICAS) is highly promising to better assess individual hemodynamic impairments. Multi-parametric MRI is ideal to gain deeper insights to cerebral hemodynamics and furthermore has great potential to improve diagnostics and support treatment decisions. However, potentially clinically applicable methods require further evaluations and the sensitivity to hemodynamic impairments needs to be improved. We thus applied MRI-based perfusion and oxygenation imaging in ICAS-patients with the hypothesis to increase the sensitivity to hemodynamic impairments by applying individual watershed areas (iWSA).

##### Methods

For this study, 29 patients with asymptomatic, unilateral, high-grade ICAS and 30 age-matched elderly healthy controls were scanned on a standard clinical 3T MRI-scanner and six different hemodynamic parameters were mapped. Specifically, cerebral blood flow (CBF) using pseudo-continuous arterial spin labeling (pCASL), cerebrovascular reactivity (CVR) using breath-hold functional MRI (BH-fMRI), relative oxygen extraction fraction (rOEF) using multi-parametric quantitative BOLD (mq-BOLD) as well as relative cerebral blood volume (rCBV), capillary transit-time heterogeneity (CTH) and oxygen extraction capacity (OEC) using dynamic susceptibility contrast (DSC) imaging were studied. Those six parameters were evaluated in GM and WM and inside versus outside of iWSAs.

##### Results

Significant impairments of CBF, CVR, rCBV, OEC, and CTH were found in ICAS-patients, but not of rOEF. Strongest lateralisation between hemispheres was found for  $\Delta CVR = -24\%$ . While the spatial overlap of compromised hemodynamic parameters within each patient varied

in a complex manner, most pronounced changes of CBF, CVR and rCBV were detected within iWSAs. Highest sensitivity improvements to hemodynamic impairments within iWSAs was found for  $\Delta CVR = +117\%$ . At the same time, OEC and CTH impairments were iWSA independent, indicating more widespread dysfunction of capillary-level oxygen diffusivity. The specificity of the applied methods was affirmed by normal results in the healthy controls without hemispheric lateralization.

### **Conclusion**

In summary, MRI-based perfusion and oxygenation sensitive parameters offer complementary information and thereby deeper perspectives on complex microvascular impairments of individual patients. Improved sensitivity to hemodynamic impairments within iWSAs was demonstrated. Thus, multi-parametric hemodynamic MRI is highly promising to improve clinical diagnostics and gain a broader perspective on pathophysiological conditions in ICAS.

### **7.3.2 Author contributions**

The first author adapted the magnetic resonance pulse sequence (proprietary hardware specific libraries and software from Philips Medical Systems (Best, The Netherlands)), developed and implemented the processing pipeline, processed the data, developed and implemented the database to interpret the multi-parametric data using Matlab (Mathworks, Natick, MA); With the help and consultation from the coauthors: designed the experiment, performed the experiments (MR measurements), developed and implemented parts of the data post-processing pipeline, interpreted the results, and wrote the paper.

# Hemodynamic impairments within individual watershed areas in asymptomatic carotid artery stenosis by multimodal MRI

Journal of Cerebral Blood Flow &amp; Metabolism

0(0) 1–17

© The Author(s) 2020



Article reuse guidelines:

[sagepub.com/journals-permissions](https://sagepub.com/journals-permissions)

DOI: 10.1177/0271678X20912364

[journals.sagepub.com/home/jcbfm](https://journals.sagepub.com/home/jcbfm)

Stephan Kaczmarz<sup>1,2,3</sup> , Jens Göttler<sup>1,2,3,4</sup> , Jan Petr<sup>5</sup> ,  
Mikkel Bo Hansen<sup>6</sup> , Kim Mouridsen<sup>6</sup>, Claus Zimmer<sup>1</sup>,  
Fahmeed Hyder<sup>3</sup> and Christine Preibisch<sup>1,2,7</sup> 

## Abstract

Improved understanding of complex hemodynamic impairments in asymptomatic internal carotid artery stenosis (ICAS) is crucial to better assess stroke risks. Multimodal MRI is ideal for measuring brain hemodynamics and has the potential to improve diagnostics and treatment selections. We applied MRI-based perfusion and oxygenation-sensitive imaging in ICAS with the hypothesis that the sensitivity to hemodynamic impairments will improve within individual watershed areas (iWSA). We studied cerebral blood flow (CBF), cerebrovascular reactivity (CVR), relative cerebral blood volume (rCBV), relative oxygen extraction fraction (rOEF), oxygen extraction capacity (OEC) and capillary transit-time heterogeneity (CTH) in 29 patients with asymptomatic, unilateral ICAS (age  $70.3 \pm 7.0$  y) and 30 age-matched healthy controls. In ICAS, we found significant impairments of CBF, CVR, rCBV, OEC, and CTH (strongest lateralization  $\Delta\text{CVR} = -24\%$ ), but not of rOEF. Although the spatial overlap of compromised hemodynamic parameters within each patient varied in a complex manner, most pronounced changes of CBF, CVR and rCBV were detected within iWSAs (strongest effect  $\Delta\text{CVR} = +117\%$ ). At the same time, CTH impairments were iWSA independent, indicating widespread dysfunction of capillary-level oxygen diffusivity. In summary, complementary MRI-based perfusion and oxygenation parameters offer deeper perspectives on complex microvascular impairments in individual patients. Furthermore, knowledge about iWSAs improves the sensitivity to hemodynamic impairments.

## Keywords

Asymptomatic internal carotid artery stenosis, cerebrovascular disease, hemodynamics, individual watershed areas, magnetic resonance imaging

Received 6 September 2019; Revised 23 December 2019; Accepted 7 February 2020

## Introduction

Asymptomatic internal carotid artery stenosis (ICAS) is a major public health issue. It causes approximately 10% of all strokes<sup>1</sup> and is also associated with cognitive decline.<sup>2,3</sup> While effective interventions are available, they come with substantial risks.<sup>4</sup> In this regard, identification of individual patients with high stroke risk who could benefit from a more invasive treatment is crucial. Multimodal magnetic resonance imaging (MRI) of perfusion and oxygenation is highly promising to understand hemodynamic dysfunctions of ICAS patients and to gain deeper insights into the pathology.

<sup>1</sup>Department of Neuroradiology, School of Medicine, Technical University of Munich (TUM), Munich, Germany

<sup>2</sup>TUM Neuroimaging Center (TUM-NIC), Technical University of Munich (TUM), Munich, Germany

<sup>3</sup>MRRC, Yale University, New Haven, CT, USA

<sup>4</sup>Department of Radiology, School of Medicine, Technical University of Munich (TUM), Munich, Germany

<sup>5</sup>PET Center, Institute of Radiopharmaceutical Cancer Research, Helmholtz-Zentrum Dresden-Rossendorf, Dresden, Germany

<sup>6</sup>Center of Functionally Integrative Neuroscience, Aarhus University, Aarhus, Denmark

<sup>7</sup>Clinic for Neurology, School of Medicine, Technical University of Munich (TUM), Munich, Germany

## Corresponding author:

Stephan Kaczmarz, Department of Neuroradiology, School of Medicine, Technical University of Munich, Ismaninger Str. 22, 81675 München, Germany.

Email: [stephan.kaczmarz@tum.de](mailto:stephan.kaczmarz@tum.de)

This could be used for personalized stroke risk assessment<sup>5</sup> and improved treatment guidelines<sup>6</sup> to reduce overall risk of ischemia. While perfusion deficits in ICAS have been investigated intensively,<sup>7–11</sup> the relationships among different types of hemodynamic impairments in individual patients remain unclear and need further characterization.<sup>5</sup> Furthermore, improved sensitivity to even subtle hemodynamic changes is necessary. It is already known that border zones between perfusion territories are most vulnerable to hemodynamic impairment.<sup>12,13</sup> ICAS significantly increases the spatial variability of these watershed areas,<sup>14</sup> e.g. by collateral flow.<sup>15</sup> Therefore, hemodynamic parameter evaluation within individually defined watershed areas (iWSA)<sup>14</sup> appears especially promising in ICAS to increase the sensitivity.

Atherosclerotic plaque in ICAS causes decreased cerebral perfusion pressure (CPP).<sup>16</sup> Its impact on hemodynamics has been studied extensively.<sup>5,10,17</sup> In 1987, Powers et al. characterized hemodynamic changes caused by reduced CPP in two sequential stages.<sup>18</sup> First, autoregulatory vasodilation causes increased cerebral blood volume (CBV) and concomitantly reduced cerebrovascular reactivity (CVR). Second, when autoregulation can no longer compensate for further decreases in CPP, the cerebral blood flow (CBF) decreases. Consequently, an increase in the oxygen extraction fraction (OEF) helps with sustaining the oxidative metabolism, thereby preventing strokes. However, experimental evidence has partially contradicted this simple picture. A positron emission tomography (PET) study in patients with carotid occlusions demonstrated increased OEF already at supposedly normal CBV.<sup>10</sup> A study in an animal ischemia model suggested reduced CBF already within the autoregulatory range.<sup>19</sup> Recent MRI studies have also reported unchanged OEF with a decreased CBF.<sup>7,11</sup> This mismatch between the OEF and CBF changes might indicate microscopic variations of oxygen diffusivity from the capillary bed to brain tissue, as proposed by Hyder et al.<sup>20–22</sup>

While earlier PET studies revealed important information on ICAS-related hemodynamic impairments, the clinical applicability is restricted by limited availability, methodological complexity, radioactive tracer application and high costs of <sup>15</sup>O PET. Emerging MRI methods now allow a comprehensive evaluation of tissue perfusion and oxygenation, and a non-invasive measurement of up to six hemodynamic parameters within a single session. This provides new possibilities to derive comprehensive information about the localization and extent of hemodynamic impairments. CBF and CVR can be measured non-invasively by pseudo-continuous arterial spin labeling (pCASL)<sup>23</sup> and breath-hold functional MRI

(BH-fMRI),<sup>24</sup> respectively. Previous studies have already demonstrated that CVR can help to predict the stroke risk.<sup>25,26</sup> Using multi-parametric quantitative BOLD (mq-BOLD) imaging, the relative oxygen extraction fraction (rOEF) can be modeled based on separate mapping of quantitative T<sub>2</sub> and T<sub>2</sub><sup>\*</sup>, together with relative CBV (rCBV) using dynamic susceptibility contrast (DSC) imaging.<sup>27</sup> In addition to perfusion and mq-BOLD-based oxygenation imaging, a parametric modeling approach for DSC data, introduced by Jespersen and Østergaard, offers the possibility of exploring capillary dysfunction in ICAS.<sup>28–30</sup> Here, capillary transit-time heterogeneity (CTH) and oxygen extraction capacity (OEC), which describes the maximum possible OEF, are modeled additionally from DSC data. In combination, these six parameters are highly promising to evaluate these novel quantitative physiological MRI techniques towards personalized stroke risk assessment.<sup>5</sup>

The aim of this study was therefore to gain deeper insights into the complex interplay of hemodynamic impairments in ICAS by measuring six microvascular MRI biomarkers (CBF, CVR, rCBV, rOEF, OEC and CTH) in patients with asymptomatic ICAS and age-matched healthy controls (HC). Moreover, we aimed to study the perfusion and oxygenation sensitive parameters inside and outside the iWSAs. We hypothesized that combinations of these perfusion and oxygenation parameters and evaluation within subject-specific iWSAs<sup>14</sup> will improve the sensitivity to hemodynamic impairments in ICAS.

## Methods

### Participants

Fifty-nine subjects participated in this prospective study. We scanned 29 patients with asymptomatic, unilateral, high-grade, extracranial ICAS (>70% according to NASCET<sup>31</sup> confirmed by duplex ultrasonography; 10 females; mean age 70.3 ± 7.0 years; without TIA/stroke-like symptoms; see Table 1) and 30 age-matched HCs (17 females; mean age 70.2 ± 4.8 years). Asymptomatic ICAS patients were identified by incidental findings. Healthy controls were enrolled by word-of-mouth advertisement from May 2015 until May 2017. The examination included medical history, basic neurological examination and MRI. Exclusion criteria were any neurological, psychiatric or systemic diseases, clinically remarkable structural MRI findings (e.g. territorial stroke lesions, bleedings, or a history of brain surgery), severe chronic kidney disease or MR contraindications. The study was approved by the medical ethical board of the Klinikum rechts der Isar, in line with Human Research

**Table 1.** Clinical characteristics for ICAS patients and healthy controls.

	Patients (n = 29)	Healthy Controls (n = 30)	p
Age (years)	70.3 ± 7.0 y	70.2 ± 4.8 y	0.94
Female sex (No. (%))	10 (34%)	17 (57%)	0.09
Stenotic degree (NASCET)	81.2 ± 10.1 %	–	
Stenosis left-/right-sided (No.)	10/19	–	
Good collateralization	17 (59%)	20 (67%)	0.34
Smoking (No. (%))	15 (52%)	11 (37%)	0.25
Mean pack-years in smokers	34.9 ± 21.9	21.5 ± 15.3	
Hypertension (No. (%))	23 (79%)	16 (53%)	0.04*
Mean BP (mmHg, sys./dias.)	154±23/86±10	140±20/84±7	0.01*/0.42
Body mass index	26.3 ± 4.7	26.6 ± 4.2	0.76
Diabetes (No. (%))	8 (28%)	2 (7%)	0.03*
Medication (No. (%))			
Antiplatelets	26 (90%)	6 (20%)	<0.01*
Statins	19 (66%)	7 (23%)	0.10
Antihypertensives	20 (69%)	12 (40%)	0.19
CHD/PAOD (No. (%))	16 (55%)	6 (20%)	<0.01*
MMSE	27.9 ± 2.6	28.6 ± 1.4	0.19
TMT-A (s)	49.3 ± 23.1	46.7 ± 29.7	0.72
TMT-B (s)	134.1 ± 65.5	116.9 ± 63.1	0.18
BDI	9.2 ± 9.9	8.4 ± 5.1	0.66
STAI	38.3 ± 14.8	24.5 ± 11.5	0.23

Note: Variables are represented by the mean values and standard deviations. Two-sample t-tests were used for age, BP, and body mass index. Chi-squared test for remaining group comparisons. Asterisks indicate significant group differences ( $p < 0.05$ ). Collateralization status of the circle of Willis was assessed by the presence of ACOM and PCOMs, based on contrast agent-based angiography scans.

BDI: Beck's depression inventory; BP: blood pressure; CHD: coronary heart disease; LBT: line bisection test; MMSE: mini-mental state examination; PAOD: peripheral artery occlusive disease; STAI: state trait anxiety inventory; TMT-A/B: trail making test–A/B.

Committee guidelines of the Technical University of Munich (TUM). All participants provided informed written consent in accordance with the standard protocol approvals.

### Image acquisition

The multimodal MRI protocol was performed using a clinical 3T Philips Ingenia MR-Scanner (Philips Healthcare, Best, The Netherlands) using a 16-channel head/neck and 32-channel head receive-coil. Custom patches were applied on software release R5.1.8 to optimize  $T_2^*$  imaging by macroscopic background gradient correction,<sup>32,33</sup> to apply multiband imaging (MB)<sup>34</sup> and to improve pCASL by 3D GraSE readout, prolonged labeling and improved background suppression (BGS).<sup>35</sup> Details of the imaging protocol were as follows (Figure 1):

- *Structural imaging* involved  $T_2$ -weighted FLAIR (TE = 289 ms, TR = 4800 ms, inversion delay 1650 ms, TSE factor 167, 163 slices, matrix size 224 × 224, voxel size 1.12 × 1.12 × 1.12 mm<sup>3</sup>, acquisition time 4:34 min) and  $T_1$ -weighted MPRAGE (TE = 4 ms, TR = 9 ms,  $\alpha = 8^\circ$ , TI = 1000 ms, shot interval 2300 ms, SENSE AP/RL 1.5/2.0, 170 slices, matrix size 240 × 238, voxel size 1 × 1 × 1 mm<sup>3</sup>, acquisition time

5:59 min) to facilitate brain screening for lesions, their rating according to the Fazekas-score<sup>36</sup> (Rater: JG) and tissue segmentation, respectively.

- *pCASL* was performed according to the ISMRM perfusion study group consensus paper<sup>23</sup> and as described previously.<sup>11</sup> Since we applied single post label delay (PLD), a prolonged PLD of 2000 ms was used, which followed the consensus recommendations.<sup>23</sup> The other imaging parameters were: Label duration 1800 ms, 4 BGS pulses, segmented 3D GraSE readout (TE = 7.4 ms, TR = 4377 ms,  $\alpha = 90^\circ$ , 16 slices, TSE factor 19, echo planar imaging (EPI) factor 7, acquisition voxel size 2.75 × 2.75 × 6.0 mm<sup>3</sup>), three dynamics including a proton density weighted (PD-weighted)  $M_0$  scan, and an acquisition time of 5:41 min.
- *BH-fMRI* was performed according to Pillai et al.<sup>24</sup> with five end-expiratory breath-holds of 15 s that were altered with 45 s of normal breathing. Imaging was performed by single-shot EPI with TE = 30 ms, TR = 1200 ms,  $\alpha = 70^\circ$ , MB 2, SENSE 2, 38 slices, matrix size 64 × 62, voxel size 3 × 3 × 3 mm<sup>3</sup>, acquisition time 5:48 min.
- *$T_2$ -mapping* was based on an eight echo gradient-spin-echo (GraSE) sequence as described previously<sup>27</sup>: TE<sub>1</sub> =  $\Delta$ TE = 16 ms, TR = 8596 ms, EPI factor



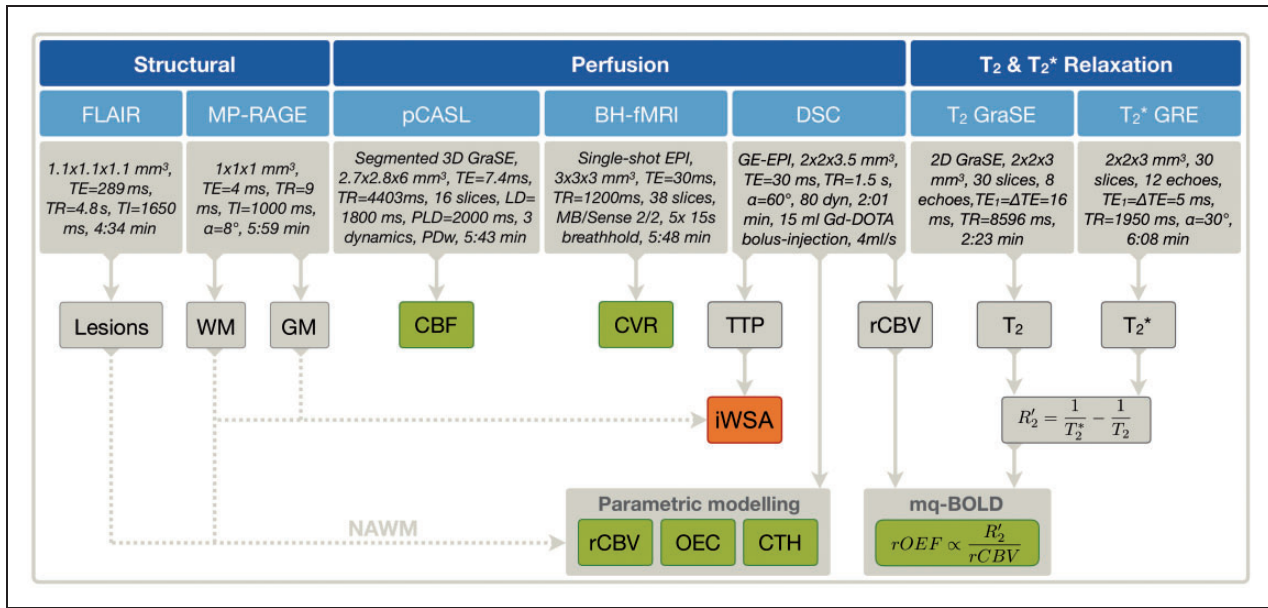


**Figure 1.** Overview of MRI protocol and derived parameters. Structural imaging comprised FLAIR and MP-RAGE for lesion detection and the generation of white matter (WM) and gray matter (GM) masks. Pseudo-continuous arterial spin labeling (pCASL) was applied to measure cerebral blood flow (CBF) and breath-hold fMRI (BH-fMRI) for cerebral vascular reactivity (CVR). By DSC-MRI, time to peak (TTP) maps were derived and used to generate individual watershed areas (iWSA) for each participant, which were additionally GM/WM masked. By parametric modeling, relative cerebral blood volume (rCBV), oxygen extraction capacity (OEC), and capillary transit-time heterogeneity (CTH) maps were calculated. By mq-BOLD, rOEF was modeled based on rCBV (normalized to CBV = 2.5% in NAWM), T<sub>2</sub> and T<sub>2</sub>\*. The iWSA-mask (orange box) was applied to each of the six hemodynamic biomarkers (green boxes) for all participants. For group level analyses, average parameter values were calculated for both hemispheres inside and outside of iWSAs in GM and WM.

47, 30 slices, gap 0.3 mm, matrix 112 × 91, voxel size 2 × 2 × 3 mm<sup>3</sup>, acquisition time 2:23 min.

- T<sub>2</sub>\*-mapping used a 12-echo gradient echo (GRE) sequence featuring exponential excitation pulses to facilitate correction of magnetic background gradients<sup>33</sup> and duplicate acquisition of the k-space center for motion correction,<sup>37</sup> as described previously<sup>27</sup>: TE<sub>1</sub> = ΔTE = 5 ms, TR = 1950 ms, α = 30°, mono-polar readout, 30 slices, matrix size 112 × 92, voxel size 2 × 2 × 3 mm<sup>3</sup>, total acquisition time 6:08 min.
- DSC-MRI used dynamic acquisition of 80 single-shot gradient-echo EPI volumes (TE = 30 ms, TR = 1513 ms, α = 60°, 26 slices, voxel size 2.0 × 2.0 × 3.5 mm<sup>3</sup>, acquisition time 2:01 min) during injection of a weight-adjusted Gd-DOTA bolus (concentration 0.5 mmol/ml, dose 0.1 mmol/kg, at least 7.5 mmol per subject, flow rate 4 ml/s, injection 7.5 s after DSC imaging onset, with a 40 ml saline flush), which followed the ASFN recommendations<sup>38</sup> and as described previously.<sup>39</sup> Contrast-enhanced angiography of the arteries of the neck and the aortic arch was also performed to exclude other relevant stenoses arteries that supply

the brain. The angiography was performed before the DSC and also served as a prebolus.

### Image analysis

All processing procedures used custom MATLAB programs (MATLAB R2016b, MathWorks, Natick, MA, USA) and SPM12 (Wellcome Trust Centre for Neuroimaging, UCL, London, UK). All parameter maps were screened, especially for motion artefacts (raters CP, SK), to exclude scans with low data quality from the final evaluation. The following parameter maps were calculated:

- GM and WM tissue masks were created by segmentation of MPRAGE images and thresholding of those maps with p > 0.70.
- Quantitative CBF was derived from pCASL, where label and control images were motion corrected, averaged, subtracted, and the M<sub>0</sub> image was included in the calculations according to Alsop et al.<sup>23</sup> An additional signal reduction of 25% was assumed due to the application of BGS.<sup>40,41</sup> The resulting CBF maps were smoothed by a 3D Gaussian kernel with FWHM of 5 mm. CBF maps did not show

evidence of arterial transit time (ATT) artefacts<sup>11</sup> on careful visual inspection of unsmoothed CBF maps (JG, CP, SK) and as implied by a spatial coefficient of variation  $<0.45$  according to Mutsaerts et al.<sup>42</sup>

- Relative CVR maps were obtained from BH-fMRI data.<sup>24</sup> Time series data were motion corrected and CVR was measured using beta-values that were calculated by regression of a respiratory response function after correcting for a global time delay in a model-driven approach according to Vondráčková et al.<sup>43</sup>
- iWSAs were defined based on temporal delays in perfusion, because of their peripheral location at the edge of vascular territories, as previously presented.<sup>14</sup> Temporal information was obtained from DSC-based time-to-peak (TTP) maps. To this end, smoothed TTP-maps were segmented semi-automatically. Their location was confirmed by comparison with an arterial transit time atlas and assessment of perfusion territories by vessel selective ASL for a subgroup of patients as previously presented.<sup>14</sup>
- Parametric modeling of DSC-data followed the approach of Jespersen and Østergaard<sup>28</sup> with semi-automated AIF definition and yielded maps of rCBV, OEC and CTH.<sup>44,45</sup> The approach is based on a single capillary model (see Figure 1 in Jespersen and Østergaard<sup>28</sup>). It assumes that oxygen extraction in a single capillary depends on the transit time of blood. Thus, oxygen extraction depends on flow and the difference in plasma and tissue oxygen concentration.<sup>46,47</sup> OEC is obtained by integrating single capillary contributions that are weighted by the transit time distribution of the capillaries within the capillary bed (see Eq. 1 in Jespersen and Østergaard<sup>28</sup>). To this end, the probability density function of capillary transit times is parametrized as a gamma variate function (see Eq.2 in Jespersen and Østergaard<sup>28</sup>), which allows estimation of CTH.<sup>44,45</sup> The CBV maps were normalized to normal appearing white matter (NAWM) as previously reported,<sup>27,39</sup> which yielded rCBV maps (Figure 1).
- rOEF was derived by a multi-parametric implementation for the quantification of the blood oxygenation level-dependent (BOLD) effect.<sup>27</sup> The method is based on an analytical relationship between  $R_2'$ , venous CBV and venous oxygenation that was originally derived by Yablonskiy and Haacke for randomly oriented magnetized cylinders assuming static dephasing conditions.<sup>48</sup> Quantitative  $T_2^*$  and  $T_2$  parameter maps were calculated by mono-exponential fitting of the multi-echo GRE and even-echoes GraSE data, correcting influences of magnetic background gradients, motion and stimulated echoes as described previously.<sup>27,49</sup> Based on

these parameter maps,  $R_2' = \frac{1}{T_2^*} - \frac{1}{T_2}$  was calculated. DSC data were processed employing leakage correction<sup>39,50</sup> to calculate CBV maps, which were normalized to  $CBV = 2.5\%$  in normal appearing WM (NAWM)<sup>51</sup> yielding rCBV. Using the mq-BOLD approach,<sup>27</sup> rOEF was calculated as  $rOEF = \frac{R_2'}{c \cdot rCBV}$  with  $c = \gamma \cdot \frac{4}{3} \cdot \pi \cdot \Delta\chi \cdot B_0$  and  $B_0 = 3 T$  with  $\Delta\chi = \Delta\chi_0 \cdot Hct = 0.924 \cdot 10^{-7}$ ,  $\Delta\chi_0 = 0.264 \cdot 10^{-6}$  and the small-vessel hematocrit  $Hct = 0.35$  and  $\gamma = 2.675 \cdot 10^8 s^{-1} T^{-1}$ .

While estimation of OEC from DSC-MRI relies on a vascular model,<sup>44,45</sup> estimation of rOEF by mq-BOLD is based on an implementation<sup>27</sup> of an analytical model<sup>48</sup> describing spin dephasing, i.e. susceptibility related transverse relaxation, in the presence of randomly oriented magnetized cylinders, i.e. blood vessels containing deoxygenated blood.

Individual parameter maps were calculated in each subject's native space, as described above. Subsequently, all data (CBF, CVR, rOEF, MPRAGE, GM and WM masks) were spatially coregistered to the individual participant's DSC-data (rCBV, OEC, CTH, and iWSA) using SPM12 to maintain iWSA-masks in native space.

### Statistical analysis

The mean values of each hemodynamic parameter were calculated separately for hemispheres ipsilateral and contralateral to the stenosis inside and outside the iWSAs with additional GM (iWSA-GM) and WM (iWSA-WM) masks for each participant. Two evaluations were conducted on a group level. First, the average values of each parameter within the iWSA were compared using paired-scatter plots between both hemispheres. This was done separately for ICAS-patients and HCs. Absolute parameter values per hemisphere were compared between ICAS-patients and HCs. Second, the parameter lateralization between hemispheres was compared inside vs. outside iWSAs for GM and WM of ICAS-patients. For comparisons between hemispheres, one-sample t-tests were applied. For comparisons between groups, two-sample t-tests were applied. Generally, values of  $p < 0.05$  were considered statistically significant.

### Results

Figure 2 shows exemplary data of two ICAS-patients. These results demonstrate impairment of multiple hemodynamic parameters. Specifically, CBF and CVR were decreased ipsilaterally to the stenosis and there was concomitant elevation of rCBV, OEC and CTH. The location and strength of the

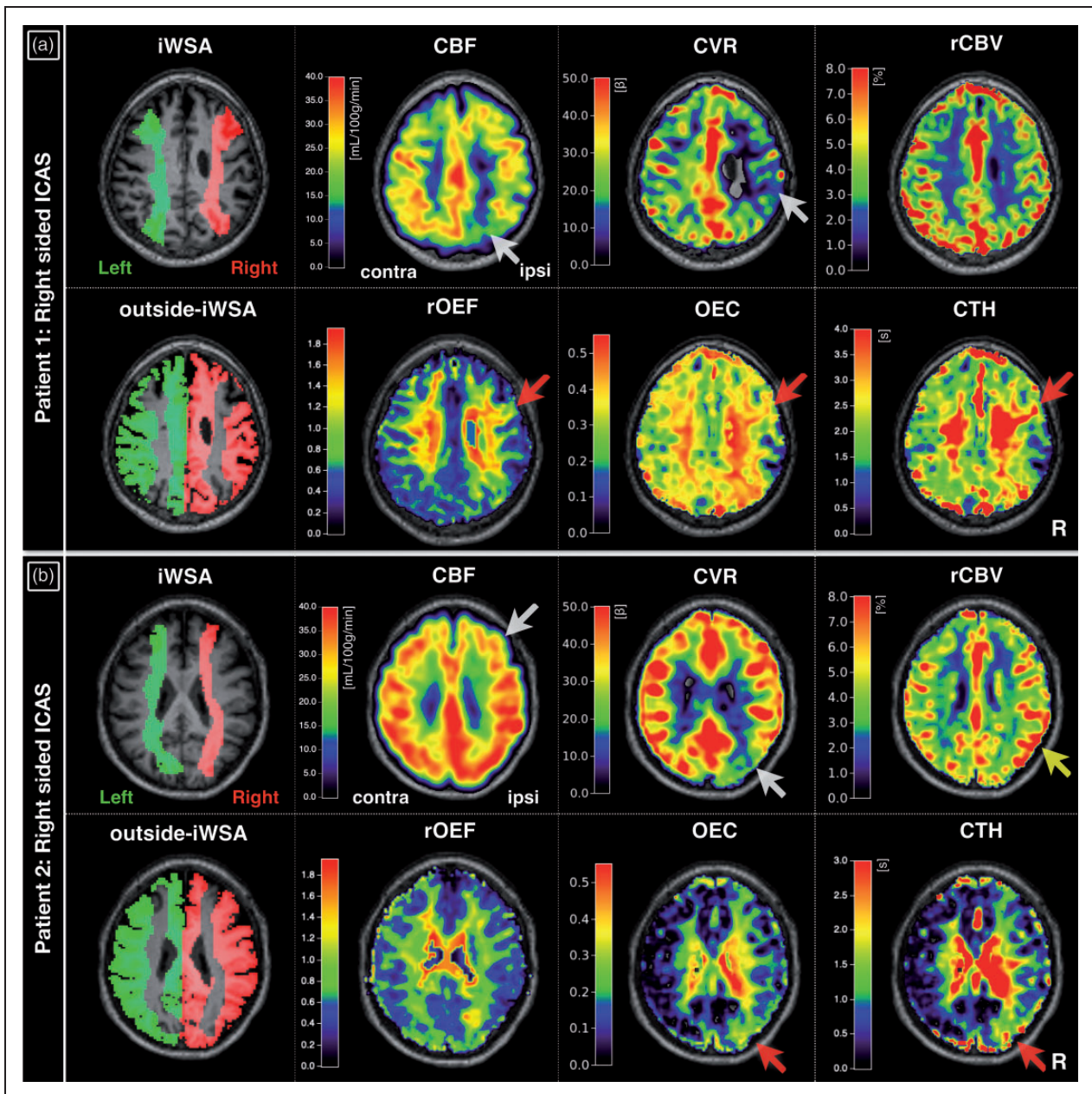


**Figure 2.** Exemplary parameter maps of two patients with right-sided ICAS. Hemodynamic parameter maps show individually defined watershed areas (iWSA), CBF, CVR, rCBV, brain regions complementary to iWSAs (outside-iWSA), rOEF, OEC and CTH. CBF and CVR were decreased ipsilateral to the stenosis in both patients (white arrows, a, b). In the first patient, focal ipsilateral rOEF increases correspond to elevated OEC and CTH (red arrows, a). In the second patient, rCBV was ipsilaterally increased (yellow arrow, b). Generally, OEC and CTH elevations appear spatially more expanded (red arrows, a, b). For group analyses, each hemisphere's subject-specific iWSA and outside-iWSA masks with additional GM/WM-masking were applied to parameter maps and average values calculated within each volume of interest (VOI). iWSA: individual watershed areas; CBF: cerebral blood flow; CVR: cerebrovascular reactivity; rCBV: relative cerebral blood volume; rOEF: relative oxygen extraction fraction; OEC: oxygen extraction capacity; CTH: capillary transit-time heterogeneity.

impairments was variable for the six parameters, e.g. regions of obvious CBF and rCBV impairments did not overlap in the second patient (Figure 2(b)). Furthermore, the first patient had much more widespread CVR decreases, but no

apparent rCBV effects in the displayed slice (Figure 2 (a)). Minor focal rOEF increases were only observed in the first patient, and they corresponded to elevated OEC and CTH, which appeared to be spatially more extended.



Group level comparisons between hemispheres in ICAS-patients showed statistically significant lateralization of all evaluated parameters ( $p < 0.01$ ), except for rOEF (Figures 3 and 4). Those lateralization of CBF, CVR, rCBV, OEC and CTH in ICAS-patients were significantly different from HCs ( $p < 0.05$ ). In HCs, all parameters were symmetrical between hemispheres. Although OEC showed significant side differences in HCs ( $p < 0.001$ ), the magnitude of differences was negligible (OEC = 0.38 in both hemispheres within iWSA-GM, Table 2). In the patients, CBF was decreased in the hemisphere ipsilateral to the stenosis (lateralization  $\Delta$ CBF =  $-18\%$  in iWSA-GM,  $p < 0.001$ , Figure 3). Absolute CBF values in the contralateral ICAS hemisphere were comparable to HCs (CBF in iWSA-GM  $\approx 30$  ml/100g/min). For CVR, beta-values were statistically significantly decreased ipsilateral to

the stenosis ( $-15\%$  in iWSA-GM,  $p < 0.001$ ). Contralateral CVR values in GM were decreased compared to HCs, while contralateral CVR values in WM were comparable to HCs. Relative CBV was significantly increased in the ipsilateral ICAS hemisphere compared to the contralateral hemisphere ( $+5\%$  in iWSA-GM,  $p < 0.01$ ). Values of rCBV in the contralateral ICAS hemispheres were comparable to HCs within WM, while rCBV in GM was decreased in both ICAS hemispheres compared to HCs. Analysis of rOEF revealed symmetry between hemispheres with comparable values to HCs (rOEF  $\approx 0.6$  in iWSA-GM, Figure 4). Only the variability of rOEF was increased across ICAS-patients (bilaterally increased standard deviation (SD) by  $+50\%$  compared to HCs within iWSA-GM, Table 2). Values of OEC and CTH were ipsilaterally increased (OEC by  $+12\%$  and CTH by

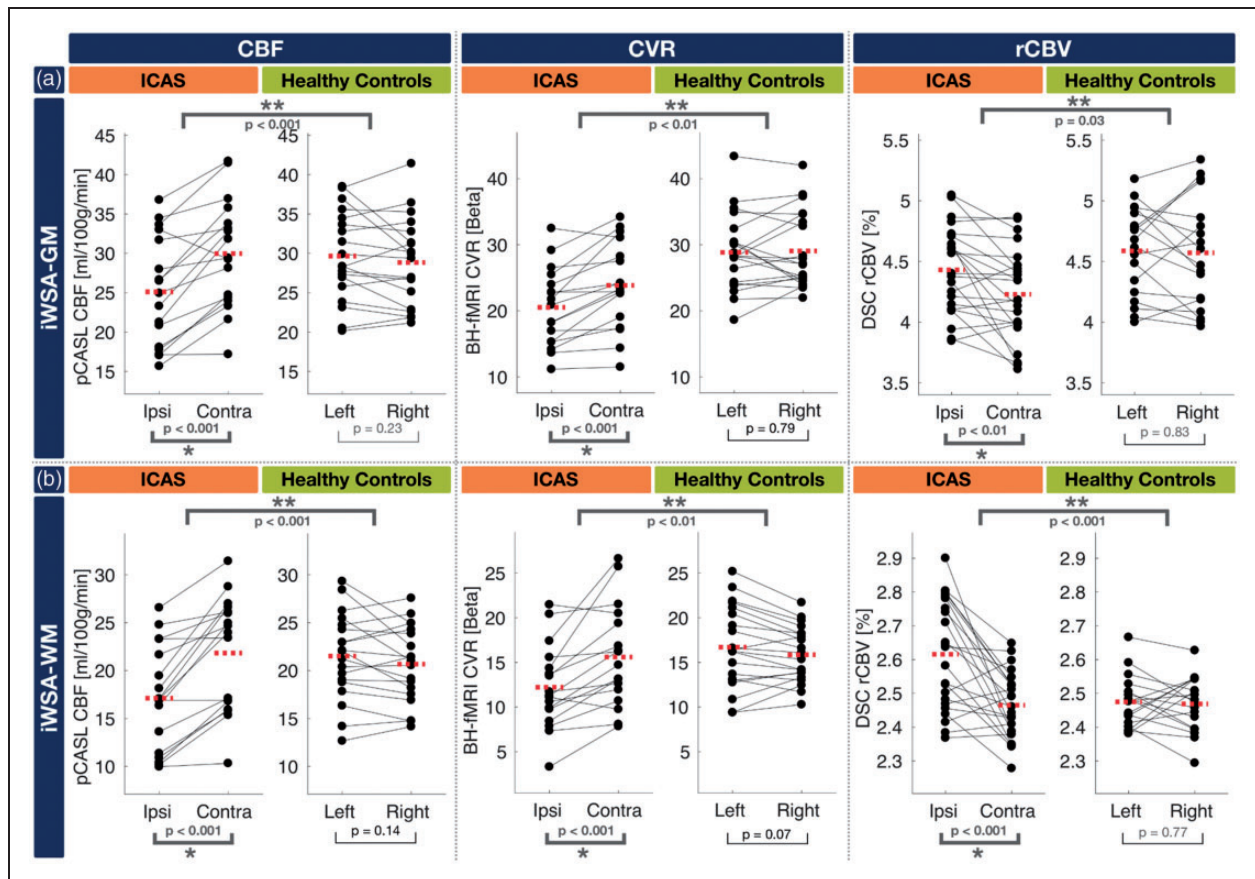


**Figure 3.** Paired scatterplots comparing perfusion-related parameters between hemispheres within iWSAs in GM (a) and WM (b). CBF, CVR, and rCBV are compared for ICAS patients and healthy controls. To facilitate direct comparisons, scatterplots of parameter values in GM and WM of iWSAs are stacked in (a) and (b). Dots represent the mean parameter values of each subject within iWSAs in GM or WM – lines connect the mean values of both hemispheres from the same subjects. Dashed red lines indicate parameter's group mean values within each hemisphere. In ICAS patients, all parameters showed statistically significant differences between hemispheres (one-sample t-test,  $p < 0.05$ , asterisks) and lateralization was also significantly different from HCs (two-sample t-test,  $p < 0.05$ , double asterisks). All parameters were symmetrical between the hemispheres of HCs. ICAS: internal carotid artery stenosis; CBF: cerebral blood flow; CVR: cerebrovascular reactivity; rCBV: relative cerebral blood volume; iWSA: individual watershed areas.

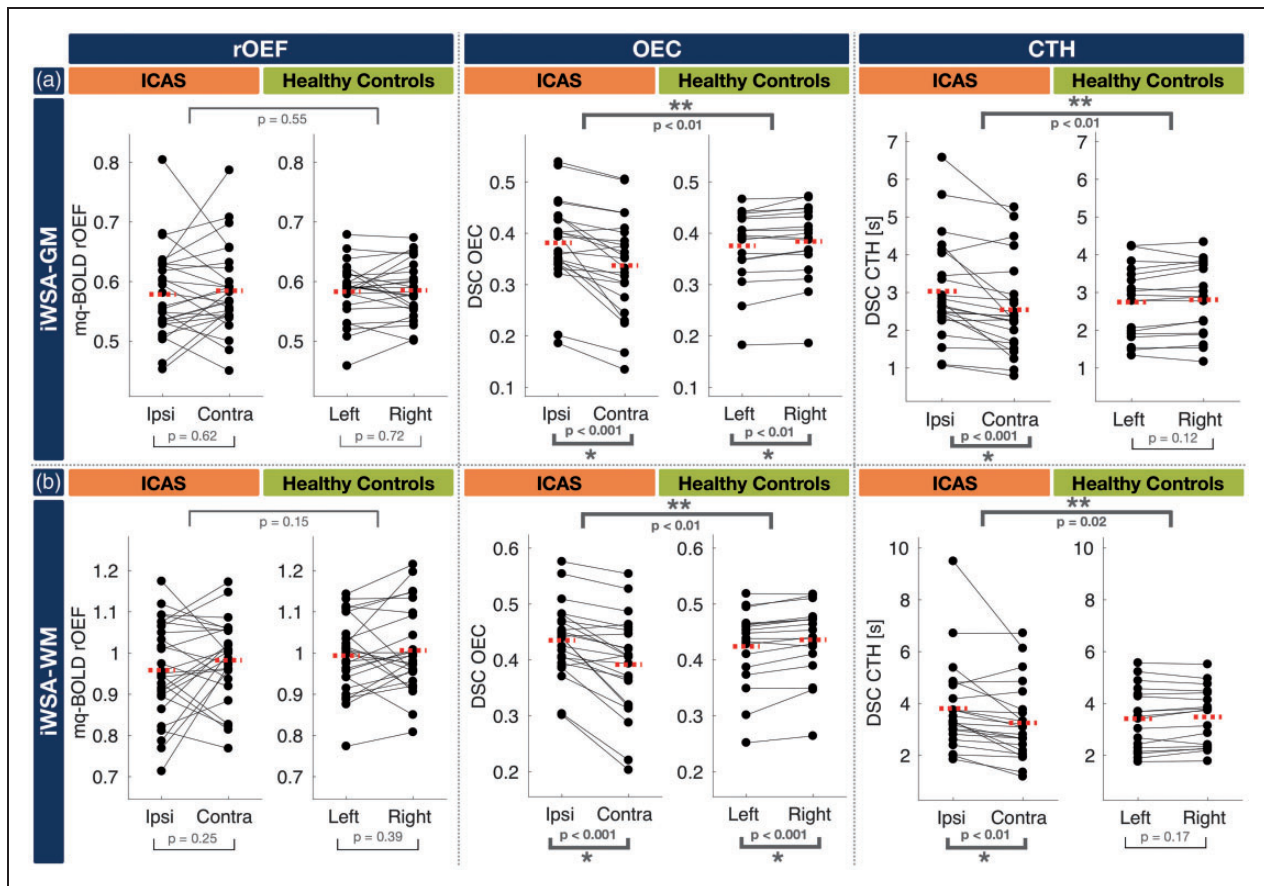


**Figure 4.** Paired scatterplots comparing oxygenation-related parameters between hemispheres within iWSAs in GM (a) and WM (b). rOEF, OEC and CTH are compared for ICAS patients and healthy controls. To facilitate direct comparisons, scatterplots of parameter values in GM and WM are stacked in (a) and (b). Dots represent mean parameter values of each subject within iWSA in GM or WM – lines connect mean values of both hemispheres from the same subjects. Dashed red lines indicate parameter's group mean values within each hemisphere. In ICAS patients, all parameters except rOEF showed statistically significant differences between hemispheres (one-sample t-test,  $p < 0.05$ , asterisks) and lateralization was also significantly different from HCs (two-sample t-test,  $p < 0.05$ , double asterisks). Although OEC showed significant side differences in HCs, the magnitude of differences was negligible. All parameters were symmetrical between the hemispheres of HCs. rOEF: relative oxygen extraction fraction; OEC: oxygen extraction capacity; CTH: capillary transit-time heterogeneity; iWSA: individual watershed areas; ICAS: internal carotid artery stenosis.

+18% within iWSA-GM,  $p < 0.001$ , Figure 4). Furthermore, the CTH variability was increased (SD by +41% in ipsilateral iWSA-GM compared to HCs, Table 2). All average hemisphere's parameter values are summarized in Table 2.

Parameter lateralization in ICAS-patients was compared inside vs. outside iWSAs and separately masked with GM and WM (Figure 5(a) and (b), respectively). Generally, CBF, CVR and rCBV showed stronger lateralization inside iWSAs compared to outside iWSAs. In detail, CBF and CVR were significantly lateralized in all masks, inside as well as outside of iWSA-GM and iWSA-WM ( $p < 0.01$ ). Despite CBF and CVR lateralization outside iWSAs, the effects inside iWSAs were still significantly stronger (+117% for  $\Delta$ CVR inside vs. outside iWSA-GM,  $p < 0.01$ ). Additionally, the effects

in WM were stronger (Figure 5(b)) compared to GM (Figure 5(a)). For example, lateralization of CBF and CVR was stronger within iWSA-WM ( $\Delta$ CBF =  $\Delta$ CVR = -24%) versus iWSA-GM ( $\Delta$ CBF = -18% and  $\Delta$ CVR = -15%). The effects of  $\Delta$ rCBV were similar to  $\Delta$ CBF and  $\Delta$ CVR but had the opposite sign. Relative CBV was also significantly lateralized outside iWSAs but was significantly stronger affected inside iWSA-WM (+96% for  $\Delta$ rCBV iWSA-WM inside vs. outside,  $p = 0.016$ ) and with a strong trend for iWSA-GM (+56%,  $p = 0.058$ ). Nevertheless, lateralization of rCBV was weaker compared to CBF or CVR ( $\Delta$ rCBV = 6% vs.  $\Delta$ CBF =  $\Delta$ CVR = -24% within iWSA-WM). Regarding OEC and CTH, lateralization was observed in all masks, specifically inside/outside iWSA-GM/WM (10% to 18%). Contrary to the

**Table 2.** Average hemodynamic parameter values inside GM and WM of iWSAs.

Mask	Group	Hemisphere	Hemodynamic parameters					
			CBF (ml/100g/min)	CVR (Beta)	rCBV (%)	rOEF	OEC	CTH (s)
iWSA-GM	Healthy	Left	29.7 ± 5.7	28.9 ± 5.8	4.59 ± 0.37	0.58 ± 0.05	0.38 ± 0.07 *	2.75 ± 0.95
		Right	28.8 ± 5.6	29.1 ± 5.8	4.57 ± 0.45	0.59 ± 0.05	0.38 ± 0.07 *	2.81 ± 0.95
	ICAS	Ipsi	25.1 ± 6.9 *	20.5 ± 5.9 *	4.43 ± 0.36 *	0.58 ± 0.08	0.38 ± 0.08 *	3.03 ± 1.34 *
		Contra	30.0 ± 6.9 *	23.8 ± 6.6 *	4.23 ± 0.38 *	0.59 ± 0.07	0.34 ± 0.10 *	2.54 ± 1.23 *
iWSA-WM	Healthy	Left	21.5 ± 4.5	16.7 ± 4.6	2.48 ± 0.08	0.99 ± 0.09	0.42 ± 0.07 *	3.42 ± 1.20
		Right	20.7 ± 4.0	15.9 ± 3.1	2.47 ± 0.08	1.01 ± 0.10	0.44 ± 0.07 *	3.48 ± 1.11
	ICAS	Ipsi	17.1 ± 5.5 *	12.2 ± 3.1 *	2.62 ± 0.16 *	0.96 ± 0.12	0.44 ± 0.07 *	3.81 ± 1.70 *
		Contra	21.8 ± 6.0 *	15.6 ± 5.6 *	2.47 ± 0.10 *	0.98 ± 0.10	0.39 ± 0.09 *	3.25 ± 1.44 *

Note: Hemodynamic parameters CBF, CVR, rCBV, rOEF, OEC and CTH were evaluated inside masks of iWSA in GM and WM for healthy controls and ICAS patients, and comparisons were made between both hemispheres. For healthy controls, left vs. right hemispheres were compared and for ICAS patients between hemispheres ipsilateral vs. contralateral to the stenosis (mean ± standard deviation). Statistically significant differences based on t-tests between hemispheres are indicated by asterisks.

CBF: cerebral blood flow; CVR: cerebrovascular reactivity; rCBV: relative cerebral blood volume; rOEF: relative oxygen extraction fraction; OEC: oxygen extraction capacity; CTH: capillary transit-time heterogeneity iWSA: individual watershed areas; ICAS: internal carotid artery stenosis.

previously reported parameters, OEC and CTH were similarly affected inside and outside iWSAs. In addition,  $\Delta$ OEC and  $\Delta$ CTH lateralization was comparable in GM (Figure 5(a)) and WM (Figure 5(b)).

## Discussion

In this study, we present a multimodal MRI-based investigation of hemodynamic impairments in unilateral ICAS. Specifically, we explored whether six perfusion and oxygenation sensitive parameters were affected more inside vs. outside iWSAs. CBF was measured with a single-PLD pCASL, CVR by breath-hold fMRI (BH-fMRI), rCBV by DSC, rOEF by mq-BOLD and OEC as well as CTH by parametric modeling of DSC-data. Individual WSAs were defined semi-automatically using DSC-based TTP maps.

We showed impairments of CBF, CVR, rCBV, OEC and CTH – but not of rOEF – in unilateral ICAS-patients. We also showed that all parameters were unaffected in our healthy control cohort, which affirmed the specificity of the selected parameters. According to our hypothesis, impairments of CBF, CVR and rCBV in ICAS were more pronounced inside iWSAs than outside. In addition, impairments were stronger in WM compared to GM. At the same time, OEC and CTH were severely impaired, but independent of iWSA locations. Measured impairments of the individual parameter values were in agreement with previously reported literature values. Beyond that, comparisons of complex multimodal parameter alterations offer a broader perspective on the pathophysiological conditions of complex microvascular impairments in ICAS, which is discussed below.

### Impaired perfusion (CBF, CVR and rCBV)

Ipsilateral to the stenosis, we measured decreased CBF (–18% in iWSA-GM), which is in agreement with previous PET<sup>52</sup> and MRI studies<sup>7,53</sup> as well as the model of Powers et al.<sup>18</sup> In the contralateral hemisphere, absolute CBF values were comparable to HCs, but the variability was increased (SD across subjects increased by +22% in patients compared to HCs within iWSA-GM). This could be explained by subject specific collateralizations of blood flow,<sup>15</sup> that affect the contralateral hemisphere, and thereby increasing the inter-subject variability of contralateral CBF. Even though no obvious signs of arterial delay artefacts were found, CBF in watershed areas of ICAS-patients may potentially be affected by delayed blood arrival.<sup>54–58</sup>

We detected decreased CVR on the side of the stenosis in ICAS-patients (–15% compared with contralateral values and –29% compared with HCs in iWSA-GM), as predicted by the basic hemodynamic model and in agreement with other studies.<sup>5,24</sup> We also found decreased CVR in the contralateral hemisphere (–18% compared with HCs in iWSA-GM). This can be explained by blood flow collateralization from the contralateral side, which caused hemodynamic stress even in the contralateral hemisphere. Those observed bilateral effects have been described previously<sup>59</sup> and highlight the fact that unilateral ICAS can affect both hemispheres. Nevertheless, CVR on a group level was still significantly lateralized between the hemispheres ( $\Delta$ CVR = –24% in iWSA-WM), which underlines the high sensitivity of hemispheric CVR comparisons.

We also found lateralization of rCBV with higher values ipsilateral to the stenosis (+5% in iWSA-GM),



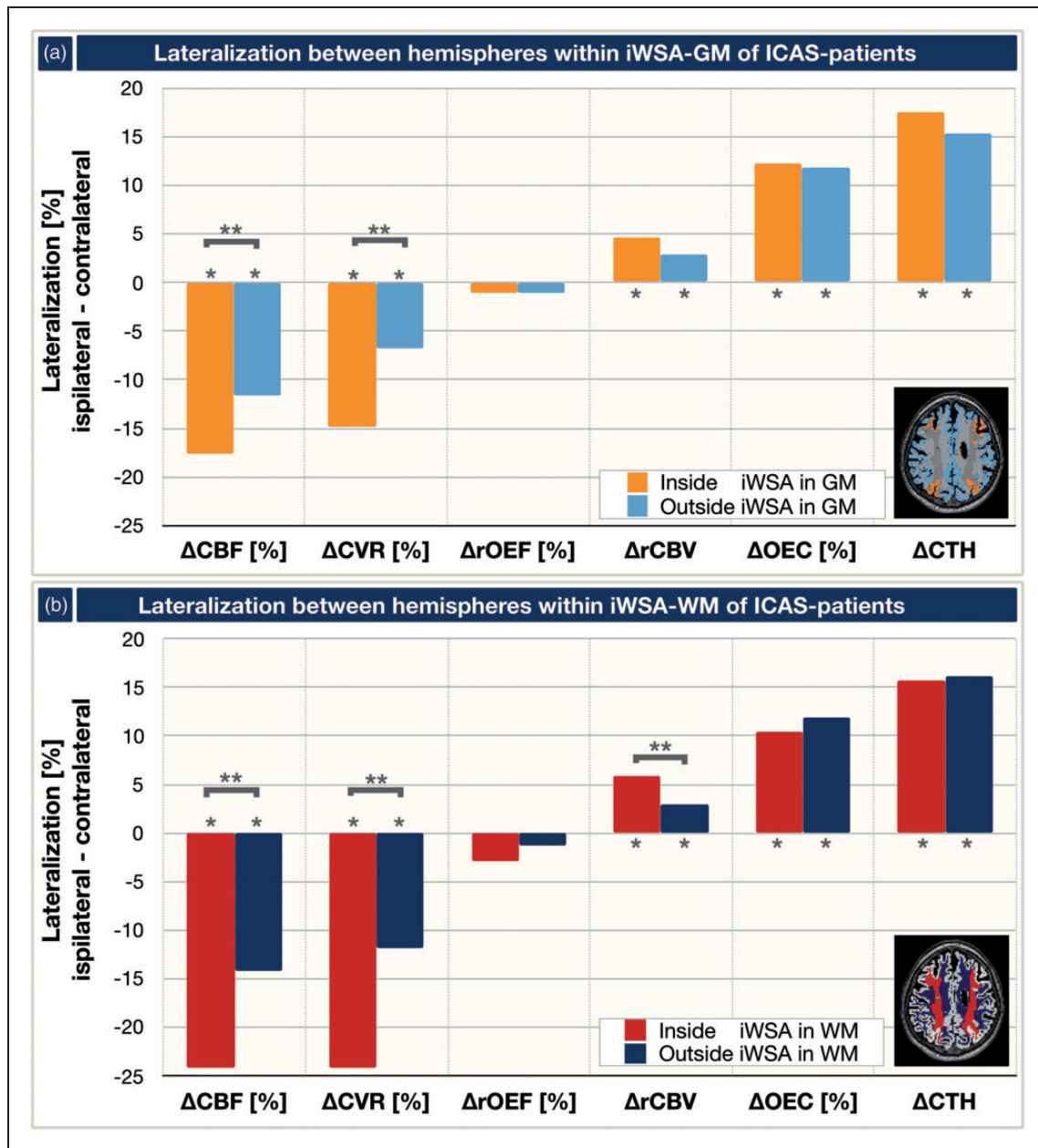


**Figure 5.** Parameter's lateralization between hemispheres inside vs. outside of iWSAs in GM (a) and WM (b). Lateralization was calculated from differences of mean values between hemispheres ipsilateral and contralateral to the stenosis. Four VOIs were compared (see exemplary inlays): inside iWSAs in GM (orange, a), outside iWSAs in GM (light blue, a), inside iWSAs in WM (red, b) and outside iWSAs in WM (dark blue, b). Negative  $\Delta$ CBF and  $\Delta$ CVR corresponded to decreased values ipsilateral to the stenosis, while  $\Delta$ rOEF was unaffected and  $\Delta$ rCBV,  $\Delta$ OEC and  $\Delta$ CTH were increased. Asterisks indicate statistically significant lateralization (one-sample t-test,  $p < 0.01$ ). ICAS-related impairments of  $\Delta$ CBF,  $\Delta$ CVR and  $\Delta$ rCBV were statistically significantly enhanced inside of iWSAs compared to the outside of iWSAs (double asterisks, one-sample t-test,  $p < 0.05$ ).

CBF: cerebral blood flow; CVR: cerebrovascular reactivity; rCBV: relative cerebral blood volume; OEC: oxygen extraction capacity; CTH: capillary transit-time heterogeneity.

which was expected from the model and also agrees with previous publications.<sup>18,52,53,60,61</sup> Ipsilateral rCBV increases alongside with decreased CVR, which confirmed the assumed chronic vasodilation.<sup>62</sup> However, we also observed bilateral effects. Values of

rCBV within iWSA-GM in both hemispheres were generally lower for ICAS-patients compared to HCs, which is in excellent agreement with previous PET measurements.<sup>60</sup> Within iWSA-WM masks, rCBV was comparable in contralateral ICAS hemispheres

and HCs ( $\approx 2.5\%$ , Table 2), due to our processing with rCBV normalization to 2.5% in NAWM.<sup>27,51</sup>

### *Spatial variability of perfusion impairments*

Interestingly, the localizations of CBF, CVR, and rCBV impairment were highly variable among patients. In addition, the spatial overlap of compromised hemodynamic biomarkers within the same subject was highly variable. These effects clearly demonstrate the limitation of the simplified model that was proposed by Powers et al.<sup>18</sup> on a single subject level. It furthermore demonstrated that the evaluated parameters indeed yielded complementary information (see Supplemental Figure 1) about different pathophysiological effects. For example, the ICAS patient presented in Figure 2(a) showed spatially non-congruent impairments of CBF and CVR without obvious rCBV effects. In contrast, the second patient shown in Figure 2(b) demonstrated rCBV and CVR effects at very similar locations, while CBF was impaired in other regions. We assume two major causes for this high inter-subject spatial variability. First, the varying degrees of the stenosis ( $81.2 \pm 10.1\%$ , Table 1) influenced the CPP decreases and this explains inter-subject variations of hemodynamic impairments. Second, configurations of the circle of Willis can vary a great deal among patients and can cause very different collateralization patterns.<sup>15,63</sup> An unilateral CPP decrease in ICAS together with high recruitment of collateral blood flow can cause strong shifts of perfusion territories in the entire brain.<sup>14,63</sup> Consequently, locations of hemodynamic impairments are highly subject specific. At the same time, different hemodynamic mechanisms are indicated to act at different locations, which complicated the interpretation of individual maps of hemodynamic biomarkers. Therefore, our proposed protocol for measurements of multiple hemodynamic biomarkers within a single imaging session is a promising method that can help to better explain highly subject specific impairments. Additionally, evaluation within iWSAs indeed helps to overcome the disturbing effects of the high spatial variability, as iWSAs specifically select the most severely impaired areas of CBF, CVR and rCBV at the same time, as initially hypothesized.

The perfusion impairments of CBF, CVR and rCBV were found to be enhanced in WM compared to GM of iWSAs. The stronger lateralization of  $\Delta$ CBF and  $\Delta$ rCBV in unilateral ICAS within WM agreed with results from a previous study.<sup>61</sup> Physiologically, the stronger effects within WM-iWSAs can be well explained by the architecture of the blood supply to GM and WM.<sup>13</sup> Sections of iWSAs in WM are expected to be located at the most distal arterial

branches, where CPP is generally assumed to be the lowest. Additional influencing factors may also be due to delay effects in single-PLD pCASL<sup>54-56</sup> and delay effects in CVR-imaging.<sup>64</sup> Even though CBF evaluation by ASL is known to be challenging in WM due to a lower SNR<sup>23</sup> and partial volume effects,<sup>65</sup> a previous study showed its sensitivity to WM perfusion deficits,<sup>66</sup> which was also supported by our successful evaluations on a group level. Overall, our measured impairments of CBF, CVR and rCBV in WM are consistent with previous reports in the literature<sup>61</sup> and indicate the highest sensitivity to hemodynamic impairments within WM of iWSAs.

### *Oxygenation*

In contrast to the previously discussed perfusion parameters, average rOEF values by mq-BOLD were found to be unaffected in ICAS-patients. On a group level, we neither found lateralization between hemispheres nor significant differences between ICAS-patients and the HC-group. This finding of an unaffected rOEF with concomitant ipsilateral CBF decreases was in excellent agreement with a recent study from Bouvier et al. using a very similar methodology.<sup>7</sup> Using the model of Power et al.,<sup>18</sup> these results implied that high-grade asymptomatic ICAS-patients are not yet in the range of misery perfusion.<sup>67</sup> Nevertheless, individual patients showed slight focal increases of rOEF, which probably contributed to the observed increase in rOEF variability in ICAS-patients within both hemispheres (bilateral SD increased by +50% in ICAS compared to HCs within iWSA-GM, Table 2). This is in agreement with a PET study, that demonstrated bilateral increases of OEF variability in ICAS-patients compared to controls.<sup>60</sup>

According to Power's model,<sup>18</sup> which is based on Fick's principle in an iso-metabolic state,<sup>68</sup> rOEF should increase in regions of reduced CBF to maintain the oxidative metabolism. An explanation for this apparent mismatch of reduced CBF and unchanged rOEF might be subtle damage to the neuronal tissue due to previous, temporary lapses in oxygen, which agrees with the subtle cognitive impairments detected in our study cohort.<sup>2</sup> Another possibility is that additional factors regulate the cerebral oxygen delivery as proposed by Hyder et al.<sup>20-22</sup> Their model permits changes in oxygen diffusivity at the capillary level due to changes in perfusion and also related alterations in rheological parameters at the microscopic level. Tube hematocrit, defined as the instantaneous volume fraction of red blood cells (RBCs) in a capillary, may change dynamically as the velocities of RBCs and plasma in capillaries are not equivalent. Tube hematocrit is uniquely different from discharge hematocrit,

which is a measure of volume percentage of RBCs in blood and consistently approximates systemic hematocrit values. Thus, differences between tube and discharge hematocrit could explain our results and this could also explain the variability in local regulation observed across our subjects.<sup>69</sup> Alternatively, variations in oxygen diffusivity may also have an association with the above discussed increased rOEF variability, i.e. oxygen diffusivity might be more severely altered in some patients. Thus, direct MRI-based measurements of oxygen diffusivity would be highly promising to better understand the complexities of cerebral oxygen delivery.

Germuska et al. recently proposed an interesting technique for modeling oxygen diffusivity based on MRI measurements during gas challenges.<sup>70</sup> However, their combination of competing models, namely where oxygen diffusion is either limited<sup>71</sup> or not,<sup>20</sup> requires further research. Oxygen diffusivity at the systemic level is determined by the discharge hematocrit. As correlations between high blood pressure and elevated discharge (or systemic) hematocrit have been demonstrated<sup>72,73</sup> and many of our ICAS-patients showed hypertension (79%, see Table 1), the systemic hematocrit level of our patients might be elevated. Following this argumentation, the higher blood pressure in ICAS could be potentially linked to a higher variability in oxygen diffusivity and thus increased rOEF variability. However, since we did not measure hematocrit levels in our participants, future studies evaluating hematocrit levels are clearly required to further evaluate this hypothesis.

### Capillary transit time heterogeneity and dysfunction

Based on parametric modeling of DSC-data, we observed increased capillary transit-time heterogeneity on the side of the stenosis, which was in accordance with a previous study in ICAS-patients.<sup>30</sup> Interestingly – and unlike previously discussed for CBF, CVR and rCBV – we found that CTH lateralization was independent of iWSA locations. These CTH impairments beyond iWSAs are in agreement with a recent study that demonstrated a spatial mismatch of CTH and  $T_{\max}$  impairments.<sup>30</sup> Since  $T_{\max}$  is closely related to TTP, which was used to delineate our iWSAs,<sup>14</sup> our finding of mismatching CTH impairments and iWSA regions excellently agreed with their findings. A possible physiological explanation might be that TTP is more sensitive to macrovascular perfusion,<sup>74</sup> while CTH is assumed to be particularly sensitive to capillary flow.<sup>30</sup>

Lateralization of CTH outside-iWSA was stronger than for any other parameter ( $\approx 16\%$  outside iWSAs). This result points to a more widespread microvascular

pathology beyond areas that are obviously affected by perfusion deficits. It is, therefore, possible that CTH offers complementary information about microscopic rheological events of capillary hemodynamics compared to CBF, CVR and rCBV, as these behave fundamentally differently inside and outside of iWSAs. Consequently, CTH is a promising early indicator of microvascular impairments in ICAS with rather subtle CPP decreases. At the same time, CTH may detect spatially more widespread microvascular involvement compared to CBF, CVR or rCBV. As DSC-imaging could be applied in standard clinical diagnostic MRI of ICAS in the future,<sup>75</sup> additional promising information could be gathered by parametric modeling with respect to CTH.

Furthermore, there might be a link between CTH and the previously discussed oxygen diffusivity. As most oxygen diffusion through the vessel walls is expected to come from the capillaries,<sup>76</sup> capillary flow patterns have also been linked with the efficacy of oxygen extraction.<sup>53</sup> Thus, variations in the oxygen diffusivity may be potentially moderated by CTH.<sup>28,77</sup> Along this line, in 2012, Jespersen and Østergaard proposed to additionally derive information on tissue oxygen supply via parametric modeling of DSC-data.<sup>28</sup> They claimed that CTH increases would at some point result in a decrease of OEC, a condition they termed ‘malignant’ CTH. Following their argumentation, ICAS-patients in our cohort would still reside in the regime of benign CTH with rather increased OEC, which agrees with our observations. With respect to a rather qualitative interpretation, exemplary parameter maps imply some congruency of spatial patterns between OEC and CTH maps in our subjects. Furthermore, lateralization of  $\Delta$ OEC and  $\Delta$ CTH was similar on a group level (Figure 4) and also among individual ICAS-patients (see Supplemental Figure 1). Thus, a mild to moderate vascular pathology is implied in our patients with reduced perfusion pressure and capillary constrictions, but rather no capillary occlusions, according to previously presented simulations.<sup>78</sup> However, the exact physiological interpretation of OEC is difficult because it relies on the validity of a complex modeling approach, which requires further investigation. Even though OEC and rOEF are both supposed to be related to cerebral oxygenation, average OEC and rOEF values did not correlate within iWSAs (see Supplemental Figure 2). This is certainly due to the fact that they rely on different models as introduced in the methods (see ‘Image analysis’ section in the methods description).

### Applicability and Limitations

This study has several strengths, but also some limitations. An obvious strength is the simultaneous multimodal assessment of cerebral perfusion and



oxygenation parameters, which allows the evaluation of specific stenosis-related hemodynamic effects within subjects. Given the high variability of the hemodynamic situation in individual patients (see Supplemental Figure 1), multimodal MRI is especially promising to evaluate subject specific impairments.

Regarding the different applied methods, CBF imaging by pCASL is a very promising non-invasive method for initial non-invasive diagnostics.<sup>23</sup> However, it is not applicable after stenting, because of SAR limitations. We sought to minimize potential delay effects of single-PLD pCASL by using longer PLDs, as suggested by the consensus recommendations.<sup>23</sup> Those delay effects are a generally known methodological issue of single-PLD pCASL.<sup>54–56</sup> We did not observe obvious signs of major delays in the label arrival by visual and quantitative inspection of our data. However, quantitative errors in the regions with potentially prolonged longer ATT, such as the watershed areas, cannot completely be excluded.<sup>57,58</sup> To address this issue in the future, time-encoded ASL could be applied.<sup>79,80</sup> Generally, measured CBF was lower than expected, which has been observed before with this dataset<sup>11</sup> and can be explained by the applied BGS.<sup>40,41</sup>

Breath-hold fMRI for CVR imaging is sensitive to impairments in ICAS, non-invasive, easy to apply, and applicable after stenting. Although our implementation of BH-fMRI was limited by use of comparably short CO<sub>2</sub> stimuli and unknown end-tidal CO<sub>2</sub> concentrations,<sup>24</sup> the applied scheme using 15 second breath-holds already demonstrated good reproducibility<sup>81</sup> and was found to be adequate for relative CVR comparisons.<sup>24</sup> To further increase the reliability, we performed a comprehensive analysis applying a respiratory response function.<sup>43</sup> Theoretically, motor cortex activation may cause minor bilateral effects. As an alternative, gas challenges could be applied that would be more precise, but also more complicated.<sup>24</sup> Using gas challenges, additional voxel-wise delay information can be derived, which already showed promising results in Moyamoya patients.<sup>82</sup>

DSC imaging offers a broad range of different parameters and promising information about capillary dysfunction when using parametric modeling. However, the currently ongoing discussion about contrast agent accumulations should be considered.<sup>83</sup>

Measurements of rOEF by mq-BOLD did not show direct benefits for diagnostic evaluation of our high-grade, asymptomatic ICAS-patients. Nevertheless, research studies can benefit from concomitant rOEF and CBF measurements when investigating the oxygen metabolism.<sup>11</sup> Despite the known systematic rOEF elevations in mq-BOLD<sup>27,84</sup> and neglect of intravascular signal contributions as well as vessel size

dependent hematocrit variations, this method has been successfully applied in studies on different brain pathologies and compares well with PET measurements.<sup>11,27,49,85–87</sup> Furthermore, improved quantitative T<sub>2</sub> mapping by a 3D GraSE sequence significantly reduces rOEF values toward lower, physiologically more realistic values.<sup>84</sup> This is a viable alternative for future studies. The application of mq-BOLD in WM could be considered another potential limitation, as the underlying model assumes randomly oriented blood vessels.<sup>48</sup> Although vessel orientation effects in WM have been observed,<sup>88</sup> recently, reasonably low orientation-related errors of mq-BOLD were demonstrated in WM.<sup>89</sup>

Future multi-center studies – such as the CREST-H study<sup>75</sup> – are clearly necessary to further resolve current limitations and to gain an even deeper understanding of the hemodynamic impairments in ICAS. Finally, improvement in the treatment guidelines could be achieved by considering perfusion and oxygen sensitive biomarkers. In addition to possible future applications in ICAS, the proposed MRI protocol is also highly promising for application in other cerebrovascular diseases (CVD), which are often also associated with elevated stroke risks.<sup>5</sup>

## Conclusion

In the presented study, we demonstrated the sensitivity of our multimodal MRI protocol to detect hemodynamic impairments in unilateral ICAS. Hemodynamic parameters were found to be clearly lateralized between hemispheres in ICAS-patients, whereas in HCs, all parameters were symmetrical between the hemispheres affirming specificity. As hypothesized, the most pronounced changes of CBF, CVR and rCBV in ICAS-patients were detected within iWSAs. Contrary to simple models, we found subject-specific impairments of the investigated six parameters CBF, CVR, rCBV, rOEF, CTH, and OEC, which demonstrated their ability to yield complementary information about the underlying pathology. We also found contralateral effects in some patients, which can be explained by collateral flow. Interestingly, CTH and OEC increases were independent of iWSA locations, which indicated more widespread impairments of capillary function. Our results offer substantial improvement in understanding the relationship of involved parameters in individual patients. Therefore, multimodal MRI is highly promising to improve clinical diagnostics of asymptomatic ICAS by accounting for individual hemodynamic impairments towards personalized stroke risk assessment. Most importantly, application of iWSAs increased the sensitivity for impairments of CBF, CVR and rCBV. Thus, knowledge about iWSA

locations can even facilitate detection of subtle hemodynamic changes using standard MRI protocols.

### Funding

The author(s) disclosed receipt of the following financial support for the research, authorship, and/or publication of this article: This work was supported by the Friedrich-Ebert-Stiftung (grant to SK), the Dr.-Ing. Leonhard Lorenz-Stiftung (grant to SK: 971/19 and JG: 915/15), by the Faculty of Medicine of the Technical University of Munich (grant to JG: KKF E12) and the German Research Foundation (DFG) – Project number PR 1039/6-1 (grant to CP). FH was supported by NIH grants (R01 MH-067528, R01 NS-100106).

### Acknowledgements

We thank Michael Kallmayer and Hans-Henning Eckstein for their support in the patient recruitment (both from TUM) as well as Kim van de Ven (Philips Healthcare, Best, Netherlands) and Hendrik Kooijman (Philips Healthcare, Hamburg, Germany) for their support with the ASL imaging.






### Authors' contributions

SK: study design, data acquisition, data analysis, interpretation of the results, article writing; JG: study design, data acquisition, interpretation of the results, article editing; JP: data analysis, interpretation of the results, article editing; MBH: data analysis, interpretation of the results, article editing; KM: interpretation of the results, proofreading; CZ: study design, proofreading; FH: interpretation of the results, article editing; CP: study design, study supervision, interpretation of the results, article editing.

### Declaration of conflicting interests

The author(s) declared no potential conflicts of interest with respect to the research, authorship, and/or publication of this article.

### ORCID iDs

Stephan Kaczmarz  <https://orcid.org/0000-0001-7694-7012>  
 Jens Göttler  <https://orcid.org/0000-0002-5746-2156>  
 Jan Petr  <https://orcid.org/0000-0002-3201-6002>  
 Mikkel Bo Hansen  <https://orcid.org/0000-0002-8619-1519>  
 Christine Preibisch  <https://orcid.org/0000-0003-4067-1928>

### Supplemental material

Supplemental material for this article is available online.

### References

- Petty GW, Brown RD Jr, Whisnant JP, et al. Ischemic stroke subtypes: a population-based study of incidence and risk factors. *Stroke* 1999; 30: 2513–2516.
- Göttler J, Kaczmarz S, Nuttall R, et al. The stronger one-sided relative hypoperfusion, the more pronounced ipsilateral spatial attentional bias in patients with asymptomatic carotid stenosis. *J Cereb Blood Flow Metab* 2020; 40: 314–327.
- Norling AM, Marshall RS, Pavol MA, et al. Is hemispheric hypoperfusion a treatable cause of cognitive impairment? *Curr Cardiol Rep* 2019; 21: 4.
- Bond R, Rerkasem K and Rothwell PM. Systematic review of the risks of carotid endarterectomy in relation to the clinical indication for and timing of surgery. *Stroke* 2003; 34: 2290–2301.
- Donahue MJ, Achten E, Cogswell PM, et al. Consensus statement on current and emerging methods for the diagnosis and evaluation of cerebrovascular disease. *J Cereb Blood Flow Metab* 2018; 38: 1391–1417.
- Jalbert JJ, Nguyen LL, Gerhard-Herman MD and et al. Outcomes after carotid artery stenting in Medicare beneficiaries, 2005 to 2009. *JAMA Neurol* 2015; 72: 276–286.
- Bouvier J, Detante O, Tahon F, et al. Reduced CMRO2 and cerebrovascular reserve in patients with severe intracranial arterial stenosis: a combined multiparametric qBOLD oxygenation and BOLD fMRI study. *Hum Brain Mapp* 2015; 36: 695–706.
- Donahue MJ, van Laar PJ, van Zijl PCM, et al. Vascular space occupancy (VASO) cerebral blood volume weighted MRI identifies hemodynamic impairment in patients with carotid artery disease. *J Magn Reson Imag* 2009; 29: 718–724.
- Vakil P, Lee JJ, Mouannes-Srour JJ, et al. Cerebrovascular occlusive disease: quantitative cerebral blood flow using dynamic susceptibility contrast MR imaging correlates with quantitative H2[15O] PET. *Radiology* 2013; 266: 879–886.
- Derdeyn CP, Videen TO, Yundt KD, et al. Variability of cerebral blood volume and oxygen extraction: stages of cerebral haemodynamic impairment revisited. *Brain* 2002; 125: 595–607.
- Göttler J, Kaczmarz S, Kallmayer M, et al. Flow-metabolism uncoupling in patients with asymptomatic unilateral carotid artery stenosis assessed by multi-modal magnetic resonance imaging. *J Cereb Blood Flow Metab* 2019; 39: 2132–2143.
- Momjian-Mayor I and Baron JC. The pathophysiology of watershed infarction in internal carotid artery disease: review of cerebral perfusion studies. *Stroke* 2005; 36: 567–577.
- Yamauchi H, Fukuyama H, Yamaguchi S, et al. High-intensity area in the deep white matter indicating hemodynamic compromise in internal carotid artery occlusive disorders. *Arch Neurol* 1991; 48: 1067–1071.
- Kaczmarz S, Griese V, Preibisch C, et al. Increased variability of watershed areas in patients with high-grade carotid stenosis. *Neuroradiology* 2018; 60: 311–323.
- Zarrinkoob L, Wahlin A, Ambarki K, et al. Blood flow lateralization and collateral compensatory mechanisms in patients with carotid artery stenosis. *Stroke* 2019; 50: 1081–1088.
- Schroeder T. Hemodynamic significance of internal carotid artery disease. *Acta Neurol Scand* 1988; 77: 353–372.
- Markus HS. Cerebral perfusion and stroke. *J Neurol Neurosurg Psychiatry* 2004; 75: 353–361.



18. Powers WJ, Press GA, Grubb RL Jr, et al. The effect of hemodynamically significant carotid artery disease on the hemodynamic status of the cerebral circulation. *Ann Intern Med* 1987; 106: 27–34.
19. Dirnagl U and Pulsinelli W. Autoregulation of cerebral blood flow in experimental focal brain ischemia. *J Cereb Blood Flow Metab* 1990; 10: 327–336.
20. Hyder F, Shulman RG and Rothman DL. A model for the regulation of cerebral oxygen delivery. *J Appl Physiol (1985)* 1998; 85: 554–564.
21. Hyder F, Kennan RP, Kida I, et al. Dependence of oxygen delivery on blood flow in rat brain: a 7 tesla nuclear magnetic resonance study. *J Cereb Blood Flow Metab* 2000; 20: 485–498.
22. Hyder F, Kida I, Behar KL, et al. Quantitative functional imaging of the brain: towards mapping neuronal activity by BOLD fMRI. *NMR Biomed* 2001; 14: 413–431.
23. Alsop DC, Detre JA, Golay X, et al. Recommended implementation of arterial spin-labeled perfusion MRI for clinical applications: a consensus of the ISMRM perfusion study group and the European consortium for ASL in dementia. *Magn Reson Med* 2015; 73: 102–116.
24. Pillai JJ and Mikulis DJ. Cerebrovascular reactivity mapping: an evolving standard for clinical functional imaging. *AJNR Am J Neuroradiol* 2015; 36: 7–13.
25. Donahue MJ, Dethrage LM, Faraco CC, et al. Routine clinical evaluation of cerebrovascular reserve capacity using carbogen in patients with intracranial stenosis. *Stroke* 2014; 45: 2335–2341.
26. Fisher JA, Venkatraghavan L and Mikulis DJ. Magnetic resonance imaging-based cerebrovascular reactivity and hemodynamic reserve. *Stroke* 2018; 49: 2011–2018.
27. Hirsch NM, Toth V, Forschler A, et al. Technical considerations on the validity of blood oxygenation level-dependent-based MR assessment of vascular deoxygenation. *NMR Biomed* 2014; 27: 853–862.
28. Jespersen SN and Ostergaard L. The roles of cerebral blood flow, capillary transit time heterogeneity, and oxygen tension in brain oxygenation and metabolism. *J Cereb Blood Flow Metab* 2012; 32: 264–277.
29. Ostergaard L, Engedal TS, Moreton F, et al. Cerebral small vessel disease: capillary pathways to stroke and cognitive decline. *J Cereb Blood Flow Metab* 2016; 36: 302–325.
30. Mundiyanapurath S, Ringleb PA, Diatschuk S, et al. Capillary transit time heterogeneity is associated with modified Rankin scale score at discharge in patients with bilateral high grade internal carotid artery stenosis. *PLoS One*. 2016; 11: e0158148.
31. NASCET SC. North American Symptomatic Carotid Endarterectomy Trial. Methods, patient characteristics, and progress. *Stroke* 1991; 22: 711–720.
32. Baudrexel S, Volz S, Preibisch C, et al. Rapid single-scan T2\*-mapping using exponential excitation pulses and image-based correction for linear background gradients. *Magn Reson Med* 2009; 62: 263–268.
33. Hirsch NM and Preibisch C. T2\* mapping with background gradient correction using different excitation pulse shapes. *AJNR Am J Neuroradiol* 2013; 34: E65–E68.
34. Preibisch C, Castrillon GJ, Buhner M, et al. Evaluation of multiband EPI acquisitions for resting State fMRI. *PLoS One* 2015; 10: e0136961.
35. Kaczmarz S, Gottler J, Kooijman H, et al. Evaluation of pCASL sequences for CBF measures in healthy participants and patients with high-grade internal carotid artery stenosis. In: *ESMRMB 2016, 33rd Annual Scientific Meeting, 29(Suppl 1): S61. Abstract 67*. Vienna, Austria, 29 September–1 October 2016.
36. Fazekas F, Chawluk JB, Alavi A, et al. MR signal abnormalities at 1.5 T in Alzheimer's dementia and normal aging. *AJR Am J Roentgenol* 1987; 149: 351–356.
37. Magerkurth J, Volz S, Wagner M, et al. Quantitative T2\*-mapping based on multi-slice multiple gradient echo flash imaging: retrospective correction for subject motion effects. *Magn Reson Med* 2011; 66: 989–997.
38. Welker K, Boxerman J, Kalnin A, et al. ASFNR recommendations for clinical performance of MR dynamic susceptibility contrast perfusion imaging of the brain. *AJNR Am J Neuroradiol* 2015; 36: E41–E51.
39. Kluge A, Lukas M, Toth V, et al. Analysis of three leakage-correction methods for DSC-based measurement of relative cerebral blood volume with respect to heterogeneity in human gliomas. *Magn Reson Imaging* 2016; 34: 410–421.
40. Mutsaerts HJ, Steketee RM, Heijtel DF, et al. Inter-vendor reproducibility of pseudo-continuous arterial spin labeling at 3 Tesla. *PLoS One* 2014; 9: e104108.
41. Garcia DM, Duhamel G and Alsop DC. Efficiency of inversion pulses for background suppressed arterial spin labeling. *Magn Reson Med*. 2005; 54: 366–372.
42. Mutsaerts HJ, Petr J, Vaclavu L, et al. The spatial coefficient of variation in arterial spin labeling cerebral blood flow images. *J Cereb Blood Flow Metab* 2017; 37: 3184–3192.
43. Vondráčková L, Krukowski P and Petr J. Data-driven model for evaluation of cerebrovascular-reserve measurement with hypercapnia BOLD. In: *Proceedings of the 24th annual meeting of ISMRM. Abstract 3801*, Singapore, 7–13 May 2016.
44. Mouridsen K, Hansen MB, Ostergaard L, et al. Reliable estimation of capillary transit time distributions using DSC-MRI. *J Cereb Blood Flow Metab* 2014; 34: 1511–1521.
45. Mouridsen K, Friston K, Hjort N, et al. Bayesian estimation of cerebral perfusion using a physiological model of microvasculature. *Neuroimage* 2006; 33: 570–579.
46. Hayashi T, Watabe H, Kudomi N, et al. A theoretical model of oxygen delivery and metabolism for physiologic interpretation of quantitative cerebral blood flow and metabolic rate of oxygen. *J Cereb Blood Flow Metab* 2003; 23: 1314–1323.
47. Mintun MA, Lundstrom BN, Snyder AZ, et al. Blood flow and oxygen delivery to human brain during functional activity: theoretical modeling and experimental data. *Proc Natl Acad Sci USA* 2001; 98: 6859–6864.
48. Yablonskiy DA and Haacke EM. Theory of NMR signal behavior in magnetically inhomogeneous tissues: the static dephasing regime. *Magn Reson Med* 1994; 32: 749–763.

49. Toth V, Forschler A, Hirsch NM, et al. MR-based hypoxia measures in human glioma. *J Neurooncol* 2013; 115: 197–207.
50. Hedderich D, Kluge A, Pyka T, et al. Consistency of normalized cerebral blood volume values in glioblastoma using different leakage correction algorithms on dynamic susceptibility contrast magnetic resonance imaging data without and with preload. *J Neuroradiol* 2019; 46: 44–51.
51. Leenders KL. PET: blood flow and oxygen consumption in brain tumors. *J Neurooncol* 1994; 22: 269–273.
52. Gibbs JM, Leenders KL, Wise RJS and Jones T. Evaluation of cerebral perfusion reserve in patients with carotid-artery occlusion. *Lancet* 1984; 323: 310–314.
53. Lythgoe DJ, Østergaard L, Williams SCR, et al. Quantitative perfusion imaging in carotid artery stenosis using dynamic susceptibility contrast-enhanced magnetic resonance imaging. *Magn Reson Imaging* 2000; 18: 1–11.
54. Fan AP, Jahanian H, Holdsworth SJ, et al. Comparison of cerebral blood flow measurement with [15O]-water positron emission tomography and arterial spin labeling magnetic resonance imaging: a systematic review. *J Cereb Blood Flow Metab* 2016; 36: 842–861.
55. Fan AP, Guo J, Khalighi MM, et al. Long-delay arterial spin labeling provides more accurate cerebral blood flow measurements in Moyamoya patients: a simultaneous positron emission tomography/MRI study. *Stroke* 2017; 48: 2441–2449.
56. Keil VC, Eichhorn L, Mutsaerts H, et al. Cerebrovascular reactivity during prolonged breath-hold in experienced Freedivers. *AJNR Am J Neuroradiol* 2018; 39: 1839–1847.
57. Waddle SL, Juttukonda MR, Lants SK, et al. Classifying intracranial stenosis disease severity from functional MRI data using machine learning. *J Cereb Blood Flow Metab* 2020; 40: 705–719.
58. Mutsaerts HJ, van Dalen JW, Heijtel DF, et al. Cerebral perfusion measurements in elderly with hypertension using arterial spin labeling. *PLoS One* 2015; 10: e0133717.
59. Sam K, Small E, Poubanc J, et al. Reduced contralateral cerebrovascular reserve in patients with unilateral stenocclusive disease. *Cerebrovasc Dis* 2014; 38: 94–100.
60. Hino A, Tenjin H, Horikawa Y, et al. Hemodynamic and metabolic changes after carotid endarterectomy in patients with high-degree carotid artery stenosis. *J Stroke Cerebrovasc Dis* 2005; 14: 234–238.
61. Kluytmans M, van der Grond J, Folkers PJ, et al. Differentiation of gray matter and white matter perfusion in patients with unilateral internal carotid artery occlusion. *J Magn Reson Imaging* 1998; 8: 767–774.
62. Vagal AS, Leach JL, Fernandez-Ulloa M, et al. The acetazolamide challenge: techniques and applications in the evaluation of chronic cerebral ischemia. *AJNR Am J Neuroradiol* 2009; 30: 876–884.
63. Richter V, Helle M, van Osch MJ, et al. MR imaging of individual perfusion reorganization using superselective pseudocontinuous arterial spin-labeling in patients with complex extracranial steno-occlusive disease. *AJNR Am J Neuroradiol* 2017; 38: 703–711.
64. Juttukonda MR and Donahue MJ. Neuroimaging of vascular reserve in patients with cerebrovascular diseases. *Neuroimage* 2019; 187: 192–208.
65. Mutsaerts HJ, Richard E, Heijtel DF, et al. Gray matter contamination in arterial spin labeling white matter perfusion measurements in patients with dementia. *Neuroimage Clin* 2014; 4: 139–144.
66. van Osch MJ, Teeuwisse WM, van Walderveen MA, et al. Can arterial spin labeling detect white matter perfusion signal? *Magn Reson Med* 2009; 62: 165–173.
67. Baron JC, Bousser MG, Rey A, et al. Reversal of focal “misery-perfusion syndrome” by extra-intracranial arterial bypass in hemodynamic cerebral ischemia. A case study with 15O positron emission tomography. *Stroke* 1981; 12: 454–459.
68. Kety SS and Schmidt CF. The effects of altered arterial tensions of carbon dioxide and oxygen on cerebral blood flow and on cerebral oxygen consumption of normal young men. *J Clin Invest* 1948; 27: 484–492.
69. Vafae MS and Gjedde A. Model of blood–brain transfer of oxygen explains nonlinear flow-metabolism coupling during stimulation of visual cortex. *J Cereb Blood Flow Metab* 2000; 20: 747–754.
70. Germuska M, Chandler HL, Stickland RC, et al. Dual-calibrated fMRI measurement of absolute cerebral metabolic rate of oxygen consumption and effective oxygen diffusivity. *Neuroimage* 2019; 184: 717–728.
71. Buxton RB and Frank LR. A model for the coupling between cerebral blood flow and oxygen metabolism during neural stimulation. *J Cereb Blood Flow Metab* 1997; 17: 64–72.
72. Cirillo M, Capasso G and DeSanto NG. Relationship between hematocrit and blood pressure: implications for primary hypertension. *Nephron* 1993; 65: 505–510.
73. Jae SY, Kurl S, Laukkanen JA, et al. Higher blood hematocrit predicts hypertension in men. *J Hypertens* 2014; 32: 245–250.
74. Calamante F, Christensen S, Desmond PM, et al. The physiological significance of the time-to-maximum (Tmax) parameter in perfusion MRI. *Stroke* 2010; 41: 1169–1174.
75. Marshall RS, Lazar RM, Liebeskind DS, et al. Carotid revascularization and medical management for asymptomatic carotid stenosis – hemodynamics (CREST-H): Study design and rationale. *Int J Stroke* 2018; 13: 985–991.
76. Pittman RN. Oxygen gradients in the microcirculation. *Acta Physiol (Oxf)* 2011; 202: 311–322.
77. Rasmussen PM, Jespersen SN and Østergaard L. The effects of transit time heterogeneity on brain oxygenation during rest and functional activation. *J Cereb Blood Flow Metab* 2015; 35: 432–442.
78. Engedal TS, Hjort N, Hougaard KD, et al. Transit time homogenization in ischemic stroke – a novel biomarker of penumbral microvascular failure? *J Cereb Blood Flow Metab* 2018; 38: 2006–2020.
79. Günther M. Highly efficient accelerated acquisition of perfusion inflow series by cycled arterial spin labeling. In: *Proceedings of the 15th annual meeting of ISMRM*. Berlin, Germany, 19–25 May 2007.

80. van Osch MJ, Teeuwisse WM, Chen Z, et al. Advances in arterial spin labelling MRI methods for measuring perfusion and collateral flow. *J Cereb Blood Flow Metab* 2018; 38: 1461–1480.
81. Magon S, Basso G, Farace P, et al. Reproducibility of BOLD signal change induced by breath holding. *Neuroimage* 2009; 45: 702–712.
82. Watchmaker JM, Frederick BD, Fusco MR, et al. Clinical use of cerebrovascular compliance imaging to evaluate revascularization in patients with Moyamoya. *Neurosurgery* 2019; 84: 261–271.
83. Kanda T, Fukusato T, Matsuda M, et al. Gadolinium-based contrast agent accumulates in the brain even in subjects without severe renal dysfunction: evaluation of autopsy brain specimens with inductively coupled plasma mass spectroscopy. *Radiology* 2015; 276: 228–232.
84. Kaczmarz S, Goettler J, Hock A, et al. Reducing T2-related bias in mq-BOLD derived maps of oxygen extraction fraction by 3D acquisition. In: *Proceedings of the 26th annual meeting of ISMRM. Abstract 5023*, Paris, France, 16–21 June 2018.
85. Gersing AS, Ankenbrank M, Schwaiger BJ, et al. Mapping of cerebral metabolic rate of oxygen using dynamic susceptibility contrast and blood oxygen level dependent MR imaging in acute ischemic stroke. *Neuroradiology* 2015; 57: 1253–1261.
86. Preibisch C, Shi K, Kluge A, et al. Characterizing hypoxia in human glioma: a simultaneous multimodal MRI and PET study. *NMR Biomed* 2017; 30: e3775.
87. Wiestler B, Kluge A, Lukas M, et al. Multiparametric MRI-based differentiation of WHO grade II/III glioma and WHO grade IV glioblastoma. *Sci Rep* 2016; 6: 35142.
88. Nonaka H, Akima M, Hatori T, et al. Microvasculature of the human cerebral white matter: arteries of the deep white matter. *Neuropathology* 2003; 23: 111–118.
89. Kaczmarz S, Gottler J, Zimmer C, et al. Characterizing white matter fiber orientation effects on multi-parametric quantitative BOLD assessment of oxygen extraction fraction. *J Cereb Blood Flow Metab* 2020; 40: 760–774.

## 7.4 Journal Publication IV: Oxygen extraction fraction mapping with multi-parametric quantitative BOLD MRI: reduced transverse relaxation bias using 3D-GraSE imaging

The publication entitled *Oxygen extraction fraction mapping with multi-parametric quantitative BOLD MRI: reduced transverse relaxation bias using 3D-GraSE imaging* was published in Neuroimage (ISSN: 1053-8119) electronically on 26 June 2020 under the Creative Commons licence BY-NC-ND [189]. The manuscript was authored by Stephan Kaczmarz, Fahmeed Hyder and Christine Preibisch. It is available online (DOI: 10.1016/j.neuroimage.2020.117095) under Copyright © by the Authors. Preliminary results were also presented in the conference contribution C15. A summary of the publication is provided in Section 7.4.1, the author contributions are listed in Section 7.4.2 and the full text included on the following pages.

### 7.4.1 Abstract

#### Purpose

Quantitative cerebral oxygen extraction fraction (OEF) mapping is of high merit for clinical applications in several diseases. Furthermore, there is high potential of OEF mapping in neuroscientific studies, as the oxygenation is closely linked with neuronal activity. The MRI-based multi-parametric quantitative BOLD (mq-BOLD) technique facilitates whole brain relative OEF (rOEF) mapping and relies on three separate measurements of the transverse relaxation times  $T_2$  and  $T_2^*$  as well as the relative cerebral blood volume (rCBV). Despite of previous successful applications in clinical studies, measured rOEF values were systematically elevated with average GM values around 0.7 instead of expected values in the range of OEF=0.35-0.56, which limits quantitative interpretations and impedes its clinical usability. Those overestimations have been assumed to be related to slice refocussing imperfections caused by stimulated echoes during  $T_2$  imaging by 2D GraSE. We thus hypothesized to improve mq-BOLD towards lower, physiologically more meaningful rOEF values by applying non-slice selective  $T_2$  mapping by 3D-GraSE. Therefore,  $T_2$  related bias in mq-BOLD was compared in vitro and in vivo, in 25 participants.

#### Methods

Scans were performed with a phantom containing six flasks with different  $T_2$  times covering typical cerebral values as well as in 25 participants, including young healthy controls (YHC), elderly healthy controls (EHC) and patients with asymptomatic, unilateral high-grade internal carotid artery stenosis (ICAS) on a 3T clinical MRI scanner. The impact of  $T_2$ -mapping on mq-BOLD was compared for the initially applied 2D GraSE and two proposed 3D GraSE sequences together with additional  $T_2^*$  and rCBV imaging. While 3D GraSE I had similar echo timings and scan time as 2D GraSE, 3D GraSE II was improved by shorter echo spacings, more echoes and prolonged echo train. Phantom reference measurements were performed by multiple single spin echoes. Additionally, a procedure was introduced to identify and exclude artefact affected voxels. Furthermore, super-selective arterial spin labeling (ss-ASL) was applied in ICAS patients to assess the individual perfusion territories.

## Results

In the phantom,  $T_2$  by 3D-GraSE agreed better with the reference values compared to 2D GraSE. Average quantitative  $T_2$  deviations decreased by 57 %. For in vivo scans, formerly overestimated rOEF values were reduced by -27 % ( $p < 0.001$ ) with 3D GraSE and artefact exclusion. While both 3D sequences significantly lowered  $T_2$  values in all groups in line with literature values, best performance was achieved by 3D GraSE II with improved echo sampling. Derived average GM rOEF=0.51 significantly improved and is much closer to literature values. Furthermore, the proposed artefact detection successfully excluded voxels with elevated fit errors, iron depositions and higher magnetic background gradients. Interestingly, a focal rOEF increase in ICAS became only apparent with 3D GraSE, indicating improved sensitivity to pathophysiological hemodynamic impairments. Pathologic origins of the focal rOEF elevation were supported by their locations at the perfusion territory border zone, measured by ss-ASL.

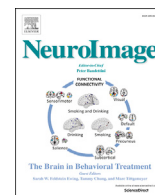
## Conclusion

In summary, 3D GraSE significantly improved rOEF mapping by mq-BOLD, which allows whole brain coverage within clinically feasible scan times and broad availability by using mainly standard clinical sequences. Thus, mq-BOLD with non-slice selective  $T_2$  imaging is highly promising for future clinical and neuroscientific applications.

### 7.4.2 Author contributions

The first author adapted the magnetic resonance pulse sequence (proprietary hardware specific libraries and software from Philips Medical Systems (Best, The Netherlands)), designed the experiment, performed the experiments (MR measurements), developed and implemented the processing pipeline, processed the data, developed and implemented the database to interpret the multi-modal data using Matlab (Mathworks, Natick, MA); With the help and consultation from the coauthors: interpreted the results and wrote the paper.

The program code for post processing of mq-BOLD data for neuroscientific applications is also publicly available at <https://doi.org/10.5281/zenodo.3909300> and [https://gitlab.lrz.de/nmrm\\_lab/public\\_projects/mq-BOLD](https://gitlab.lrz.de/nmrm_lab/public_projects/mq-BOLD).



## Technical Note

## Oxygen extraction fraction mapping with multi-parametric quantitative BOLD MRI: Reduced transverse relaxation bias using 3D-GraSE imaging

Stephan Kaczmarz<sup>a,b,c,\*</sup>, Fahmeed Hyder<sup>b</sup>, Christine Preibisch<sup>a,c,d</sup><sup>a</sup> Technical University of Munich, School of Medicine, Klinikum rechts der Isar, Department of Diagnostic and Interventional Neuroradiology, Munich, Germany<sup>b</sup> Departments of Radiology & Biomedical Imaging and of Biomedical Engineering, Magnetic Resonance Research Center, Yale University, New Haven, CT, 06520, USA<sup>c</sup> Technical University of Munich, School of Medicine, Klinikum rechts der Isar, TUM Neuroimaging Center, Munich, Germany<sup>d</sup> Technical University of Munich, School of Medicine, Klinikum rechts der Isar, Clinic for Neurology, Munich, Germany

## ARTICLE INFO

## Keywords:

Oxygen extraction fraction OEF  
 Multi-parametric quantitative BOLD  
 mq-BOLD  
 $T_2$   
 $R_2'$   
 3D GraSE

## ABSTRACT

Magnetic resonance imaging (MRI)-based quantification of the blood-oxygenation-level-dependent (BOLD) effect allows oxygen extraction fraction (OEF) mapping. The multi-parametric quantitative BOLD (mq-BOLD) technique facilitates relative OEF (rOEF) measurements with whole brain coverage in clinically applicable scan times. mq-BOLD requires three separate scans of cerebral blood volume and transverse relaxation rates measured by gradient-echo ( $1/T_2^*$ ) and spin-echo ( $1/T_2$ ). Although the current method is of clinical merit in patients with stroke, glioma and internal carotid artery stenosis (ICAS), there are relaxation measurement artefacts that impede the sensitivity of mq-BOLD and artificially elevate reported rOEF values.

We posited that  $T_2$ -related biases caused by slice refocusing imperfections during rapid 2D-GraSE (Gradient and Spin Echo) imaging can be reduced by applying 3D-GraSE imaging sequences, because the latter requires no slice selective pulses. The removal of  $T_2$ -related biases would decrease overestimated rOEF values measured by mq-BOLD. We characterized effects of  $T_2$ -related bias in mq-BOLD by comparing the initially employed 2D-GraSE and two proposed 3D-GraSE sequences to multiple single spin-echo reference measurements, both in vitro and in vivo. A phantom and 25 participants, including young and elderly healthy controls as well as ICAS-patients, were scanned. We additionally proposed a procedure to reliably identify and exclude artefact affected voxels. In the phantom, 3D-GraSE derived  $T_2$  values had 57% lower deviation from the reference. For in vivo scans, the formerly overestimated rOEF was reduced by  $-27\%$  ( $p < 0.001$ ). We obtained rOEF = 0.51, which is much closer to literature values from positron emission tomography (PET) measurements. Furthermore, increased sensitivity to a focal rOEF elevation in an ICAS-patient was demonstrated.

In summary, the application of 3D-GraSE improves the mq-BOLD-based rOEF quantification while maintaining clinically feasible scan times. Thus, mq-BOLD with non-slice selective  $T_2$  imaging is highly promising to improve clinical diagnostics of cerebrovascular diseases such as ICAS.

## 1. Introduction

As the brain has high energy demands without oxygen storage capacities, cerebral oxygen supply is crucial (Hyder, 2009). An important parameter of oxygen supply is the oxygen extraction fraction (OEF), which is defined as the ratio of oxygen consumed by the brain to oxygen delivered. OEF has high potential to improve diagnosis of cerebrovascular diseases (CVD) as a biomarker of hemodynamic function (Donahue et al., 2018). In patients with internal carotid artery stenosis (ICAS), correlations between higher OEF and increased stroke risks were found

(Baron et al., 1981; Derdeyn et al., 2002; Powers et al., 2011) as well as local flow-metabolism uncoupling (Goettler et al., 2019). Furthermore, OEF is of interest for neuroscientific applications (Epp et al., 2019), as cerebral oxygen consumption supports neuronal activity (Hyder et al., 2002; Shu et al., 2016a, 2016b; Smith et al., 2002).

OEF measurements were originally established by  $^{15}\text{O}$  labeled water PET (Donahue et al., 2018). However, its application is limited due to the administration of short-lived radioactive  $^{15}\text{O}$ -tracers, invasive arterial blood sampling and restricted availability of PET-facilities with an onsite cyclotron. Thus, several non-invasive MRI-based alternatives have been proposed (Blockley et al., 2012; Pike, 2012). An easily applicable

\* Corresponding author. Technical University of Munich, School of Medicine, Klinikum rechts der Isar, Department of Diagnostic and Interventional Neuroradiology, Ismaninger Str. 22, 81675, Muenchen, Germany.

E-mail address: [stephan.kaczmarz@tum.de](mailto:stephan.kaczmarz@tum.de) (S. Kaczmarz).

<https://doi.org/10.1016/j.neuroimage.2020.117095>

Received 28 February 2020; Received in revised form 11 June 2020; Accepted 18 June 2020

Available online 26 June 2020

1053-8119/© 2020 The Author(s). Published by Elsevier Inc. This is an open access article under the CC BY-NC-ND license (<http://creativecommons.org/licenses/by-nc-nd/4.0/>).



Abbreviations	
ANOVA	Analysis of variance
ASE	Asymmetric spin echo
BOLD	Blood-oxygenation-level-dependent
CBV	Cerebral blood volume
CSF	Cerebrospinal fluid
DSC	Dynamic susceptibility contrast
EHC	Elderly healthy control
EPI	Echo planar imaging
FID	Free induction decay
FLAIR	Fluid-attenuated inversion recovery
GESFIDE	Gradient Echo Sampling of FID and Echo
GESSE	Gradient Echo Sampling of Spin Echo
GM	Gray matter
GraSE	Gradient and spin echo
GRE	Gradient echo
ICAS	Internal carotid artery stenosis
MPRAGE	Magnetization prepared rapid acquisition gradient echo
mq-BOLD	Multi-parametric quantitative BOLD
MRI	Magnetic resonance imaging
NAWM	Normal appearing white matter
OEF	Oxygen extraction fraction
PET	Positron Emission Tomography
PVE	Partial volume effect
q-BOLD	Quantitative BOLD
rCBV	Relative cerebral blood volume
rOEF	Relative oxygen extraction fraction
single-SE	Single spin echo
TE	Echo time
TI	Inversion time
TR	Repetition time
TSE	Turbo spin echo
VOI	Volume of interest
WM	White matter
YHC	Young healthy control

technique with full brain coverage is multi-parametric quantitative BOLD (mq-BOLD) (Hirsch et al., 2014). This approach relies on the biophysical model of Yablonskiy and Haacke (1994) and derives relative OEF (rOEF) based on three separate measurements of transverse relaxation times by spin-echo ( $T_2$ ) and gradient-echo ( $T_2^*$ ) as well as the relative cerebral blood volume (rCBV) (Hirsch et al., 2014). Mq-BOLD is highly promising in several pathologies, such as stroke (Gersing et al., 2015), glioma (Preibisch et al., 2017; Toth et al., 2013; Wiestler et al., 2016) and ICAS (Goettler et al., 2019; Kaczmarz et al., 2020a).

However, systematic errors still limit quantitative interpretations and impede the clinical usability of mq-BOLD. Measured rOEF = 0.6–0.7 in healthy GM was systematically elevated (Goettler et al., 2019; Kaczmarz et al., 2020b) compared to physiologically expected OEF = 0.35–0.56 (Donahue et al., 2018; Marchal et al., 1992), and was thus appropriately named relative OEF (Hirsch et al., 2014). In that regard,  $T_2$  overestimations can occur by 2D-GraSE (Gradient and Spin Echo) (Hirsch

et al., 2014) as well as 2D-TSE (Turbo Spin Echo) imaging (Seiler et al., 2019). A known issue in  $T_2$ -mapping is stimulated echoes, which arise from imperfect matching between the excitation and refocusing pulse profiles (Hennig, 1988; Uddin et al., 2013). This is specific to 2D-acquisitions because of slice-selection pulse imperfections near slice edges. To overcome this limitation, non-slice selective (Prasloski et al., 2012a) and 3D-acquisition techniques are advisable (Prasloski et al., 2012b; Whittall et al., 1997), making 3D-GraSE (Oshio and Feinberg, 1991) ideal to overcome  $T_2$ -related bias in mq-BOLD.

The aim of this study was therefore to improve rOEF mapping by mq-BOLD towards lower, physiologically more meaningful values. We hypothesized significantly reduced  $T_2$ -related bias by applying 3D-GraSE. We further proposed a procedure to reliably identify and exclude artefact voxels to enhance the sensitivity to pathophysiological focal rOEF increases. To this end,  $T_2$  and rOEF were compared between mq-BOLD with 2D-GraSE and 3D-GraSE in a phantom and in 25 subjects, including ICAS-patients.

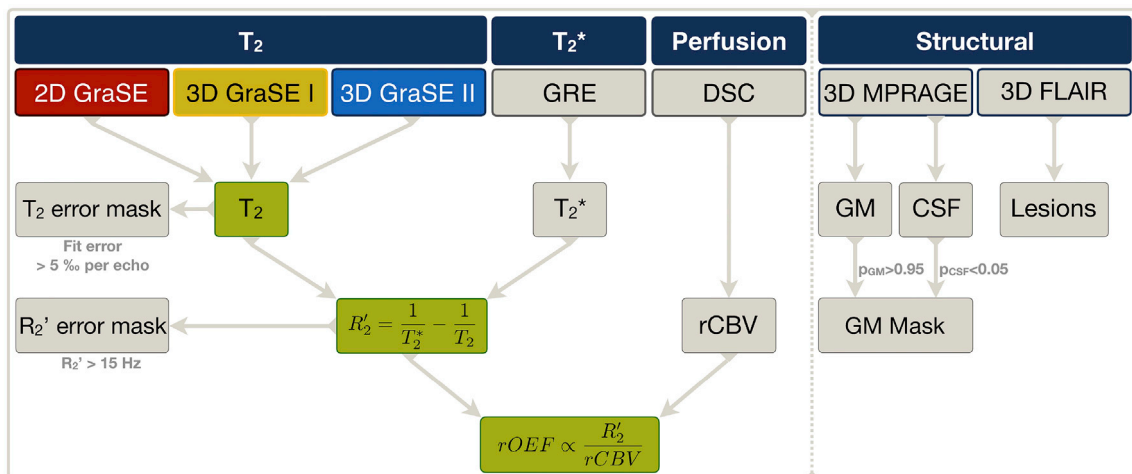


Fig. 1. Overview of applied MRI sequences and derived parameters.

The main purpose of this study was to compare the impact of three different GraSE sequences on  $T_2$  mapping,  $R_2'$  and rOEF calculations by mq-BOLD. We therefore measured the formerly applied 2D-GraSE (red) as well as the proposed 3D-GraSE-I (yellow) and II sequences (blue). Quantitative  $T_2^*$  imaging was performed by multi-echo gradient echo (GRE) imaging.  $R_2'$  was subsequently calculated from  $T_2$  and  $T_2^*$ , separately for all three GraSE sequences. Masks of elevated  $T_2$  fit-errors ( $T_2$  error mask) and of  $R_2'$  elevations ( $R_2'$  error mask) were generated to exclude artefact voxels. Dynamic susceptibility contrast (DSC) imaging was applied to obtain relative cerebral blood volume (rCBV) maps. By applying the mq-BOLD model to rCBV and  $R_2'$ , each voxel's rOEF was calculated for each  $T_2$  GraSE sequence, respectively. The impact of the three different GraSE sequences on  $T_2$ ,  $R_2'$  and rOEF was evaluated (green). Besides, restrictive GM masks excluding CSF were generated and FLAIR lesions evaluated by structural imaging.

## 2. Methods

Quantitative  $T_2$ -mapping and its impact on mq-BOLD were compared for the initially applied 2D-GraSE and two proposed 3D-GraSE sequences (Fig. 1). The echo timings and scan time of 3D-GraSE-I were similar to 2D-GraSE, whereas 3D-GraSE-II used shorter echo spacing (16 ms  $\rightarrow$  10 ms) with more echoes (8  $\rightarrow$  16) and prolonged echo train (128 ms  $\rightarrow$  160 ms). Evaluations were conducted in four steps. First, in a phantom compared with multiple single spin echoes (single-SE) as a reference. Second,  $R_2'$  was calculated with additionally acquired  $T_2^*$ -maps in young healthy controls (YHC). In the last two steps, rOEF by mq-BOLD was evaluated in elderly healthy controls (EHC) and ICAS-patients based on the different  $T_2$ -sequences with additional  $T_2^*$  and rCBV mapping.

### 2.1. Phantom and participants

The gel phantom contained six flasks with different  $T_2$  relaxation times covering typical GM values (see inlay in Fig. 2B and Supplemental Table 1). For in vivo evaluations, 25 volunteers participated in this prospective study. Participants were enrolled by word-of-mouth advertisement from March until October 2017. Ten YHC (4 females, mean age  $28.4 \pm 4.1$  years, range 21–35 years), twelve EHC (7 females, mean age  $71.8 \pm 5.3$  years, range 63–78 years) and three patients with unilateral, high-grade, asymptomatic, extracranial ICAS were scanned (2 females, mean age  $63.0 \pm 9.6$  years, range 52–70 years). The study was approved by the medical ethical board of the Klinikum rechts der Isar, in line with Human Research Committee guidelines of the Technical University of Munich (TUM). All participants provided informed consent in accordance with the standard protocol approvals. Data of two YHC needed to be excluded due to technical problems during data acquisition.

### 2.2. Image acquisition

Scanning was performed on a 3T Philips Ingenia MR-Scanner (Philips Healthcare, Best, The Netherlands) on software release R5.1.8 with a custom patch. Standard 32-channel head-receive and 16-channel head/neck-receive coils were used. The following imaging protocol was applied (see Fig. 1):

- **2D-GraSE:** 8 echoes;  $TE_1 = \Delta TE = 16$  ms; TR = 8596 ms; EPI-factor = 7;  $\alpha = 90^\circ$ ;  $180^\circ$  refocusing control; 30 slices; 0.3 mm gap; voxel size  $2.0 \times 2.1 \times 3.0$  mm<sup>3</sup>; matrix  $112 \times 91$ ; acq. time 2:23 min.
- **3D-GraSE-I:** 8 echoes;  $TE_1 = \Delta TE = 16$  ms; TR = 251 ms; oversampling 1.3; EPI-factor = 7; TSE-factor = 8;  $\alpha = 90^\circ$ ;  $180^\circ$  refocusing control; 30 slices; voxel size  $2.0 \times 2.1 \times 3.0$  mm<sup>3</sup>; matrix  $112 \times 91$ ; acq. time 2:08 min.
- **3D-GraSE-II:** 16 echoes,  $TE_1 = \Delta TE = 10$  ms; TR = 487 ms; oversampling 1.3; EPI-factor = 7; TSE-factor = 16;  $\alpha = 90^\circ$ ;  $180^\circ$  refocusing control; 30 slices; voxel size  $2.0 \times 2.1 \times 3.0$  mm<sup>3</sup>; matrix  $112 \times 91$ ; acq. time 4:09 min.
- **Single-SE** for phantom reference measurements: TE = 60, 70, 80, 100, 120, 140, 160 ms; TR = 3000 ms, each; 5 slices, acquired voxel size  $3.5 \times 4.0 \times 4.0$  mm<sup>3</sup>; acq. time 2:36 min per TE.
- **Multi-echo gradient echo (GRE):** 12 echoes,  $TE_1 = \Delta TE = 5$  ms, TR = 1950 ms,  $\alpha = 30^\circ$ , 30 slices, matrix  $112 \times 92$ , voxel size  $2.0 \times 2.0 \times 3.0$  mm<sup>3</sup>, total acq. time 6:08 min.
- **DSC-MRI:** single-shot GRE-EPI, 80 volumes during injection of weight-adjusted Gd-DOTA bolus (concentration 0.5 mmol/ml; dose 0.1 mmol/kg; minimum 7.5 mmol per subject; flow rate 4 ml/s) with TE = 30 ms, TR = 1513 ms;  $\alpha = 60^\circ$ ; 26 slices; voxel size  $2.0 \times 2.0 \times 3.5$  mm<sup>3</sup>, acq. time 2:01 min.
- **MPRAGE:** 3D acquisition, TE = 4 ms; TR = 9 ms;  $\alpha = 8^\circ$ ; TI = 1000 ms; shot interval 2300 ms; SENSE AP/RL 1.5/2.0; 170 slices; matrix  $240 \times 238$ ; voxel size  $1.0 \times 1.0 \times 1.0$  mm<sup>3</sup>; acq. time 5:59 min

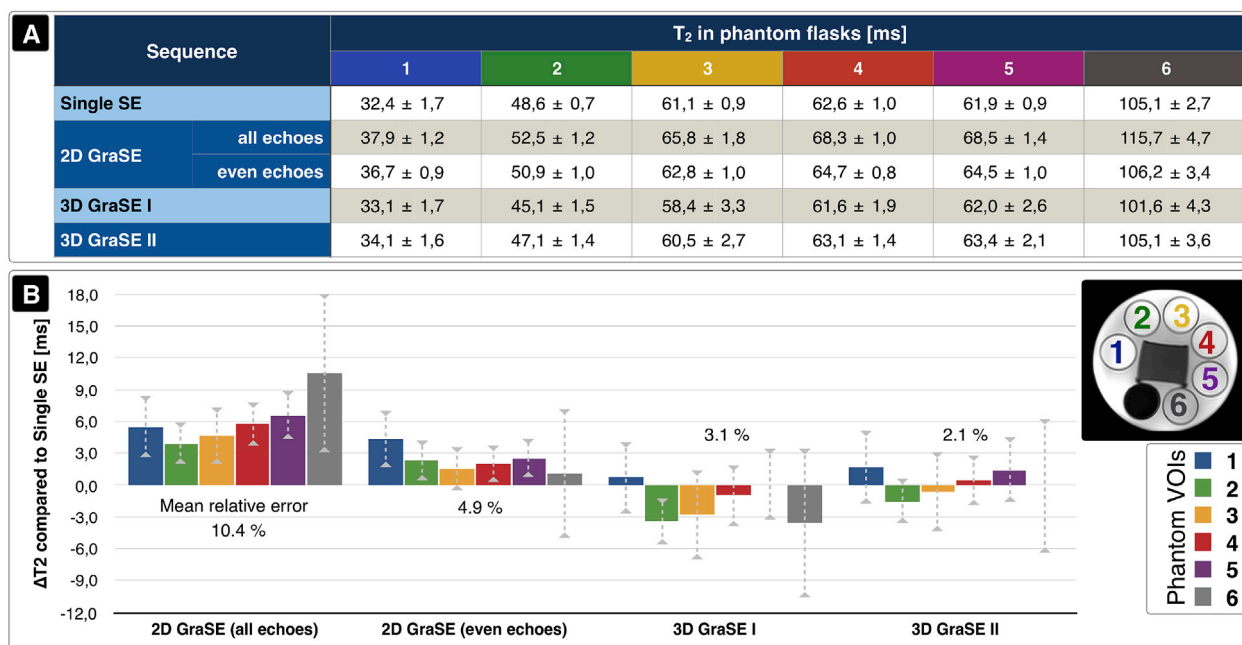


**Fig. 2. Comparison of quantitative  $T_2$  values measured by different sequences in a phantom.**

The phantom contained six flasks with different  $T_2$  relaxation times. (A) Average  $T_2$  values within each flask are summarized for the multiple single spin echo (Single SE) reference sequence, 2D-GraSE with all and even echoes fitted, 3D-GraSE-I and 3D-GraSE-II (mean  $\pm$  standard deviation) with all echoes fitted. (B)  $T_2$  values derived from single-SE data were used as references and compared to the GraSE results. This  $\Delta T_2$  is plotted for all phantom flasks and GraSE sequences and scaled in ms. Corresponding values within each flask are shown by consistent color coding (see inlay in B). The average  $T_2$  deviation of each GraSE sequence is noted in percent. Best accordance was found for 3D-GraSE-II.



- **FLAIR**: 3D acquisition, TE = 289 ms; TR = 4800 ms; TI = 1650 ms;  $\alpha = 90^\circ$ ; TSE-factor = 167; 163 slices; matrix  $224 \times 224$ ; voxel size  $1.1 \times 1.1 \times 1.1 \text{ mm}^3$ ; acq. time 4:34 min.

### 2.3. Image analysis

Data evaluations were performed using MATLAB R2016b (The MathWorks Inc., Natick, USA) and SPM12 (v6225) (Penny et al., 2011) with custom programs. Quantitative  $T_2$  parameter maps were derived by mono-exponential fittings of all echoes for 3D-GraSE and only even echoes for 2D-GraSE in vivo, as initially implemented to reduce stimulated echoes (Hirsch et al., 2014). Multi-echo GRE data were corrected for macroscopic background gradients (Baudrexel et al., 2009; Hirsch and Preibisch, 2013) and motion (Magerkurth et al., 2011) before mono-exponential fitting for  $T_2^*$  and spatial coregistration to  $T_2$ . Both,  $T_2^*$  and  $T_2$ -maps were smoothed with a 3D Gaussian filter-kernel of 3 mm prior to the calculation of

$$R_2' = \frac{1}{T_2^*} - \frac{1}{T_2} \quad [1]$$

DSC data was processed as described previously (Hedderich et al., 2019; Kluge et al., 2016) with CBV normalization to 2.5% in normal appearing white matter (NAWM) (Leenders, 1994), yielding relative CBV (rCBV). Following the mq-BOLD approach, rOEF was calculated as

$$rOEF = \frac{R_2'}{c \cdot rCBV} \quad [2]$$

with  $c = \gamma \cdot \frac{4}{3} \cdot \pi \cdot \Delta\chi \cdot B_0$ ,  $B_0 = 3T$  and  $\Delta\chi = \text{Hct} \cdot \Delta\chi_0 = 0.35 \cdot 0.264 \cdot 10^{-6} = 0.924 \cdot 10^{-7}$  (Hirsch et al., 2014).

To investigate the impact of the different  $T_2$ -mapping sequences,  $R_2'$  and rOEF were calculated with the same  $T_2^*$  and rCBV (Fig. 1). For quality assessment, all parameter maps were screened specifically for motion artefacts and spatial misregistration (raters: SK, CP).

### 2.4. Artefact removal

To account for mismatches between the measured data and mono-exponential fittings of  $T_2$  and  $T_2^*$ , fit-errors were evaluated on a voxel-wise basis and normalized by the number of acquired echoes. Empirically set thresholds were applied and checked carefully (SK, CP). Voxels with fit-errors >5% per echo were excluded from data evaluation (Supplemental Fig. 1). An additional threshold of  $R_2' < 15 \text{ s}^{-1}$  was applied (Kaczmarz et al., 2020b) to exclude areas with iron-induced focal  $R_2'$  increases, especially in deep GM regions. This also excluded areas with higher macroscopic background gradients, as corrections are only reliable up to approximately  $220 \mu\text{T/m}$  (Hirsch and Preibisch, 2013).

### 2.5. Statistical analyses

Phantom measurements were evaluated by averaging  $T_2$ -values within VOIs in each flask. 2D-GraSE was compared with 3D-GraSE-I, II and single-SE reference values (Prasloski et al., 2012b). For in-vivo evaluations, restrictive GM masks were generated from MPRAGE segmentations ( $p_{GM} > 0.95$ ) with additional CSF exclusion ( $p_{CSF} < 0.05$ ). Within these masks, average  $T_2$ ,  $T_2^*$ ,  $R_2'$ , rCBV, and rOEF values were calculated. The impact of 2D vs. 3D-GraSE on  $T_2$ ,  $R_2'$  and rOEF values in GM on group level was illustrated by paired scatter plots. Significance of group mean value differences was tested by ANOVA, homogeneity of variance asserted using Levene's test and pairwise correlations corrected for multiple comparisons with Tukey or Games-Howell post-hoc analysis in SPSS (v26, IBM Corp., Armonk, USA). Values of  $p < 0.05$  were considered statistically significant. Distributions of the fit-errors and parameter values were compared by histograms.

## 3. Results

In the phantom, single-SE reference measurements revealed average transverse  $T_2$  relaxation times between 32.4 and 105.1 ms within the six flasks. By comparison, the original 2D-GraSE sequence overestimated  $T_2$  by 10.4% with all echo fitting and 4.9% with even echoes only. The 3D-GraSE-I and II sequences reduced overestimations to 3.1% and 2.1%, respectively (Fig. 2).

In YHC, quantitative  $T_2$ -mapping by 2D-GraSE with even echo fitting yielded  $T_2 = 83.9 \pm 1.1 \text{ ms}$ . 3D-GraSE-I and II decreased  $T_2$  by  $-8.8\%$  and  $-6.8\%$ , respectively ( $T_2 = 76.5 \pm 1.2 \text{ ms}$  and  $78.2 \pm 1.1 \text{ ms}$ ;  $p < 0.001$ , each). Consequently,  $R_2'$  decreased by  $-14.5\%$  and  $-13.3\%$  for 3D-GraSE-I and II ( $R_2' = 6.9 \pm 0.3 \text{ s}^{-1}$  and  $7.2 \pm 0.4 \text{ s}^{-1}$ ) compared to  $R_2' = 8.3 \pm 0.4 \text{ s}^{-1}$  by 2D-GraSE with  $T_2^* = 53.9 \pm 1.7 \text{ ms}$  (Table 1). Additional artefact exclusion further reduced the  $T_2$  and  $R_2'$  values (3D-GraSE-I:  $T_2 = 75.2 \pm 1.0 \text{ ms}$  and  $R_2' = 5.6 \pm 0.2 \text{ s}^{-1}$ ; 3D-GraSE-II:  $T_2 = 77.9 \pm 1.0 \text{ ms}$  and  $R_2' = 6.1 \pm 0.2 \text{ s}^{-1}$ ). While artefact exclusion effects on  $T_2$ -values were comparably weak ( $p > 0.5$ ; Fig. 3A),  $R_2'$  values decreased by up to  $-32.5\%$  ( $p < 0.001$ ; Fig. 3B). Fit-errors of 3D-GraSE-II were much lower (0.1%) compared to 3D-GraSE-I (19.6%) and 2D-GraSE (15.3%, Fig. 3C; Table 2). For 3D-GraSE-II, most excluded voxels were affected by  $T_2^*$  fit-errors (83.3%), followed by  $R_2'$  elevations (51.5%) and only minor  $T_2$  fit-errors (0.9%). The fraction of voxels in GM excluded due to  $R_2'$  thresholding was similar between 2D (9.7%) and 3D-GraSE-II (7.3%). Due to lowest errors and time restrictions, 3D-GraSE-II was applied in the following evaluations in EHC as well as ICAS-patients and compared with 2D-GraSE.

In EHC, 2D-GraSE yielded  $T_2$ -values of  $89.2 \pm 3.1 \text{ ms}$ . Average GM values of  $R_2' = 8.5 \pm 0.7 \text{ s}^{-1}$  and rOEF =  $0.70 \pm 0.08$  were calculated from additional measurements of  $T_2^*$  ( $55.7 \pm 4.0 \text{ ms}$ ) and rCBV ( $4.71 \pm 0.27\%$ ) (Table 1). The application of 3D-GraSE-II significantly decreased  $T_2$  by  $-8.5\%$  ( $T_2 = 81.6 \pm 1.9 \text{ ms}$ ;  $p < 0.001$ ),  $R_2'$  by  $-12.9\%$  ( $R_2' = 7.4 \pm 0.7 \text{ s}^{-1}$ ,  $p < 0.001$ ) and rOEF by  $-15.7\%$  (rOEF =  $0.59 \pm 0.08$ ,  $p < 0.03$ ). Artefact exclusion further decreased  $R_2'$  and rOEF by up to  $-27.1\%$  in total ( $R_2' = 6.6 \pm 0.6 \text{ s}^{-1}$ ; rOEF =  $0.51 \pm 0.06$ ;  $p < 0.03$ ; Fig. 4). FLAIR lesion gradings with an average Fazekas-score of 1.3 indicated only minor microangiopathic changes (Fazekas et al., 1987). None of the participants had subacute or older territorial infarct lesions.

In ICAS, all parameter values decreased with 3D-GraSE-II and artefact exclusion, yielding similar values as in EHC (Table 1). Furthermore, focal rOEF hyperintensities ipsilateral to the stenosis were enhanced and only recognizable by 3D-GraSE-II (Fig. 5A). Two regions stand out in the artefact maps. First, well-known iron deposition in the striatum corresponds to maximum rOEF-values. Second, artefact voxels occur along the brains' surface towards the cranial bone (Fig. 5A). Artefact removal in 3D-GraSE-II improved rOEF towards lower values and additionally decreased the number of voxels with maximum rOEF values (Fig. 5B).

## 4. Discussion

$T_2$ -mapping by 2D-vs 3D-GraSE was compared with regard to their impact on rOEF values modeled by mq-BOLD. Formerly overestimated  $T_2$ ,  $R_2'$  and rOEF values significantly improved by 3D-GraSE, as hypothesized. Remarkably, 3D-GraSE-II also improved the fit quality, lowering the number of excluded artefact voxels due to  $T_2$  fit-errors in ICAS-patients by the factor 30. The specific impact of 3D-GraSE on  $T_2$ ,  $R_2'$  and rOEF are discussed below.

### 4.1. Impact on $T_2$

The phantom measurements confirmed  $T_2$  overestimations by 2D-GraSE (Hirsch et al., 2014). 3D-GraSE lowered  $T_2$ -values, as hypothesized, only deviating 2.1% from single-SE values. Similarly, comparisons in YHC confirmed overestimations by 2D-GraSE, whereas lower average GM values of  $T_2 = 76.5 \text{ ms}$  were measured with 3D-GraSE-I. This agrees well with literature values at 3T of  $T_2 = 73.5 \text{ ms}$  in YHC by single-SE

**Table 1**  
**Summary of average parameter values for all groups.**

Quantitative parameter values were compared for YHC, EHC and ICAS-patients. The number of scanned participants is shown for each group. Two YHC were excluded due to data acquisitions problems. Average  $T_2$  values in GM were calculated for all GraSE sequences (group mean  $\pm$  standard deviation), each with and without artefact exclusion ("corrected"). Displayed 2D-GraSE values were generated by fitting of even echoes only. Resulting  $R_2'$  values were calculated from GraSE-based  $T_2$  values and GRE-based  $T_2^*$ . For EHC and ICAS-patients, rOEF values were calculated from  $R_2'$  and additionally acquired DSC-based rCBV maps. Note, 3D-GraSE-I and II decreased  $T_2$ ,  $R_2'$  and rOEF towards physiologically more realistic values for all subject groups.

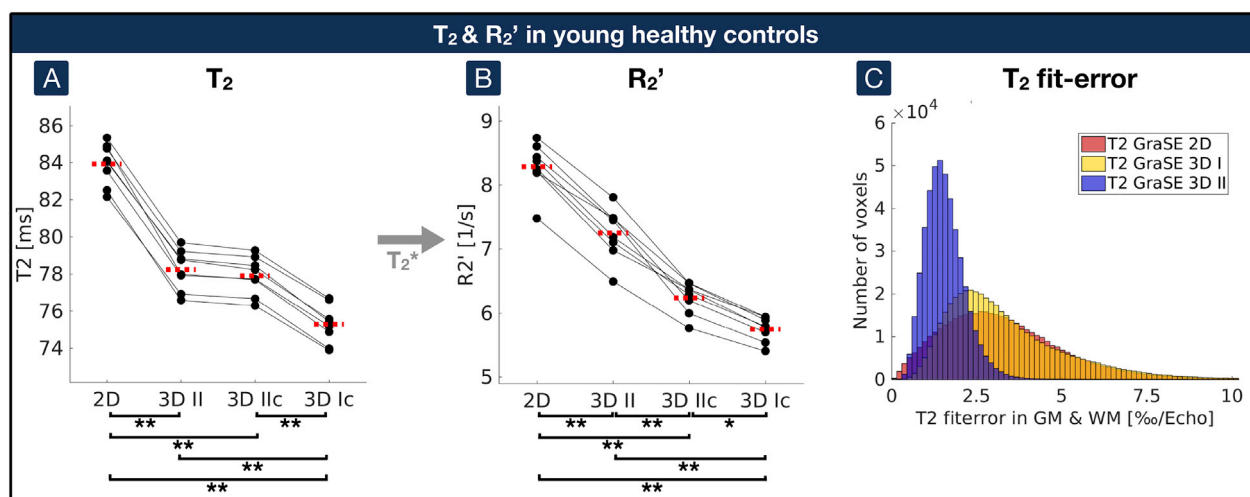
Participants	Average $T_2$ in GM [ms]						
Group	n	2D GraSE	2D GraSE corrected	3D GraSE I	3D GraSE I corrected	3D GraSE II	3D GraSE II corrected
YHC	10	83.9 $\pm$ 1.1	81.6 $\pm$ 0.9	76.5 $\pm$ 1.2	75.2 $\pm$ 1.0	78.2 $\pm$ 1.1	77.9 $\pm$ 1.0
EHC	12	89.2 $\pm$ 3.1	85.4 $\pm$ 2.5	–	–	81.6 $\pm$ 1.9	81.2 $\pm$ 2.0
ICAS	3	89.6 $\pm$ 1.3	85.9 $\pm$ 1.8	–	–	82.9 $\pm$ 0.7	82.2 $\pm$ 1.2

Participants	Average $R_2'$ in GM [1/s]							$T_2^*$ [ms]
Group	n	2D GraSE	2D GraSE corrected	3D GraSE I	3D GraSE I corrected	3D GraSE II	3D GraSE II corrected	
YHC	10	8.3 $\pm$ 0.4	6.9 $\pm$ 0.3	6.9 $\pm$ 0.3	5.6 $\pm$ 0.2	7.2 $\pm$ 0.4	6.1 $\pm$ 0.2	53.9 $\pm$ 1.7
EHC	12	8.5 $\pm$ 0.7	7.7 $\pm$ 0.6	–	–	7.4 $\pm$ 0.7	6.6 $\pm$ 0.6	55.7 $\pm$ 4.0
ICAS	3	8.4 $\pm$ 0.7	7.3 $\pm$ 0.4	–	–	7.6 $\pm$ 0.9	6.6 $\pm$ 0.5	56.5 $\pm$ 2.4

Participants	Average rOEF in GM [%]							rCBV [%]
Group	n	2D GraSE	2D GraSE corrected	3D GraSE I	3D GraSE I corrected	3D GraSE II	3D GraSE II corrected	
YHC	10	–	–	–	–	–	–	–
EHC	12	0.70 $\pm$ 0.08	0.61 $\pm$ 0.06	–	–	0.59 $\pm$ 0.08	0.51 $\pm$ 0.06	4.71 $\pm$ 0.27
ICAS	3	0.65 $\pm$ 0.05	0.59 $\pm$ 0.02	–	–	0.58 $\pm$ 0.06	0.52 $\pm$ 0.03	4.68 $\pm$ 0.04



**Fig. 3. Impact of GraSE sequences and artefact exclusion on  $T_2$  and  $R_2'$  compared by paired scatterplots in young healthy controls.**

(A) Quantitative  $T_2$  values in GM were compared between the 2D-GraSE ("2D"), 3D-GraSE-II ("3D II"), 3D-GraSE-II with additional artefact exclusion ("3D IIc") and 3D-GraSE-I with artefact exclusion ("3D Ic"). Voxels with elevated  $T_2$  fit-errors or  $R_2'$  elevations were excluded by artefact exclusion. (B)  $R_2'$  was calculated based on  $T_2$  values from the different GraSE sequences with the same quantitative  $T_2^*$  map. (A, B) Single participant's average parameter values in GM are represented by black dots. Corresponding values of the same participant are connected by black lines. Median values on group level are indicated by red dashed lines for each parameter and acquisition technique. Asterisks indicate significant differences with  $p < 0.03$ , double asterisks  $p < 0.001$  with correction for multiple comparisons. (C) Errors of the  $T_2$  fits were compared for the three GraSE sequences. Average errors within GM of all participants are shown in the histogram. Voxels with fit-errors  $> 5\%$  per echo were excluded from the artefact-corrected analyses ("3D Ic" and "3D IIc"). Note much lower fit-errors in 3D-GraSE-II, indicating better fitting quality (blue).

(Hirsch et al., 2014) and  $T_2 = 76.2$  ms in EHC by multi-SE (Christen et al., 2012). The proposed artefact voxel exclusion further improved  $T_2$ -values. While both 3D-GraSE sequences improved  $T_2$ , 3D-GraSE-II performed best with regards to lowest fit errors, due to its improved echo sampling. Evaluations of average fit-errors revealed improvements in 3D-GraSE vs. 2D-GraSE by a factor up to 2 (Supplemental Fig. 2) and reduced voxel exclusions due to  $T_2$  fit-errors up 150 times (Table 2).

Literature values of alternative  $T_2$ -mapping by TSE yielded much higher healthy average GM values of 119 ms (Sedlacik et al., 2014; Wagner et al., 2012, 2015), which necessitates sophisticated quantitative  $T_2$  post-processing corrections (Noth et al., 2017). Thus, 3D-GraSE is ideal for fast, quantitative  $T_2$ -mapping with full brain coverage (Prasloski et al., 2012b; Whittall et al., 1997).

#### 4.2. Impact on $R_2'$

$R_2'$  was calculated based on  $T_2$  and additional  $T_2^*$ -mapping. As for  $T_2$ , average  $R_2'$  values decreased with 3D-GraSE to  $R_2' = 6.1$  s $^{-1}$  in YHC, with artefact exclusion. This is in good agreement with literature values by GRE and TSE of similar aged healthy participants in frontal cortex with  $R_2' = 7.4$  s $^{-1}$  (Sedlacik et al., 2014) and  $R_2' = 7.9$  s $^{-1}$  (Wagner et al., 2012). Remaining deviations may be due to fittings of only 3 and 5 echoes for  $T_2$  in those studies, respectively, which might be insufficient (Whittall et al., 1997). In general, reported average  $R_2'$  values vary. While much higher average GM values of  $R_2' = 12.0$  s $^{-1}$  have been reported by GRE and TSE (Wagner et al., 2015), other methods reported lower values, specifically  $R_2' = 5.1$  s $^{-1}$  by GRE (Ulrich and Yablonskiy,

**Table 2**  
Summary of average fit-errors for all groups.

Fit-errors were compared for YHC, EHC and ICAS-patients. The number of scanned participants is shown for each group. Fit-errors in GM were evaluated for the 2D-GraSE, 3D-GraSE-I and 3D-GraSE-II, scaled in permille per echo (group mean  $\pm$  standard deviation). Voxels with fit-errors  $>5\%$  per echo were excluded. The corresponding fraction of excluded GM voxels due to  $T_2$  fit-errors are compared for all sequences and groups. Note, clearly decreased errors by 3D-GraSE-II with only few excluded voxels ( $\leq 1\%$ ).

Participants	n	Average T2 fit-error in GM [%/echo]			Fraction of excluded GM voxels (with error $> 5\%$ /echo) [%]		
		2D GraSE	3D GraSE I	3D GraSE II	2D GraSE	3D GraSE I	3D GraSE II
YHC	10	3.2 $\pm$ 0.2	3.5 $\pm$ 0.3	1.5 $\pm$ 0.1	15.3	19.6	0.1
EHC	12	4.0 $\pm$ 0.3	–	1.8 $\pm$ 0.1	26.4	–	0.3
ICAS	3	4.0 $\pm$ 0.2	–	1.8 $\pm$ 0.2	28.4	–	1.0

2015),  $R_2' = 3.0 \text{ s}^{-1}$  and  $4.4 \text{ s}^{-1}$  by asymmetric spin echo (ASE) (An and Lin, 2003; Blockley and Stone, 2016),  $R_2' = 2.9 \text{ s}^{-1}$  by GESSE (He and Yablonskiy, 2007) and  $R_2' = 2.7 \text{ s}^{-1}$  by Gradient Echo Sampling of FID and Echo (GESFIDE) (Ni et al., 2014).

The proposed artefact exclusion had stronger effects on average  $R_2'$  than  $T_2$  values, due to removal of  $R_2'$  elevations, which were caused by strong susceptibility gradients at the borders and in fronto-basal and temporal brain regions as well as iron deposition in the striatum (Fig. 5A and Supplemental Fig. 3). As  $R_2'$  values decreased with 3D-GraSE-II compared to 2D-GraSE, slightly fewer voxels were excluded by  $R_2'$  thresholding. Iron concentration increases with age could explain increased number of artefact voxels in EHC vs. YHC. The observed  $R_2'$  increases with age also agree with literature (Sedlacik et al., 2014).

#### 4.3. Impact on rOEF

Maps of rOEF were calculated in EHC and ICAS-patients based on  $R_2'$  and additional rCBV measurements. 2D-GraSE yielded rOEF = 0.70 in accordance with previously reported overestimations (Hirsch et al., 2014). But rOEF was significantly lower with 3D-GraSE. Artefact

exclusion further decreased the average GM value to rOEF = 0.51 in EHC. Overall, rOEF values decreased by  $-27.1\%$  by 3D-GraSE and artefact exclusion, which is more similar to literature values from PET measurements (Donahue et al., 2018; Marchal et al., 1992). While a similar mq-BOLD implementation using the same model yielded much lower average OEF = 0.33 in healthy controls (Christen et al., 2012), they restricted  $T_2$  imaging echo-times to maximum 55 ms. Together with comparably high CBV values, this explains their systematically lower OEF values (see Eqs. (1) and (2)).

Values of  $T_2$ ,  $R_2'$  and rOEF with 3D-GraSE were comparable in EHC and ICAS-patients. This is in line with previously observed unaffected rOEF on group level in high-grade stenosis patients (Bouvier et al., 2015; Goettler et al., 2019). Nevertheless, focal rOEF increases have been found (Kaczmarz et al., 2020a), which potentially have a high clinical relevance as an indicator of misery perfusion to assess individual stroke risks (Baron et al., 1981). Interestingly, those focal rOEF elevations were only visible with 3D-GraSE (Fig. 5A). Pathophysiological origins of rOEF elevations are supported by their localization at the border zone between perfusion territories (Supplemental Fig. 4), measured by super-selective arterial spin labeling (Helle et al., 2010). This increased sensitivity of mq-BOLD with 3D-GraSE in an ICAS-patient, as a proof-of-principle, is highly promising for the detection of even subtle oxygenation changes.

#### 4.4. Applicability and limitations

An obvious strength of this study is its potential for widespread clinical applications due to standard sequences. Minor remaining  $T_2$  variations may be attributed to diffusion effects, especially for single-SE (Carr and Purcell, 1954), and known echo timing dependencies, which are also related to diffusion (Poon and Henkelman, 1992; Whittall et al., 1999). In vivo scans can be additionally affected by partial volume effects (PVE), especially in presence of CSF contamination (Whittall et al., 1999), and multi-compartmental tissue structures (MacKay et al., 2006). Nevertheless, mono-exponential fittings were applied to achieve full brain volume coverage within clinically feasible scan times, while multi-exponential fittings would require higher SNR (Whittall et al., 1997).

Measured rOEF values may be slightly higher than literature PET values due to PVE, especially with CSF (He and Yablonskiy, 2007; Stone

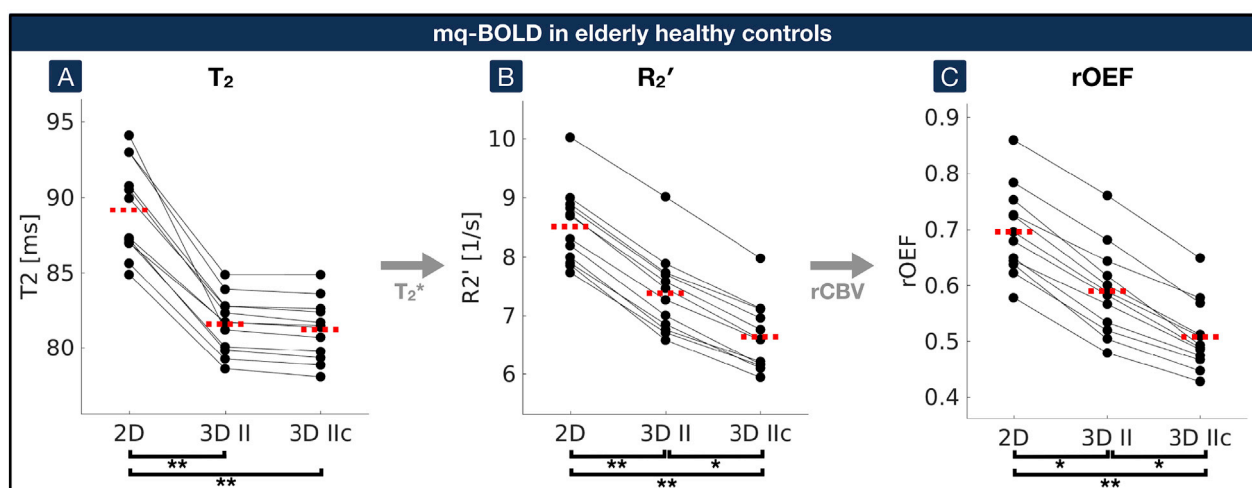


**Fig. 4.** Impact of 2D and 3D-GraSE-II sequences on mq-BOLD parameters by paired scatterplots in elderly healthy controls.

(A) Quantitative  $T_2$ -values acquired by 2D-GraSE ("2D"), 3D-GraSE-II ("3D II") and with additional artefact correction ("3D IIc") were compared. (B)  $R_2'$  was calculated based on  $T_2$  values obtained by the different GraSE sequences and the quantitative  $T_2^*$ -map. (C)  $R_2'$  values were combined with DSC-based rCBV to calculate rOEF according to the mq-BOLD model. Single participant's average parameter values in GM are represented by black dots. Corresponding values of the same participant are connected by black lines. Median values on group level are indicated by red dashed lines for each parameter and sequence. Asterisks indicate significant differences with  $p < 0.03$ , double asterisks  $p < 0.001$  with correction for multiple comparisons. While artefact correction of 3D-GraSE ("3D IIc") has a comparably low impact on  $T_2$ , corresponding  $R_2'$  and rOEF values were significantly decreased.

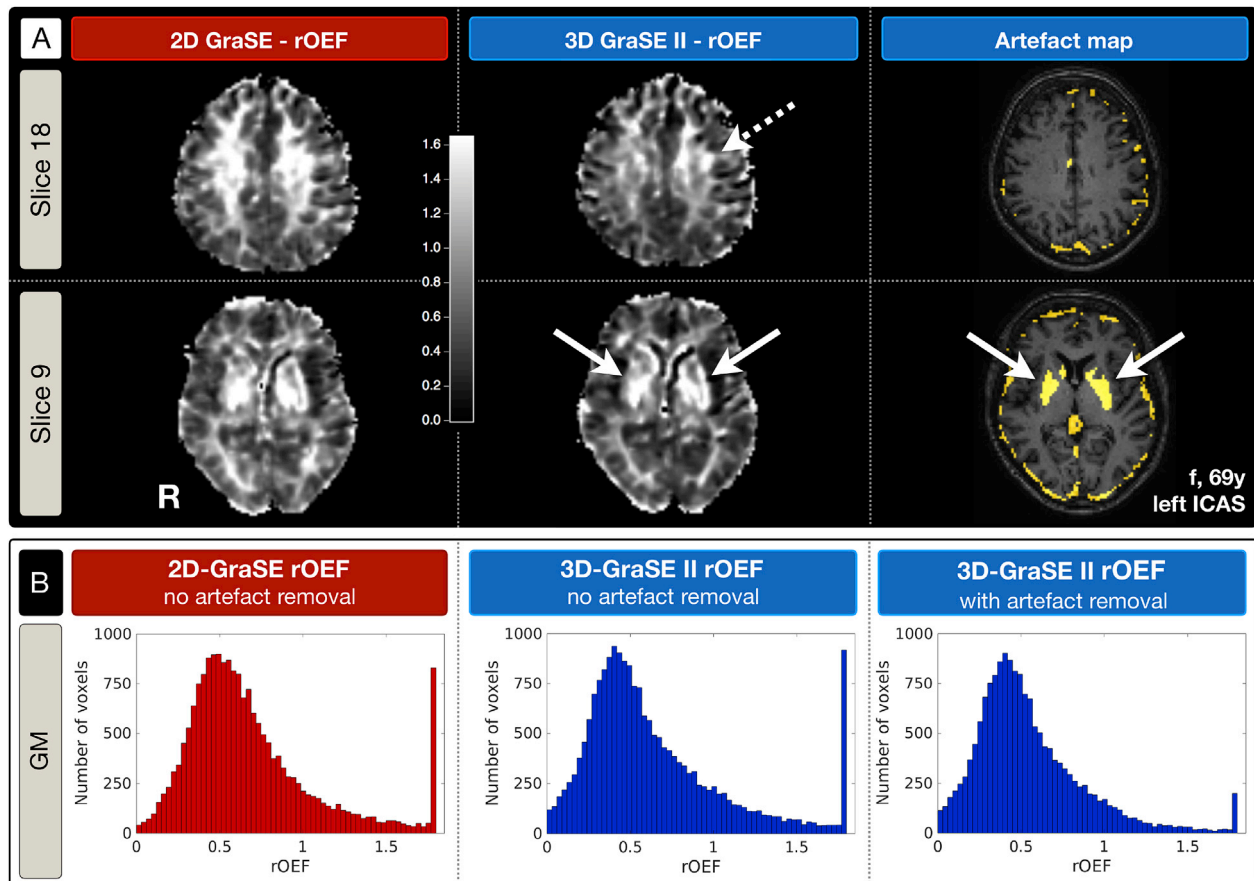


Fig. 5. Exemplary rOEF and artefact maps of a left-sided ICAS-patient comparing 2D-GraSE vs. 3D-GraSE-II.

(A) rOEF-maps derived by 2D-GraSE (indicated in red) vs. 3D-GraSE-II (blue) and the corresponding artefact map of 3D-GraSE-II are compared in two axial slices. All rOEF-maps are displayed within the same colormap scaling (0 to 1.6). Note that focal rOEF hyperintensities ipsilateral to the stenosis, potentially related to pathophysiological effects, are located at the perfusion territories border zone (Supplemental Fig. 4) and only apparent by 3D-GraSE-II based rOEF (dashed arrow). Artefact voxels with elevated fitting errors of  $T_2$  and  $T_2^*$  or  $R_2'$  increases are shown in yellow. The striatum with high-iron content is clearly visible in the artefact-map and corresponds to maximum rOEF values (solid arrows). (B) rOEF value distributions are compared by histograms. They highlight the lower rOEF values by 3D-GraSE-II compared to 2D-GraSE. Moreover, additional artefact removal of 3D-GraSE-II reduced the frequency of maximum values of rOEF = 1.8.

and Blockley, 2017). Smoothing may further enhance those effects, but was applied as spatial resolutions of the sequences were only harmonized as far as possible, while maintaining parameters of standard clinical protocols. Those effects were accounted for by restrictive GM thresholding and CSF exclusion.

Furthermore, the mq-BOLD implementation neglects intravascular signals (Hirsch et al., 2014; Yablonskiy and Haacke, 1994), even though effects on  $T_2^*$  might be non-negligible at 3T (Donahue et al., 2011; Li and van Zijl, 2020). While profound investigations based on a recent model (Berman and Pike, 2018) found minor intravascular effects on q-BOLD parameter estimates in ASE, intravascular effects were demonstrated in simulations of a GESSE sequence (Stone et al., 2019). Thus, future consideration of intravascular signal contributions in mq-BOLD may be beneficial (He and Yablonskiy, 2007). Other potential confounders are neglects of vessel size dependent hematocrit variations and imperfect SE refocusing (Berman et al., 2018). While 3D-GraSE lowered whole brain rOEF values (Fig. 5A), evaluations were restricted to GM due to known artefactual GM-WM rOEF contrast, mainly caused by approximating venous CBV by total rCBV (Hirsch et al., 2014) and, although minor on average, vessel orientation effects in WM (Kaczmarz et al., 2020b). CBV normalization to NAWM might limit sensitivity to global differences between subjects, groups and in longitudinal studies. While the threshold of  $R_2' < 15 \text{ s}^{-1}$  was applied based on previous work, lower thresholds, in general, directly result in lower average rOEF values. Thus, excluded voxels were carefully evaluated to avoid potential confounds.

#### 4.5. Outlook

The presented improvements by 3D-GraSE are also highly promising for  $R_2'$ -based calibrated BOLD measurements as a viable alternative to complex gas challenges (He and Yablonskiy, 2007; Kida et al., 2000; Liu et al., 2019; Shu et al., 2016a). Physiological underpinnings of the BOLD signal could hereby be measured in activation studies (Blockley et al., 2012).

#### 5. Conclusions

We demonstrated the successful implementation of 3D-GraSE-based  $T_2$ -imaging in mq-BOLD for whole brain rOEF mapping within clinically applicable scan times. Measured  $T_2$  values with 3D-GraSE were in excellent agreement with the literature. With additional artefact exclusion, formerly overestimated rOEF decreased up to  $-27\%$ . Measured average rOEF = 0.51 in GM is considerably closer to literature values. Interestingly, focal rOEF increases in an ICAS-patient only became apparent by 3D-GraSE, which shows great promise for future clinical applications of mq-BOLD.

#### Data and code availability

For reasons of ethics and privacy issues of the acquired clinical data, the data is only available via a request to the authors.



Institutional restrictions of patient privacy then require a formal data sharing agreement. The applied MATLAB code is available upon request. Sharing of applied sequence modifications is limited by a non-disclosure agreement. The applied sequence changes have been published (Hirsch and Preibisch, 2013) and further information will be shared on request. Custom MATLAB code for post-processing of mq-BOLD MRI data for neuro-scientific studies is available at <https://doi.org/10.5281/zenodo.3909300> and [https://gitlab.lrz.de/nmmr\\_lab/public\\_projects/mq-BOLD](https://gitlab.lrz.de/nmmr_lab/public_projects/mq-BOLD).

#### Declaration of conflicting interest

The authors declared no potential conflicts of interest with respect to the research, authorship, and/or publication of this article.

#### CRediT authorship contribution statement

**Stephan Kaczmarz:** Funding acquisition, Formal analysis, Writing - original draft. **Fahmeed Hyder:** Writing - review & editing. **Christine Preibisch:** Supervision, Writing - review & editing.

#### Acknowledgments

We would like to thank Dr. Jens Göttler, Dr. Nico Sollmann and Ilias Tsiachristos for their support in participant recruitment and during the MRI measurements. We are very grateful to Dr. Andreas Hock from Philips Healthcare for his support regarding the MR-sequences and PD Dr. Michael Helle, also from Philips Healthcare, for his support on the perfusion territory mapping. We also thank Prof. Dr. Ralf Deichmann from the Goethe University in Frankfurt/Main for his support to correct  $T_2^*$  parameter maps for motion and macroscopic background gradients. We thank all our study participants for their efforts to take part in this study.

This work was supported by the Friedrich-Ebert-Stiftung (grant to SK), the Dr.-Ing. Leonhard Lorenz-Stiftung (grant to SK 971/19) and the German Research Foundation (DFG) – Project number PR 1039/6-1 (grant to CP). FH was supported by NIH grants (R01 MH-067528, R01 NS-100106, P30 NS-052519).

#### Appendix A. Supplementary data

Supplementary data to this article can be found online at <https://doi.org/10.1016/j.neuroimage.2020.117095>.

#### References

- An, H., Lin, W., 2003. Impact of intravascular signal on quantitative measures of cerebral oxygen extraction and blood volume under normo- and hypercapnic conditions using an asymmetric spin echo approach. *Magn. Reson. Med.* 50, 708–716.
- Baron, J.C., Boussier, M.G., Rey, A., Guillard, A., Comar, D., Castaigne, P., 1981. Reversal of focal misery-perfusion syndrome by extra-intracranial arterial bypass in hemodynamic cerebral ischemia. A case study with 150 positron emission tomography. *Stroke* 12, 454–459.
- Baudrexel, S., Volz, S., Preibisch, C., Klein, J.C., Steinmetz, H., Hilker, R., Deichmann, R., 2009. Rapid single-scan  $T_2^*$ -mapping using exponential excitation pulses and image-based correction for linear background gradients. *Magn. Reson. Med.* 62, 263–268.
- Berman, A.J.L., Mazerolle, E.L., MacDonald, M.E., Blockley, N.P., Luh, W.M., Pike, G.B., 2018. Gas-free calibrated fMRI with a correction for vessel-size sensitivity. *Neuroimage* 169, 176–188.
- Berman, A.J.L., Pike, G.B., 2018. Transverse signal decay under the weak field approximation: theory and validation. *Magn. Reson. Med.* 80, 341–350.
- Blockley, N.P., Griffith, V.E.M., Buxton, R.B., 2012. A general analysis of calibrated BOLD methodology for measuring CMRO(2) responses: comparison of a new approach with existing methods. *Neuroimage* 60, 279–289.
- Blockley, N.P., Stone, A.J., 2016. Improving the specificity of R2' to the deoxyhaemoglobin content of brain tissue: prospective correction of macroscopic magnetic field gradients. *Neuroimage* 135, 253–260.
- Bouvier, J., Detante, O., Tahon, F., Attye, A., Perret, T., Chechin, D., Barbieux, M., Boubagra, K., Garambois, K., Tropres, I., Grand, S., Barbier, E.L., Krainik, A., 2015. Reduced CMRO2 and cerebrovascular reserve in patients with severe intracranial arterial stenosis: a combined multiparametric qBOLD oxygenation and BOLD fMRI study. *Hum. Brain Mapp.* 36, 695–706.

- Carr, H.Y., Purcell, E.M., 1954. Effects of diffusion on free precession in nuclear magnetic resonance experiments. *Phys. Rev.* 94, 630–638.
- Christen, T., Schmiedeskamp, H., Straka, M., Bammer, R., Zaharchuk, G., 2012. Measuring brain oxygenation in humans using a multiparametric quantitative blood oxygenation level dependent MRI approach. *Magn. Reson. Med.* 68, 905–911.
- Derdeyn, C.P., Videen, T.O., Yundt, K.D., Fritsch, S.M., Carpenter, D.A., Grubb, R.L., Powers, W.J., 2002. Variability of cerebral blood volume and oxygen extraction: stages of cerebral haemodynamic impairment revisited. *Brain* 125, 595–607.
- Donahue, M.J., Achten, E., Cogswell, P.M., De Leeuw, F.E., Derdeyn, C.P., Dijkhuizen, R.M., Fan, A.P., Ghaznawi, R., Heit, J.J., Ikram, M.A., Jezzard, P., Jordan, L.C., Jouvent, E., Knutsson, L., Leigh, R., Liebeskind, D.S., Lin, W., Okell, T.W., Qureshi, A.I., Stagg, C.J., van Osch, M.J., van Zijl, P.C., Watchmaker, J.M., Wintermark, M., Wu, O., Zaharchuk, G., Zhou, J., Hendrikse, J., 2018. Consensus statement on current and emerging methods for the diagnosis and evaluation of cerebrovascular disease. *J. Cerebr. Blood Flow Metabol.* 38, 1391–1417.
- Donahue, M.J., Hoogduin, H., van Zijl, P.C., Jezzard, P., Luijten, P.R., Hendrikse, J., 2011. Blood oxygenation level-dependent (BOLD) total and extravascular signal changes and DeltaR2\* in human visual cortex at 1.5, 3.0 and 7.0 T. *NMR Biomed.* 24, 25–34.
- Epp, S., Preibisch, C., Andrews-Hanna, J., Riedl, V., 2019. Towards a Metabolic Baseline for Default Mode Network Activations and Deactivations. OHBM, Rome, Italy.
- Fazekas, F., Chawluk, J.B., Alavi, A., Hurtig, H.I., Zimmerman, R.A., 1987. MR signal abnormalities at 1.5 T in Alzheimer's dementia and normal aging. *AJR Am. J. Roentgenol.* 149, 351–356.
- Gersing, A.S., Ankenbrank, M., Schwaiger, B.J., Toth, V., Janssen, I., Kooijman, H., Wunderlich, S., Bauer, J.S., Zimmer, C., Preibisch, C., 2015. Mapping of cerebral metabolic rate of oxygen using dynamic susceptibility contrast and blood oxygen level dependent MR imaging in acute ischemic stroke. *Neuroradiology* 57, 1253–1261.
- Goettler, J., Kaczmarz, S., Kallmayer, M., Wustrow, I., Eckstein, H.H., Zimmer, C., Sorg, C., Preibisch, C., Hyder, F., 2019. Flow-metabolism uncoupling in patients with asymptomatic unilateral carotid artery stenosis assessed by multi-modal magnetic resonance imaging. *J. Cerebr. Blood Flow Metabol.* 39, 2132–2143.
- He, X., Yablonskiy, D.A., 2007. Quantitative BOLD: mapping of human cerebral deoxygenated blood volume and oxygen extraction fraction: default state. *Magn. Reson. Med.* 57, 115–126.
- Hedderich, D., Kluge, A., Pyka, T., Zimmer, C., Kirschke, J.S., Wiestler, B., Preibisch, C., 2019. Consistency of normalized cerebral blood volume values in glioblastoma using different leakage correction algorithms on dynamic susceptibility contrast magnetic resonance imaging data without and with prebolus. *J. Neuroradiol.* 46 (1), 44–51.
- Helle, M., Norris, D.G., Rüfer, S., Alfke, K., Jansen, O., van Osch, M.J.P., 2010. Superselective pseudocontinuous arterial spin labeling. *Magn. Reson. Med.* 64, 777–786.
- Hennig, J., 1988. Multiecho imaging sequences with low refocusing flip angles. *J. Magn. Reson.* 78, 397–407, 1969.
- Hirsch, N.M., Preibisch, C., 2013.  $T_2^*$  mapping with background gradient correction using different excitation pulse shapes. *AJNR Am. J. Neuroradiol.* 34, E65–E68.
- Hirsch, N.M., Toth, V., Forscher, A., Kooijman, H., Zimmer, C., Preibisch, C., 2014. Technical considerations on the validity of blood oxygenation level-dependent-based MR assessment of vascular deoxygenation. *NMR Biomed.* 27, 853–862.
- Hyder, F., 2009. Dynamic imaging of brain function. *Methods Mol. Biol.* 489, 3–21.
- Hyder, F., Rothman, D.L., Shulman, R.G., 2002. Total neuroenergetics support localized brain activity: implications for the interpretation of fMRI. *Proc. Natl. Acad. Sci. U. S. A.* 99, 10771–10776.
- Kaczmarz, S., Götter, J., Petr, J., Hansen, M.B., Mouridsen, K., Zimmer, C., Hyder, F., Preibisch, C., 2020a. Hemodynamic impairments within individual watershed areas in asymptomatic carotid artery stenosis by multimodal MRI. *J. Cerebr. Blood Flow Metabol.* 271678x20912364.
- Kaczmarz, S., Götter, J., Zimmer, C., Hyder, F., Preibisch, C., 2020b. Characterizing white matter fiber orientation effects on multi-parametric quantitative BOLD assessment of oxygen extraction fraction. *J. Cerebr. Blood Flow Metabol.* 40, 760–774.
- Kida, I., Kennan, R.P., Rothman, D.L., Behar, K.L., Hyder, F., 2000. High-resolution CMRO2 mapping in rat cortex: a multiparametric approach to calibration of BOLD image contrast at 7 tesla. *J. Cerebr. Blood Flow Metabol.* 20, 847–860.
- Kluge, A., Lukas, M., Toth, V., Pyka, T., Zimmer, C., Preibisch, C., 2016. Analysis of three leakage-correction methods for DSC-based measurement of relative cerebral blood volume with respect to heterogeneity in human gliomas. *Magn. Reson. Imaging* 34, 410–421.
- Leenders, K.L., 1994. PET: blood flow and oxygen consumption in brain tumors. *J. Neuro Oncol.* 22, 269–273.
- Li, W., van Zijl, P.C.M., 2020. Quantitative theory for the transverse relaxation time of blood water. *NMR Biomed.* 33, e4207.
- Liu, E.Y., Guo, J., Simon, A.B., Haist, F., Dubowitz, D.J., Buxton, R.B., 2019. The potential for gas-free measurements of absolute oxygen metabolism during both baseline and activation states in the human brain. *Neuroimage*, 116342.
- MacKay, A., Laule, C., Vavasour, I., Bjarnason, T., Kolind, S., Mäder, B., 2006. Insights into brain microstructure from the T2 distribution. *Magn. Reson. Imag.* 24, 515–525.
- Magerkurth, J., Volz, S., Wagner, M., Jurcoane, A., Anti, S., Seiler, A., Hattingen, E., Deichmann, R., 2011. Quantitative  $T_2^*$ -mapping based on multi-slice multiple gradient echo flash imaging: retrospective correction for subject motion effects. *Magn. Reson. Med.* 66, 989–997.
- Marchal, G., Rioux, P., Petit-Taboué, M.-C., Sette, G., Travère, J.-M., Le Poec, C., Courtheoux, P., Derlon, J.-M., Baron, J.-C., 1992. Regional cerebral oxygen consumption, blood flow, and blood volume in healthy human aging. *Arch. Neurol.* 49, 1013–1020.

- Ni, W., Christen, T., Zun, Z., Zaharchuk, G., 2014. Comparison of  $R_2'$  measurement methods in the normal brain at 3 tesla. *Magn. Reson. Med.* 73, 1228–1236.
- Noth, U., Shrestha, M., Schure, J.R., Deichmann, R., 2017. Quantitative in vivo  $T_2$  mapping using fast spin echo techniques - a linear correction procedure. *Neuroimage* 157, 476–485.
- Oshio, K., Feinberg, D.A., 1991. GRASE (Gradient-and Spin-Echo) imaging: a novel fast MRI technique. *Magn. Reson. Med.* 20, 344–349.
- Penny, W.D., Friston, K.J., Ashburner, J.T., Kiebel, S.J., Nichols, T.E., 2011. *Statistical Parametric Mapping: the Analysis of Functional Brain Images*. Elsevier Science.
- Pike, G.B., 2012. Quantitative functional MRI: Concepts, issues and future challenges. *Neuroimage* 62, 1234–1240.
- Poon, C.S., Henkelman, R.M., 1992. Practical  $T_2$  quantitation for clinical applications. *J. Magn. Reson. Imag.* 2, 541–553.
- Powers, W.J., Clarke, W.R., Grubb Jr., R.L., Videen, T.O., Adams Jr., H.P., Derdeyn, C.P., Investigators, C., 2011. Extracranial-intracranial bypass surgery for stroke prevention in hemodynamic cerebral ischemia: the Carotid Occlusion Surgery Study randomized trial. *J. Am. Med. Assoc.* 306, 1983–1992.
- Prasloski, T., Madler, B., Xiang, Q.S., MacKay, A., Jones, C., 2012a. Applications of stimulated echo correction to multicomponent  $T_2$  analysis. *Magn. Reson. Med.* 67, 1803–1814.
- Prasloski, T., Rauscher, A., MacKay, A.L., Hodgson, M., Vavasour, I.M., Laule, C., Madler, B., 2012b. Rapid whole cerebrum myelin water imaging using a 3D GRASE sequence. *Neuroimage* 63, 533–539.
- Preibisch, C., Shi, K., Kluge, A., Lukas, M., Wiestler, B., Gottler, J., Gempt, J., Ringel, F., Al Jaber, M., Schlegel, J., Meyer, B., Zimmer, C., Pyka, T., Förster, S., 2017. Characterizing hypoxia in human glioma: a simultaneous multimodal MRI and PET study. *NMR Biomed.* 30.
- Sedlacik, J., Boelmans, K., Löbel, U., Holst, B., Siemonsen, S., Fiehler, J., 2014. Reversible, irreversible and effective transverse relaxation rates in normal aging brain at 3T. *Neuroimage* 84, 1032–1041.
- Seiler, A., Lauer, A., Deichmann, R., Noth, U., You, S.J., Pfeilschifter, W., Singer, O.C., Pilatus, U., Wagner, M., 2019. Complete restitution of the ischemic penumbra after successful Thrombectomy: a pilot study using quantitative MRI. *Clin. Neuroradiol.* 29 (3), 415–423.
- Shu, C.Y., Herman, P., Coman, D., Sanganahalli, B.G., Wang, H., Juchem, C., Rothman, D.L., de Graaf, R.A., Hyder, F., 2016a. Brain region and activity-dependent properties of  $M$  for calibrated fMRI. *Neuroimage* 125, 848–856.
- Shu, C.Y., Sanganahalli, B.G., Coman, D., Herman, P., Rothman, D.L., Hyder, F., 2016b. Quantitative beta mapping for calibrated fMRI. *Neuroimage* 126, 219–228.
- Smith, A.J., Blumenfeld, H., Behar, K.L., Rothman, D.L., Shulman, R.G., Hyder, F., 2002. Cerebral energetics and spiking frequency: the neurophysiological basis of fMRI. *Proc. Natl. Acad. Sci. U. S. A.* 99, 10765–10770.
- Stone, A.J., Blockley, N.P., 2017. A streamlined acquisition for mapping baseline brain oxygenation using quantitative BOLD. *Neuroimage* 147, 79–88.
- Stone, A.J., Holland, N.C., Berman, A.J.L., Blockley, N.P., 2019. Simulations of the effect of diffusion on asymmetric spin echo based quantitative BOLD: an investigation of the origin of deoxygenated blood volume overestimation. *Neuroimage* 201, 116035.
- Toth, V., Forschler, A., Hirsch, N.M., den Hollander, J., Kooijman, H., Gempt, J., Ringel, F., Schlegel, J., Zimmer, C., Preibisch, C., 2013. MR-based hypoxia measures in human glioma. *J. Neuro Oncol.* 115, 197–207.
- Uddin, M.N., Marc Lebel, R., Wilman, A.H., 2013. Transverse relaxometry with reduced echo train lengths via stimulated echo compensation. *Magn. Reson. Med.* 70, 1340–1346.
- Ulrich, X., Yablonskiy, D.A., 2015. Separation of cellular and BOLD contributions to  $T_2^*$  signal relaxation. *Magn. Reson. Med.* 75, 606–615.
- Wagner, M., Helfrich, M., Volz, S., Magerkurth, J., Blasel, S., Porto, L., Singer, O.C., Deichmann, R., Jurcoane, A., Hattingen, E., 2015. Quantitative  $T_2$ ,  $T_2^*$ , and  $T_2'$  MR imaging in patients with ischemic leukoaraiosis might detect microstructural changes and cortical hypoxia. *Neuroradiology* 57, 1023–1030.
- Wagner, M., Magerkurth, J., Volz, S., Jurcoane, A., Singer, O.C., Neumann-Haefelin, T., Zanella, F.E., Deichmann, R., Hattingen, E., 2012.  $T_2'$ - and PASL-based perfusion mapping at 3 Tesla: influence of oxygen-ventilation on cerebral autoregulation. *J. Magn. Reson. Imag.* 36, 1347–1352.
- Whittall, K.P., MacKay, A.L., Graeb, D.A., Nugent, R.A., Li, D.K., Paty, D.W., 1997. In vivo measurement of  $T_2$  distributions and water contents in normal human brain. *Magn. Reson. Med.* 37, 34–43.
- Whittall, K.P., MacKay, A.L., Li, D.K., 1999. Are mono-exponential fits to a few echoes sufficient to determine  $T_2$  relaxation for in vivo human brain? *Magn. Reson. Med.* 41, 1255–1257.
- Wiestler, B., Kluge, A., Lukas, M., Gempt, J., Ringel, F., Schlegel, J., Meyer, B., Zimmer, C., Förster, S., Pyka, T., Preibisch, C., 2016. Multiparametric MRI-based differentiation of WHO grade II/III glioma and WHO grade IV glioblastoma. *Sci. Rep.* 6, 35142.
- Yablonskiy, D.A., Haacke, E.M., 1994. Theory of NMR signal behavior in magnetically inhomogeneous tissues: the static dephasing regime. *Magn. Reson. Med.* 32, 749–763.

## 8 Discussion

The research field of quantitative hemodynamic MRI is rapidly evolving and pushed by its high clinical potential. Applications in CVDs such as ICAS are highly promising to improve diagnostics, treatment decisions and longitudinal treatment efficacy monitoring. However, despite of previous sophisticated methodological developments, especially clinically applicable techniques as well as their translation to clinical applications were lacking. Aiming for this gap, the embedded research articles of this work as presented in Chapter 7 will be discussed in this chapter. The work is contextualized in the current literature in Section 8.1, clinical novelty as well as limitations of the embedded publications are discussed in Section 8.2 and concluded with an outlook in Section 8.3.

### 8.1 Review of Existing Literature

The present work is based upon several preceding publications. The existing literature is reviewed with respect to a multi-parametric ICAS impairment model in Section 8.1.1, watershed areas in Section 8.1.2, perfusion and oxygenation imaging in Sections 8.1.3 and 8.1.4, respectively, WM anisotropy effects in Section 8.1.5 and summarized in Section 8.1.6.

#### 8.1.1 ICAS Impairment Model

In current clinical ICAS diagnostics, MRI is commonly applied for angiography,  $T_1w$  and  $T_2w$  sequences (see Section 4.4). While the neck arteries can be depicted and structural tissue information is given, no connections of pathophysiological processes on the brain tissue are provided at all (see Section 4.4.3). To better understand those effects, several studies have investigated hemodynamic impairments in ICAS [170, 171, 180, 190–200]. However, many studies included evaluations of just a few hemodynamic parameters at the same time.

To describe relationships between those parameters, a widely accepted model was published by Powers et al. in 1987 [179, 201]. The progression of hemodynamic impairments due to CPP reductions (see Section 3.1.2) leading to ischemia was described in two sequential stages:

- First, autoregulation causes chronic vasodilation, which leads to decreasing CVR with concomitantly increasing CBV
- Second, when autoregulation cannot compensate the progressing CPP reductions anymore, CBF decreases. To sustain the oxygen metabolism and thereby prevent strokes, OEF increases based on Fick's principle, while assuming an iso-metabolic state [107]

Meanwhile, several studies contradict this simple model. For example, increased OEF was found at normal CBV in patients with ICA occlusion in a PET study [117]. An animal ischemia model indicated decreased CBF already at the first stage during autoregulation [202]. And an MRI study showed decreased CBF, while OEF was unchanged [203]. To resolve those discrepancies, quantitative multi-parametric evaluations of hemodynamic parameters with state-of-the-art MRI methods are indicated.

### 8.1.2 Watershed Areas

Another factor influencing Power's model (see Section 8.1.1) is collateral blood flow within the CoW (see Section 4.2) [201, 204]. Caused by collateral flow, perfusion territories and their border zones, i.e. watershed areas, can individually shift. Those areas are especially vulnerable to hypoperfusion and ischemia [190]. Furthermore, CVR and OEF alternations were found [205, 206]. Thus, WSAs are of clinical interest in ICAS [164] with high potential for enhanced diagnostics by improved sensitivity to hemodynamic impairments [190, 207, 208].

However, no WSA mapping technique was proposed so far for several reasons. Atlas based assessments are inadequate, due to known subject specific WSA variations [201, 209, 210]. While MRI can depict the CoW anatomy, vascular territory shifts cannot be reliably predicted due to the complex intracranial blood supply [209, 210]. As a matter of fact, 4D blood flow measurements of the CoW also cannot depict WSAs [180]. And even though ss-ASL allows perfusion territory mapping (see Section 3.2.3) [211, 212], no border zone segmentation method was proposed yet. Interestingly, DSC-based TTP maps (see Section 3.2.1) are sensitive to macro-vascular perfusion delays [213–215], which is promising for individual WSA delineation. In those regions of prolonged perfusion delay, alternations of CVR have been reported [216], whereas independent ICAS-related effects on TTP and CTH have been implied [194].

### 8.1.3 Perfusion Imaging

To quantify cerebral hemodynamics, perfusion imaging is highly important (see Section 3.1.2). Several MR-based imaging methods have been proposed, but their clinical applicability often remained limited, especially in WM. At the same time, imaging in WM could increase the sensitivity to hemodynamic perturbations compared to GM [217], due to the different blood supply architecture [132]. In the following, an overview on relevant perfusion imaging techniques is provided including their applicability in WM and previous results in ICAS.

The clinically most widely applied MR perfusion imaging method is DSC (see Section 3.2.1). Already in 1998, its great potential was shown with high spatial resolution and sensitivity to GM and WM impairments [217]. Methodological concerns about the interpretation of bolus tracking data [77] with regard to arterial input function definition [83, 87, 218] were accounted for by robust automated DSC data post-processing [86]. To additionally harmonize varying sequence implementations, a recommendations statement has been recently published [80] and considered in this work. Studies in unilateral ICAS patients demonstrated the sensitivity of DSC to prolonged perfusion delays and CBV increases (see Section 3.1) [195, 217, 219], which was supported by bilateral CBV effects in PET studies [199]. Despite its relatively widespread application, DSC is still not part of clinical guidelines in ICAS (see Section 4.4).

Additional parameters have been recently proposed to be derived from existing DSC data by parametric modelling (see Section 3.2.1) [88, 89]. Applications in ICAS showed capillary dysfunction as measured by CTH [220], which were shown to be reversible eight hours after stenting (see Section 4.4.2) [221]. This novel parameter was proposed to relate to the effective surface of the capillary bed and thereby the oxygen extraction efficiency [222], which is highly relevant in ICAS. Similarities between the additionally derived parameter OEC (see Section 3.2.1) and PET-based OEF were shown in two ICAS patients [220]. Even though monitoring of capillary dysfunction effects via clinically applicable DSC has great potential, future comparisons with other hemodynamic parameters are required. In general, recently reported contrast agent accumulations [10] warrant stricter indications for DSC MRI and non-invasive perfusion imaging alternatives are gaining high additional interest.



In spite of being absolutely non-invasive, ASL does currently not play a role in ICAS diagnostics. Methodological limitations of PASL and CASL (see Section 3.2.2) hindered wider clinical applications [84, 223] before pCASL was introduced in 2008 [97]. Accounting for the demands in standardization [104] and reproducibility [224], the ISMRM perfusion study group ASL consensus paper in 2015 [98] was a milestone towards wider applications [225].

In ICAS, pCASL was shown to be sensitive to CBF decreases in GM [203], in agreement with PET [219]. However, another study found neither hemispherical differences by ICA occlusions, nor group differences to healthy controls [226]. While a study by van Osch et al. demonstrated that ASL can in principle detect WM perfusion abnormalities [227], no CBF signal was measured at all in the corresponding brain region due to the severe perfusion delay. Thus, the capability of ASL to quantify impairments in WM remained unclear.

On top of CBF, evaluations of additional parameters such as CVR were proposed to differentiate vascular and neuronal contributions (see Section 3.1) [228]. However, CVR measurement is also not widely clinically applied. For imaging, BOLD weighted MRI seems ideal due to the almost linear relation of %BOLD signal change with increasing arterial partial CO<sub>2</sub> pressure [109]. But the choice of vasoactive stimuli remains a main challenge for clinical implementations (see Section 3.2.4). Exogenous hypercapnia application with end-tidal gas monitoring is known as a reference with good repeatability [229], but widely limited by complicated and costly additional equipment. While easily applicable resting-state fMRI (rs-fMRI) fluctuations were proposed, vasoactive stimuli seem required for reliable CVR mapping [230]. Another alternative with easily applicable vasoactive stimulation is breath-holding (see Section 3.2.4). Promisingly, Bright and Murphy demonstrated CVR mapping by BH-fMRI with end-tidal CO<sub>2</sub> measurement [55]. However, the repeatability and thereby applicability in follow-up studies was put into question [109].

In general, previous results pointed to high clinical value of CVR imaging and predicted increasing relevance [109, 231]. A meta analysis in ICAS indicated the great potential of CVR for individual stroke risk stratification [200]. In unilateral ICAS, CVR reductions were found [232] with even bilateral effects [233]. Characterization of CVR also included WM [234, 235]. However, most of those studies applied hypercapnia and thus, the quantifiability of CVR impairments in GM and WM by easily applicable BH-fMRI remained unknown.

#### 8.1.4 Oxygenation Imaging

As the oxygen supply plays a major role in cerebral energy metabolism (see Section 3.1.2), its MR-based quantification has gained high attention (see Section 3.3). Despite several MR-based OEF measurement techniques have been developed, none of them was clinically applied yet. Most methods of regional OEF mapping lack whole brain coverage or scan times are way beyond clinical applicability. In general, those techniques can be classified in 4 groups.

First, based on  $T_2$  imaging using spin tagging [236]. A fast implementation is  $T_2$ -relaxation-under-spin-tagging (TRUST), which measures the cerebral oxygenation globally in the draining superior sagittal sinus (SSS) vein [237]. But this contradicts known regional oxygenation variations in CVDs [238]. Two alternative implementations based on velocity selective labeling are called velocity-selective excitation and arterial nulling (VSEAN) [239] and quantitative imaging of extraction of oxygen and tissue consumption (QUIXOTIC) [240]. However, scan times are clinically unfeasible as the latter takes 30 minutes per slice.

Second, magnetic susceptibility differences between veins and the surrounding tissue can be used for OEF mapping [241]. However, those quantitative susceptibility mapping (QSM) based methods mainly relate to the oxygenation in larger vessels [119, 240].

Third, dual calibrated experiments combining hypercapnia and hyperoxia applications can be used for OEF mapping [242–244]. However, the additionally required gas setups are complicated to use, require additional costly equipment and are thus not clinically applicable.

Fourth,  $R'_2$ -based measurement of susceptibility induced intra-voxel dephasing enable OEF mapping within applicable scan times. Simultaneous imaging of  $R'_2$  and deoxygenated blood volume is offered by three implementations called gradient echo sampling of FID and echo (GESFIDE) [245], gradient echo sampling of spin echo (GESSE) [246] and asymmetric spin echo (ASE, see Section 2.3.1) [247–249]. However, those three methods suffer from coupling effects of measured parameters and deoxygenated blood volume overestimations related to echo sampling dependencies [238, 250]. Alternatively, mq-BOLD (see Section 3.3.1) relies on three separate measurements of  $T_2$  by GraSE,  $T_2^*$  by GRE and rCBV by DSC [120, 251]. Known perturbations by macroscopic background gradients were already accommodated by exponentially shaped excitation pulses and corrections in the post-processing [122, 252].

In general, OEF is expected to be a sensitive biomarker of critical impairments (see Section 8.1.1) [253, 254]. But so far, no significant effects of ICAS on rOEF were found by mq-BOLD [203] or calibrated fMRI [226]. Thus, ICAS effects on rOEF and the sensitivity of mq-BOLD to potential pathological rOEF effects remained unclear. In other pathologies, mq-BOLD was successfully applied in GM [120, 126–129, 203, 251]. However, mq-BOLD was always biased by systematic rOEF elevations, which relate to the term relative OEF rather than OEF [120]. Wider applications were moreover limited by unknown reliability in WM.

### 8.1.5 Anisotropy Effects

The applicability of mq-BOLD in WM is potentially hindered by anisotropy effects. While the biophysical model assumptions (see Section 3.3.1) are reasonable in GM, known preferential orientations in WM contradict them. Related to orientation dependencies of WM structures relative to the main magnetic field  $B_0$  [255], anisotropy effects on  $T_2^*$  were investigated extensively [256–265] and also shown for DSC [137] as well as  $T_2$  imaging [257]. Anisotropy effects were assumed to mainly arise from myelin in the highly oriented fiber structures (see Section 3.4.3) [149] and preferential vessel orientations parallel to fiber tracts [133–135, 137].

The most favourable method to investigate anisotropy effects in terms of applicability and accuracy is DTI-based (see Section 3.4.3) fiber orientation mapping [135–137, 261, 266, 267]. It allows voxel wise correlations of main fiber orientations with functional parameter values. To explain anisotropy effects, different models were proposed [121, 257, 259, 260, 268, 268–272]. However, a systematic comparison of those models was lacking. Moreover, interpretations of measured data was impeded by rather confusing results in x- and y-directions when using Cartesian coordinates [135]. And most importantly, the reliability of mq-BOLD in WM remained unclear as no study systematically investigated rOEF anisotropy effects so far.

### 8.1.6 Literature Summary

To summarize the existing literature, promising methods were proposed, but most of them are clinically not widely applied in ICAS yet. A recent consensus statement by Donahue et al. highlighted the potential of hemodynamic MRI for personalized stroke risk assessment and improved treatment guidelines [9]. However, major methodological improvements were requested and their applications in clinical studies demanded. Furthermore, multi-parametric imaging is needed to characterize the complex relationships of hemodynamic parameters.

## 8.2 Present Work

The present work includes significant contributions to the field of quantitative hemodynamic MRI. JP-I introduced a novel method to individually delineate WSAs. Comparably small average anisotropy variations in JP-II pointed to meaningful rOEF values in WM. Findings from the latter two publications were exploited in JP-III. Multi-parametric quantitative hemodynamic imaging in GM and WM of ICAS patients demonstrated the applicability of the proposed methods with increased sensitivity within iWSAs. Finally, significant methodological improvements to oxygenation sensitive mq-BOLD were introduced and demonstrated in JP-IV.

These embedded publications are discussed regarding their novelty in Section 8.2.1, their limitations in Section 8.2.3 and completed by upcoming perspectives in Section 8.3.

### 8.2.1 Novelty

The four embedded journal publications (see Chapter 7) contribute new insights to the field of quantitative hemodynamic MRI and its application in ICAS.

Specifically, JP-I demonstrated the feasibility of individual WSA segmentation based on regional perfusion delay information from standard clinical DSC. In healthy controls, a global WSA atlas seemed sufficient. Contrary, spatially widely varying watershed locations were found in ICAS patients. Locations of iWSAs were successfully verified with additionally acquired vascular territory mapping by ss-ASL (see Section 3.2.3). Thereby, the feasibility and necessity of individual WSA segmentation was demonstrated for the first time.

JP-II provided detailed novel insights on WM orientation effects of mq-BOLD. The fully automated coordinate system transformation of main fiber orientation from the DTI FOV to the scanner coordinate system was introduced and combined with the transformation from Cartesian to spherical coordinates, which successfully resolved rather confusing results of previous publications. By demonstrating the absence of orientation effects in the x-y-plane perpendicular to  $B_0$ , the applied processing was validated and further evidence for  $B_0$  related orientation effects was provided. Known orientation effects between main fiber orientations and  $B_0$  were confirmed for  $T_2^*$  and rCBV with variations up to 37.1%. By fitting and comparing different models, major contributions were attributed to highly oriented myelinated fiber structures and related preferential vasculature orientations. Quantitative  $T_2$  imaging by 2D GraSE showed orientation related variations of 7.5%, which was mainly attributed to diffusion. The main finding was the comparably weak average orientation related rOEF variation of 3.8% in healthy controls, due to partially counteracting effects of  $R_2'$  and rCBV.

In JP-III, a detailed overview on ICAS-related impairments of six quantitative hemodynamic parameters in GM and WM was given. Furthermore, iWSAs were applied via the automated multi-parametric evaluation framework (see Chapter 5). In line with the literature, decreases of CBF and CVR as well as increases of rCBV, OEC and CTH were found ipsilateral to the stenosis. Contralateral perturbations underlined the importance of collateral flow. According to our initial hypothesis, stronger effects were found in WM for most parameters, even with pCASL and BH-fMRI. For the first time, rOEF was also evaluated in WM based on the findings in JP-II. Similarly in GM and WM, rOEF was symmetrical among hemispheres, but with increased standard deviation. From a methodological point of view, the sensitivity and specificity of several proposed methods was shown. And multi-parametric imaging yielded additional value by providing complementary information. Within subjects, the parameters showed spatially varying impairments, indicating complex pathophysiological effects at different brain locations. Furthermore, the impairment patterns across ICAS patients differed, which is

potentially due to the individual collateral blood supply and more complex hemodynamic relationships than proposed by simple models. Despite those extensive intra- and inter-subject variations, the hypothesized increased sensitivity to hemodynamic impairments within iWSAs, as proposed in JP-I, was confirmed. Within iWSAs, CBF, CVR and rCBV were significantly stronger lateralized up to +117%. At the same time, locations of CTH increases were independent from iWSAs, which points to more widespread microvascular impairments.

Even though mq-BOLD applications in the latter two embedded publications JP-II and JP-III showed great potential, no rOEF elevation were found in ICAS. Moreover, bias by well-known systematic rOEF overestimations remained unresolved. Those issues were successfully addressed in JP-IV by applying improved  $T_2$  imaging in mq-BOLD. The formerly used 2D GraSE was replaced by 3D GraSE, which allowed to reduce slice profile related stimulated echo effects. Moreover, the proposed consideration of fit-errors in quantitative  $T_2$  and  $T_2^*$  calculations in combination with exclusion of mainly iron deposition related  $R_2'$  elevations further improved mq-BOLD. Consequently, quantitative  $T_2$ ,  $R_2'$  and rOEF values significantly decreased, being much closer to physiologically expected values. Thus,  $T_2$  related bias on rOEF calculations in mq-BOLD was resolved while maintaining clinically applicable scan times. Moreover, focal rOEF increases in ICAS became apparent with improved mq-BOLD, but not with the formerly applied method as used in JP-III. Pathophysiological origins of rOEF increases were affirmed by their location between perfusion territories, imaged by ss-ASL.

Hemodynamic impairments were also demonstrated to affect cognitive function. Chronic ipsilateral hypoperfusion correlated with lateralized visual attention deficits as shown in journal publication J3. And in contrast to complicated hypercapnia measurements [244, 273], the combination of easily applicable pCASL and mq-BOLD allowed to calculate CMRO<sub>2</sub> and investigate ICAS-related regional flow metabolism uncoupling in journal publication J4.

### 8.2.2 Clinical Relevance

The present work greatly advances the field of quantitative hemodynamic brain imaging. Individual WSAs were reliably delineated based on perfusion delay maps in JP-I. Their application to hemodynamic parameters was hypothesized to increase the sensitivity to perturbations, which was verified in JP-III. By offering complementary information, high clinical value of multi-parametric hemodynamic imaging was demonstrated. At the same time, sensitivity and specificity were affirmed in GM and WM. Furthermore, the sensitivity to oxygenation impairments was enhanced by enabling careful rOEF evaluation in WM, based on findings in JP-II, and significant methodological improvements, as demonstrated in JP-IV.

In detail, pCASL was sensitive to strong ipsilateral CBF decreases in ICAS. Its lateralization was further enhanced within iWSAs. And even WM perfusion was measured within clinically applicable scan time, which makes pCASL highly promising to improve ICAS diagnostics.

As hypothesized, CVR was also severely affected in ICAS (see Section 8.1.1). Easily applicable BH-fMRI was sensitive to ipsilateral CVR decreases in GM and even WM. Its lateralization was also significantly enhanced by iWSAs. Despite previous concerns about repeatability and applicability in follow-up studies (see Section 8.1.3), BH-fMRI was sensitive to CVR recovery after treatment (see Section 4.4.2) as presented in abstracts C10 and C11.

Ipsilaterally decreased CVR by 15% with concomitantly increased rCBV by 5% in GM indicates chronic vasodilation in asymptomatic ICAS and agrees with expected smaller CBV effects [274]. Nevertheless, DSC has great clinical potential for clinical use in ICAS due to its easy and robust applicability [171]. Furthermore, hemodynamic parameters with complementary information can be derived from just one 2 minute sequence. Spatial similarities

of CTH and OEC increases indicate 'benign' CTH effects [88]. Following recent simulations [275], those findings imply a mild to moderate vascular pathology with capillary constrictions, while capillary occlusions are not expected. In agreement with previous findings [194], strongest lateralization outside of iWSAs was found for CTH. As other parameters were still unaffected in brain regions with capillary impairments, CTH is likely to offer important information on the pathophysiology and may serve as a clinical indicator at early disease stages.

Regarding rOEF in ICAS, bilaterally increased standard deviation was found in JP-III in line with previous studies [199, 203]. Promisingly, the increased sensitivity by methodological mq-BOLD improvements in JP-IV additionally revealed focal rOEF hyperintensities. Regarding anisotropy effects, just slight increases of average rOEF variations were found in ICAS patients compared to healthy controls in abstract C12. Those findings support meaningful rOEF evaluations in WM of ICAS patients, which can enhance the sensitivity to pathophysiological oxygenation effects and thereby substantially improve the clinical relevance of mq-BOLD.

The demonstrated regional flow-metabolism uncoupling in ICAS is potentially related to subtle tissue damage, in line with detected cognitive impairments. Thus, readily available multi-parametric hemodynamic imaging enables to investigate pathways of cognitive decline.

In conclusion, the broad clinical relevance of multi-parametric quantitative hemodynamic MRI was demonstrated and the initial hypothesis was confirmed (see Section 1.2). The sensitivity of all proposed methods to ICAS impairments was demonstrated and furthermore significantly improved by applying iWSAs. As optimal ICAS treatment is currently under debate (see section 4.4.2), the proposed quantitative imaging can support comparisons of long term effects. Furthermore, the proposed methods improve the understanding of pathophysiological mechanisms in ICAS, e.g., with respect to effects of capillary dysfunction.

### 8.2.3 Limitations

While the applied methods have several strengths, some limitations persist. Despite of significantly improved sensitivity within iWSAs, the proposed semi-automated segmentation is not clinically feasible due to required time consuming manual corrections. In addition, the Gd application of contrast agent is a general major disadvantage of all DSC applications. The ongoing debate about Gd depositions (see Section 3.2.1) [10] is enhancing the demand for non-invasive alternatives. At the same time, neither Gd depositions of macrocyclic agents nor harmful effects of Gd depositions were proven so far. Furthermore, DSC offers the reliable measurement of several parameters with high diagnostic value in short scan time. Regarding OEC, some similarities with rOEF were found in abstract C25. However, OEC is just derived from DSC data and critically depends on the validity of the applied vascular model. In contrast, mq-BOLD relies on an analytical model [121], which is more directly related to vascular oxygenation. Consequently, further validations of OEC are required.

In pCASL, potential bias arises from several factors (see Section 3.2.2) such as operator dependent labeling, flow velocity dependent labeling, unknown labeling efficiencies, faster label decay in tissue due to varying  $T_1$  in tissue and blood as well as gender related lower hematocrit in women causing longer blood  $T_1$  and CBF overestimations [102]. Moreover, ASL is not applicable after stenting, due to potential heating effects as well as image distortions and signal loss due to magnetic susceptibility effects. In WM, ASL is known to be challenged by physiologically lower CBF and increased delay. In general, delay effects may confound detected hypoperfusion in single-PLD ASL [6, 276–278]. Even though no severe delays were indicated [279], remaining uncertainties could be resolved by time-encoded ASL (see Section 3.2.2) [280–282], as shown in comparisons with DSC MRI [283], CT [3] and PET [276].

Delay effects do not only cause potential bias in ASL, but also CVR imaging [284, 285]. Furthermore, BH-fMRI is limited by the simple setup without end-tidal gas monitoring. Consequently, CO<sub>2</sub> stimulation levels are unknown, no reference CO<sub>2</sub> waveform is available for regression analysis (see Section 3.2.4) and effects of subject specific CO<sub>2</sub> chemoreflex sensitivity on ventilation and arterial CO<sub>2</sub> partial pressure remain unconsidered. Further limitations may arise from steal phenomena, which describe blood flow directed away from maximally vasodilated vascular territories to surrounding tissue with preserved vasodilatory reserve [286]. Steal has high relevance to estimate stroke risks [191], but may not be detectable by comparably weak CO<sub>2</sub> stimuli in BH-fMRI in case of impaired but not exhausted vascular reserve [109]. Promisingly, novel camera-based breathing monitoring of MR scanners showed good preliminary results to replace breathing belts and further simplify BH-fMRI setups.

Finally, mq-BOLD is potentially limited by neglecting intravascular signals, vessel size dependent hematocrit variations, iron depositions, motion artefacts in  $R_2'$ , CSF influences and artifactual GM-WM contrast of rOEF (see Section 3.3.1). At the same time, the proposed improvements resolved formerly systematically elevated rOEF and improved its sensitivity. Despite comparably low average rOEF anisotropy effects in WM, single voxels may be more severely affected. Furthermore, WM evaluation of mq-BOLD in other pathologies requires previous characterization in this specific cohort, due to potential disease effects on the myelination or cerebral vasculature, which can affect anisotropy effects. Taking a wider perspective, orientation effects potentially affect a wide range of functional and structural parameters, which can add bias when comparing different WM brain regions or hemispheres.

### 8.3 Perspectives

Despite of the limitations stated in the last section, this work provides interesting perspectives on methodological improvements as well as further clinical and neuroscientific applications.

The high demand for stroke risk prediction arises from delicate treatment decisions in asymptomatic ICAS (see Section 4.4.2). Even though this is far beyond the scope of this work, multi-parametric hemodynamic MRI offers promising perspectives on personalized stroke risk stratification [9], as already indicated for CVR and OEF [191, 254]. And while PET-based OEF results of clinical ICAS therapy outcome studies were critically debated [118, 287], the improved mq-BOLD implementation may enable to resolve those uncertainties in the future.

A subsample of ICAS patients received revascularization and was scanned again. The results in abstracts C1, C2 and C11 showed improved hemodynamic status with positive treatment effects on chronic vasodilation and capillary function. Furthermore, spatially normalized iWSAs indicated reversible collateral blood supply in abstract C33. Thus, BH-fMRI and DSC are promising for treatment efficacy monitoring, being even applicable after stenting.

To further validate clinical benefits of DSC imaging and cognitive testing, the multi-center study CREST-H is currently conducted [171]. Regarding additional DSC post-processing, identification of leptomeningeal collateral flow in pial arteries was shown [288], which may help to explain spatial iWSA shifts and could be verified by 4D flow mapping, as applied in journal publications J2 and J6. Moreover, shorter TR in DSC will improve the iWSA accuracy. As an alternative to DSC, time-encoded ASL may even enable non-invasive iWSAs [100, 289]. And automated segmentation would greatly enhance their future applicability.

Non-invasive perfusion imaging by pCASL is highly appealing for preventive screening and longitudinal monitoring. Its clinical translation is supported by increasing availability as a product sequence from multiple vendors. A major methodical improvement is time-encoded



ASL to minimize delay related bias and provide additional temporal perfusion information.

In addition, vessel selective ASL uniquely offers non-invasive vascular territory mapping (see Section 4.4.3) and may support future diagnostics in CVDs [209], such as moyamoya. In this non-atherosclerotic steno-occlusive disease, the stroke risk is highly elevated [290, 291]. Treatment of symptoms is possible by invasive revascularization, but imaging methods for stroke risk stratification are lacking. As a wide network of collaterals is commonly recruited [292], ss-ASL and vessel-selective ASL angiography were successfully compared with DSA in journal publication J1. Furthermore, a novel automated labeling [293] was successfully applied to resolve previous limitations by offering fast, robust and user independent planning.

Regarding oxygen delivery, additional regulating factors were assumed in journal publication J4, such as oxygen diffusivity variations as proposed by Hyder et al. [13, 294, 295]. Interestingly, oxygen diffusivity can be calculated by existing mq-BOLD and pCASL data, as demonstrated in abstract C22 and supported by good correlations with CTH [296] in abstract C26. Oxygen diffusivity mapping may thus yield novel insights to the highly complex oxygen metabolism.

Hemodynamic imaging can even provide detailed information on mechanisms of structural WM damage [297–299] and cognitive decline [300]. On the one hand, ageing-related involvement of capillary dysfunction in WM lesions (WML) formation and increased lesion load within iWSAs were shown in abstract C4. On the other hand, hypoperfusion was linked with cognitive decline in ICAS and AD in journal publications J3 and J5, respectively. According to the literature [192], cognitive impairments persisted after treatment in contrast to reversible hemodynamic impairments as shown in abstracts C1 and C2. Perfusion imaging may thus be used to adapt treatment plans and minimize irreversible structural brain damage [301].

To widen the perspective, whole-body physiology such as cardiovascular contributions to infarcts [228, 302] could be evaluated to optimize prevention in ICAS. Moreover, quantitative plaque morphology characterization may additionally support treatment decisions.

Besides CVDs, hemodynamic MRI also showed great benefits in other pathologies such as brain tumours. Specifically, rCBV by DSC showed complementary information compared to PET in journal publication J7. Furthermore, ss-ASL can visualize collateral recruitment [303] and CVR can depict critical NVC impairments (see Section 3.1) [109]. And after treatment, perfusion MRI can be applied in longitudinal monitoring to detect tumour neoangiogenesis [304].

Further fascinating hemodynamic MRI applications are healthy ageing [305] and neuroscientific studies. Quantitative assessment of the energy metabolism (see Section 3.1.1) will help to improve interpretations of the BOLD signal by revealing physiological signal underpinnings (see Section 3.1.3) [61, 306]. Specifically, simulations indicated effects of perfusion and oxygenation impairments on rs-fMRI in abstract C29, which were affirmed in AD in journal publication J5. Hemodynamic effects during stimulation experiments were successfully quantified by mq-BOLD in abstracts C31 and C35. And  $R'_2$ -based gas-free calibrated-fMRI greatly agreed with hypercapnia in abstract C3. Thus, hemodynamic MRI will be much more applied in neuroscience in the future and help to better understand brain physiology [307].

In conclusion, there are broad perspectives of quantitative cerebral hemodynamic imaging for clinical and neuroscientific applications. The quantitative measurement of the cerebral energy metabolism including related cerebral perfusion and oxygenation parameters offers countless fascinating insights and numerous applications. For example, diagnostics of CVDs such as ICAS could greatly benefit from individual stroke risk predictions and allow personalized therapy to finally improve the quality of life and prolong the average life expectancy of patients. Therefore, it will be a challenge for future large clinical trials to validate the clinical value of specific hemodynamic parameters and synergy effects by multi-parametric imaging.



# Bibliography

- [1] P. Reimer, P. Parizel, J. Meaney, and F. Stichnoth, *Clinical MR imaging: A practical approach*. Springer Berlin Heidelberg, 2010.
- [2] Z. Liang, P. Lauterbur, and IEEE Engineering in Medicine and Biology Society, *Principles of magnetic resonance imaging: A signal processing perspective*. SPIE Optical Engineering Press, 2000.
- [3] R. Wang, S. Yu, J. R. Alger, Z. Zuo, J. Chen, R. Wang, J. An, B. Wang, J. Zhao, R. Xue, and D. J. J. Wang, “Multi-delay arterial spin labeling perfusion MRI in moyamoya disease - comparison with CT perfusion imaging,” *European Radiology*, vol. 24, no. 5, pp. 1135–1144, 2014.
- [4] F. Pfeiffer, T. Weitkamp, O. Bunk, and C. David, “Phase retrieval and differential phase-contrast imaging with low-brilliance X-ray sources,” *Nature Physics*, vol. 2, no. 4, pp. 258–261, 2006.
- [5] S. Kaczmarz, *Advanced image quality enhancement with the single-photon-counting LAMBDA detector*. Thesis, Technical University of Munich (TUM), 2014.
- [6] A. P. Fan, H. Jahanian, S. J. Holdsworth, and G. Zaharchuk, “Comparison of cerebral blood flow measurement with [15O]-water positron emission tomography and arterial spin labeling magnetic resonance imaging: A systematic review,” *J Cereb Blood Flow Metab*, vol. 36, no. 5, pp. 842–861, 2016.
- [7] R. Brown, Y. Cheng, E. Haacke, M. Thompson, and R. Venkatesan, *Magnetic Resonance Imaging: Physical Principles and Sequence Design*. Wiley, 2014.
- [8] M. Cercignani, N. Dowell, and P. Tofts, *Quantitative MRI of the Brain: Principles of Physical Measurement, Second edition*. CRC Press, 2018.
- [9] M. J. Donahue, E. Achten, P. M. Cogswell, F. E. De Leeuw, C. P. Derdeyn, R. M. Dijkhuizen, A. P. Fan, R. Ghaznawi, J. J. Heit, M. A. Ikram, P. Jezzard, L. C. Jordan, E. Jouvent, L. Knutsson, R. Leigh, D. S. Liebeskind, W. Lin, T. W. Okell, A. I. Qureshi, C. J. Stagg, M. J. van Osch, P. C. van Zijl, J. M. Watchmaker, M. Wintermark, O. Wu, G. Zaharchuk, J. Zhou, and J. Hendrikse, “Consensus statement on current and emerging methods for the diagnosis and evaluation of cerebrovascular disease,” *J Cereb Blood Flow Metab*, vol. 38, no. 9, pp. 1391–1417, 2018.
- [10] T. Kanda, T. Fukusato, M. Matsuda, K. Toyoda, H. Oba, J. Kotoku, T. Haruyama, K. Kitajima, and S. Furui, “Gadolinium-based contrast agent accumulates in the brain even in subjects without severe renal dysfunction: Evaluation of autopsy brain specimens with inductively coupled plasma mass spectroscopy,” *Radiology*, vol. 276, no. 1, pp. 228–232, 2015.

- [11] Bundesinstitut fuer Arzneimittel und Medizinprodukte, “Abwehr von Gefahren durch Arzneimittel, Stufe II,” Feb. 2020. [https://www.bfarm.de/SharedDocs/Downloads/DE/Arzneimittel/Pharmakovigilanz/Risikoinformationen/RisikoBewVerf/g-1/gadolinium\\_bescheid20200221.pdf](https://www.bfarm.de/SharedDocs/Downloads/DE/Arzneimittel/Pharmakovigilanz/Risikoinformationen/RisikoBewVerf/g-1/gadolinium_bescheid20200221.pdf), accessed 07.07.2020.
- [12] European Medicines Agency, “Ema’s final opinion confirms restrictions on use of linear gadolinium agents in body scans,” Nov. 2017. [https://www.ema.europa.eu/en/documents/referral/gadolinium-article-31-referral-emas-final-opinion-confirms-restrictions-use-linear-gadolinium-agents\\_en.pdf](https://www.ema.europa.eu/en/documents/referral/gadolinium-article-31-referral-emas-final-opinion-confirms-restrictions-use-linear-gadolinium-agents_en.pdf), accessed 07.07.2020.
- [13] F. Hyder, I. Kida, K. L. Behar, R. P. Kennan, P. K. Maciejewski, and D. L. Rothman, “Quantitative functional imaging of the brain: Towards mapping neuronal activity by BOLD fMRI,” *NMR in Biomed*, vol. 14, no. 7-8, pp. 413–431, 2001.
- [14] E. Wilkins, L. Wilson, K. Wickramasinghe, P. Bhatnagar, J. Leal, R. Luengo-Fernandez, R. Burns, M. Rayner, and N. Townsend, “European cardiovascular disease statistics 2017,” report, European Heart Network, 2017.
- [15] J. Olesen, A. Gustavsson, M. Svensson, H. U. Wittchen, B. Jonsson, CDBE Study Group, and European Brain Council, “The economic cost of brain disorders in Europe,” *Eur J Neurol*, vol. 19, no. 1, pp. 155–162, 2012.
- [16] G. W. Petty, R. D. Brown, J. P. Whisnant, J. D. Sicks, W. M. O’Fallon, and D. O. Wiebers, “Ischemic stroke subtypes: A population-based study of incidence and risk factors,” *Stroke*, vol. 30, no. 12, pp. 2513–2516, 1999.
- [17] J. J. Jalbert, L. L. Nguyen, M. D. Gerhard-Herman, and et al., “Outcomes after carotid artery stenting in medicare beneficiaries, 2005 to 2009,” *JAMA Neurology*, vol. 72, no. 3, pp. 276–286, 2015.
- [18] C. J. Lin, F. C. Chang, K. H. Chou, P. C. Tu, Y. H. Lee, C. P. Lin, P. N. Wang, and I. H. Lee, “Intervention versus aggressive medical therapy for cognition in severe asymptomatic carotid stenosis,” *Am J Neuroradiol*, vol. 37, no. 10, pp. 1889–1897, 2016.
- [19] G. B. Pike, “Quantitative functional MRI: Concepts, issues and future challenges,” *NeuroImage*, vol. 62, no. 2, pp. 1234–1240, 2012.
- [20] R. Buxton, *Introduction to functional magnetic resonance imaging: Principles and techniques*. Cambridge University Press, 2002.
- [21] M. Bernstein, K. King, and X. Zhou, *Handbook of MRI Pulse Sequences*. Elsevier Science, 2004.
- [22] I. I. Rabi, “Space quantization in a gyrating magnetic field,” *Physical Review*, vol. 51, no. 8, pp. 652–654, 1937.
- [23] C. J. Gorter and L. J. F. Broer, “Negative result of an attempt to observe nuclear magnetic resonance in solids,” *Physica*, vol. 9, no. 6, pp. 591–596, 1942.
- [24] F. Bloch, W. W. Hansen, and M. Packard, “Nuclear induction,” *Physical Review*, vol. 69, no. 3-4, pp. 127–127, 1946.

- 
- [25] E. M. Purcell, H. C. Torrey, and R. V. Pound, “Resonance absorption by nuclear magnetic moments in a solid,” *Physical Review*, vol. 69, no. 1-2, pp. 37–38, 1946.
- [26] E. L. Hahn, “Spin echoes,” *Physical Review*, vol. 80, no. 4, pp. 580–594, 1950.
- [27] H. Y. Carr, *Free precession techniques in nuclear magnetic resonance*. Thesis, Harvard University, 1952.
- [28] B. MacWilliams, “Russian claims first in magnetic imaging,” *Nature*, vol. 426, no. 6965, pp. 375–375, 2003.
- [29] P. C. Lauterbur, “Image formation by induced local interactions: Examples employing nuclear magnetic resonance,” *Nature*, vol. 242, no. 5394, pp. 190–191, 1973.
- [30] P. Mansfield and P. K. Grannell, “Diffraction and microscopy in solids and liquids by NMR,” *Physical Review B*, vol. 12, no. 9, pp. 3618–3634, 1975.
- [31] OECD, *Health at a Glance 2019: OECD Indicators*. OECD Publishing, 2019.
- [32] L. G. Hanson, “Is quantum mechanics necessary for understanding magnetic resonance?,” *Concepts in Magnetic Resonance Part A*, vol. 32A, no. 5, pp. 329–340, 2008.
- [33] D. Ma, V. Gulani, N. Seiberlich, K. Liu, J. L. Sunshine, J. L. Duerk, and M. A. Griswold, “Magnetic resonance fingerprinting,” *Nature*, vol. 495, no. 7440, pp. 187–192, 2013.
- [34] N. P. Blockley, V. E. M. Griffeth, A. B. Simon, D. J. Dubowitz, and R. B. Buxton, “Calibrating the BOLD response without administering gases: Comparison of hypercapnia calibration with calibration using an asymmetric spin echo,” *NeuroImage*, vol. 104, pp. 423–429, 2015.
- [35] H. Y. Carr and E. M. Purcell, “Effects of diffusion on free precession in nuclear magnetic resonance experiments,” *Physical Review*, vol. 94, no. 3, pp. 630–638, 1954.
- [36] S. Meiboom and D. Gill, “Modified spin-echo method for measuring nuclear relaxation times,” *Review of Scientific Instruments*, vol. 29, no. 8, pp. 688–691, 1958.
- [37] A. Haase, J. Frahm, D. Matthaei, W. Hanicke, and K. D. Merboldt, “FLASH imaging. Rapid NMR imaging using low flip-angle pulses,” *J Magn Reson*, vol. 67, no. 2, pp. 258–266, 1986.
- [38] P. Mansfield, “Multi-planar image formation using NMR spin echoes,” *J of Physics C: Solid State Physics*, vol. 10, no. 3, pp. L55–L58, 1977.
- [39] J. Hennig, A. Nauerth, and H. Friedburg, “RARE imaging: A fast imaging method for clinical MR,” *Magn Reson Med*, vol. 3, no. 6, pp. 823–833, 1986.
- [40] K. Oshio and D. A. Feinberg, “GRASE (Gradient-and Spin-Echo) imaging: A novel fast MRI technique,” *Magn Reson Med*, vol. 20, no. 2, pp. 344–349, 1991.
- [41] K. P. Pruessmann, M. Weiger, M. B. Scheidegger, and P. Boesiger, “SENSE: Sensitivity encoding for fast MRI,” *Magn Reson Med*, vol. 42, no. 5, pp. 952–962, 1999.

- [42] M. A. Griswold, P. M. Jakob, R. M. Heidemann, M. Nittka, V. Jellus, J. Wang, B. Kiefer, and A. Haase, “Generalized autocalibrating partially parallel acquisitions (GRAPPA),” *Magn Reson Med*, vol. 47, no. 6, pp. 1202–1210, 2002.
- [43] G. Glover, “Phase-offset multiplanar (POMP) volume imaging: A new technique,” *J Magn Res Imaging*, vol. 1, no. 4, pp. 457–461, 1991.
- [44] D. J. Larkman, J. V. Hajnal, A. H. Herlihy, G. A. Coutts, I. R. Young, and G. Ehnholm, “Use of multicoil arrays for separation of signal from multiple slices simultaneously excited,” *J Magn Res Imaging*, vol. 13, no. 2, pp. 313–317, 2001.
- [45] C. Preibisch, G. J. Castrillon, M. Buhner, and V. Riedl, “Evaluation of Multiband EPI Acquisitions for Resting State fMRI,” *PLoS One*, vol. 10, no. 9, p. e0136961, 2015.
- [46] Blausen.com, “Red blood cells,” *WikiJournal of Medicine: Medical gallery of Blausen Medical 2014*, vol. 1, no. 2, 2014.
- [47] H. Fischer, “Three basic types of neuronal arrangements,” Jan. 2013. [https://upload.wikimedia.org/wikipedia/commons/6/61/Three\\_Basic\\_Types\\_of\\_Neuronal\\_Arrangements.png](https://upload.wikimedia.org/wikipedia/commons/6/61/Three_Basic_Types_of_Neuronal_Arrangements.png), accessed 07.07.2020.
- [48] A. Kuebelbeck, “Astrocyte endothel interaction 01,” Mar. 2009. [https://upload.wikimedia.org/wikipedia/commons/4/45/Astrocyte\\_endothel\\_interaction\\_01.png](https://upload.wikimedia.org/wikipedia/commons/4/45/Astrocyte_endothel_interaction_01.png), accessed 07.07.2020.
- [49] D. Attwell and C. Iadecola, “The neural basis of functional brain imaging signals,” *Trends Neurosci*, vol. 25, no. 12, pp. 621–625, 2002.
- [50] D. Attwell and S. B. Laughlin, “An energy budget for signaling in the grey matter of the brain,” *J Cereb Blood Flow Metab*, vol. 21, no. 10, pp. 1133–1145, 2001.
- [51] J. Andresen, N. I. Shafi, and R. M. Bryan, “Endothelial influences on cerebrovascular tone,” *J Appl Physiol (1985)*, vol. 100, no. 1, pp. 318–27, 2006.
- [52] D. Attwell, A. M. Buchan, S. Charpak, M. Lauritzen, B. A. Macvicar, and E. A. Newman, “Glial and neuronal control of brain blood flow,” *Nature*, vol. 468, no. 7321, pp. 232–243, 2010.
- [53] R. A. Hill, L. Tong, P. Yuan, S. Murikinati, S. Gupta, and J. Grutzendler, “Regional blood flow in the normal and ischemic brain is controlled by arteriolar smooth muscle cell contractility and not by capillary pericytes,” *Neuron*, vol. 87, no. 1, pp. 95–110, 2015.
- [54] H. L. Xu, L. Mao, S. Ye, C. Paisansathan, F. Vetri, and D. A. Pelligrino, “Astrocytes are a key conduit for upstream signaling of vasodilation during cerebral cortical neuronal activation in vivo,” *Am J Physiol Heart Circ Physiol*, vol. 294, no. 2, pp. H622–632, 2008.
- [55] M. G. Bright and K. Murphy, “Reliable quantification of BOLD fMRI cerebrovascular reactivity despite poor breath-hold performance,” *NeuroImage*, vol. 83, pp. 559–568, 2013.



- 
- [56] E. Y. Liu, J. Guo, A. B. Simon, F. Haist, D. J. Dubowitz, and R. B. Buxton, “The potential for gas-free measurements of absolute oxygen metabolism during both baseline and activation states in the human brain,” *NeuroImage*, vol. 207, p. 116342, 2020.
- [57] M. Reivich, D. Kuhl, A. Wolf, J. Greenberg, M. Phelps, T. Ido, V. Casella, J. Fowler, E. Hoffman, A. Alavi, P. Som, and L. Sokoloff, “The [18F]fluorodeoxyglucose method for the measurement of local cerebral glucose utilization in man,” *Circ Res*, vol. 44, no. 1, pp. 127–137, 1979.
- [58] R. S. Frackowiak, G. L. Lenzi, T. Jones, and J. D. Heather, “Quantitative measurement of regional cerebral blood flow and oxygen metabolism in man using  $^{15}\text{O}$  and positron emission tomography: Theory, procedure, and normal values,” *J Comput Assist Tomogr*, vol. 4, no. 6, pp. 727–736, 1980.
- [59] M. A. Mintun, M. E. Raichle, W. R. Martin, and P. Herscovitch, “Brain oxygen utilization measured with O-15 radiotracers and positron emission tomography,” *J Nucl Med*, vol. 25, no. 2, pp. 177–187, 1984.
- [60] H. Ito, M. Ibaraki, I. Kanno, H. Fukuda, and S. Miura, “Changes in cerebral blood flow and cerebral oxygen metabolism during neural activation measured by positron emission tomography: Comparison with blood oxygenation level-dependent contrast measured by functional magnetic resonance imaging,” *J Cereb Blood Flow Metab*, vol. 25, no. 3, pp. 371–377, 2005.
- [61] N. P. Blockley, V. E. M. Griffeth, and R. B. Buxton, “A general analysis of calibrated BOLD methodology for measuring CMRO<sub>2</sub> responses: Comparison of a new approach with existing methods,” *NeuroImage*, vol. 60, no. 1, pp. 279–289, 2012.
- [62] N. P. Blockley, V. E. M. Griffeth, M. A. Germuska, D. P. Bulte, and R. B. Buxton, “An analysis of the use of hyperoxia for measuring venous cerebral blood volume: Comparison of the existing method with a new analysis approach,” *NeuroImage*, vol. 72, pp. 33–40, 2013.
- [63] W. James, *The Principles of Physiology*. Cambridge, MA, USA: Harvard University Press, 1890.
- [64] S. Ogawa, T. M. Lee, A. S. Nayak, and P. Glynn, “Oxygenation-sensitive contrast in magnetic resonance image of rodent brain at high magnetic fields,” *Magn Reson Med*, vol. 14, no. 1, pp. 68–78, 1990.
- [65] S. Ogawa, T. M. Lee, A. R. Kay, and D. W. Tank, “Brain magnetic resonance imaging with contrast dependent on blood oxygenation,” *Proc Natl Acad Sci USA*, vol. 87, no. 24, pp. 9868–9872, 1990.
- [66] D. A. Gusnard, M. E. Raichle, and M. E. Raichle, “Searching for a baseline: Functional imaging and the resting human brain,” *Nat Rev Neurosci*, vol. 2, no. 10, pp. 685–694, 2001.
- [67] P. T. Fox and M. E. Raichle, “Focal physiological uncoupling of cerebral blood flow and oxidative metabolism during somatosensory stimulation in human subjects,” *Proc Natl Acad Sci USA*, vol. 83, no. 4, pp. 1140–1144, 1986.

- [68] P. T. Fox, M. E. Raichle, M. A. Mintun, and C. Dence, "Nonoxidative glucose consumption during focal physiologic neural activity," *Science*, vol. 241, no. 4864, pp. 462–464, 1988.
- [69] L. Pauling, "The oxygen equilibrium of hemoglobin and its structural interpretation," *Proc Natl Acad Sci USA*, vol. 21, no. 4, pp. 186–191, 1935.
- [70] K. R. Thulborn, J. C. Waterton, P. M. Matthews, and G. K. Radda, "Oxygenation dependence of the transverse relaxation time of water protons in whole blood at high field," *Biochimica et Biophysica Acta (BBA) - General Subjects*, vol. 714, no. 2, pp. 265–270, 1982.
- [71] S. Ogawa, D. W. Tank, R. Menon, J. M. Ellermann, S. G. Kim, H. Merkle, and K. Ugurbil, "Intrinsic signal changes accompanying sensory stimulation: Functional brain mapping with magnetic resonance imaging," *Proc Natl Acad Sci USA*, vol. 89, no. 13, pp. 5951–5955, 1992.
- [72] J. W. Belliveau, D. N. Kennedy, R. C. McKinstry, B. R. Buchbinder, R. M. Weisskoff, M. S. Cohen, J. M. Vevea, T. J. Brady, and B. R. Rosen, "Functional mapping of the human visual cortex by magnetic resonance imaging," *Science*, vol. 254, no. 5032, pp. 716–719, 1991.
- [73] N. K. Logothetis, J. Pauls, M. Augath, T. Trinath, and A. Oeltermann, "Neurophysiological investigation of the basis of the fMRI signal," *Nature*, vol. 412, no. 6843, pp. 150–157, 2001.
- [74] P. T. Fox and M. E. Raichle, "Stimulus rate dependence of regional cerebral blood flow in human striate cortex, demonstrated by positron emission tomography," *J Neurophysiol*, vol. 51, no. 5, pp. 1109–1120, 1984.
- [75] N. K. Logothetis, "What we can do and what we cannot do with fMRI," *Nature*, vol. 453, no. 7197, pp. 869–878, 2008.
- [76] F. Hyder, D. L. Rothman, and R. G. Shulman, "Total neuroenergetics support localized brain activity: Implications for the interpretation of fMRI," *Proc Natl Acad Sci USA*, vol. 99, no. 16, pp. 10771–10776, 2002.
- [77] F. Calamante, D. G. Gadian, and A. Connelly, "Quantification of perfusion using bolus tracking magnetic resonance imaging in stroke: Assumptions, limitations, and potential implications for clinical use," *Stroke*, vol. 33, no. 4, pp. 1146–1151, 2002.
- [78] J. A. Detre, J. S. Leigh, D. S. Williams, and A. P. Koretsky, "Perfusion imaging," *Magn Reson Med*, vol. 23, no. 1, pp. 37–45, 1992.
- [79] A. Villringer, B. R. Rosen, J. W. Belliveau, J. L. Ackerman, R. B. Lauffer, R. B. Buxton, Y. S. Chao, V. J. Wedeen, and T. J. Brady, "Dynamic imaging with lanthanide chelates in normal brain: Contrast due to magnetic susceptibility effects," *Magn Reson Med*, vol. 6, no. 2, pp. 164–174, 1988.
- [80] K. Welker, J. Boxerman, A. Kalnin, T. Kaufmann, M. Shiroishi, and M. Wintermark, "ASFN recommendations for clinical performance of MR dynamic susceptibility contrast perfusion imaging of the brain," *Am J Neuroradiol*, vol. 36, no. 6, pp. E41–51, 2015.

- 
- [81] R. Weisskoff, C. S. Zuo, J. L. Boxerman, and B. R. Rosen, "Microscopic susceptibility variation and transverse relaxation: Theory and experiment," *Magn Reson Med*, vol. 31, no. 6, pp. 601–610, 1994.
- [82] J. L. Boxerman, L. M. Hamberg, B. R. Rosen, and R. M. Weisskoff, "MR contrast due to intravascular magnetic susceptibility perturbations," *Magn Reson Med*, vol. 34, no. 4, pp. 555–566, 1995.
- [83] F. Calamante, E. J. Vonken, and M. J. van Osch, "Contrast agent concentration measurements affecting quantification of bolus-tracking perfusion MRI," *Magn Reson Med*, vol. 58, no. 3, pp. 544–553, 2007.
- [84] F. Calamante, D. L. Thomas, G. S. Pell, J. Wiersma, and R. Turner, "Measuring cerebral blood flow using magnetic resonance imaging techniques," *J Cereb Blood Flow Metab*, vol. 19, no. 7, pp. 701–735, 1999.
- [85] S. Cha, E. A. Knopp, G. Johnson, S. G. Wetzel, A. W. Litt, and D. Zagzag, "Intracranial mass lesions: Dynamic contrast-enhanced susceptibility-weighted echo-planar perfusion MR imaging," *Radiology*, vol. 223, no. 1, pp. 11–29, 2002.
- [86] A. Kluge, M. Lukas, V. Toth, T. Pyka, C. Zimmer, and C. Preibisch, "Analysis of three leakage-correction methods for DSC-based measurement of relative cerebral blood volume with respect to heterogeneity in human gliomas," *Magn Reson Imaging*, vol. 34, no. 4, pp. 410–421, 2016.
- [87] F. Calamante, "Arterial input function in perfusion MRI: A comprehensive review," *Prog Nucl Magn Reson Spectrosc*, vol. 74, pp. 1–32, 2013.
- [88] S. N. Jespersen and L. Østergaard, "The roles of cerebral blood flow, capillary transit time heterogeneity, and oxygen tension in brain oxygenation and metabolism," *J Cereb Blood Flow Metab*, vol. 32, no. 2, pp. 264–277, 2012.
- [89] K. Mouridsen, K. Friston, N. Hjort, L. Gyldensted, L. Østergaard, and S. Kiebel, "Bayesian estimation of cerebral perfusion using a physiological model of microvasculature," *NeuroImage*, vol. 33, no. 2, pp. 570–579, 2006.
- [90] K. Mouridsen, M. B. Hansen, L. Østergaard, and S. N. Jespersen, "Reliable estimation of capillary transit time distributions using DSC-MRI," *J Cereb Blood Flow Metab*, vol. 34, no. 9, pp. 1511–1521, 2014.
- [91] L. Østergaard, R. M. Weisskoff, D. A. Chesler, C. Gyldensted, and B. R. Rosen, "High resolution measurement of cerebral blood flow using intravascular tracer bolus passages. Part I: Mathematical approach and statistical analysis," *Magn Reson Med*, vol. 36, no. 5, pp. 715–725, 1996.
- [92] L. Østergaard, A. G. Sorensen, K. K. Kwong, R. M. Weisskoff, C. Gyldensted, and B. R. Rosen, "High resolution measurement of cerebral blood flow using intravascular tracer bolus passages. Part II: Experimental comparison and preliminary results," *Magn Reson Med*, vol. 36, no. 5, pp. 726–736, 1996.
- [93] R. M. Weisskoff, D. Chesler, J. L. Boxerman, and B. R. Rosen, "Pitfalls in MR measurement of tissue blood flow with intravascular tracers: Which mean transit time?," *Magn Reson Med*, vol. 29, no. 4, pp. 553–558, 1993.

- [94] S. E. Cowper, H. S. Robin, S. M. Steinberg, L. D. Su, S. Gupta, and P. E. LeBoit, "Scleromyxoedema-like cutaneous diseases in renal-dialysis patients," *Lancet*, vol. 356, no. 9234, pp. 1000–1001, 2000.
- [95] D. S. Williams, J. A. Detre, J. S. Leigh, and A. P. Koretsky, "Magnetic resonance imaging of perfusion using spin inversion of arterial water," *Proc Natl Acad Sci USA*, vol. 89, no. 1, pp. 212–216, 1992.
- [96] W. T. Dixon, "Simple proton spectroscopic imaging," *Radiology*, vol. 153, no. 1, pp. 189–94, 1984.
- [97] W. Dai, D. Garcia, C. de Bazelaire, and D. C. Alsop, "Continuous flow-driven inversion for arterial spin labeling using pulsed radio frequency and gradient fields," *Magn Reson Med*, vol. 60, no. 6, pp. 1488–1497, 2008.
- [98] D. C. Alsop, J. A. Detre, X. Golay, M. Günther, J. Hendrikse, L. Hernandez-Garcia, H. Lu, B. J. MacIntosh, L. M. Parkes, M. Smits, M. J. P. van Osch, D. J. J. Wang, E. C. Wong, and G. Zaharchuk, "Recommended implementation of arterial spin-labeled perfusion MRI for clinical applications: A consensus of the ISMRM perfusion study group and the European consortium for ASL in dementia," *Magn Reson Med*, vol. 73, no. 1, pp. 102–116, 2015.
- [99] A. Bush, Y. Chai, S. Y. Choi, L. Vaclavu, S. Holland, A. Nederveen, T. Coates, and J. Wood, "Pseudo continuous arterial spin labeling quantification in anemic subjects with hyperemic cerebral blood flow," *Magn Reson Imaging*, vol. 47, pp. 137–146, 2018.
- [100] E. T. Petersen, K. Mouridsen, X. Golay, and all named co-authors of the Quasar test-retest study, "The QUASAR reproducibility study, Part II: Results from a multi-center arterial spin labeling test-retest study," *NeuroImage*, vol. 49, no. 1, pp. 104–113, 2010.
- [101] R. B. Buxton, L. R. Frank, E. C. Wong, B. Siewert, S. Warach, and R. R. Edelman, "A general kinetic model for quantitative perfusion imaging with arterial spin labeling," *Magn Reson Med*, vol. 40, no. 3, pp. 383–396, 1998.
- [102] M. J. van Osch, W. M. Teeuwisse, Z. Chen, Y. Suzuki, M. Helle, and S. Schmid, "Advances in arterial spin labelling MRI methods for measuring perfusion and collateral flow," *J Cereb Blood Flow Metab*, vol. 38, no. 9, pp. 1461–1480, 2018.
- [103] P. W. Hales, J. M. Kawadler, S. E. Aylett, F. J. Kirkham, and C. A. Clark, "Arterial spin labeling characterization of cerebral perfusion during normal maturation from late childhood into adulthood: Normal 'reference range' values and their use in clinical studies," *J Cereb Blood Flow Metab*, vol. 34, no. 5, pp. 776–784, 2014.
- [104] X. Golay and M. Guenther, "Arterial spin labelling: Final steps to make it a clinical reality," *Magma*, vol. 25, no. 2, pp. 79–82, 2012.
- [105] J. A. Detre, H. Rao, D. J. J. Wang, Y. F. Chen, and Z. Wang, "Applications of arterial spin labeled MRI in the brain," *J Magn Res Imaging*, vol. 35, no. 5, pp. 1026–1037, 2012.
- [106] C. S. Roy and C. S. Sherrington, "On the regulation of the blood-supply of the brain," *J of physiology*, vol. 11, no. 1-2, pp. 85–108; 158.7–158.17, 1890.

- 
- [107] S. S. Kety and C. F. Schmidt, “The effects of altered arterial tensions of carbon dioxide and oxygen on cerebral blood flow and on cerebral oxygen consumption of normal young men,” *J Clin Invest*, vol. 27, no. 4, pp. 484–492, 1948.
- [108] R. L. Grubb, M. E. Raichle, J. O. Eichling, and M. M. Ter-Pogossian, “The effects of changes in PaCO<sub>2</sub> on cerebral blood volume, blood flow, and vascular mean transit time,” *Stroke*, vol. 5, no. 5, pp. 630–639, 1974.
- [109] J. J. Pillai and D. J. Mikulis, “Cerebrovascular reactivity mapping: An evolving standard for clinical functional imaging,” *Am J Neuroradiol*, vol. 36, no. 1, pp. 7–13, 2015.
- [110] V. R. Spano, D. M. Mandell, J. Poublanc, K. Sam, A. Battisti-Charbonney, O. Pucci, J. S. Han, A. P. Crawley, J. A. Fisher, and D. J. Mikulis, “CO<sub>2</sub> blood oxygen level-dependent MR mapping of cerebrovascular reserve in a clinical population: Safety, tolerability, and technical feasibility,” *Radiology*, vol. 266, no. 2, pp. 592–598, 2013.
- [111] S. Magon, G. Basso, P. Farace, G. K. Ricciardi, A. Beltramello, and A. Sbarbati, “Reproducibility of BOLD signal change induced by breath holding,” *NeuroImage*, vol. 45, no. 3, pp. 702–712, 2009.
- [112] L. Vondráčková, P. Krukowski, and J. Petr, “Data-driven model for evaluation of cerebrovascular-reserve measurement with hypercapnia bold,” in *Proc of the 24th Annual Meeting of ISMRM: 3801*, 2016.
- [113] C. Y. Shu, P. Herman, D. Coman, B. G. Sanganahalli, H. Wang, C. Juchem, D. L. Rothman, R. A. de Graaf, and F. Hyder, “Brain region and activity-dependent properties of M for calibrated fMRI,” *NeuroImage*, vol. 125, pp. 848–856, 2016.
- [114] C. Y. Shu, B. G. Sanganahalli, D. Coman, P. Herman, D. L. Rothman, and F. Hyder, “Quantitative beta mapping for calibrated fMRI,” *NeuroImage*, vol. 126, pp. 219–228, 2016.
- [115] S. M. Smith, “Fast robust automated brain extraction,” *Hum Brain Mapp*, vol. 17, no. 3, pp. 143–155, 2002.
- [116] J. C. Baron, M. G. Bousser, A. Rey, A. Guillard, D. Comar, and P. Castaigne, “Reversal of focal misery-perfusion syndrome by extra-intracranial arterial bypass in hemodynamic cerebral ischemia. A case study with <sup>15</sup>O positron emission tomography,” *Stroke*, vol. 12, no. 4, pp. 454–459, 1981.
- [117] C. P. Derdeyn, T. O. Videen, K. D. Yundt, S. M. Fritsch, D. A. Carpenter, R. L. Grubb, and W. J. Powers, “Variability of cerebral blood volume and oxygen extraction: Stages of cerebral haemodynamic impairment revisited,” *Brain*, vol. 125, no. 3, pp. 595–607, 2002.
- [118] W. J. Powers, W. R. Clarke, R. L. Grubb, T. O. Videen, H. P. Adams, C. P. Derdeyn, and C. Investigators, “Extracranial-intracranial bypass surgery for stroke prevention in hemodynamic cerebral ischemia: The carotid occlusion surgery study randomized trial,” *JAMA*, vol. 306, no. 18, pp. 1983–1992, 2011.

- [119] A. P. Fan, A. A. Khalil, J. B. Fiebach, G. Zaharchuk, A. Villringer, K. Villringer, and C. J. Gauthier, “Elevated brain oxygen extraction fraction measured by MRI susceptibility relates to perfusion status in acute ischemic stroke,” *J Cereb Blood Flow Metab*, vol. 40, no. 3, pp. 539–551, 2020.
- [120] N. M. Hirsch, V. Toth, A. Forschler, H. Kooijman, C. Zimmer, and C. Preibisch, “Technical considerations on the validity of blood oxygenation level-dependent-based MR assessment of vascular deoxygenation,” *NMR in Biomed*, vol. 27, no. 7, pp. 853–862, 2014.
- [121] D. A. Yablonskiy and E. M. Haacke, “Theory of NMR signal behavior in magnetically inhomogeneous tissues: The static dephasing regime,” *Magn Reson Med*, vol. 32, no. 6, pp. 749–763, 1994.
- [122] S. Baudrexel, S. Volz, C. Preibisch, J. C. Klein, H. Steinmetz, R. Hilker, and R. Deichmann, “Rapid single-scan T2\*-mapping using exponential excitation pulses and image-based correction for linear background gradients,” *Magn Reson Med*, vol. 62, no. 1, pp. 263–268, 2009.
- [123] N. M. Hirsch, *BOLD-based Magnetic Resonance Imaging of Hypoxia in the Human Brain*. Thesis, Technical University of Munich (TUM), 2013.
- [124] W. M. Spees, D. A. Yablonskiy, M. C. Oswood, and J. J. Ackerman, “Water proton MR properties of human blood at 1.5 Tesla: Magnetic susceptibility, T1, T2, T2\*, and non-Lorentzian signal behavior,” *Magn Reson Med*, vol. 45, no. 4, pp. 533–542, 2001.
- [125] M. J. Silvennoinen, C. S. Clingman, X. Golay, R. A. Kauppinen, and P. C. van Zijl, “Comparison of the dependence of blood R2 and R2\* on oxygen saturation at 1.5 and 4.7 Tesla,” *Magn Reson Med*, vol. 49, no. 1, pp. 47–60, 2003.
- [126] A. S. Gersing, M. Ankenbrank, B. J. Schwaiger, V. Toth, I. Janssen, H. Kooijman, S. Wunderlich, J. S. Bauer, C. Zimmer, and C. Preibisch, “Mapping of cerebral metabolic rate of oxygen using dynamic susceptibility contrast and blood oxygen level dependent MR imaging in acute ischemic stroke,” *Neuroradiology*, vol. 57, no. 12, pp. 1253–1261, 2015.
- [127] V. Toth, A. Forschler, N. M. Hirsch, J. den Hollander, H. Kooijman, J. Gempt, F. Ringel, J. Schlegel, C. Zimmer, and C. Preibisch, “MR-based hypoxia measures in human glioma,” *J Neurooncol*, vol. 115, no. 2, pp. 197–207, 2013.
- [128] C. Preibisch, K. Shi, A. Kluge, M. Lukas, B. Wiestler, J. Goettler, J. Gempt, F. Ringel, M. Al Jaber, J. Schlegel, B. Meyer, C. Zimmer, T. Pyka, and S. Forster, “Characterizing hypoxia in human glioma: A simultaneous multimodal MRI and PET study,” *NMR in Biomed*, vol. 30, no. 11, p. e3775, 2017.
- [129] B. Wiestler, A. Kluge, M. Lukas, J. Gempt, F. Ringel, J. Schlegel, B. Meyer, C. Zimmer, S. Förster, T. Pyka, and C. Preibisch, “Multiparametric MRI-based differentiation of WHO grade II/III glioma and WHO grade IV glioblastoma,” *Scientific Reports*, vol. 6, p. 35142, 2016.

- 
- [130] G. Marchal, P. Rioux, M.-C. Petit-Taboué, G. Sette, J.-M. Travère, C. Le Poec, P. Courtheoux, J.-M. Derlon, and J.-C. Baron, “Regional cerebral oxygen consumption, blood flow, and blood volume in healthy human aging,” *Archives of Neurology*, vol. 49, no. 10, pp. 1013–1020, 1992.
- [131] R. Mangla, B. Kolar, J. Almast, and S. E. Ekholm, “Border zone infarcts: Pathophysiological and imaging characteristics,” *Radiographics*, vol. 31, no. 5, pp. 1201–1214, 2011.
- [132] H. Yamauchi, H. Fukuyama, S. Yamaguchi, T. Miyoshi, J. Kimura, and J. Konishi, “High-intensity area in the deep white matter indicating hemodynamic compromise in internal carotid artery occlusive disorders,” *Arch Neurol*, vol. 48, no. 10, pp. 1067–1071, 1991.
- [133] H. Nonaka, M. Akima, T. Hatori, T. Nagayama, Z. Zhang, and F. Ihara, “Microvasculature of the human cerebral white matter: Arteries of the deep white matter,” *Neuropathology*, vol. 23, no. 2, pp. 111–118, 2003.
- [134] M. Cavaglia, S. M. Dombrowski, J. Drazba, A. Vasanji, P. M. Bokesch, and D. Janigro, “Regional variation in brain capillary density and vascular response to ischemia,” *Brain Res*, vol. 910, no. 1-2, pp. 81–93, 2001.
- [135] B. Bender and U. Klose, “The in vivo influence of white matter fiber orientation towards B0 on T2\* in the human brain,” *NMR in Biomed*, vol. 23, no. 9, pp. 1071–1076, 2010.
- [136] C. Denk, E. H. Torres, A. MacKay, and A. Rauscher, “The influence of white matter fibre orientation on mr signal phase and decay,” *NMR in Biomed*, vol. 24, no. 3, pp. 246–252, 2011.
- [137] E. Hernandez-Torres, N. Kassner, N. D. Forkert, L. Wei, V. Wiggermann, M. Daemen, L. Machan, A. Traboulsee, D. Li, and A. Rauscher, “Anisotropic cerebral vascular architecture causes orientation dependency in cerebral blood flow and volume measured with dynamic susceptibility contrast magnetic resonance imaging,” *J Cereb Blood Flow Metab*, vol. 37, no. 3, pp. 1108–1119, 2017.
- [138] J. P. Mugler and J. R. Brookeman, “Three-dimensional magnetization-prepared rapid gradient-echo imaging (3D MP RAGE),” *Magn Reson Med*, vol. 15, no. 1, pp. 152–157, 1990.
- [139] W. Penny, K. Friston, J. Ashburner, S. Kiebel, and T. Nichols, *Statistical parametric mapping: The analysis of functional brain images*. Elsevier Science, 2011.
- [140] J. V. Hajnal, D. J. Bryant, L. Kasuboski, P. M. Pattany, B. De Coene, P. D. Lewis, J. M. Pennock, A. Oatridge, I. R. Young, and G. M. Bydder, “Use of fluid attenuated inversion recovery (FLAIR) pulse sequences in MRI of the brain,” *J Comput Assist Tomogr*, vol. 16, no. 6, pp. 841–844, 1992.
- [141] J. V. Hajnal, B. De Coene, P. D. Lewis, C. J. Baudouin, F. M. Cowan, J. M. Pennock, I. R. Young, and G. M. Bydder, “High signal regions in normal white matter shown by heavily T2-weighted CSF nulled IR sequences,” *J Comput Assist Tomogr*, vol. 16, no. 4, pp. 506–513, 1992.



- [142] J. C. de Groot, F. E. de Leeuw, M. Oudkerk, J. van Gijn, A. Hofman, J. Jolles, and M. M. Breteler, "Cerebral white matter lesions and cognitive function: The Rotterdam scan study," *Ann Neurol*, vol. 47, no. 2, pp. 145–151, 2000.
- [143] R. Bakshi, S. Ariyaratana, R. H. Benedict, and L. Jacobs, "Fluid-attenuated inversion recovery magnetic resonance imaging detects cortical and juxtacortical multiple sclerosis lesions," *Arch Neurol*, vol. 58, no. 5, pp. 742–748, 2001.
- [144] F. Fazekas, J. B. Chawluk, A. Alavi, H. I. Hurtig, and R. A. Zimmerman, "MR signal abnormalities at 1.5 T in Alzheimer's dementia and normal aging," *AJR Am J Roentgenol*, vol. 149, no. 2, pp. 351–356, 1987.
- [145] E. Stejskal and J. Tanner, "Spin diffusion measurements: Spin echoes in the presence of a time-dependent field gradient," *J. Chem. Phys.*, vol. 42, no. 1, pp. 288–292, 1965.
- [146] A. E. Baird and S. Warach, "Magnetic resonance imaging of acute stroke," *J Cereb Blood Flow Metab*, vol. 18, no. 6, pp. 583–609, 1998.
- [147] D. Le Bihan, R. Turner, and P. Douek, "Is water diffusion restricted in human brain white matter? An echo-planar NMR imaging study," *Neuroreport*, vol. 4, no. 7, pp. 887–890, 1993.
- [148] P. J. Basser, J. Mattiello, and D. LeBihan, "Estimation of the effective self-diffusion tensor from the NMR spin echo," *J Magn Reson B*, vol. 103, no. 3, pp. 247–254, 1994.
- [149] D. Le Bihan, J. F. Mangin, C. Poupon, C. A. Clark, S. Pappata, N. Molko, and H. Chabriat, "Diffusion tensor imaging: Concepts and applications," *J Magn Reson Imaging*, vol. 13, no. 4, pp. 534–546, 2001.
- [150] M. W. Woolrich, S. Jbabdi, B. Patenaude, M. Chappell, S. Makni, T. Behrens, C. Beckmann, M. Jenkinson, and S. M. Smith, "Bayesian analysis of neuroimaging data in FSL," *NeuroImage*, vol. 45, no. 1 Suppl, pp. S173–186, 2009.
- [151] M. Jenkinson and S. Smith, "A global optimisation method for robust affine registration of brain images," *Med Image Anal*, vol. 5, no. 2, pp. 143–156, 2001.
- [152] M. Jenkinson, P. Bannister, M. Brady, and S. Smith, "Improved optimization for the robust and accurate linear registration and motion correction of brain images," *NeuroImage*, vol. 17, no. 2, pp. 825–841, 2002.
- [153] T. E. Behrens, M. W. Woolrich, M. Jenkinson, H. Johansen-Berg, R. G. Nunes, S. Clare, P. M. Matthews, J. M. Brady, and S. M. Smith, "Characterization and propagation of uncertainty in diffusion-weighted MR imaging," *Magn Reson Med*, vol. 50, no. 5, pp. 1077–1088, 2003.
- [154] T. E. Behrens, H. J. Berg, S. Jbabdi, M. F. Rushworth, and M. W. Woolrich, "Probabilistic diffusion tractography with multiple fibre orientations: What can we gain?," *NeuroImage*, vol. 34, no. 1, pp. 144–155, 2007.
- [155] P. J. Basser and C. Pierpaoli, "A simplified method to measure the diffusion tensor from seven MR images," *Magn Reson Med*, vol. 39, no. 6, pp. 928–934, 1998.

- 
- [156] F. Hyder, “Dynamic imaging of brain function,” *Methods Mol Biol*, vol. 489, pp. 3–21, 2009.
- [157] M. E. Raichle and D. A. Gusnard, “Appraising the brain’s energy budget,” *Proc Natl Acad Sci USA*, vol. 99, no. 16, pp. 10237–10239, 2002.
- [158] H. Gray and W. Lewis, *Anatomy of the Human Body*. Lea and Febiger, 1918.
- [159] J. Linn, *Atlas Klinische Neuroradiologie des Gehirns*, book section Anatomie. Berlin, Heidelberg: Springer, 2011.
- [160] N. D. Forkert, J. Fiehler, S. Suniaga, H. Wersching, S. Knecht, and A. Kemmling, “A statistical cerebroarterial atlas derived from 700 MRA datasets,” *Methods Inf Med*, vol. 52, no. 6, pp. 467–474, 2013.
- [161] Rbcastilhos, “Schematic representation of the circle of willis, arteries of the brain and brain stem,” 2007. [https://en.wikipedia.org/wiki/Circle\\_of\\_Willis#/media/File:Circle\\_of\\_Willis\\_en.svg](https://en.wikipedia.org/wiki/Circle_of_Willis#/media/File:Circle_of_Willis_en.svg), accessed 04.04.2020.
- [162] A. van der Zwan, B. Hillen, C. A. Tulleken, M. Dujovny, and L. Dragovic, “Variability of the territories of the major cerebral arteries,” *J Neurosurg*, vol. 77, no. 6, pp. 927–940, 1992.
- [163] A. van der Zwan, B. Hillen, C. A. Tulleken, and M. Dujovny, “A quantitative investigation of the variability of the major cerebral arterial territories,” *Stroke*, vol. 24, no. 12, pp. 1951–1959, 1993.
- [164] I. Momjian-Mayor and J. C. Baron, “The pathophysiology of watershed infarction in internal carotid artery disease: Review of cerebral perfusion studies,” *Stroke*, vol. 36, no. 3, pp. 567–577, 2005.
- [165] J. Linn, M. Wiesmann, and H. Brückmann, *Vaskuläre Erkrankungen*, pp. 77–192. Berlin, Heidelberg: Springer Berlin Heidelberg, 2011.
- [166] H.-H. Eckstein, A. Kuehnl, J. Berkefeld, R. Diel, A. Doerfler, I. Kopp, R. Langhoff, H. Lawall, P. Ringleb, D. Sander, M. Storck, G. Antoniadis, C. Arning, H. Brueckmann, C. Diehm, I. Flessenkaemper, G. Fraedrich, A. Fruend, S. George, M. Goertler, H. Goertz, W. Gross-Fengels, M. Hennerici, U. Hoffmann, A. Hoerstgen, P. Huppert, O. Jansen, R. Litz, H. Mudra, D. G. Nabavi, E. Neugebauer, H. Niedermeier, C. Ploenes, R. Stingege, B. Rantner, J. Tacke, O. Schnell, K. Schulte, K. Schwerdtfeger, D. Vorwerk, K. P. Wallushek, and G. Walter-Busch, “S3-leitlinie zur diagnostik, therapie und nachsorge der extracraniellen carotisstenose,” Report AWMF-Register Nr. 004/028, Technical University of Munich (TUM), 2012.
- [167] D. Sander, C. Diehm, H. H. Eckstein, A. Kühnl, J. Berkefeld, R. Diel, A. Dörfler, I. Kopp, R. Langhoff, H. Lawall, P. Ringleb, and M. Storck, “S3-leitlinie extracranielle carotisstenose,” *Gefässchirurgie*, vol. 17, no. 6, pp. 497–501, 2012.
- [168] Blausen.com, “Carotid artery stenosis,” *WikiJournal of Medicine: Medical gallery of Blausen Medical 2014*, vol. 1, no. 2, 2014.
- [169] A. Ringer and L. Jimenez, 2018. <https://mayfieldclinic.com/pe-stroke.htm>, accessed 04.04.2020.

- [170] M. D. Walker, J. R. Marler, M. Goldstein, P. A. Grady, J. F. Toole, W. H. Baker, J. E. Castaldo, L. E. Chambless, W. S. Moore, J. T. Robertson, B. Young, V. J. Howard, S. Purvis, D. D. Vernon, K. Needham, P. Beck, V. J. Celani, L. Sauerbeck, J. A. von Rajes, and D. Atkins, "Endarterectomy for asymptomatic carotid artery stenosis," *JAMA*, vol. 273, no. 18, pp. 1421–1428, 1995.
- [171] R. S. Marshall, R. M. Lazar, D. S. Liebeskind, E. S. Connolly, G. Howard, B. K. Lal, J. Huston, J. F. Meschia, and T. G. Brott, "Carotid revascularization and medical management for asymptomatic carotid stenosis - hemodynamics (CREST-H): Study design and rationale," *Int J Stroke*, vol. 13, no. 9, pp. 985–991, 2018.
- [172] R. Rezzani, *Carotid Artery Disease: From Bench to Bedside and Beyond*. IntechOpen, 2014.
- [173] NASCET Steering Committee, "North american symptomatic carotid endarterectomy trial. Methods, patient characteristics, and progress," *Stroke*, vol. 22, no. 6, pp. 711–720, 1991.
- [174] D. Vyas, N. Gupta, S. Changgani, and V. Mittal, *Comprehensive Textbook of Surgery*. Jaypee Brothers, Medical Publishers Pvt. Limited, 2012.
- [175] S. Demirel, D. Böckler, and M. Storck, "Comparison of long-term results of carotid endarterectomy for asymptomatic carotid artery stenosis," *Gefasschirurgie*, vol. 23, no. Suppl 1, pp. 1–7, 2018.
- [176] G. G. Ferguson, M. Eliasziw, H. W. Barr, G. P. Clagett, R. W. Barnes, M. C. Wallace, D. W. Taylor, R. B. Haynes, J. W. Finan, V. C. Hachinski, and H. J. Barnett, "The north american symptomatic carotid endarterectomy trial: Surgical results in 1415 patients," *Stroke*, vol. 30, no. 9, pp. 1751–1758, 1999.
- [177] B. R. Chambers and J. W. Norris, "Outcome in patients with asymptomatic neck bruits," *N Engl J Med*, vol. 315, no. 14, pp. 860–865, 1986.
- [178] M. O'Brien and A. Chandra, "Carotid revascularization: Risks and benefits," *Vasc Health Risk Manag*, vol. 10, pp. 403–416, 2014.
- [179] W. J. Powers, G. A. Press, R. L. Grubb, M. Gado, and M. E. Raichle, "The effect of hemodynamically significant carotid artery disease on the hemodynamic status of the cerebral circulation," *Ann Intern Med*, vol. 106, no. 1, pp. 27–34, 1987.
- [180] L. Zarrinkoob, A. Wahlin, K. Ambarki, R. Birgander, A. Eklund, and J. Malm, "Blood flow lateralization and collateral compensatory mechanisms in patients with carotid artery stenosis," *Stroke*, vol. 50, no. 5, pp. 1081–1088, 2019.
- [181] P. J. van Laar, J. van der Grond, J. P. Bremmer, C. J. Klijn, and J. Hendrikse, "Assessment of the contribution of the external carotid artery to brain perfusion in patients with internal carotid artery occlusion," *Stroke*, vol. 39, no. 11, pp. 3003–3008, 2008.
- [182] R. Willinsky, *Diseases of the Brain, Head and Neck, Spine: Diagnostic Imaging and Interventional Techniques 40th International Diagnostic Course in Davos (IDKD)*. Springer Milan, 2008.

- [183] A. L. Manninen, J. M. Isokangas, A. Karttunen, T. Siniluoto, and M. T. Nieminen, "A comparison of radiation exposure between diagnostic cta and dsa examinations of cerebral and cervicocerebral vessels," *Am J Neuroradiol*, vol. 33, no. 11, pp. 2038–2042, 2012.
- [184] M. Menken and United States. Congress. Office of Technology Assessment, *The Cost Effectiveness of Digital Subtraction Angiography in the Diagnosis of Cerebrovascular Disease*. Congress of the U.S., Office of Technology Assessment, 1985.
- [185] K. J. Gorgolewski, T. Auer, V. D. Calhoun, R. C. Craddock, S. Das, E. P. Duff, G. Flandin, S. S. Ghosh, T. Glatard, Y. O. Halchenko, D. A. Handwerker, M. Hanke, D. Keator, X. Li, Z. Michael, C. Maumet, B. N. Nichols, T. E. Nichols, J. Pellman, J. B. Poline, A. Rokem, G. Schaefer, V. Sochat, W. Triplett, J. A. Turner, G. Varoquaux, and R. A. Poldrack, "The brain imaging data structure, a format for organizing and describing outputs of neuroimaging experiments," *Sci Data*, vol. 3, p. 160044, 2016.
- [186] S. Kaczmarz, V. Griese, C. Preibisch, M. Kallmayer, M. Helle, I. Wustrow, E. T. Petersen, H. H. Eckstein, C. Zimmer, C. Sorg, and J. Goettler, "Increased variability of watershed areas in patients with high-grade carotid stenosis," *Neuroradiology*, vol. 60, no. 3, pp. 311–323, 2018.
- [187] S. Kaczmarz, J. Goettler, C. Zimmer, F. Hyder, and C. Preibisch, "Characterizing white matter fiber orientation effects on multi-parametric quantitative bold assessment of oxygen extraction fraction," *J Cereb Blood Flow Metab*, vol. 40, no. 4, pp. 760–774, 2020.
- [188] S. Kaczmarz, J. Goettler, J. Petr, M. B. Hansen, K. Mouridsen, C. Zimmer, F. Hyder, and C. Preibisch, "Hemodynamic impairments within individual watershed areas in asymptomatic carotid artery stenosis by multimodal MRI," *J Cereb Blood Flow Metab*, p. 271678X20912364, 2020.
- [189] S. Kaczmarz, F. Hyder, and C. Preibisch, "Oxygen extraction fraction mapping with multi-parametric quantitative BOLD MRI: Reduced transverse relaxation bias using 3D-GraSE imaging," *NeuroImage*, vol. 220, p. 117095, 2020.
- [190] M. Wiart, Y. Berthezène, P. Adeleine, P. Feugier, P. Trouillas, J.-C. Froment, and N. Nighoghossian, "Vasodilatory response of border zones to acetazolamide before and after endarterectomy," *Stroke*, vol. 31, no. 7, pp. 1561–1565, 2000.
- [191] M. Silvestrini, F. Vernieri, P. Pasqualetti, M. Matteis, F. Passarelli, E. Troisi, and C. Caltagirone, "Impaired cerebral vasoreactivity and risk of stroke in patients with asymptomatic carotid artery stenosis," *JAMA*, vol. 283, no. 16, pp. 2122–2127, 2000.
- [192] J. Schroeder, M. Heinze, M. Guenther, B. Cheng, A. Nickel, T. Schroeder, F. Fischer, S. S. Kessner, T. Magnus, J. Fiehler, A. Larena-Avellaneda, C. Gerloff, and G. Thomalla, "Dynamics of brain perfusion and cognitive performance in revascularization of carotid artery stenosis," *NeuroImage: Clinical*, vol. 22, p. 101779, 2019.
- [193] M. S. Park, S. Kwon, M. J. Lee, K. H. Kim, P. Jeon, Y. J. Park, D. I. Kim, Y. W. Kim, O. Y. Bang, C. S. Chung, K. H. Lee, and G. M. Kim, "Identification of high risk carotid artery stenosis: A multimodal vascular and perfusion imaging study," *Front Neurol*, vol. 10, p. 765, 2019.

- [194] S. Mundiyanapurath, P. A. Ringleb, S. Diatschuk, M. B. Hansen, K. Mouridsen, L. Østergaard, W. Wick, M. Bendszus, and A. Radbruch, “Capillary transit time heterogeneity is associated with modified rankin scale score at discharge in patients with bilateral high grade internal carotid artery stenosis,” *PLoS One*, vol. 11, no. 6, p. e0158148, 2016.
- [195] D. J. Lythgoe, L. Østergaard, S. C. R. Williams, A. Cluckie, M. Buxton-Thomas, A. Simmons, and H. S. Markus, “Quantitative perfusion imaging in carotid artery stenosis using dynamic susceptibility contrast-enhanced magnetic resonance imaging,” *Magn Reson Imaging*, vol. 18, no. 1, pp. 1–11, 2000.
- [196] B. K. Lal, M. C. Dux, S. Sikdar, C. Goldstein, A. A. Khan, J. Yokemick, and L. Zhao, “Asymptomatic carotid stenosis is associated with cognitive impairment,” *J Vasc Surg*, vol. 66, no. 4, pp. 1083–1092, 2017.
- [197] B. K. Lal, J. F. Meschia, and T. G. Brott, “Clinical need, design, and goals for the carotid revascularization and medical management for asymptomatic carotid stenosis trial,” *Semin Vasc Surg*, vol. 30, no. 1, pp. 2–7, 2017.
- [198] V. J. Howard, J. F. Meschia, B. K. Lal, T. N. Turan, G. S. Roubin, R. D. Brown, J. H. Voeks, K. M. Barrett, B. M. Demaerschalk, J. Huston, R. M. Lazar, W. S. Moore, V. G. Wadley, S. Chaturvedi, C. S. Moy, M. Chimowitz, G. Howard, T. G. Brott, and CREST-study investigators, “Carotid revascularization and medical management for asymptomatic carotid stenosis: Protocol of the CREST-2 clinical trials,” *Int J Stroke*, vol. 12, no. 7, pp. 770–778, 2017.
- [199] A. Hino, H. Tenjin, Y. Horikawa, M. Fujimoto, and Y. Imahori, “Hemodynamic and metabolic changes after carotid endarterectomy in patients with high-degree carotid artery stenosis,” *J Stroke Cerebrovasc Dis*, vol. 14, no. 6, pp. 234–238, 2005.
- [200] A. Gupta, J. L. Chazen, M. Hartman, D. Delgado, N. Anumula, H. Shao, M. Mazumdar, A. Z. Segal, H. Kamel, D. Leifer, and P. C. Sanelli, “Cerebrovascular reserve and stroke risk in patients with carotid stenosis or occlusion: A systematic review and meta-analysis,” *Stroke*, vol. 43, no. 11, pp. 2884–2891, 2012.
- [201] W. J. Powers, “Cerebral hemodynamics in ischemic cerebrovascular disease,” *Ann Neurol*, vol. 29, no. 3, pp. 231–240, 1991.
- [202] U. Dirnagl and W. Pulsinelli, “Autoregulation of cerebral blood flow in experimental focal brain ischemia,” *J Cereb Blood Flow Metab*, vol. 10, no. 3, pp. 327–336, 1990.
- [203] J. Bouvier, O. Detante, F. Tahon, A. Attie, T. Perret, D. Chechin, M. Barbieux, K. Boubagra, K. Garambois, I. Tropres, S. Grand, E. L. Barbier, and A. Krainik, “Reduced CMRO<sub>2</sub> and cerebrovascular reserve in patients with severe intracranial arterial stenosis: A combined multiparametric qBOLD oxygenation and BOLD fMRI study,” *Hum Brain Mapp*, vol. 36, no. 2, pp. 695–706, 2015.
- [204] J. Hendrikse, M. J. Hartkamp, B. Hillen, W. P. Mali, and J. van der Grond, “Collateral ability of the circle of willis in patients with unilateral internal carotid artery occlusion: Border zone infarcts and clinical symptoms,” *Stroke*, vol. 32, no. 12, pp. 2768–2773, 2001.

- [205] J. A. Fisher, O. Sobczyk, A. Crawley, J. Poubanc, P. Dufort, L. Venkatraghavan, K. Sam, D. Mikulis, and J. Duffin, "Assessing cerebrovascular reactivity by the pattern of response to progressive hypercapnia," *Hum Brain Mapp*, vol. 38, no. 7, pp. 3415–3427, 2017.
- [206] S. Xie, L. H. Hui, J. X. Xiao, X. D. Zhang, and Q. Peng, "Detecting misery perfusion in unilateral steno-occlusive disease of the internal carotid artery or middle cerebral artery by MR imaging," *Am J Neuroradiol*, vol. 32, no. 8, pp. 1504–1509, 2011.
- [207] R. Leblanc, Y. Lucas Yamamoto, J. L. Tyler, M. Diksic, and A. Hakim, "Borderzone ischemia," *Annals of Neurology*, vol. 22, no. 6, pp. 707–713, 1987.
- [208] M. D. Sette, M. Eliasziw, J. Y. Streifler, V. C. Hachinski, A. J. Fox, and H. J. M. Barnett, "Internal borderzone infarction," *Stroke*, vol. 31, no. 3, pp. 631–636, 2000.
- [209] V. Richter, M. Helle, M. J. van Osch, T. Lindner, A. S. Gersing, P. Tsantilas, H. H. Eckstein, C. Preibisch, and C. Zimmer, "MR Imaging of individual perfusion reorganization using superselective pseudocontinuous arterial spin-labeling in patients with complex extracranial steno-occlusive disease," *Am J Neuroradiol*, vol. 38, no. 4, pp. 703–711, 2017.
- [210] P. J. van Laar, J. Hendrikse, C. J. Klijn, L. J. Kappelle, M. J. van Osch, and J. van der Grond, "Symptomatic carotid artery occlusion: Flow territories of major brain-feeding arteries," *Radiology*, vol. 242, no. 2, pp. 526–534, 2007.
- [211] M. Helle, S. Rufer, M. J. van Osch, A. Nabavi, K. Alfke, D. G. Norris, and O. Jansen, "Superselective arterial spin labeling applied for flow territory mapping in various cerebrovascular diseases," *J Magn Reson Imaging*, vol. 38, no. 2, pp. 496–503, 2013.
- [212] D. F. Arteaga, M. K. Strother, L. T. Davis, M. R. Fusco, C. C. Faraco, B. A. Roach, A. O. Scott, and M. J. Donahue, "Planning-free cerebral blood flow territory mapping in patients with intracranial arterial stenosis," *J Cereb Blood Flow Metab*, vol. 37, no. 6, pp. 1944–1958, 2017.
- [213] J. Sobesky, O. Zaro Weber, F. G. Lehnhardt, V. Hesselmann, A. Thiel, C. Dohmen, A. Jacobs, M. Neveling, and W. D. Heiss, "Which time-to-peak threshold best identifies penumbral flow? A comparison of perfusion-weighted magnetic resonance imaging and positron emission tomography in acute ischemic stroke," *Stroke*, vol. 35, no. 12, pp. 2843–2847, 2004.
- [214] C. B. Grandin, T. P. Duprez, A. M. Smith, C. Oppenheim, A. Peeters, A. R. Robert, and G. Cosnard, "Which MR-derived perfusion parameters are the best predictors of infarct growth in hyperacute stroke? Comparative study between relative and quantitative measurements," *Radiology*, vol. 223, no. 2, pp. 361–370, 2002.
- [215] M. Lee, G. Zaharchuk, R. Guzman, A. Achrol, T. Bell-Stephens, and G. K. Steinberg, "Quantitative hemodynamic studies in moyamoya disease: A review," *Neurosurg Focus*, vol. 26, no. 4, p. E5, 2009.
- [216] K. Taneja, H. Lu, B. G. Welch, B. P. Thomas, M. Pinho, D. Lin, A. E. Hillis, and P. Liu, "Evaluation of cerebrovascular reserve in patients with cerebrovascular diseases using resting-state MRI: A feasibility study," *Magn Reson Imaging*, vol. 59, pp. 46–52, 2019.

- [217] M. Kluytmans, J. van der Grond, P. J. Folkers, W. P. Mali, and M. A. Viergever, "Differentiation of gray matter and white matter perfusion in patients with unilateral internal carotid artery occlusion," *J Magn Reson Imaging*, vol. 8, no. 4, pp. 767–774, 1998.
- [218] F. Calamante, M. Morup, and L. K. Hansen, "Defining a local arterial input function for perfusion MRI using independent component analysis," *Magn Reson Med*, vol. 52, no. 4, pp. 789–797, 2004.
- [219] J. M. Gibbs, K. L. Leenders, R. J. S. Wise, and T. Jones, "Evaluation of cerebral perfusion reserve in patients with carotid-artery occlusion," *The Lancet*, vol. 323, no. 8372, pp. 310–314, 1984.
- [220] L. Østergaard, S. N. Jespersen, T. Engedahl, E. Gutierrez Jimenez, M. Ashkanian, M. B. Hansen, S. Eskildsen, and K. Mouridsen, "Capillary dysfunction: Its detection and causative role in dementias and stroke," *Curr Neurol Neurosci Rep*, vol. 15, no. 6, p. 37, 2015.
- [221] E. M. Arsava, M. B. Hansen, B. Kaplan, A. Peker, R. Gocmen, A. Arat, K. K. Oguz, M. A. Topcuoglu, L. Østergaard, and T. Dalkara, "The effect of carotid artery stenting on capillary transit time heterogeneity in patients with carotid artery stenosis," *Eur Stroke J*, vol. 3, no. 3, pp. 263–271, 2018.
- [222] H. Angleys, L. Østergaard, and S. N. Jespersen, "The effects of capillary transit time heterogeneity (CTH) on brain oxygenation," *J Cereb Blood Flow Metab*, vol. 35, no. 5, pp. 806–817, 2015.
- [223] E. T. Petersen, I. Zimine, Y. C. Ho, and X. Golay, "Non-invasive measurement of perfusion: A critical review of arterial spin labelling techniques," *Br J Radiol*, vol. 79, no. 944, pp. 688–701, 2006.
- [224] H. J. M. M. Mutsaerts, M. J. P. van Osch, F. O. Zelaya, D. J. J. Wang, W. Nordhøy, Y. Wang, S. Wastling, M. A. Fernandez-Seara, E. T. Petersen, F. B. Pizzini, S. Fallatah, J. Hendrikse, O. Geier, M. Günther, X. Golay, A. J. Nederveen, A. Bjørnerud, and I. R. Groote, "Multi-vendor reliability of arterial spin labeling perfusion MRI using a near-identical sequence: Implications for multi-center studies," *NeuroImage*, vol. 113, pp. 143–152, 2015.
- [225] M. Grade, J. A. Hernandez Tamames, F. B. Pizzini, E. Achten, X. Golay, and M. Smits, "A neuroradiologist's guide to arterial spin labeling MRI in clinical practice," *Neuroradiology*, vol. 57, no. 12, pp. 1181–1202, 2015.
- [226] J. B. De Vis, E. T. Petersen, A. Bhogal, N. S. Hartkamp, C. J. Klijn, L. J. Kappelle, and J. Hendrikse, "Calibrated MRI to evaluate cerebral hemodynamics in patients with an internal carotid artery occlusion," *J Cereb Blood Flow Metab*, vol. 35, no. 6, pp. 1015–1023, 2015.
- [227] M. J. van Osch, W. M. Teeuwisse, M. A. van Walderveen, J. Hendrikse, D. A. Kies, and M. A. van Buchem, "Can arterial spin labeling detect white matter perfusion signal?," *Magn Reson Med*, vol. 62, no. 1, pp. 165–173, 2009.



- 
- [228] J. J. Chen, “Functional MRI of brain physiology in aging and neurodegenerative diseases,” *NeuroImage*, vol. 187, pp. 209–225, 2019.
- [229] F. B. Tancredi, I. Lajoie, and R. D. Hoge, “Test-retest reliability of cerebral blood flow and blood oxygenation level-dependent responses to hypercapnia and hyperoxia using dual-echo pseudo-continuous arterial spin labeling and step changes in the fractional composition of inspired gases,” *J Magn Reson Imaging*, vol. 42, no. 4, pp. 1144–1157, 2015.
- [230] J. B. De Vis, A. A. Bhogal, J. Hendrikse, E. T. Petersen, and J. C. W. Siero, “Effect sizes of BOLD CVR, resting-state signal fluctuations and time delay measures for the assessment of hemodynamic impairment in carotid occlusion patients,” *NeuroImage*, vol. 179, pp. 530–539, 2018.
- [231] M. J. Donahue, L. M. Dethrage, C. C. Faraco, L. C. Jordan, P. Clemmons, R. Singer, J. Mocco, Y. Shyr, A. Desai, A. O’Duffy, D. Riebau, L. Hermann, J. Connors, H. Kirshner, and M. K. Strother, “Routine clinical evaluation of cerebrovascular reserve capacity using carbogen in patients with intracranial stenosis,” *Stroke*, vol. 45, no. 8, pp. 2335–2341, 2014.
- [232] K. Sam, E. Small, J. Poubanc, J. S. Han, D. M. Mandell, J. A. Fisher, A. P. Crawley, and D. J. Mikulis, “Reduced contralateral cerebrovascular reserve in patients with unilateral steno-occlusive disease,” *Cerebrovasc Dis*, vol. 38, no. 2, pp. 94–100, 2014.
- [233] K. Sam, J. Poubanc, O. Sobczyk, J. S. Han, A. Battisti-Charbonney, D. M. Mandell, M. Tymianski, A. P. Crawley, J. A. Fisher, and D. J. Mikulis, “Assessing the effect of unilateral cerebral revascularisation on the vascular reactivity of the non-intervened hemisphere: A retrospective observational study,” *BMJ Open*, vol. 5, no. 2, p. e006014, 2015.
- [234] D. M. Mandell, J. S. Han, J. Poubanc, A. P. Crawley, A. Kassner, J. A. Fisher, and D. J. Mikulis, “Selective reduction of blood flow to white matter during hypercapnia corresponds with leukoaraiosis,” *Stroke*, vol. 39, no. 7, pp. 1993–1998, 2008.
- [235] B. P. Thomas, P. Liu, D. C. Park, M. J. van Osch, and H. Lu, “Cerebrovascular reactivity in the brain white matter: Magnitude, temporal characteristics, and age effects,” *J Cereb Blood Flow Metab*, vol. 34, no. 2, pp. 242–247, 2014.
- [236] P. C. van Zijl, S. M. Eleff, J. A. Ulatowski, J. M. Oja, A. M. Uluğ, R. J. Traystman, and R. A. Kauppinen, “Quantitative assessment of blood flow, blood volume and blood oxygenation effects in functional magnetic resonance imaging,” *Nat Med*, vol. 4, no. 2, pp. 159–167, 1998.
- [237] H. Lu and Y. Ge, “Quantitative evaluation of oxygenation in venous vessels using T2-Relaxation-Under-Spin-Tagging MRI,” *Magn Reson Med*, vol. 60, no. 2, pp. 357–363, 2008.
- [238] A. J. Stone, G. W. J. Harston, D. Carone, T. W. Okell, J. Kennedy, and N. P. Blockley, “Prospects for investigating brain oxygenation in acute stroke: Experience with a non-contrast quantitative BOLD based approach,” *Hum Brain Mapp*, vol. 40, no. 10, pp. 2853–2866, 2019.

- [239] J. Guo and E. C. Wong, "Venous oxygenation mapping using velocity-selective excitation and arterial nulling," *Magn Reson Med*, vol. 68, no. 5, pp. 1458–1471, 2012.
- [240] D. S. Bolar, B. R. Rosen, A. G. Sorensen, and E. Adalsteinsson, "QUantitative Imaging of eXtraction of oxygen and TIssue consumption (QUIXOTIC) using venular-targeted velocity-selective spin labeling," *Magn Reson Med*, vol. 66, no. 6, pp. 1550–1562, 2011.
- [241] E. M. Haacke, S. Lai, J. R. Reichenbach, K. Kuppusamy, F. G. Hoogenraad, H. Takeichi, and W. Lin, "In vivo measurement of blood oxygen saturation using magnetic resonance imaging: A direct validation of the blood oxygen level-dependent concept in functional brain imaging," *Hum Brain Mapp*, vol. 5, no. 5, pp. 341–346, 1997.
- [242] M. G. Bright, P. L. Croal, N. P. Blockley, and D. P. Bulte, "Multiparametric measurement of cerebral physiology using calibrated fMRI," *NeuroImage*, vol. 187, pp. 128–144, 2019.
- [243] C. J. Gauthier, L. Desjardins-Crepeau, C. Madjar, L. Bherer, and R. D. Hoge, "Absolute quantification of resting oxygen metabolism and metabolic reactivity during functional activation using QUO2 MRI," *NeuroImage*, vol. 63, no. 3, pp. 1353–1363, 2012.
- [244] R. G. Wise, A. D. Harris, A. J. Stone, and K. Murphy, "Measurement of OEF and absolute CMRO2: MRI-based methods using interleaved and combined hypercapnia and hyperoxia," *NeuroImage*, vol. 83, pp. 135–147, 2013.
- [245] J. Ma and F. W. Wehrli, "Method for image-based measurement of the reversible and irreversible contribution to the transverse-relaxation rate," *J Magn Reson B*, vol. 111, no. 1, pp. 61–69, 1996.
- [246] A. B. Simon, D. J. Dubowitz, N. P. Blockley, and R. B. Buxton, "A novel Bayesian approach to accounting for uncertainty in fMRI-derived estimates of cerebral oxygen metabolism fluctuations," *NeuroImage*, vol. 129, pp. 198–213, 2016.
- [247] A. J. Stone and N. P. Blockley, "A streamlined acquisition for mapping baseline brain oxygenation using quantitative bold," *NeuroImage*, vol. 147, pp. 79–88, 2017.
- [248] H. An and W. Lin, "Impact of intravascular signal on quantitative measures of cerebral oxygen extraction and blood volume under normo- and hypercapnic conditions using an asymmetric spin echo approach," *Magn Reson Med*, vol. 50, no. 4, pp. 708–716, 2003.
- [249] H. An and W. Lin, "Quantitative measurements of cerebral blood oxygen saturation using magnetic resonance imaging," *J Cereb Blood Flow Metab*, vol. 20, no. 8, pp. 1225–1236, 2000.
- [250] W. Ni, T. Christen, Z. Zun, and G. Zaharchuk, "Comparison of R2' measurement methods in the normal brain at 3 Tesla," *Magn Reson Med*, vol. 73, no. 3, pp. 1228–1236, 2014.
- [251] T. Christen, H. Schmiedeskamp, M. Straka, R. Bammer, and G. Zaharchuk, "Measuring brain oxygenation in humans using a multiparametric quantitative blood oxygenation level dependent MRI approach," *Magn Reson Med*, vol. 68, no. 3, pp. 905–911, 2012.
- [252] N. M. Hirsch and C. Preibisch, "T2\* mapping with background gradient correction using different excitation pulse shapes," *Am J Neuroradiol*, vol. 34, no. 6, pp. E65–8, 2013.

- [253] C. Derdeyn, R. Grubb, and W. Powers, “Cerebral hemodynamic impairment,” *Methods of measurement and association with stroke risk*, vol. 53, no. 2, pp. 251–251, 1999.
- [254] C. P. Derdeyn, T. O. Videen, R. L. Grubb, and W. J. Powers, “Comparison of PET oxygen extraction fraction methods for the prediction of stroke risk,” *J Nucl Med*, vol. 42, no. 8, pp. 1195–1197, 2001.
- [255] L. Gagnon, S. Sakadzic, F. Lesage, J. J. Musacchia, J. Lefebvre, Q. Fang, M. A. Yucel, K. C. Evans, E. T. Mandeville, J. Cohen-Adad, J. R. Polimeni, M. A. Yaseen, E. H. Lo, D. N. Greve, R. B. Buxton, A. M. Dale, A. Devor, and D. A. Boas, “Quantifying the microvascular origin of BOLD-fMRI from first principles with two-photon microscopy and an oxygen-sensitive nanoprobe,” *J Neurosci*, vol. 35, no. 8, pp. 3663–3675, 2015.
- [256] J. Lee, H. G. Shin, W. Jung, Y. Nam, S. H. Oh, and J. Lee, “An R2\* model of white matter for fiber orientation and myelin concentration,” *NeuroImage*, vol. 162, pp. 269–275, 2017.
- [257] S.-H. Oh, Y.-B. Kim, Z.-H. Cho, and J. Lee, “Origin of B0 orientation dependent R2\* = 1/T2\* in white matter,” *NeuroImage*, vol. 73, pp. 71–79, 2013.
- [258] X. He and D. A. Yablonskiy, “Biophysical mechanisms of phase contrast in gradient echo MRI,” *Proc Natl Acad Sci USA*, vol. 106, no. 32, pp. 13558–13563, 2009.
- [259] J. Lee, P. van Gelderen, L. W. Kuo, H. Merkle, A. C. Silva, and J. H. Duyn, “T2\*-based fiber orientation mapping,” *NeuroImage*, vol. 57, no. 1, pp. 225–234, 2011.
- [260] S. Wharton and R. Bowtell, “Fiber orientation-dependent white matter contrast in gradient echo MRI,” *Proceedings of the National Academy of Sciences*, vol. 109, no. 45, p. 18559, 2012.
- [261] W. C. Chen, S. Foxley, and K. L. Miller, “Detecting microstructural properties of white matter based on compartmentalization of magnetic susceptibility,” *NeuroImage*, vol. 70, pp. 1–9, 2013.
- [262] S. Wharton and R. Bowtell, “Gradient echo based fiber orientation mapping using R2\* and frequency difference measurements,” *NeuroImage*, vol. 83, pp. 1011–1023, 2013.
- [263] D. A. Yablonskiy and A. L. Sukstanskii, “Generalized Lorentzian Tensor Approach (GLTA) as a Biophysical Background for Quantitative Susceptibility Mapping,” *Magn Reson Med*, vol. 73, no. 2, pp. 757–764, 2015.
- [264] D. A. Yablonskiy, W. R. Reinius, H. Stark, and E. M. Haacke, “Quantitation of T2’ anisotropic effects on magnetic resonance bone mineral density measurement,” *Magn Reson Med*, vol. 37, no. 2, pp. 214–221, 1997.
- [265] P. Sati, A. C. Silva, P. van Gelderen, M. I. Gaitan, J. E. Wohler, S. Jacobson, J. H. Duyn, and D. S. Reich, “In vivo quantification of T2\* anisotropy in white matter fibers in marmoset monkeys,” *NeuroImage*, vol. 59, no. 2, pp. 979–985, 2012.
- [266] A. Cherubini, P. Peran, G. E. Hagberg, A. E. Varsi, G. Luccichenti, C. Caltagirone, U. Sabatini, and G. Spalletta, “Characterization of white matter fiber bundles with T2\* relaxometry and diffusion tensor imaging,” *Magn Reson Med*, vol. 61, no. 5, pp. 1066–1072, 2009.

- [267] E. Hernandez-Torres, V. Wiggermann, S. Hametner, T. R. Baumeister, A. D. Sadovnick, Y. Zhao, L. Machan, D. K. Li, A. Traboulsee, and A. Rauscher, "Orientation dependent MR signal decay differentiates between people with ms, their asymptomatic siblings and unrelated healthy controls," *PLoS One*, vol. 10, no. 10, p. e0140956, 2015.
- [268] C. Liu, "Susceptibility tensor imaging," *Magn Reson Med*, vol. 63, no. 6, pp. 1471–1477, 2010.
- [269] J. Lee, K. Shmueli, M. Fukunaga, P. van Gelderen, H. Merkle, A. C. Silva, and J. H. Duyn, "Sensitivity of MRI resonance frequency to the orientation of brain tissue microstructure," *Proc Natl Acad Sci USA*, vol. 107, no. 11, pp. 5130–5135, 2010.
- [270] T. Q. Li, P. van Gelderen, H. Merkle, L. Talagala, A. P. Koretsky, and J. Duyn, "Extensive heterogeneity in white matter intensity in high-resolution T2\*-weighted MRI of the human brain at 7.0 T," *NeuroImage*, vol. 32, no. 3, pp. 1032–1040, 2006.
- [271] W. Li, B. Wu, A. V. Avram, and C. Liu, "Magnetic susceptibility anisotropy of human brain in vivo and its molecular underpinnings," *NeuroImage*, vol. 59, no. 3, pp. 2088–2097, 2012.
- [272] K. E. Chappell, M. D. Robson, A. Stonebridge-Foster, A. Glover, J. M. Allsop, A. D. Williams, A. H. Herlihy, J. Moss, P. Gishen, and G. M. Bydder, "Magic angle effects in MR neurography," *Am J Neuroradiol*, vol. 25, no. 3, pp. 431–440, 2004.
- [273] M. Germuska and R. G. Wise, "Calibrated fMRI for mapping absolute CMRO<sub>2</sub>: Practicalities and prospects," *NeuroImage*, vol. 187, pp. 145–153, 2019.
- [274] G. Zaharchuk, J. B. Mandeville, A. A. Bogdanov, R. Weissleder, B. R. Rosen, and J. J. Marota, "Cerebrovascular dynamics of autoregulation and hypoperfusion. An MRI study of CBF and changes in total and microvascular cerebral blood volume during hemorrhagic hypotension," *Stroke*, vol. 30, no. 10, pp. 2197–2045, 1999.
- [275] T. S. Engedal, N. Hjort, K. D. Hougaard, C. Z. Simonsen, G. Andersen, I. K. Mikkelsen, J. K. Boldsen, S. F. Eskildsen, M. B. Hansen, H. Angleys, S. N. Jespersen, S. Pedraza, T. H. Cho, J. Serena, S. Siemonsen, G. Thomalla, N. Nighoghossian, J. Fiehler, K. Mouridsen, and L. Østergaard, "Transit time homogenization in ischemic stroke - a novel biomarker of penumbral microvascular failure?," *J Cereb Blood Flow Metab*, vol. 38, no. 11, pp. 2006–2020, 2018.
- [276] A. P. Fan, J. Guo, M. M. Khalighi, P. K. Gulaka, B. Shen, J. H. Park, H. Gandhi, D. Holley, O. Rutledge, P. Singh, T. Haywood, G. K. Steinberg, F. T. Chin, and G. Zaharchuk, "Long-delay arterial spin labeling provides more accurate cerebral blood flow measurements in moyamoya patients: A simultaneous positron emission tomography/MRI study," *Stroke*, vol. 48, no. 9, pp. 2441–2449, 2017.
- [277] V. C. Keil, L. Eichhorn, H. Mutsaerts, F. Traber, W. Block, B. Madler, K. van de Ven, J. C. W. Siero, B. J. MacIntosh, J. Petr, R. Fimmers, H. H. Schild, and E. Hattingen, "Cerebrovascular reactivity during prolonged breath-hold in experienced freedivers," *Am J Neuroradiol*, vol. 39, no. 10, pp. 1839–1847, 2018.

- [278] T. W. Okell, M. A. Chappell, M. E. Kelly, and P. Jezzard, "Cerebral blood flow quantification using vessel-encoded arterial spin labeling," *J Cereb Blood Flow Metab*, vol. 33, no. 11, pp. 1716–1724, 2013.
- [279] H. J. Mutsaerts, J. Petr, L. Vaclavu, J. W. van Dalen, A. D. Robertson, M. W. Caan, M. Masellis, A. J. Nederveen, E. Richard, and B. J. MacIntosh, "The spatial coefficient of variation in arterial spin labeling cerebral blood flow images," *J Cereb Blood Flow Metab*, vol. 37, no. 9, pp. 3184–3192, 2017.
- [280] W. Dai, A. Shankaranarayanan, and D. C. Alsop, "Volumetric measurement of perfusion and arterial transit delay using hadamard encoded continuous arterial spin labeling," *Magn Reson Med*, vol. 69, no. 4, pp. 1014–1022, 2013.
- [281] W. M. Teeuwisse, S. Schmid, E. Ghariq, I. M. Veer, and M. J. van Osch, "Time-encoded pseudocontinuous arterial spin labeling: Basic properties and timing strategies for human applications," *Magn Reson Med*, vol. 72, no. 6, pp. 1712–1722, 2014.
- [282] F. von Samson-Himmelstjerna, V. I. Madai, J. Sobesky, and M. Guenther, "Walsh-ordered hadamard time-encoded pseudocontinuous ASL (WH pCASL)," *Magn Reson Med*, vol. 76, no. 6, pp. 1814–1824, 2015.
- [283] D. J. J. Wang, J. R. Alger, J. X. Qiao, M. Guenther, W. B. Pope, J. L. Saver, N. Salamon, D. S. Liebeskind, and U. S. I. for the, "Multi-delay multi-parametric arterial spin-labeled perfusion MRI in acute ischemic stroke - Comparison with dynamic susceptibility contrast enhanced perfusion imaging," *NeuroImage: Clinical*, vol. 3, pp. 1–7, 2013.
- [284] J. M. Watchmaker, B. D. Frederick, M. R. Fusco, L. T. Davis, M. R. Juttukonda, S. K. Lants, H. S. Kirshner, and M. J. Donahue, "Clinical use of cerebrovascular compliance imaging to evaluate revascularization in patients with moyamoya," *Neurosurgery*, vol. 84, no. 1, pp. 261–271, 2019.
- [285] M. R. Juttukonda and M. J. Donahue, "Neuroimaging of vascular reserve in patients with cerebrovascular diseases," *NeuroImage*, vol. 187, pp. 192–208, 2019.
- [286] J. Poublanc, J. S. Han, D. M. Mandell, J. Conklin, J. A. Stainsby, J. A. Fisher, D. J. Mikulis, and A. P. Crawley, "Vascular steal explains early paradoxical blood oxygen level-dependent cerebrovascular response in brain regions with delayed arterial transit times," *Cerebrovascular Diseases Extra*, vol. 3, no. 1, pp. 55–64, 2013.
- [287] A. P. Carlson, H. Yonas, Y. F. Chang, and E. M. Nemoto, "Failure of cerebral hemodynamic selection in general or of specific positron emission tomography methodology?: Carotid Occlusion Surgery Study (COSS)," *Stroke*, vol. 42, no. 12, pp. 3637–3639, 2011.
- [288] A. Seiler, A. Lauer, R. Deichmann, U. Noth, E. Herrmann, J. Berkefeld, O. C. Singer, W. Pfeilschifter, J. C. Klein, and M. Wagner, "Signal variance-based collateral index in dsc perfusion: A novel method to assess leptomeningeal collateralization in acute ischaemic stroke," *J Cereb Blood Flow Metab*, vol. 40, no. 3, pp. 574–587, 2020.
- [289] S. Schmid, W. M. Teeuwisse, H. Lu, and M. J. P. van Osch, "Time-efficient determination of spin compartments by time-encoded pCASL T2-Relaxation-Under-Spin-Tagging and its application in hemodynamic characterization of the cerebral border zones," *NeuroImage*, vol. 123, pp. 72–79, 2015.

- [290] M. S. Goyal, C. L. Hallemeier, G. J. Zipfel, K. M. Rich, R. L. Grubb, M. R. Chicoine, C. J. Moran, D. T. Cross, R. G. Dacey, and C. P. Derdeyn, "Clinical features and outcome in north american adults with idiopathic basal arterial occlusive disease without moyamoya collaterals," *Neurosurgery*, vol. 67, no. 2, pp. 278–285, 2010.
- [291] C. L. Hallemeier, K. M. Rich, R. L. Grubb, M. R. Chicoine, C. J. Moran, D. T. Cross, G. J. Zipfel, R. G. Dacey, and C. P. Derdeyn, "Clinical features and outcome in north american adults with moyamoya phenomenon," *Stroke*, vol. 37, no. 6, pp. 1490–1496, 2006.
- [292] R. M. Scott and E. R. Smith, "Moyamoya disease and moyamoya syndrome," *N Engl J Med*, vol. 360, no. 12, pp. 1226–1237, 2009.
- [293] M. Helle, F. Wenzel, K. van de Ven, and P. Boernert, "Advanced automatic planning for super-selective arterial spin labeling flow territory mapping," in *Proc of the 26th Annual Meeting of ISMRM*, 2018.
- [294] F. Hyder, R. G. Shulman, and D. L. Rothman, "A model for the regulation of cerebral oxygen delivery," *J Appl Physiol (1985)*, vol. 85, no. 2, pp. 554–564, 1998.
- [295] F. Hyder, R. P. Kennan, I. Kida, G. F. Mason, K. L. Behar, and D. Rothman, "Dependence of oxygen delivery on blood flow in rat brain: A 7 Tesla nuclear magnetic resonance study," *J Cereb Blood Flow Metab*, vol. 20, no. 3, pp. 485–498, 2000.
- [296] P. M. Rasmussen, S. N. Jespersen, and L. Østergaard, "The effects of transit time heterogeneity on brain oxygenation during rest and functional activation," *J Cereb Blood Flow Metab*, vol. 35, no. 3, pp. 432–442, 2015.
- [297] W. Reginold, K. Sam, J. Poublanc, J. Fisher, A. Crawley, and D. J. Mikulis, "The efficiency of the brain connectome is associated with cerebrovascular reactivity in persons with white matter hyperintensities," *Hum Brain Mapp*, vol. 40, no. 12, pp. 3647–3656, 2019.
- [298] K. Sam, A. P. Crawley, J. Poublanc, J. Conklin, O. Sobczyk, D. M. Mandell, J. Duffin, L. Venkatraghavan, J. A. Fisher, S. E. Black, and D. J. Mikulis, "Vascular dysfunction in leukoaraiosis," *Am J Neuroradiol*, vol. 37, no. 12, pp. 2258–2264, 2016.
- [299] K. Sam, J. Conklin, K. R. Holmes, O. Sobczyk, J. Poublanc, A. P. Crawley, D. M. Mandell, L. Venkatraghavan, J. Duffin, J. A. Fisher, S. E. Black, and D. J. Mikulis, "Impaired dynamic cerebrovascular response to hypercapnia predicts development of white matter hyperintensities," *NeuroImage: Clinical*, vol. 11, pp. 796–801, 2016.
- [300] L. Østergaard, T. S. Engedal, F. Moreton, M. B. Hansen, J. M. Wardlaw, T. Dalkara, H. S. Markus, and K. W. Muir, "Cerebral small vessel disease: Capillary pathways to stroke and cognitive decline," *J Cereb Blood Flow Metab*, vol. 36, no. 2, pp. 302–325, 2016.
- [301] O. C. Suter, T. Sunthorn, R. Kraftsik, J. Straubel, P. Darekar, K. Khalili, and J. Miklossy, "Cerebral hypoperfusion generates cortical watershed microinfarcts in alzheimer disease," *Stroke*, vol. 33, no. 8, pp. 1986–1992, 2002.

- 
- [302] M. E. Wolf, T. Sauer, R. Kern, K. Szabo, and M. G. Hennerici, “Multiple subcortical acute ischemic lesions reflect small vessel disease rather than cardiogenic embolism,” *J Neurol*, vol. 259, no. 9, pp. 1951–1957, 2012.
- [303] U. Jensen-Kondering, M. Helle, T. Lindner, O. Jansen, and A. Nabavi, “Non-invasive qualitative and semiquantitative presurgical investigation of the feeding vasculature to intracranial meningiomas using superselective arterial spin labeling,” *PLoS One*, vol. 14, no. 4, p. e0215145, 2019.
- [304] S. Schoen, J. Cabello, F. Liesche-Starnecker, M. Molina-Romero, P. Eichinger, M. Metz, I. Karimov, C. Preibisch, J. Keupp, A. Hock, B. Meyer, W. Weber, C. Zimmer, T. Pyka, I. Yakushev, J. Gempt, and B. Wiestler, “Imaging glioma biology: Spatial comparison of amino acid PET, amide proton transfer, and perfusion-weighted MRI in newly diagnosed gliomas,” *Eur J Nucl Med Mol Imaging*, vol. 47, no. 6, pp. 1468–1475, 2020.
- [305] C. Preibisch, C. Sorg, A. Förschler, T. Grimmer, I. Sax, A. M. Wohlschläger, R. Perneczky, H. Förstl, A. Kurz, C. Zimmer, and P. Alexopoulos, “Age-related cerebral perfusion changes in the parietal and temporal lobes measured by pulsed arterial spin labeling,” *J Magn Res Imaging*, vol. 34, no. 6, pp. 1295–1302, 2011.
- [306] R. B. Buxton, V. E. M. Griffeth, A. B. Simon, and F. Moradi, “Variability of the coupling of blood flow and oxygen metabolism responses in the brain: A problem for interpreting bold studies but potentially a new window on the underlying neural activity,” *Frontiers in Neuroscience*, vol. 8, p. 139, 2014.
- [307] H. Lu, “Physiological MRI of the brain: Emerging techniques and clinical applications,” *NeuroImage*, vol. 187, pp. 1–2, 2019.





# List of Symbols and Abbreviations

## Symbols

$\alpha$	flip angle [°]
$\chi$	magnetic susceptibility [–]
$\Delta B_i$	local magnetic field inhomogeneity [ $T$ ]
$\gamma$	gyromagnetic ratio [ $\text{Hz T}^{-1}$ ]
$\hbar$	reduced Planck constant [ $\text{J s rad}^{-1}$ ]
$\mu$	magnetic moment [ $\text{N m T}^{-1}$ ]
$\omega$	precession frequency [ $\text{rad s}^{-1}$ ]
$\omega_0$	Larmor frequency [ $\text{rad s}^{-1}$ ]
$\Phi$	phase angle [rad]
$\rho$	spin density [ $\text{m}^{-3}$ ]
$\tau$	magnetic torque [ $\text{N m}$ ]
$\tau_p$	radio frequency pulse duration [s]
$B$	magnetic field [ $T$ ]
$B_0$	static main magnetic field [ $T$ ]
$B_1$	radio frequency field [Hz]
$G$	gradient strength [ $\text{T m}^{-1}$ ]
$G_x$	magnetic gradient field along x dimension [ $\text{T m}^{-1}$ ]
$G_y$	magnetic gradient field along y dimension [ $\text{T m}^{-1}$ ]
$G_z$	magnetic gradient field along z dimension [ $\text{T m}^{-1}$ ]
$J$	intrinsic angular moment [ $\text{kg m}^2 \text{s}^{-1}$ ]
$k_B$	Boltzmann constant [ $\text{J K}^{-1}$ ]
$M$	bulk magnetic moment [ $\text{N m T}^{-1}$ ]
$M_0$	amplitude of the magnetization vector [–]

## List of Symbols and Abbreviations

---

$M_x$	spatial x component of the magnetization vector [–]
$M_y$	spatial y component of the magnetization vector [–]
$M_z$	spatial z component of the magnetization vector [–]
$R_2$	transverse relaxation rate [s <sup>-1</sup> ]
$R'_2$	reversible relaxation rate [s <sup>-1</sup> ]
$R_2^*$	effective relaxation rate [s <sup>-1</sup> ]
$T$	temperature [K]
$t$	time [s]
$T_1$	spin-lattice (longitudinal) relaxation time [s]
$T_2$	spin-spin (transverse) relaxation time [s]
$T'_2$	reversible relaxation time [s]
$T_2^*$	effective relaxation time [s]
$T_{pe}$	phase encoding time [s]

### Abbreviations

CMRO <sub>2</sub>	cerebral metabolic rate of oxygen consumption
CMRO <sub>Glc</sub>	cerebral metabolic rate of glucose metabolism
1D	one-dimensional
2D	two-dimensional
3D	three-dimensional
4D	four-dimensional
ACA	anterior cerebral artery
AD	Alzheimer's disease
ASE	asymmetric spin echo
ASL	arterial spin labeling
ATP	adenosine triphosphate
ATT	arterial transit time
BA	basilar artery
BAT	bolus arrival time
BBB	blood brain barrier

BET	brain extraction tool
BGS	background suppression
BH-fMRI	breath-hold functional magnetic resonance imaging
BIDS	standardized brain imaging data structure
BOLD	blood oxygenation level dependent
CA	contrast agent
CAS	carotid artery stenting
CASL	continuous arterial spin labeling
CBF	cerebral blood flow
CBV	cerebral blood volume
CEA	carotid endarterectomy
CoW	circle of Willis
CPMG	Carr-Purcell-Meiboom-Gill
CPP	cerebral perfusion pressure
CSF	cerebro spinal fluid
CT	computed tomography
CTH	capillary transit-time heterogeneity
CVD	cerebrovascular disease
CVR	cerebrovascular reactivity
DCE	dynamic contrast enhanced
DSA	digital subtraction angiography
DSC	dynamic susceptibility contrast
DTI	diffusion tensor imaging
DWI	diffusion weighted imaging
ECA	external carotid artery
EHC	elderly healthy control
EMA	European Medicines Agency
EPI	echo planar imaging
EU	European Union

## List of Symbols and Abbreviations

---

FA	fractional anisotropy
FDG	fluorodeoxyglucose
FDT	FMRIB diffusion toolbox
FID	free induction decay
FLAIR	fluid-attenuated inversion recovery
FLASH	fast low-angle shot
FLIRT	FMRIB linear image registration tool
fMRI	functional magnetic resonance imaging
FMRIB	Functional Magnetic Resonance Imaging of the Brain
FOV	field-of-view
FSL	FMRIB software library
Gd	gadolinium
Gd-DTPA	gadolinium-linked diethylenetriaminepentaacetic
GESFIDE	gradient echo sampling of free induction decay and echo
GESSE	gradient echo sampling of spin echo
GM	grey matter
GRAPPA	generalized autocalibrating partial parallel acquisition
GraSE	gradient and spin echo
GRE	gradient recalled echo
HC	healthy control
ICA	internal carotid artery
ICAS	internal carotid artery stenosis
IR	inversion recovery
iWSA	individual watershed area
MB	multi-band
MCA	middle cerebral artery
MNI	Montreal Neurological Institute
MP-RAGE	magnetization prepared rapid acquisition gradient echo
mq-BOLD	multi-parametric quantitative blood oxygenation level dependent

MRF	magnetic resonance fingerprinting
MRI	magnetic resonance imaging
MS	multiple sclerosis
NMR	nuclear magnetic resonance
NSF	nephrogenic systemic fibrosis
NVC	neuro-vascular coupling
OEC	oxygen extraction capacity
OECD	Organisation for Economic Co-operation and Development
OEF	oxygen extraction fraction
PASL	pulsed arterial spin labeling
PCA	posterior cerebral artery
pCASL	pseudo-continuous arterial spin labeling
PD	proton density
PET	positron emission tomography
PLD	post label delay
QSM	quantitative susceptibility mapping
QUIXOTIC	quantitative imaging of extraction of oxygen and tissue consumption
RARE	rapid acquisition with relaxation enhancement
rCBV	relative cerebral blood volume
rOEF	relative oxygen extraction fraction
rs-fMRI	resting-state functional magnetic resonance imaging
Rx	radio frequency reception
SAR	specific absorption rate
SE	spin echo
SENSE	sensitivity encoding
SNR	signal to noise ratio
SPM	statistical parametric mapping
ss-ASL	super-selective arterial spin labeling
SSS	superior sagittal sinus

## List of Symbols and Abbreviations

---

TE	echo time
TI	inversion time
TIA	transient ischemic attack
TR	repetition time
TRUST	T2-relaxation-under-spin-tagging
TTP	time-to-peak
Tx	radio frequency transmission
VA	vertebral arteries
VSEAN	velocity-selective excitation and arterial nulling
WM	white matter
WML	white matter lesion
WSA	watershed area
YHC	young healthy control



# List of Figures

2.1	<b>Pulse sequence diagram of free induction decay (FID) and spin echo (SE).</b> After excitation with a $90^\circ$ pulse, the FID signal decays with the time constant $T_2^*$ . By application of a $180^\circ$ inversion pulse at $TE/2$ , the transversal magnetization vector recovers and a (primary) spin echo (SE) is generated at $TE$ . The SE signal decays with the time constant $T_2$ . The secondary echo is not shown. Note that oscillations with the Larmor frequency would be much faster. Abbreviations: Tx, transmission; Rx, reception; TE, echo time; TR, repetition time. . . . .	26
2.2	<b>Pulse sequence diagram of a gradient recalled echo (GRE).</b> After excitation with a $90^\circ$ pulse, dephasing and rephasing gradients are subsequently applied go generate a GRE. Peaks of the GRE signal decay with the time constant $T_2^*$ , when assuming magnetic field inhomogeneities. Additional GRE could be generated by adding a series of dephasing and rephasing gradients at multiples of $TE$ . The higher order echoes are not shown. Note that oscillations with the Larmor frequency would be much faster. Abbreviations: Tx, transmission; G, gradient; Rx, reception; TE, echo time; TR, repetition time. . . . .	27
3.1	<b>Cerebral hemodynamic function.</b> (A) The vessels branch in the vascular tree to supply the capillaries with blood. (B) A magnified capillary shows the neuro-vascular unit. Red blood cells transport the oxygen, which diffuses through the vessel wall. Four major hemodynamic parameters are shown. The vessel diameter regulation by smooth muscle cells relates to the cerebrovascular reactivity (CVR), which affects the blood supply by cerebral blood flow (CBF) and the total cerebral blood volume (CBV), which can cause regulations of the oxygen diffusion to the tissue measured by the oxygen extraction fraction (OEF). Astrocytes extract glucose from the capillaries and supply the neurons with energy, which is required for neuronal signalling involving exchange of neurotransmitters through the synaptic gap. Images modified licensed under CC BY 3.0 from [46–48] and under public domain. . . . .	32
3.2	<b>Cerebral oxygen gradients.</b> Typical oxygen pressures in the blood compartments are illustrated. While the arterial oxygen pressure is fixed and determined by the lungs, oxygen pressure in the capillaries, veins and tissue can be modulated. For comparisons, atmospheric oxygen pressures are also shown. Image adapted from [20]. . . . .	34
3.3	<b>Tissue concentration-time curve in DSC imaging.</b> Time-dependent tissue concentration curves are acquired for every imaging voxel in DSC. In this case, 80 dynamics were acquired with a TR of approximately 1.5 s. The cerebral blood volume (CBV) is proportional to the area under the curve (blue, full pass integration). Local perfusion delay information are derived by the time-to-peak (TTP) (orange). . . . .	36

3.4	<b>Capillary transit time effects on capillary oxygen extraction.</b> During the passage of blood through the capillary bed, its oxygenation decreases (color coded). (A) Under healthy conditions, the flow is equally distributed across the capillaries with similar flow velocities (black arrows) with accordingly low capillary transit-time heterogeneity (CTH). (B) Contrary, several pathologies can cause CTH increases, which relates to varying flow velocities and oxygen extractions among capillaries. Note, that CTH can also affect the venous oxygen saturation. Figure adapted from [88, Fig.3]. . . . .	37
3.5	<b>Arterial spin labeling (ASL) workflow.</b> Control and label images, with labeling of inflowing arterial blood water, are acquired. During post processing, control and label images are subtracted to yield a cerebral blood flow weighted (CBFw) image. By an additionally acquired proton density weighted (PDw) image and further constants (see eq. 3.4), the quantitative CBF image is calculated. . . . .	38
3.6	<b>ASL kinetic curves.</b> The time dependencies of perfusion weighted signals are illustrated in two brain regions with shorter arterial transit time $ATT_1$ and longer $ATT_2$ . CBF imaging is supposed in the perfusion phase after bolus arrival at $PLD > ATT$ . In both regions, the bolus arrival time (BAT) is equal. Image adapted from [103, Fig.5]. . . . .	40
3.7	<b>Breathhold-fMRI post processing for cerebrovascular reactivity (CVR) mapping.</b> The time series of EPI images was acquired during a block design of 45 s normal breathing and 15 s breathhold with five repetitions. In model driven post-processing, regression analysis is applied with a respiratory response function for each voxel to calculate CVR maps [112]. Here, patient data with CVR impairments is shown, see Section 4.3. The locally reduced CVR indicates impaired hemodynamic function. . . . .	42
4.1	<b>Cerebral blood supply illustration.</b> Arteries (in red) show the blood passage from the two vertebral arteries in the neck, via principle intracranial arteries to arterial branching within the brain. Parts of the right hemisphere are not shown. Image under public domain from [158, Fig.516]. . . . .	47
4.2	<b>The major arteries in the right side of the neck.</b> The common carotid artery bifurcates into the external carotid artery and internal carotid artery, which supplies the brain with blood. The vertebral artery courses along the side of the neck and unites with the contralateral vertebral artery to the basilar artery. Image under public domain from [158, Fig.513]. . . . .	48
4.3	<b>Arterial circulation within the circle of Willis (CoW).</b> The internal carotid arteries and vertebral arteries can be connected via the anterior communicating artery and the posterior communicating arteries. Image under public domain from [161], adapted from image under public domain from [158, Fig.519].	49
4.4	<b>Perfusion territories on the outer surface of the cerebral hemisphere.</b> Typical areas supplied by the anterior cerebral artery (ACA) are shown in blue, middle cerebral artery (MCA) in red and posterior cerebral artery (PCA) in yellow. Image under public domain from [158, Fig.517]. . . . .	50

- 
- 4.5 **Illustration of right sided internal carotid artery stenosis.** Magnifications of the common carotid artery bifurcation (black box) under healthy conditions (A) is compared to a plaque at the ICA (B), which narrows the arterial lumen. Image modified licensed under CC BY 3.0 from [168]. . . . . 51
- 5.1 **Data processing pipeline.** (A) Based on the applied MRI sequences (light blue boxes), hemodynamic (orange) and structural parameter maps (green) were calculated with separate specific programs. (B) Those parameter maps were used to generate a uniform data base following the standardized brain imaging data structure (BIDS) structure. (C) Based on this data base, multi-parametric evaluations were performed on group level. For each journal publication, the evaluated parameters are summarized. . . . . 54



## List of Tables

- 5.1 **Summary of in-vivo study participants.** For each cohort, the number of scanned participants, related publications and selected abstracts are noted. . 53



# Acknowledgments

I am very grateful for the support during my time as a Ph.D. student at TUM. First of all, I want to thank my first supervisor PD Dr. Christine Preibisch for her outstanding supervision and providing me the freedom to realise my own projects. It is a great pleasure working in her NMRM group. Furthermore I want to thank my second supervisor Prof. Dr. Axel Haase and the head of the department Prof. Dr. Claus Zimmer for their exceptional support. This project was initially enabled by the trust and support of all three of you. During the project, PD Dr. Jens Goettler has been the major source of clinical input, thank you very much for the very enjoyable and highly successful cooperation over the last years at TUM and at Yale.

The close cooperation with Prof. Dr. Fahmeed Hyder from Yale University was an important milestone of this research project. I deeply thank him for giving me the opportunity to work in his group. His extraordinary and continuous support over the last years greatly contributed to the success of this work. I want to thank his whole research lab for creating such an enjoyable atmosphere while researching at Yale together with Jens: Dr. Peter Herman, Prof. Dr. Daniel Coman, John Walsh, Dave O'Connor, Dr. Yury Koush, Dr. Sam Maritim, Prof. Dr. Garth Thompson, Dr. Basav Sanganahalli, Dr. Muhammad Khan and Dr. Maxime Parent.

The stimulating atmosphere in the Kirchenhof essentially contributed to this project. I want to deeply thank Prof. Dr. Dimitrios Karampinos for enabling such an outstanding teamwork with the BMRR research group. Cordial thanks to our NMRM group and the whole Kirchenhof office team, who commonly created an incredibly enjoyable atmosphere over the last years: Stefan, Barbara, Markus, Dominik, Anne, Michael, Jens, Christian, Max, Vanessa, Rachel, Cagdas, Ilias, Sarah, Jan S., Sophia, Sean, Ronja, Daniela, Christoph, Christof, Jan K., Lena, Gabriel, Jim, Mario, Carina, Mark, Miriam and Ely. It was a great pleasure working together with all of you and attending numerous conferences and workshops together.

The extensively applied multi-parametric imaging was possible due to numerous collaborations with internationally leading experts in the field. In particular, I want to thank Dr. Jan Petr, Prof. Dr. Kim Mouridsen and Dr. Mikkel Bo Hansen for their great input and the successful collaboration. I also want to deeply thank PD Dr. Michael Helle, Dr. Andreas Hock, Dr. Hendrik Kooijman, Dr. Kim van de Ven, Dr. Makoto Obara and Dr. Carsten Liess from Philips Healthcare for their incredible support, especially on ASL imaging. Furthermore, great thanks to Prof. Dr. Matthias van Osch, Dr. Lena Václavů, Prof. Dr. Audrey Fan, Prof. Dr. Matthias Günther, Prof. Dr. Nicholas Blockley, Prof. Dr. Manus Donahue, Prof. Dr. Bruce Pike, Prof. Dr. Claudine Gauthier and Prof. Dr. Saito for their great input during fruitful discussions. Thank you all very much for the extremely positive experiences within the last years, which made it even more enjoyable to research. Those personal interactions were fundamentally facilitated by workshops and meetings of the ISMRM, ESMRMB, ISCBFM, SFN and DGMR. In particular, I want to thank the ESMRMB for being awarded as an Early Career Fellow 2020 and the opportunity to work in the Early Career Researchers Committee.

Furthermore, the interdisciplinary exchange within the Department of Neuroradiology and the TUM Neuro Imaging Center offered great opportunities to learn from each others different backgrounds. I want to thank especially PD Dr. Christian Sorg, PD Dr. Jan Kirschke, PD Dr. Nico Sollmann and PD Dr. Benedikt Wiestler.



## Acknowledgments

---

I am very grateful for the successful collaboration with Prof. Dr. Hans-Henning Eckstein and Dr. Michael Kallmayer from the Department of Vascular and Endovascular Surgery at TUM in the recruitment of ICAS patients. And I want to thank all participants of the included clinical studies.

This work would not have been possible without the great support by the administration. Thank you very much Sigrid Matussek from TUM, Simone Stoehr from Friedrich-Ebert-Stiftung (FES), Almut Barden, Manca Novinec Drenik, Nanna Gehrlein and Sarah Huber from TUM, as well as Lesley Nadeau-Foti from Yale University.

I am very grateful for the support from TUM Graduate School (TUM GS) and Medical Graduate Center (MGC) by providing a genuine framework with numerous excellent training and exchange opportunities.

Besides the personal support, I highly appreciate funding of this project by the FES, Deutsche Forschungsgemeinschaft (DFG), Deutscher Akademischer Austauschdienst (DAAD), European Union (EU), ISMRM, German chapter of ISMRM, ESMRMB, ISCBFM as well as Dr.-Ing. Leonhard Lorenz Stiftung.

And last but not least, I want to express my deepest thankfulness to my parents Peter and Martina, my partner and true love Christina as well as my friends, who were always loving and supportive. Thank you very much!

